PRIMARY AND SECONDARY CONTROLS ON PERMEABILITY OF THE PENNSYLVANIAN MASSILLON SANDSTONE, STARK COUNTY, OHIO, USA: IMPLICATIONS FOR THE CORRELATION OF DIAGENETIC ALTERATIONS AND STRUCTURAL AND TEXTURAL CHARACTERISTICS WITH LABORATORY BASED PERMEABILITY MEASUREMENTS

by

D. Michael Chapin, Jr.

Submitted in Partial Fulfillment
of the Requirements for the

Master of Science in Geology

New Mexico Institute of Mining and Technology
Department of Earth and Environmental Sciences
Socorro, New Mexico

November, 2001

ACKNOWLEDGMENTS

TABLE OF CONTENTS

LIST OF FIGURES

viii

LIST OF TABLES

ABSTRACT

An understanding of the primary (depositional) and secondary (diagenetic) controls on reservoir quality (specifically, porosity evolution and the permeability distribution) is essential for the accurate characterization of fluid flow within hydrocarbon reservoirs and aquifers. To better understand these controls, this thesis investigates porosity and permeability development in the cross-stratified, Pennsylvanian Massillon Sandstone, a coarse-grained, mature, hematitic and kaolinitic sublitharenite, which was deposited in a relatively high-energy, subaqueous environment. Petrographic modal analysis was performed on thin section subsections of: 1) four (horizontal to sub-horizontal), first and second-order, erosional bounding surface structures; and 2) 11, depositional, third-order, cross-stratification structures that lie at higher angles to and between the bounding structures. In addition, an extensive, single-phase permeability data set was generated in the lab from a face of the block, using a computer controlled, gas minipermeameter equipped with a tip seal having an inner radius of 0.15 cm.

Observations from modal analysis reveal that first-order bounding structures exhibit: the lowest mean permeabilities and porosities; the narrowest mean intergranular pore widths; the highest, mean volume % of ferroan cements; and the lowest, mean volume % of clay minerals. Third-order cross-stratification structures exhibit: the highest mean permeabilities and porosities; the largest, mean intergranular pore widths; the

lowest, mean volume % of matrix material including cements; and the highest, mean volume % of clay minerals.

Primary mineralogical and textural characteristics including framework grain composition, mean grain size and degree of sorting do not singularly control the laboratory measured permeability in the Massillon. The lack of strong relationships between permeability and textural elements is explained by the minor heterogeneities between mean grain sizes and the degree of grain sorting in each of the three structures. That is, the variation in grain size and sorting is too small to have caused considerable porosity and permeability differences.

Processes that reduced the effective pore connectivity are chemical and mechanical diagenesis, in particular, the precipitation of ferroan cements and authigenic kaolinite and a high degree of compaction evident from the high incidence of sutured framework grains. Late-stage, secondary dissolution porosity has significantly increased the reservoir quality and pore connectivity in the sandstone. Unfortunately, the diagenetic relationships with permeability are not as strong as expected. Despite this, multi-stage, secondary diagenetic alterations that produced pore occluding cements and matrix, grain rearrangement (compaction) and mineral dissolution are the most significant controls noted.

In an attempt to explain the absence of strong relationships between petrographic data and permeability measurements, structural image analysis was applied to rendered and binarized, thin section subsection images that isolated: 1) intergranular and intragranular macroporosity, and 2) non-framework, allogenic and authigenic matrix material and cements. The spatial continuity of pores and matrix were analyzed

employing three spectral analysis models: 1) the correlation length scale, 2) the fractal dimension, and 3) the radial spectra. Image analysis reveals that large, oversized, intergranular and intragranular pores are generally isolated features, whereas thinner lenses of dissolved clays and ferroan cements between the predominant quartz grains are more continuous lineaments. The mean fractal dimension supports this observation; the fractal dimension determined for matrix material and cements is lower than that for macroporosity, explaining a somewhat stronger correlation between matrix and permeability. Application of the correlation length scale and the radial spectra does not resolve the correlation problems. Weak relationships between measured permeability and primary, secondary and spatial controls reveal the complexity of diagenetic alterations affecting this sandstone and the inadequacy of relating two-dimensional modal and image analysis to three-dimensional permeability data.

CHAPTER 1: INTRODUCTION

1.1. Controls on Permeability Heterogeneity

Proficiency in modeling and prediction of subsurface fluid flow is an integral component of aquifer and reservoir analysis. The ability to positively correlate geologic variables controlling porosity and permeability with multi-scale laboratory derived data will contribute to a better understanding of hydrocarbon transport, enhanced oil recovery strategies from different reservoir lithologies, the removal of nonaqueous phase liquid contaminants from the vadose and phreatic zones, as well as other enhanced remediation and recovery techniques within the subsurface. With this in mind, many workers have directed their attention toward understanding the compositional, textural, depositional and diagenetic variables that potentially control permeability in sedimentary basins worldwide (Pryor, 1973; Mou and Brenner, 1982; Ehrlich et al., 1984; Berryman and Blair, 1986; Scherer, 1987; Daws and Prosser, 1992; Dutton and Diggs, 1992; Jordan and Pryor, 1992; Bjørlykke, 1993; Bryant et al., 1993; Clelland et al., 1993; Coskun et al., 1993; Ehrenberg and Boasson, 1993; Nelson, 1994; Wilson, 1994; Bryant et al., 1995; Tidwell and Wilson, 1997; Prince, 1999; and others). This thesis investigates the controls on the permeability distribution of the Pennsylvanian Massillon Sandstone in order to increase our understanding of the processes influencing fluid flux in a cross-stratified, sandstone aquifer. Controls on permeability addressed in this study include mineralogy and composition, textural and structural characteristics, diagenetic alterations, porosity types, as well as pore connectivity.

1.2. Objectives

The primary objectives of this study are: 1) to investigate the composition, structure, texture and diagenetic history of a cross-stratified block of the Massillon Sandstone, and 2) to assess the principal controls on the sandstone's porosity, pore structure and pore connectivity by correlating these geologic characteristics and controls to laboratory measured permeability data.

1.3. The Multisupport Gas Permeameter and the Massillon Sandstone

A multisupport gas permeameter (MSP) was developed at Sandia National Laboratory, Albuquerque, New Mexico, to investigate permeability upscaling in a controlled, laboratory environment (see Section 3.1 for a detailed description). Permeability is a measure of the capacity of a porous medium to transmit fluids and is a function of the pore size distribution and pore tortuosity. Permeability is also an important physical property of porous materials having connected void spaces, be they intergranular pores, vugs or fractures. The MSP measures the permeability of samples by compressing specifically designed tip seals across freshly cut, flat surfaces of selected lithologic blocks and regulating the flow of nitrogen passing through the tip seal into the rock faces. Tip seals with various inner radii are employed by the MSP, the diameters of which define the investigation's sample support (measurement scale) and establish the boundary conditions of the study (Tidwell and Wilson, 1997).

To date, the Mississippian Berea and the Pennsylvanian Massillon Sandstones, as well as several Quaternary welded tuffs and fossiliferous limestones have been examined at Sandia's lab to evaluate permeability upscaling. The cross-stratified Massillon

2

Sandstone was selected for this study due to it's structural heterogeneity, inherent permeability range and correlation scale. Tidwell and Wilson (1997) emphasize the importance of scale analysis when investigating the spatially distributed controls on measured permeability within reservoir lithologies.

1.4. Processes Controlling Porosity and Permeability in Sandstones

The effects of composition and texture on sandstone reservoirs have been studied by Beard and Weyl (1973), Davies and Ethridge (1975), Schmidt and McDonald (1979), Mou and Brenner (1982), Houseknecht (1984), Coskun et al. (1993), Hartkamp et al. (1993), Bloch (1994), Doyle and Sweet (1995), Hamlin et al. (1996), Ehrenberg (1997), and many others. Primary textural characteristics of sandstones include framework grain sizes, framework grain sorting, shape, roundness and fabric, such as grain to grain relationships addressing orientation and packing. Studies conducted by Beard and Weyl (1973), show that grain size and sorting are the most significant textural controls on porosity and permeability in unconsolidated sands, whereas individual grain shapes and roundness are of secondary importance. Their data indicates that porosity increases with better grain sorting and that the permeability of unconsolidated sand increases with increasing grain size and the degree of sorting. Poorly-sorted sediments generally have lower porosities and permeabilities than well-sorted sediments, because grains are packed more tightly in these sediments, with fines filling spaces among larger grains (Boggs, 1995). The grain size controls both the structural framework of the unconsolidated sediment as well as the mean size of voids between framework grains (Prince, 1999).

Various factors that control the grain size and the sorting of sandstones include differences in depositional energy, biogenic activity and depositional climate (Bloch and McGowen, 1994), whereas grain shape and rounding are a function of grain composition, grain size, provenance, and transport distance (Pettijohn et al., 1973). Structural (megoscopic features that represent a discontinuity in sedimentary rocks, i.e. cross-stratification) and fabric heterogeneities can also adversely affect reservoir quality, and are primarily determined by lithology, grain shape, sorting and diagenetic alterations. Sands typically exhibit cross-stratification, the structure of which is controlled by the type of depositional environment and energy fluctuations within the depositional system. Few studies have addressed the controls on permeability in a cross-stratified sandstone using the pore and microscopic scales investigated in this thesis.

The characterization of sandstone reservoir properties requires an understanding of the geologic features that control the distribution of permeability pathways, conduits, barriers and baffles, as well as the distribution of micro- and macroporosity (Ehrenberg, 1990; Dullien, 1991; Ehrlich et al., 1991; Doyle and Sweet, 1995; Bliefnick and Kaldi, 1996; Tang et al., 1997; and others). Considerable interest has been shown in describing the three-dimensional distribution of fluvial sand bodies and facies at the outcrop scale by studying architectural elements separated by various bounding structures (Jordan and Pryor, 1992; Miall, 1996). Individual, erosional bounding structures have characteristic geometric shapes and areal extents that are controlled, in part, by the environment of deposition (Miall, 1996) and may have inherently different permeabilities due to the fabric and composition of these different structures. Depositional environments determine the basic architecture and geometry of siliciclastic reservoir rocks (Reineck

4

and Singh, 1975; Rubin, 1987; Morse, 1994) and will control the effective porosity and ultimately a sandstone's permeability. Siliciclastic reservoirs consist of particular facies that display characteristic or distinct mineral compositions, individual lithologies, external geometries, as well as sedimentary and biogenic structures and textures (Miall, 1992; Bloch and McGowen, 1994; Aharonov et al., 1997).

Diagenetic alterations are also important controls on reservoir quality and permeability. Alteration processes are influenced by a number of variables, including sediment texture and structure, maximum burial depth, temperature and pressure, formation age, grain orientations and pore water chemistry. Of particular interest is the concept of secondary porosity generation (Schmidt et al., 1977; Blatt, 1979; Galloway, 1979; Schmidt and McDonald, 1979; Bjørlykke, 1984; Siebert et al., 1984 et al.; Harris, 1989; Bloch, 1994; Marfil et al, 1996; and others). More mature sandstones have been found to exhibit greater secondary dissolution porosity compared to texturally submature sandstones (poorly sorted sands exhibiting more angular framework grains and a higher clay content).

Various mechanical and chemical diagenetic alterations of sediments occur throughout a wide range of temperatures (10-300°C) and pressures (1-5 kb). The mechanical alteration of compaction promotes: 1) pore occlusion by grain rearrangement and ductile deformation of labile grains; 2) the redistribution of silica precipitating as authigenic overgrowths due to pressure solution; and 3) the opening of fluid pathways by grain fracturing (Land and Dutton, 1978; Sanderson, 1984; Houseknecht, 1987; McBride, 1989; Pate, 1989; Lundegard, 1991; Pittman and Larese, 1991; Bjørlykke and Egeberg, 1993; Ehrenberg, 1995; Weedman et al., 1996; Dutton, 1997; Heydari, 1997; and others).

Chemical diagenetic alterations include the precipitation and replacement of authigenic matrix material, including authigenic clay minerals and cements, as well as the dissolution of these minerals (Heald and Renton, 1966; Pittman, 1979; Mitra and Beard, 1980; Williams and Crerar, 1985; Williams et al., 1985; Leder and Park, 1986; Pollastro, 1991; Muchez et al., 1992; Wood, 1994; and others).

Geostatistical models are also developed to incorporate the principal processes that control the porosity and permeability of sandstone aquifers. Geostatistical methods are concerned with characterizing and simulating the spatial variability of petrophysical properties, as well as the relationship between the petrology of reservoirs, such as pore geometries and the surface area of mineral phases to acquired petrophysical data and measured permeabilities (Ehrlich et al., 1984). In addition, an important aspect of image based geostatistical analysis includes the use of regionalized variables (variables having properties that lie between truly random and completely deterministic) to assess the structure of pore networks, investigate pore connectivity and pore throat architecture, and to predict fluid movement within reservoir rocks (Ruzyla, 1986). Unlike purely random variables, regionalized variables have continuity from one point to some other point in space. In these thin sections, porosity and matrix material are assumed to be regionalized variables, and although both are spatially continuous, to various degrees, their position in space can only be determined by examining samples at specific locations in a specified field or boundary employing geostatistical methods (Davis, 1986).

CHAPTER 2: GEOLOGIC SETTING

2.1. Introduction

Face 7 of a block of the Massillon Sandstone, a member of the Pennsylvanian Pottsville Formation, Stark County, Ohio, was used to conduct this study. The block was quarried by the Briar Hill Stone Company, Glenmont, Ohio, and shipped to the New Mexico Travertine Company, Sossimo Padilla, New Mexico, where it was cut to its current dimensions (Figure 2.1). Excellent three dimensional exposures of the Massillon Sandstone are observed in the Briar Hill quarries, as well as in road cuts and on natural slopes in parts of northeastern Ohio (Schmidley, 1987; Rizzo, 1993). Low-angle cross-stratification is observed throughout the Massillon Sandstone block. These depositional structures resemble the thin, cross-bed sets observed in the Plane Bedded Facies and the Tabular Set/Coset Facies described by Schmidley (1987) and Rizzo (1993). For this reason, their observations are of particular interest to this study.

2.2. Lithofacies

Schmidley (1987) and Rizzo (1993) described the internal sedimentary structures and composition of the Massillon Sandstone, as well as the relationships to bounding lithologies to interpret the depositional environment. The following discussion is based primarily on their work.

The Massillon Sandstone consists of nine lithofacies that occur in regular order (Table 2.1), suggesting that the factors controlling their deposition are inherent to a particular environment within a depositional system or systems.

7

6.5 cm
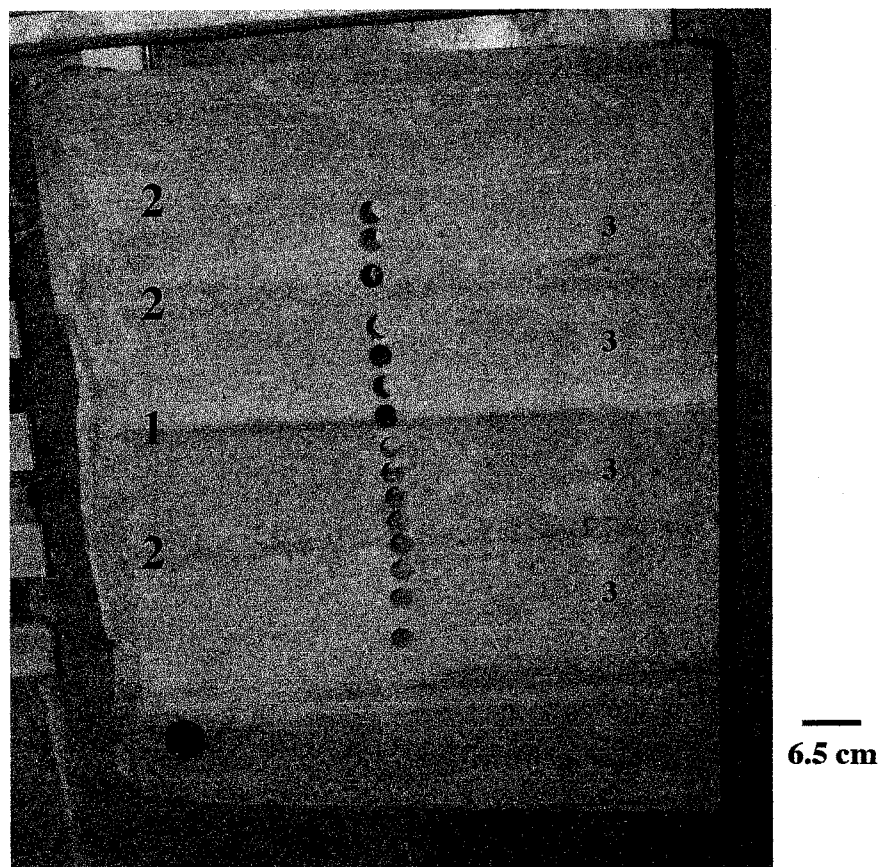
Figure 2.1

Photograph of a block cut from a boulder of the Massillon Sandstone (dimensions are: 102.87 cm x 86.36 cm x 15.24 cm). The parent boulder of this block was quarried by the Briar Hill Stone Company, Glenmont, Ohio, USA. The cored transect across Face 7 (shown here), spans a first (1) and several second-order (2) erosional, bounding surface structures, as well as depositional, cross-stratification structures called third-order structures (3). Core procured from this block face was selected for permeability, porosity, petrographic and geostatistical image analysis.

Table 2.1: The major lithofacies found in an ideal section of the Massillon Sandstone.

TOP	Coal
	Clayshale Facies
	Clayshale/Scour and Fill Facies
	Ripple Coset Facies
	Tabular Set/Coset Facies
	Distinct Trough Coset Facies
	Indistinct Trough Coset Facies
	Plane Bedded Facies
BASE	Conglomerate Facies

Here I focus on the two facies identified by Schmidley (1987) and Rizzo (1993) that most resemble the depositional, cross-stratified structures inherent to this study's sandstone block.

2.2.1. Plane Bedded Facies

The Plane Bedded Facies consists of horizontal to slightly undular, laminated to thinly bedded, coarse to fine sand. Coarse-grained laminations are accentuated by horizontal to slightly imbricated, 1 to 10 cm clayshale clasts and muscovite flakes. Fossil plant molds 3 to 50 cm long are common. Fine-grained laminations have little muscovite and no clayshale clasts or fossil fragments. Grain size of the planar laminations is uniform for a single occurrence of the facies, but variable from one facies location to another. Facies consisting of fine sand are thin (approximately 8 to 12 cm thick) whereas facies with coarse-grained sand and clayshale clasts tend to have a more variable thickness (approximately 1 to 1.7 m). The thinner, finer-laminated facies are horizontal, whereas the coarser-laminated facies are undular on the order of tens of centimeters.

2.2.2. Tabular Coset Facies

The Tabular Coset Facies is made up of groups of planar to slightly tangential cross-stratified beds. The individual beds range in thickness from 8 to 80 cm, with an approximate mean of 45 cm. The cross-laminations are distinguishable by differential weathering and grain size segregation. In most cases, laminae fine upward from medium and coarse to fine sand. Mica is commonly found at the base of the cross-laminations. Cross-lamination shape is essentially planar, but some curve near the toe, suggesting slight reworking by lee-eddy currents. Set thickness is essentially uniform. Laterally, the beds maintain a uniform thickness, although flow parallel exposures show individual beds pinching out within 7 to 10 m. Thickness of the facies ranges from 20 cm to 2.5 m. The facies commonly extends laterally up to 10 m before pinching out.

2.3. Depositional Environment

Characteristic features of the Massillon are found in different modern depositional systems. When the Massillon facies assemblage is viewed as a sequence, the order and association of this sequence greatly increases its usefulness interpreting the depositional environment. Six characteristics of this assemblage stand out as most significant: 1) clayshales underlying the Conglomerate Facies lack fossils; 2) the Conglomerate Facies is comprised of coalspar and iron nodules and has a sharp basal contact with the underlying Clayshale Facies; 3) trough cross-beds are unidirectional; 4) scoured, vertical accretion deposits contain plant fragments; 5) a low sulfur coal tops the assemblage; and 6) a fining upward grain size trend exists throughout the sequence. Schmidley (1987) compared this assemblage to three common, fining upwards systems: 1) a tidal inlet (Fire

10

Island Inlet Sequence); 2) a distal braided stream (Battery Point Sequence); and 3) a meandering stream (Old Red Sandstone Sequence) to determine the environment of deposition for the Massillon Sandstone (Appendix A).

Schmidley (1987) concluded that the depositional environment of the Massillon was either a distal braided stream complex or a meandering stream complex. The fining upward in-channel grain size trend and the appreciable scoured vertical accretion deposits are best explained by a fluvial system. Nodular, plant rich clayshales capped by low sulfur coals overlying medium to coarse-grained sandstone support deposition in an upper delta plain as opposed to a barrier or transgressive marine sand (McCubbin, 1982). The planar beds, with their sharp lower contacts (most likely erosional bounding or reactivation surfaces created as a result of planing off by slightly higher flow velocities within the system) may be shallow water deposits that formed higher up on a meandering point bar. The tabular sets or cosets may have formed as a large scroll bar occupying the upper point bar of a convex bank moving downstream. They may also have formed slightly lower on the point bar as single sets of planar cross laminations migrate both normal and offset to local channel flow, truncating other trough-like forms (Schmidley, 1987).

CHAPTER 3: METHODOLOGY

3.1. Multisupport Gas Permeameter

The primary functions of the MSP (Figure 3.1) are: 1) to rapidly and inexpensively collect extensive permeability data sets from the flat surfaces of different lithologic samples (sandstones, tuffs, carbonates) in a nondestructive matter, and 2) to investigate permeability upscaling by using a variety of tip seal sizes in conjunction with the MSP. For a comprehensive investigation of this methodology see Tidwell and Wilson (1977).

The permeameter penetrates the sample with a predetermined gas injection pressure while measuring the resultant steady state gas flow rate and gas temperature within the sandstone. Four mass-flow meters (0-50, 0-500, 0-2000 and 0-20,000 sccm), two pressure transducers (0-100 and 0-350 kPa gauge), a barometer and a temperature sensor are connected to a regulated source of compressed nitrogen on the MSP. Gas flow rate is measured as laboratory grade nitrogen is directed into the sandstone via a series of distinctly sized, spring-loaded tip seals (Figure 3.2). The diameter of each tip seal defines the scale of measurement and is used to establish boundary conditions on the sandstone surface. By changing the size of the tip seal, the permeameter interrogates volumes of rock ranging in scale from tenths to thousands of cubic centimeters. The employment and exchange of these tip seals with the computer controlled, electronic gas permeameter allows for the exhaustive collection of permeability data from the sandstone block at different spatial scales.

Permeability is then calculated directly from information on the specific tip seal geometry, the measured nitrogen flow rate, the injection pressure, the barometric pressure
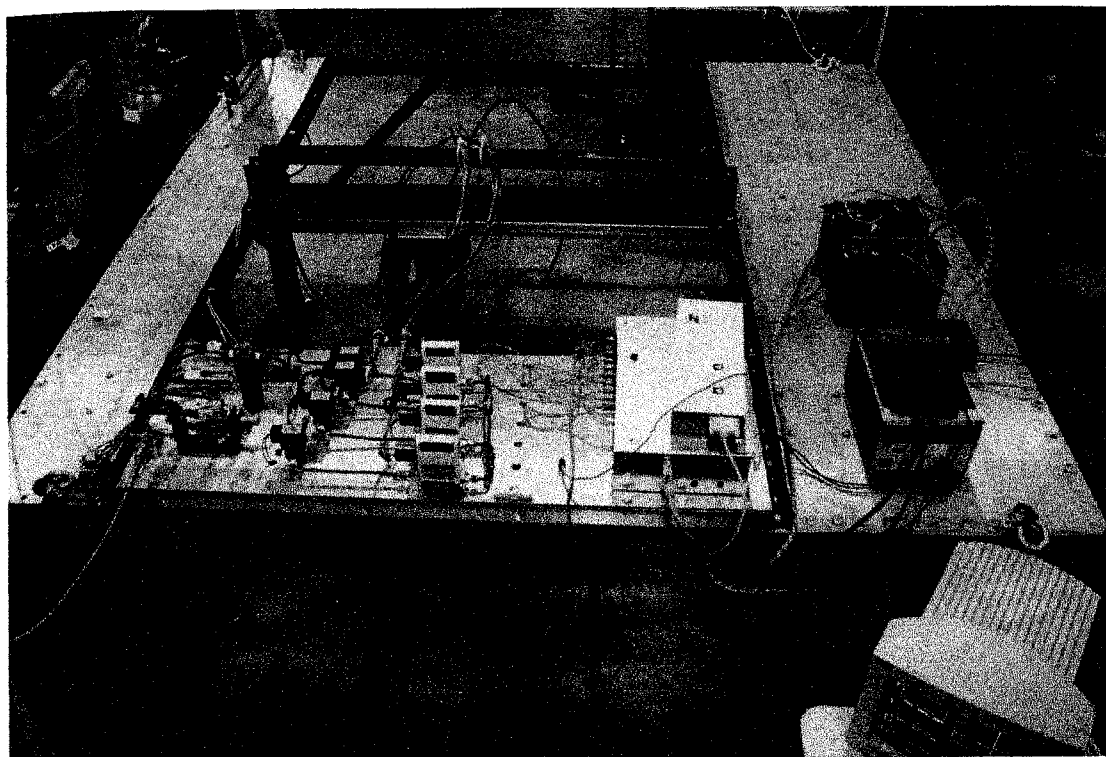
Figure 3.1

Photograph of the multisupport permeameter (MSP), the x-y positioner and computer control system. Permeability measurements are acquired by compressing a selected tip seal squarely against the flat, sandstone surface while injecting laboratory grade nitrogen into the rock at a constant pressure. Measurements are made following a user designed sampling grid programmed into the x-y positioner. Automation of the MSP is achieved by the integration of two stepper motors and three belt drives on the positioner. The positioning system is affixed to a rigid table supported by a unistrut frame, the height of which may be adjusted over a 1.5 m distance to accommodate for differences in lithologic sample sizes. Sample blocks are placed under the positioning system where they remain stationary during sampling by virtue of their own weight (after Tidwell and Wilson, 1997).
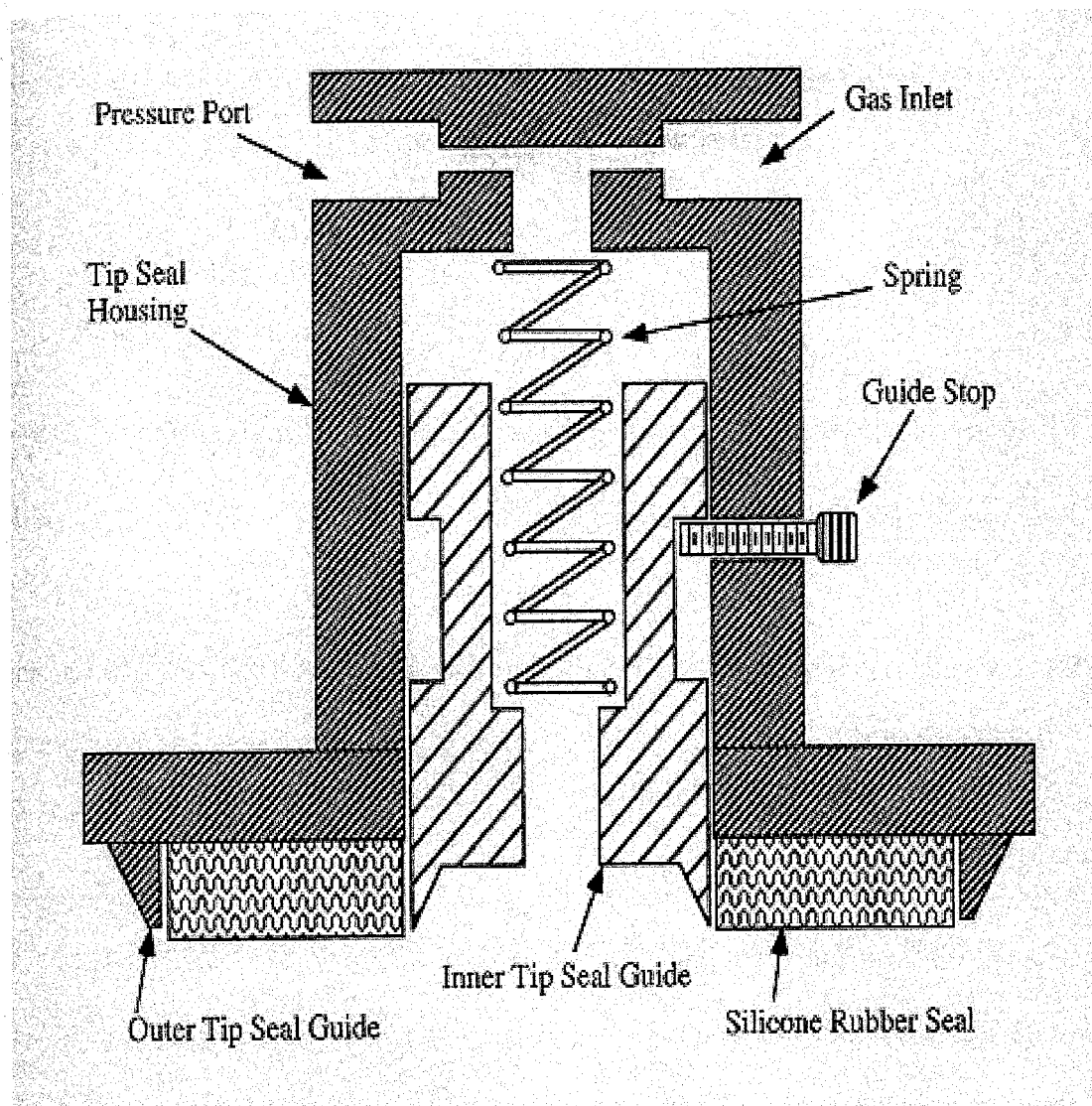
Figure 3.2

Schematic of an MSP tip seal. Laboratory grade nitrogen is directed into the sandstone sample via the tip seal. A molded ring of silicon rubber is used to form the seal with the rock surface, while a spring loaded inner guide and immobile outer guide constrain the shape of the seal under compression. A consistent and known tip seal geometry under compressed conditions is required to ensure precise permeability measurements. For this reason, each tip seal is constructed with an internal spring driven guide to maintain a constant inner seal diameter. A similar design is employed for each of the six tip seals currently in use at the Sandia National Laboratory, however, only the smallest three; the 0.15, 0.31 and 0.63 cm inner radii tip seals require the outer tip seal guide (after Tidwell and Wilson, 1997).

and the gas temperature (Tidwell and Wilson, 1997). For this investigation, permeability calculations were derived using a modified form of Darcy's Law developed by Goggin et al. (1988):

$$k\ (Q_1, P_1, P_0, r_i, r_0) = \frac{Q_1 P_1 \mu(T)}{(0.5)\ r_i\ G_0\ (r_0/r_i)[\ P_1^2 - P_0^2]}$$

where $k\ (Q_1, P_1, P_0, r_i, r_0)$ is the permeability; Q_1 is the gas flow rate; P_0 is atmospheric pressure; P_1 is the gas injection pressure; $\mu(T)$ is the gas viscosity (a function of temperature); and $G_0\ (r_0/r_i)$ is a geometric factor. G_0 varies according to the ratio of the outer tip seal radius (r_0) to the inner tip seal radius (r_i) (Tidwell and Wilson, 1977).

3.2. Sampling

The boulder of the Massillon Sandstone was cut into a block with dimensions 102.87 cm x 86.36 cm x 15.24 cm (Figure 2.1) using a diamond impregnated, industrial wire line saw. Fresh water was used to cool the saw's wire line, to remove aggregated debris and to pressure wash the sawn faces. The block was subsequently shipped to Sandia National Laboratory, Albuquerque, NM, where it was allowed to dry for a period of one month. Care was taken to fashion one block face (hereafter referred to as Face 7, cut parallel to cross-stratification, in the direction of paleo-flow), providing a fresh, flat surface suitable for permeability data acquisition. To properly investigate a block of any lithology using the MSP, facial asperities cannot exceed a height of 1.5 mm (Tidwell and Wilson, 1997). Such preparation constrains the shape of the MSP's tip seal under

15

compression, providing the tightest seal possible to create a consistent and known tip seal geometry.

Outcrop scale mapping was performed on Face 7 to locate areas of structural, textural and diagenetic variability and to map a transect across the face from which to core for petrographic, scanning electron and image based, statistical pore structure data (Figure 3.3). Along this transect: 1) erosional, reactivation or bounding surfaces; 2) depositional, cross-stratified foresets; 3) heavily cemented domains; and 4) coarse to medium-grained areas was encountered. Bounding surface classification is taken (and modified) from Brookfield, (1977). First-order bounding structures resulted from interdune areas that developed between bed-sets or cosets and separated accumulations of the second and third-order structures. Second-order structures were probably generated by the migration of dunes on the lee face of the main bedform. For this study, third-order structures are defined as cross-stratification structures that formed between the first and second, or second and second-order structures (Figure 2.1). Although Brookfield's nomenclature is more appropriately applied to eolian sands, his characterization describes well the first and second-order erosional structures present in the Massillon Sandstone block (Figure 3.4).

Permeability measurements were then procured directly from Face 7 using five different tip seals, with inner radii (r_i) of 0.15 cm, 0.31 cm, 0.63 cm, 1.27cm and 2.54 cm (Figure 3.5; for a detailed explanation of this methodology, refer to Tidwell and Wilson, 2000). Sampling was performed within a 60.325 cm x 12.065 cm area (728 point grid) set on 1.00 cm centers. Plots of two-dimensional, natural log permeability fields were then generated using the tip seal data. These permeability field maps reveal a strong

16
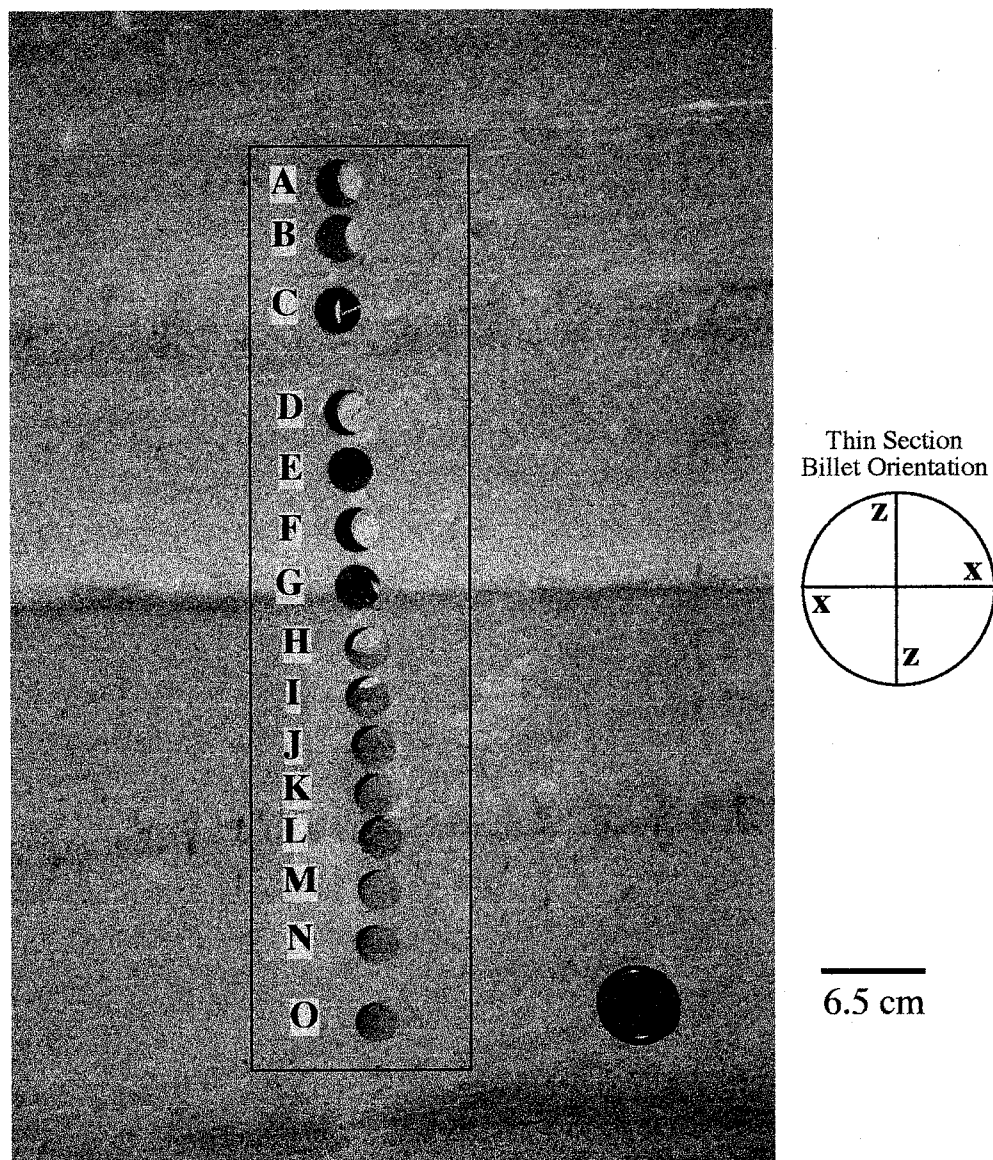
Figure 3.3

Photograph of the cored transect crossing Massillon's Face 7. Each of the 15, 2.5 cm plugs, cored across this transect, from top to bottom, were lettered from A to O. Strata at core A are younger than those deposited at O. Thin sections were fabricated from each of these core plugs, cut either in the plane oriented normal to stratification (z-direction), or parallel to stratification (x-direction; see inset figure). The rectangle surrounding the cored transect represents the area investigated by the MSP (dimensions are: 60.325 cm x 12.065 cm). Core G is sampled from a first-order bounding surface structure (Brookfield, 1977), the only such structure inherent to this face. Cores A, C and L were procured from second-order bounding structures. Cores B, D, E, F, H, I, J, K, M, N and O are sampled from cross-stratification structures that were originally deposited between first and second, or second and second-order reactivation surfaces, and are named third-order structures in this investigation.

17

C

Compound sets of cross strata
which together form a coset
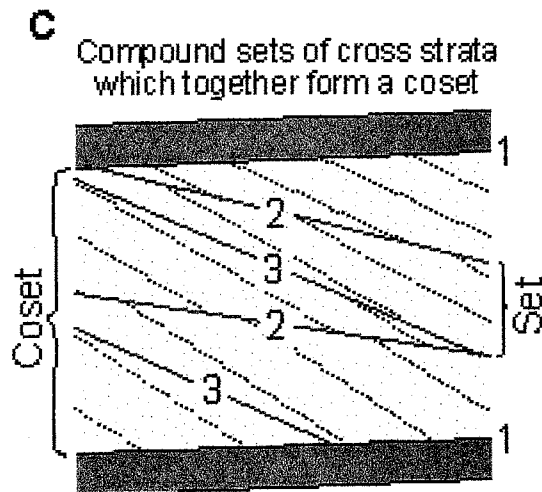
Figure 3.4

Image showing a model of bounding surface formation hierarchies created by climbing dunes within interdunal areas. This figure represents the cross-section of superimposed, eolian dunes. First, second and third-order bounding surface structures are indicated by 1, 2 and 3, respectively. Third-order structures are reactivation structures, and form the boundaries of accumulated strata within co-sets of cross-bedding. They are attributed to erosion followed by renewed deposition on a dune's lee face, due to either a fluctuation in flow direction and/or intensity. For this study, third-order structures are defined as cross-stratification that form between the first and second, or second and second-order structures. Second-order structures probably formed by the migration of dunes on the lee face of the main bedform. First-order bounding structures resulted from interdune areas that developed between bed sets or co-sets and separated accumulations of second and third-order structures. These distinct erosional surface structures are generated by the passage of interdune troughs that bound dune scale bedforms. Although this terminology usually refers to structures found in eolian dune and interdune facies, for the scope of this investigation, the terminology was considered appropriate (figure and model taken from Brookfield, 1977).
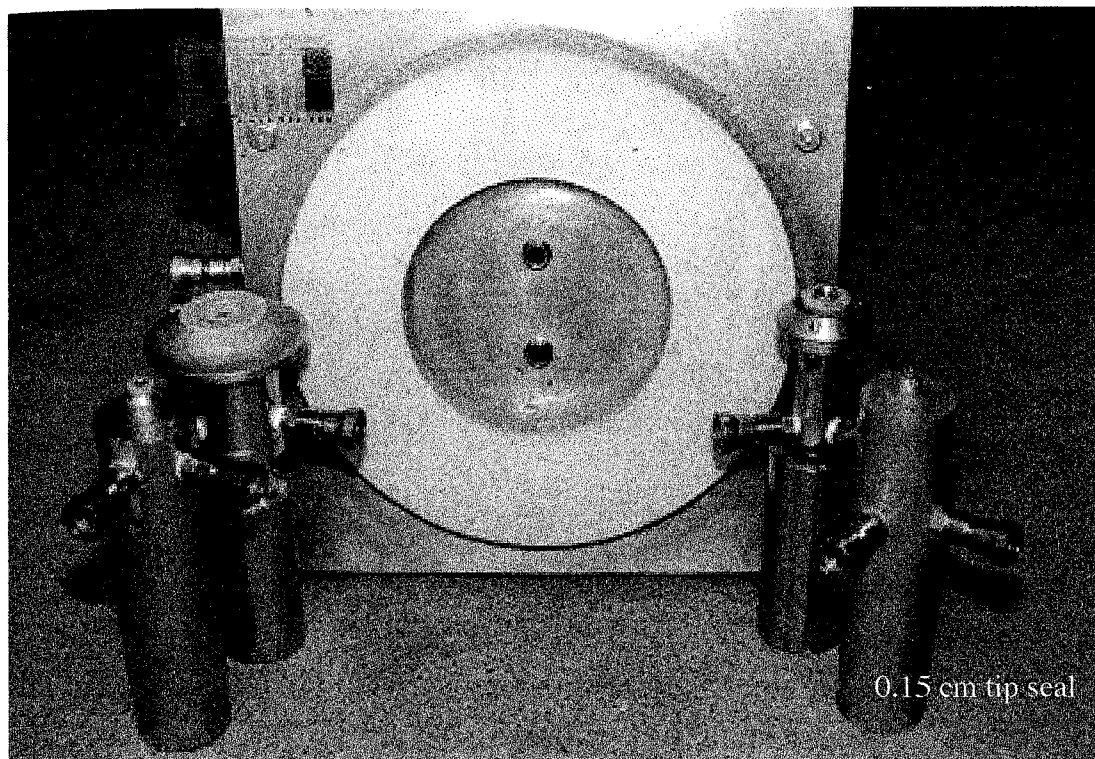
Figure 3.5

Photograph of five of the six tip seals currently employed by the MSP. Tip seals shown have inner radii of 0.15, 0.31, 1.27, 2.54 and 7.62 cm and an outer radii measuring twice that of the inner radii. A molded ring of soft silicon rubber, 1.6 cm in thickness, is employed to create a seal between the injection nozzle and the sandstone surface for the 0.63 (not shown), 1.27, 2.54 and 7.62 cm inner radii tip seals. A thinner seal (0.5 cm thick) constructed of harder silicone rubber is used for the 0.15 and 0.31 cm inner radii tip seals (after Tidwell and Wilson, 1997).

correlation between the spatial patterns visible on the sampled rock face (distinct structural features inherent to Face 7) and the spatial patterns characterizing the three-dimensional permeability measurements (Appendix B). Comparison of these permeability maps measured at variable tip seal supports systematically exposes discrete upscaling trends (Tidwell and Wilson, 1997).

Individual billets cut from cores of first, second and third-order structures were measured for permeability employing the 0.15 cm r_i tip seal. Six permeability measurements were made on each of 15 billets cut normal to stratification (Figure 3.6) and two measurements were made on each of 5 billets cut from core oriented parallel to bedding (Figure 3.7).

3.3. Petrographic Analysis

Petrologic studies have been employed to understand how variations in porosity and permeability are controlled by mineralogy, texture, provenance, depositional facies and diagenesis (Burns and Ethridge, 1979; Scherer, 1987; Clelland and Fens, 1991; Ehrlich et al., 1991; Bryant et al., 1993; Ehrenberg and Boassen, 1993; Bloch, 1994; Byrnes, 1994; and others). This investigation relies on modal analysis and scanning electron microscopy to develop primary and secondary controls on laboratory measured permeability.

3.3.1. Modal Analysis

Fifteen (15 x 2.5 cm) cores were extracted from Face 7 (Figure 3.3). From these cores, billets were cut from which thin sections were then fabricated. Modal analysis was
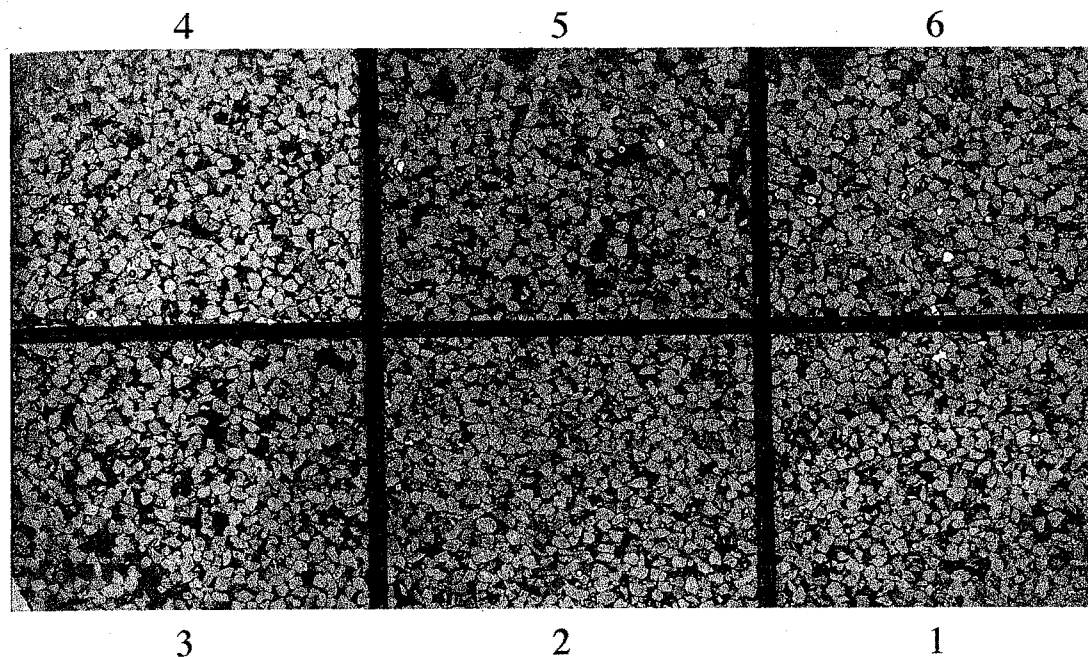
Figure 3.6

Image of scanned thin section 7B3z. The billet from which this thin section was prepared is oriented normal to cross-stratification. The thin section is segregated into sixths (numbered subsections). Permeability of each subsection was measured on the billet in the laboratory using the MSP's 0.15 cm inner radii tip seal; 400 point counts were determined from each subsection (2400 total), to determine framework grains, non-framework constituents, authigenic minerals and porosity types (image width = 3.39 cm).

2   1
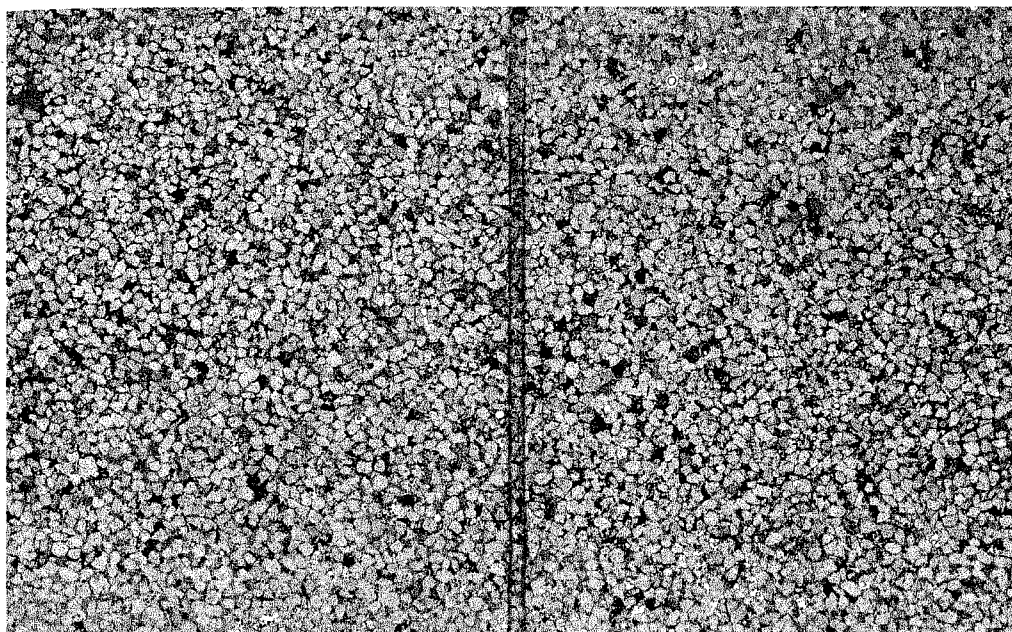
Figure 3.7

Image of scanned thin section 7G1x. The billet from which this thin section was prepared is oriented parallel to cross-stratification. The thin section is segregated into numbered halves (subsections). The permeability of each subsection was measured on the billet surface in the laboratory using the MSP's 0.15 cm inner radii tip seal; 400 point counts were made on each subsection (800 total), to determine framework grains, non-framework constituents, authigenic minerals and porosity types (width of image = 3.17 cm).

performed on 20 thin sections (100 subsections), to determine the abundance of framework grains, non-framework components and porosity in Face 7. David Mann Petrographics of Los Alamos, New Mexico prepared all thin sections, each of which were ground to a thickness of 30 microns and impregnated with blue-dyed resin epoxy to differentiate true porosity from pore spaces created during thin section preparation. Point counting was performed on a Nikon petrographic microscope.

Core and corresponding thin section subsections were named from A through O; Core A is from the stratigraphic top of the block, representing the youngest strata. Each cored position across the transect was selected from a first, second or third-order structure, or a transitional zone between bounding structures. Cores A and C, although positioned along with core L within the second-order structural regime, were actually taken from the transition between second-order bounding structures and third-order depositional structures. One thin section was created from each piece of core, fabricated such that the thin section represents a cross-sectional window oriented normal to the paleoflow direction, as indicated by the cross-stratification (z-direction). These billets were large enough to support six permeability measurements made directly on the billet surface using the 0.15 cm r_i tip seal (Figure 3.6). Each thin section was then segregated into six subsections. Each subsection was correlated to a billet permeability measurement and was described independently. From each subsection, 400 points were counted (36,000 total point counts within 90 subsections; 2400 counts for each standard, 2 cm x 3.5 cm thin section). Applied nomenclature given to all subsections (i.e., 7A2z.1) is as follows:

7 – sample taken from Massillon Sandstone Block Face 7.

23

A – sample taken from core A (A-O).

2 – sample taken from a second-order structure (1st, 2nd or 3rd).

z – sample oriented normal to cross-stratification (x is oriented parallel to cross-stratification).

1 – sampled from thin section subsection 1 (1-6).

Five thin sections were created from billets oriented parallel to cross-stratification (x-direction); one each from cores A, C, G, I and O. These thin sections were divided in half (two subsections), and 400 points were counted from each half, for a total of 800 counts per thin section (4,000 total point counts within 10 subsections). The smaller size of these circular billets could only support two, in-situ permeability measurements (Figure 3.7).

All permeability measurements used in relation to the petrographic data were collected using the MSP equipped with the 0.15 cm r_i tip seal on both parallel and perpendicularly oriented core billets. All thin sections used for the correlations were created from these billets. Four hundred points were used for each subsection to allow a counting accuracy of approximately 95% (Van der Plas and Tobi, 1965). The mean grain size of Face 7 was determined by measuring the major, or long axes of 25,502 framework grains.

During the modal investigation, porosity was segregated into macroporosity and microporosity groups. Macroporosity divisions include intergranular primary, secondary and fracture porosity, and intragranular secondary and fracture porosity. Due to the complex nature of diagenetic alterations (i.e., cementation and dissolution events), intergranular primary and secondary porosity distinctions were not always obvious. As a

result, their distributions were determined solely considering pore size and grain boundary dissolution, and therefore should be evaluated simply as intergranular macroporosity.

3.3.2. Scanning Electron Microscopy

Four, 2.5 cm diameter cores of the Massillon Sandstone were broken and cut into one centimeter thick discs in preparation for three-dimensional, qualitative scanning electron microscopy (SEM) analysis. Each cored disc was wrapped with electrical tape to retard the spalling of sand grains and then coated with a thin layer (approximately 25 angstroms in thickness) of carbon to enhance electron conductivity during the analysis. A Cameca SX-100 Electron Microprobe maintained by the New Mexico Bureau of Mines and Mineral Resources, Socorro, New Mexico, was used to analyze the coated discs. Operating conditions were as follows: 1) an accelerating voltage of 25 kV; 2) a current of 0.10 nA; and 3) an electron beam aperture of 150 microns. Topographic images of the broken disc surfaces were analyzed to assess paragenetic relationships and to determine the mineralogy of unknown phases.

Two thin sections were polished to a thickness less than 30 microns for two-dimensional, qualitative back-scattered electron (BSE) analysis, using a JEOL JSM-5900 LV Scanning Electron Microscope. The Sandia National Laboratory's Carlsbad Operations Group, Carlsbad, New Mexico, maintain this microscope. Each thin section was coated with gold (approximately 100 angstroms in thickness), which enhances electron conductivity during analysis. Images were captured using the high resolution imaging mode (SEI), and then qualitatively analyzed for mineralogy using the

compositional mode (BSE). The following settings were employed during thin section analysis for both modes: 1) an accelerating voltage of 15 kV; 2) a working distance of 11 mm; 3) a spot size of 35 (a machine specific, unitless setting); and 4) a setup frame store with a photo speed resolution of 2560 x 1920 pixels for 160 seconds (Reed, 1997).

3.3.3. Cathodoluminescence

Portions of selected thin sections exhibiting both minimum and maximum percentages of precipitated authigenic quartz overgrowths were investigated under cathodoluminescence to verify point count abundances. Visual estimates of samples determined to contain between 0.25% and 5.5% authigenic quartz were analyzed using a MAAS Nuclide ELM-3R Series luminoscope coupled with an Olympus BH-2 polarizing microscope. Operating conditions were: 1) a 60-80 millitorr vacuum; 2) a 0.5 mA current; and 3) a 21 kV cathode beam.

3.4. Structural Analysis of Petrographic Images

Geostatistical analysis was employed to characterize the spatial patterns created by the bounding structures, cross-stratification, pore voids and matrix material as quantified in the rendered, binarized, two-dimensional, subsection images.

3.4.1. Image Preparation

Each of the 20 thin sections fabricated for this investigation (15 oriented normal to cross-stratification, 6 subsections each; 5 oriented parallel to cross-stratification, 2 subsections each) were scanned, imported into Adobe Photoshop 5.0 and then rendered

26

into three-phase photomicrographs (Figure 3.8). The three phases of porosity, matrix material and framework grains in each subsection were transformed and assigned a distinct color. Three-phase images depict: 1) white areas (detrital grains and authigenic quartz cement); 2) black areas (matrix material; comprised solely of hematite, ferroan dolomite, and allogenic and authigenic clay minerals); and 3) blue areas (intragranular and intergranular macroporosity). Identifying the pixels associated with point count macroporosity and matrix material in thin sections allows for the rendering and the creation of binarized images. A binarized image is an image that has been reduced to two components; each pixel in the rendered images will isolate either intergranular and intragranular macroporosity or the matrix material from the framework grains. Isolated pixels (macroporosity or matrix) will be black (1), and all other pixels will be white (0). Image analysis was performed on the binarized, two-phase subsection photomicrographs using the image analysis software package Image Processing Lab (IP Lab). Point count porosity includes intragranular microporosity, whereas the porosity derived from this rendering does not. Two-phase images are binarized three-phase images that isolate either porosity, matrix material (not including authigenic quartz) or detrital grains (including authigenic quartz; Figure 3.9).

3.4.2. Fourier Transform Function and the Power Spectra

A two-dimensional (2-D), Fourier transform (FT) was applied to the binarized photomicrograph images to measure the spatial correlation between: 1) individual pores, and 2) matrix material (ferroan cements and allogenic and authigenic clays), and to evaluate the structural assemblages of both. The physical significance of micro- or

27
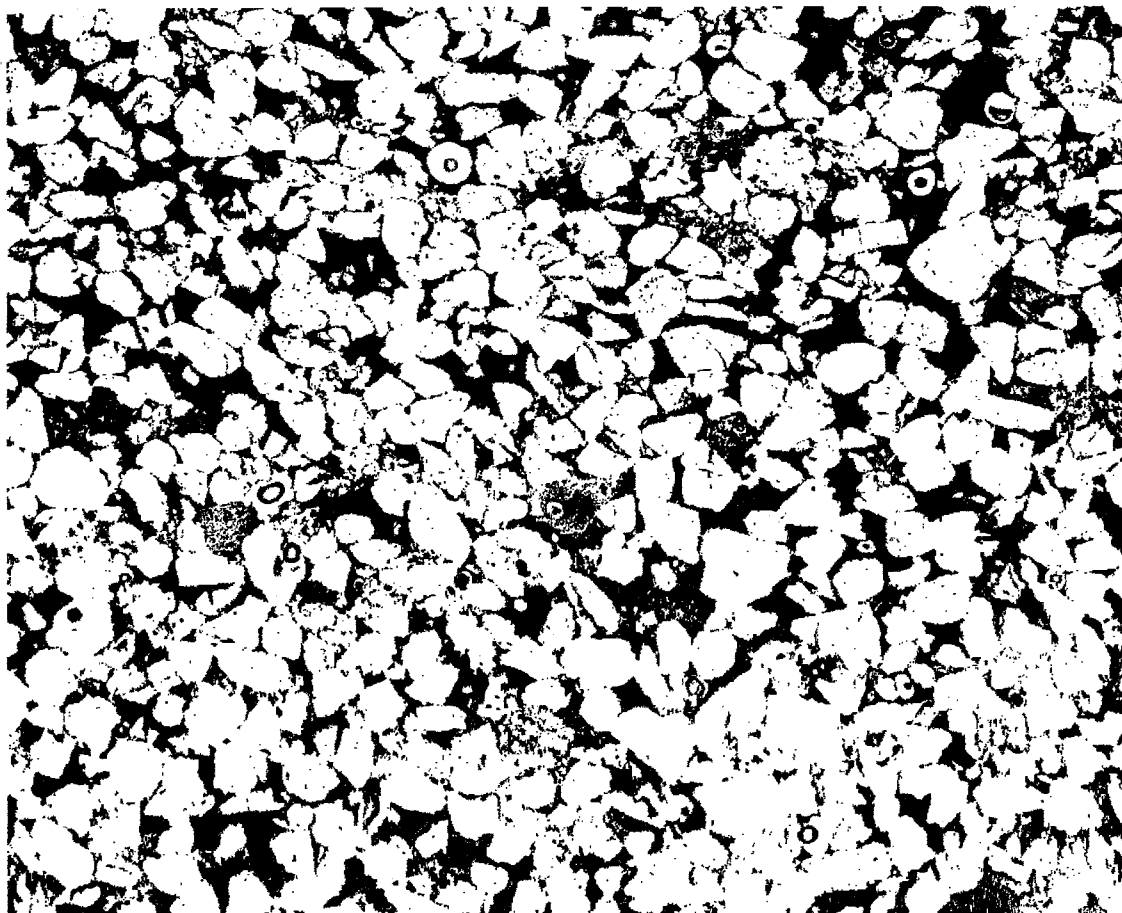
Figure 3.8

Rendered three-phase photomicrograph of thin section subsection 7N3z.1. White pixels are
detrital, framework grains including authigenic micro- and megaquartz. Black pixels are matrix
material, including authigenic iron oxide minerals, ferroan dolomite rhombohedra and allogenic
and authigenic clay minerals. Blue pixels are intergranular and intragranular macroporosity. This
subsection was prepared from 2.5 cm core drilled from a third-order structure and has the 3rd
highest permeability of all measured subsections: $k = 5.78E\text{-}12$ m^2; $\ln k = -25.8765$ m^2,
$k = 5856$ millidarcies. Point count porosity, determined from modal analysis is 26.25%, porosity
derived from image analysis is 20.23% and matrix material, determined from modal analysis
consumes 12.75% of the subsection. The mean grain size is 0.793 phi (coarse-lower sand). The
sorting is 0.37 phi (well-sorted sand) and was determined using the inclusive graphic standard
deviation between the measured major axes of 237 QFL framework grains (Folk, 1974). Image
dimensions are 10.170 mm x 8.199 mm: magnification is 850X.
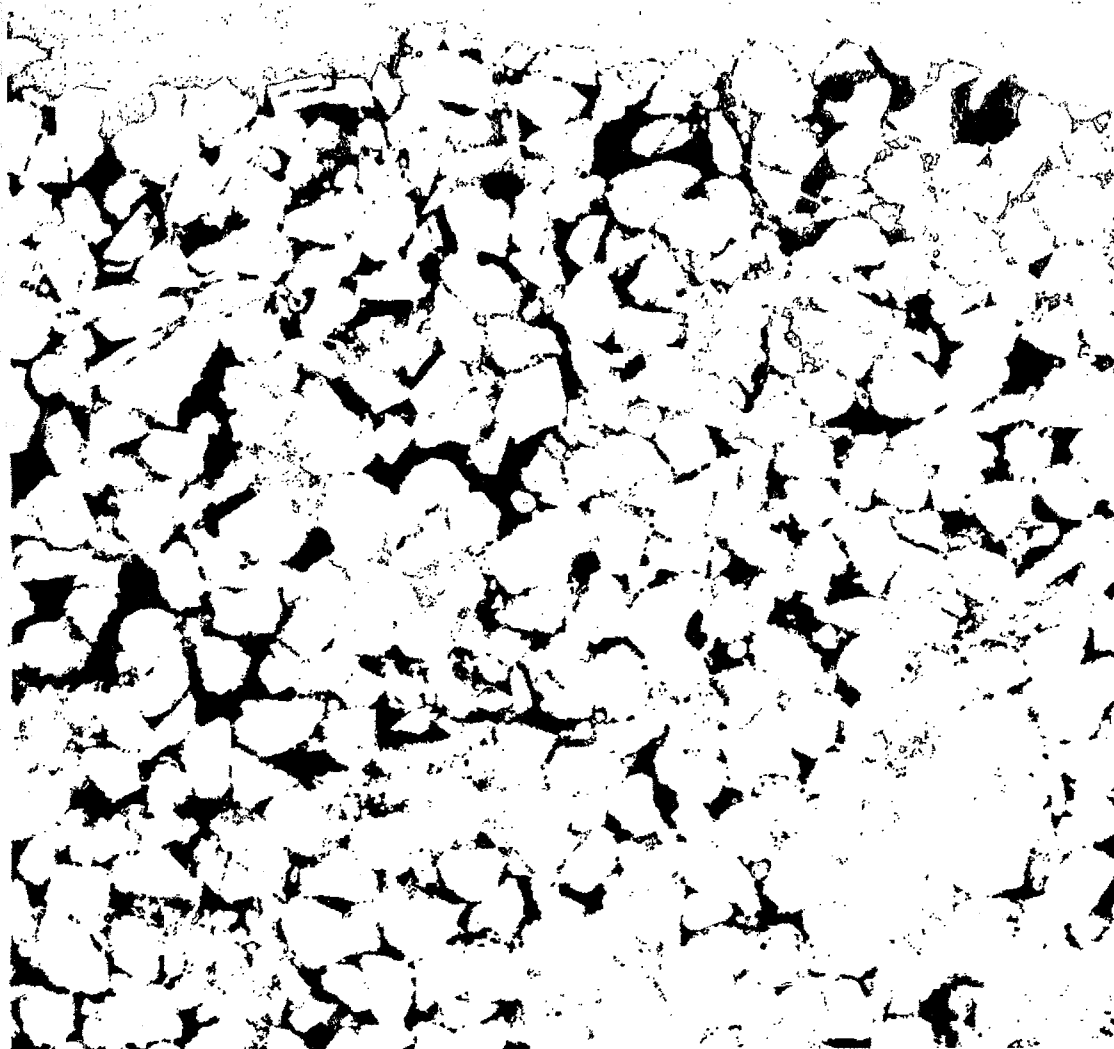
Figure 3.9

Rendered two-phase photomicrograph of thin section subsection 7C2z.4. White pixels are detrital, framework grains including authigenic micro- and megaquartz and matrix material, including authigenic iron oxide minerals, ferroan dolomite rhombohedra and allogenic and authigenic clay minerals. Black pixels are intergranular and intragranular macroporosity. This subsection was prepared from 2.5 cm core drilled from a second-order bounding structure and has the highest permeability of all measured subsections: $k = 6.75E-12$ m^2; $\ln k = -25.7213$ m^2; $k = 6839$ millidarcies. Point count porosity, determined from modal analysis is 19.0%, porosity derived from image analysis is 16.21% and matrix material, determined from modal analysis consumes 15.5% of the subsection. The mean grain size is 0.50 phi (coarse-lower sand). The sorting is 0.33 phi (very well-sorted sand) and was determined using the inclusive graphic standard deviation between the measured major axes of 242 QFL framework grains (Folk, 1974). Image dimensions are 7.929 mm x 7.929 mm: magnification is 850X.

29

macrostructures may be determined by relating Fourier analysis to porosity and matrix material areas determined from petrographic image analysis. The 2-D Fourier transform converts rendered and binarized images of thin section subsections into a series of discrete spatial frequencies, fitting a series of sinusoidal wave forms to the images (normalized to a mean of 0), at which point the resultant, or variance, is referred to as the power spectra. The power spectra is the natural analogue of variance in classical statistical analysis, and the systematic consideration of variance properties as a function of period or frequency is referred to as spectral analysis (Shumway, 1988). The Fourier power spectra is normally distributed with a frequency inversely proportional to the separation between binarized points and: 1) provides a means to assess any periodicity between individual pores and the matrix material; 2) measures the spatial density of both pores and matrix, including the scale at which they may exist; 3) measures the direction and degree of spatial heterogeneity between binarized points (individual pores or matrix islands) when applied in discrete directions (along the x-axis [parallel to cross-stratification]; along the y-axes [normal to cross-stratification]), or radially (in all directions).

From the power spectra, the correlation length scale can be estimated. The correlation length scale is the distance from a certain point, beyond which there is no longer a significant covariation or correlation of some physical property, in this case porosity and matrix material. To determine the correlation length scale, (λ), the following model is fit to the power spectral density function:

$$f(\lambda) = (2\sigma\lambda/[1 + (2\pi f\lambda)^2])$$

σ = variance
λ = correlation length scale
f = frequency

Another way to describe the spatial correlation of large scale geologic structures is to apply a fractal type description to the rendered binarized images. Specifically, the fractal dimension (FD), can be determined from the slope of the natural log of the power spectra plotted against the natural log of the frequency; FD = (6-m)/2, where 'm' is the slope of the equation (nine porosity images having the highest permeabilities [11-19] are displayed; Figure 3.10). The fractal dimension is but another measure of the spatial structure of the medium, describing a continuously evolving system where heterogeneity is assumed at every sample support, and where no 'distinct' correlation length scale is attained. The larger the fractal dimension, the less linear and continuous, or the more tortuous the path between like points (macroporosity or matrix material).

The size, shape, orientation and the spatial arrangement of these samples constitute the support (scale) of the regionalized variable, and the regionalized variable will have different characteristics if any one sample support is changed (tip seals with diameter differences). A principal concern is to relate results obtained at one sample support to those obtained at a different support or scale (Davis, 1986). This investigation is primarily concerned with the correlation of regionalized variables to permeability measured at the pore scale, using the MSP equipped with the 0.15 cm r_i tip seal. Future studies may consider how these correlations change when increasing the sample support.

31

Power Spectra vs. Frequency for Binarized
Porosity Images Along the XY Transect
11th - 19th Highest Measured Permeabilities
[Data adjusted (-10 top/-20 bottom)]
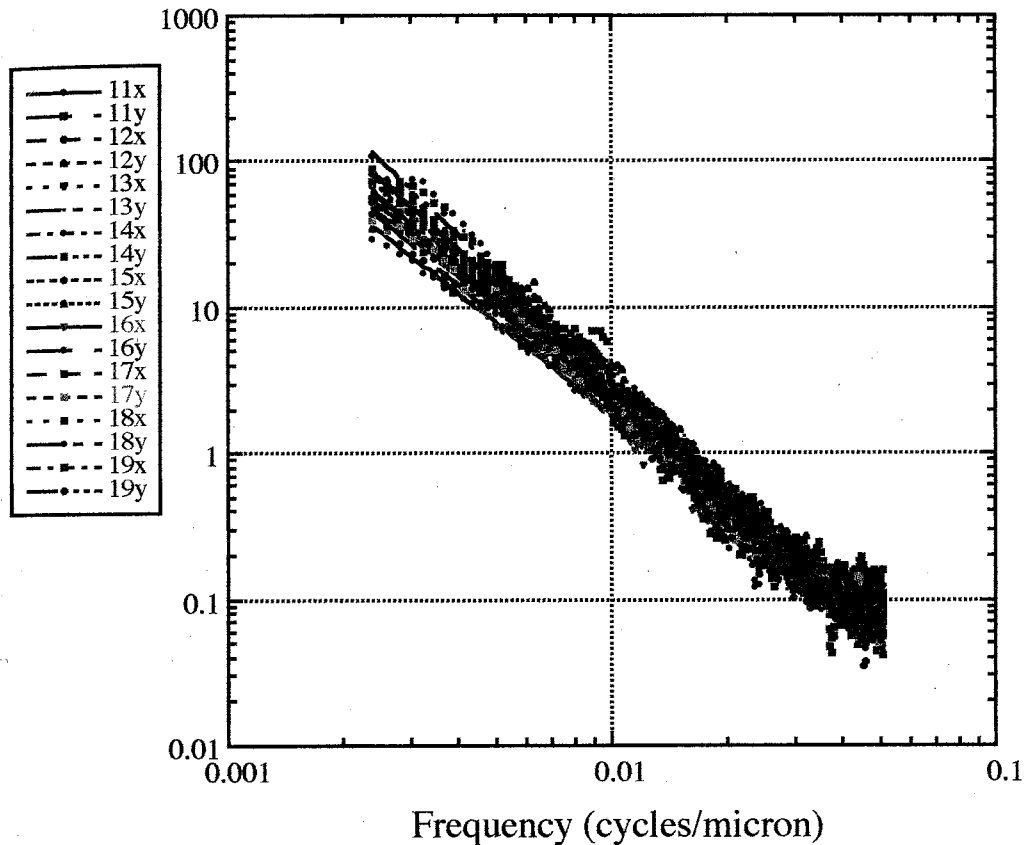
Figure 3.10

Diagram showing the power spectra plotted against the frequency for pores measured parallel (x-axis) and normal (y-axis) to cross-stratification. The data to produce this plot was generated from the two-phase, binarized, subsections exhibiting the 11th to 19th highest MSP measured permeabilities. The Fourier transform is fit to the two-dimensional power spectral density function to ultimately determine the fractal dimension associated with each binarized image.

CHAPTER 4: RESULTS

4.1. Macroscopic Observations

The Massillon Sandstone block is a rose-tan to dark burgundy sandstone, composed primarily of medium to coarse-grained quartz, feldspar and lithic grains. The framework grains were episodically deposited within packages of internal, planar-tabular cross-beds, cemented and compacted within a matrix of hematite, quartz and clay minerals.

A single, horizontal, first-order bounding surface structure is present in Face 7. This unconformable plane is sharp and dark in appearance and is 0.5-2 cm thick across the face. There are four, sub-horizontal, second-order structural surfaces that are more diffuse linearly (a less sharp bounding contact) compared to the first-order structure, are lighter in color, are horizontal to subhorizontal, and are between 1.0 and 2.5 cm thick. Erosional, bounding surfaces are spaced approximately 20 cm apart. More than 15, low-angle, third-order, cross-stratification structures are observed across Face 7. These depositional structures lie at higher angles to and between the first and second-order structures and are no more than 2 cm thick (Figures 2.1 and 3.3).

4.2. Sedimentary Petrology

4.2.1. Composition and Texture of the Massillon Sandstone

Face 7 of the block is a coarse, mature, hematitic, kaolinitic sublitharenite (classification of Folk, 1974). The sandstone has a mean framework composition of %QFL = (91, 3, 6). Point count data derived from modal analysis, including individual and mean statistics, are recorded in Appendices C and D (a petrographic index of

nomenclature used in recording modal analysis is presented in Appendix C). The predominant, detrital framework grains are monocrystalline and polycrystalline quartz, plagioclase, k-feldspar and lithic fragments. Accessory detrital grains include chert, muscovite, biotite, zircon and hornblende. Framework grains comprise an average of 64% of the sandstone and range from medium to very coarse (mean grain size is 0.98ϕ; coarse-lower sand). Grains in the first-order bounding surface structure have the smallest mean sizes, averaging 1.1ϕ (medium-upper sand). Grains within and between second and third-order structures have the largest mean grain sizes, 0.92ϕ and 0.98ϕ (both coarse-lower sand), respectively. Overall, Face 7 is well-sorted; $\sigma_I = 0.39\phi$ (determined using Folk's 1974 method for calculating the inclusive graphic standard deviation).

Quartz grains are the most abundant framework grains (mean = 58 vol %) and include monocrystalline, polycrystalline (including recrystallized metamorphic and stretched metamorphic types) and vein quartz. The majority of quartz grains are sub-rounded to rounded and are monocrystalline (mean = 46 vol %).

Feldspars are less common than quartz (mean = 2 vol %) and are present as plagioclase, microcline and orthoclase. Some have been partially sericitized (Figure 4.1). The majority of feldspar grains are partially dissolved, replaced by authigenic clay and ferroan cements, have experienced various degrees of compaction, and are fractured (Figures 4.2 and 4.3).

Metamorphic and sedimentary rock fragments are the most common lithic components (mean = 4 vol %), and are predominantly labile and compacted. Some appear to have been completely replaced by authigenic minerals (hematite, illite, kaolinite, and possibly albite and paragonite; Figure 4.4). Metamorphic lithics are
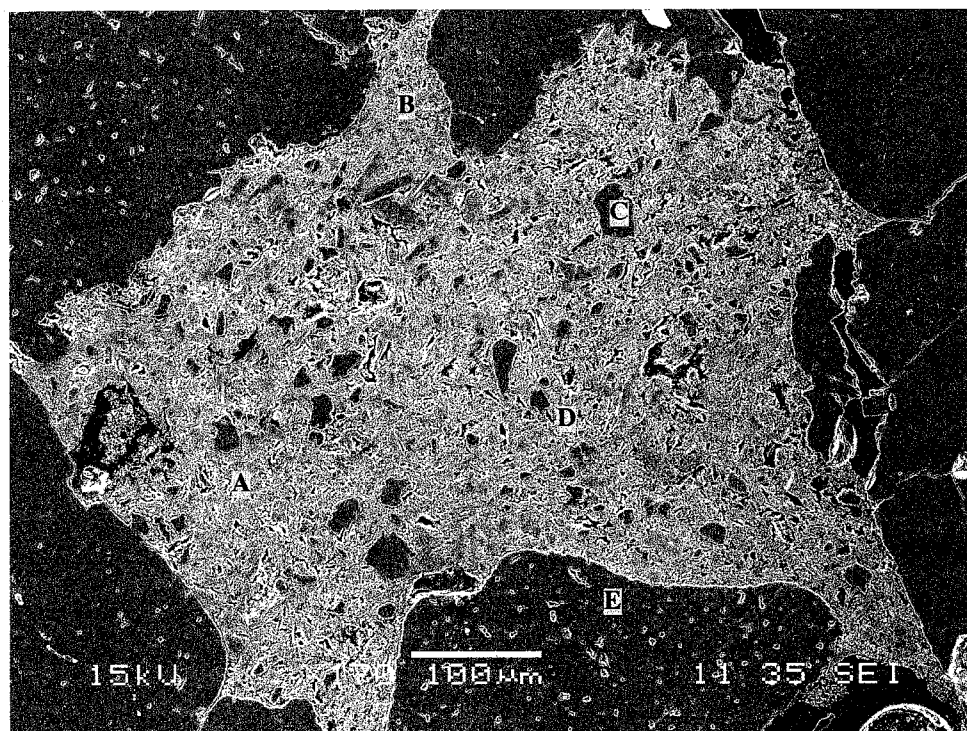
Figure 4.1 BSE photomicrograph of a fine-grained, sericitized k-feldspar grain. This grain has not been replaced or infiltrated by iron-oxides or hematite. Many feldspars in the Massillon have altered to sericite (a fine-grained muscovite), or have been replaced by kaolinite or illite.

Mineral Phases Investigated:

A: Al, Si, K, O (sericite:illite)
B: Al, Si, O, K (sericite:illite)
C: Si, O (quartz)
D: Al, Si, O (kaolinite)
E: Si, O (quartz)
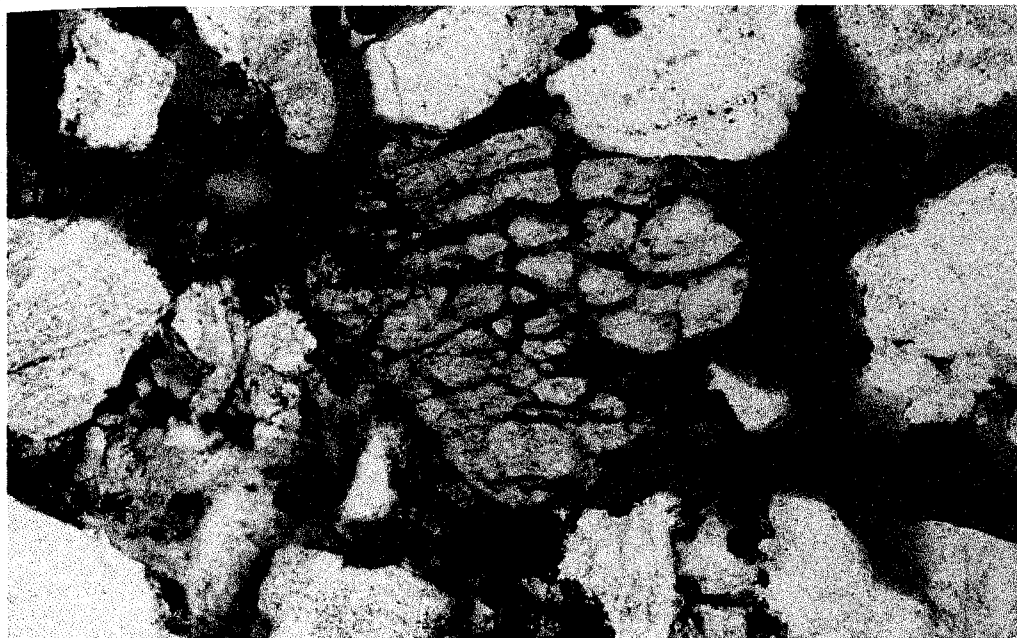
Figure 4.2   Photomicrograph of a partially and preferentially dissolved, microcline grain. Selective dissolution along the cross-hatched twin planes is a common occurrence in these grains. The increased secondary porosity developed through intragranular dissolution has been largely filled by authigenic hematite and kaolinite (image width = 1.3 mm).
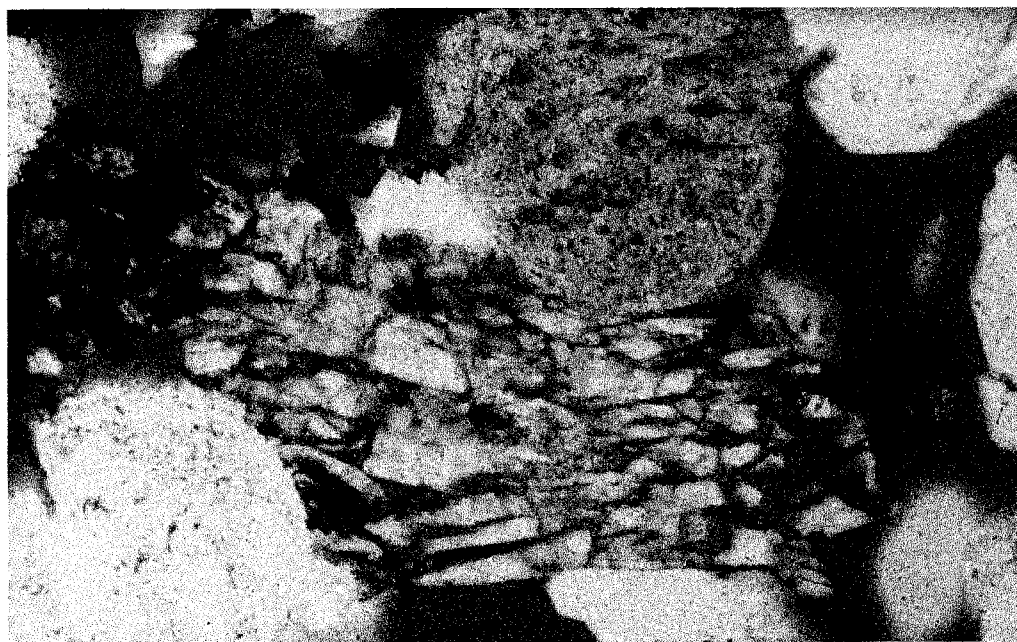
Figure 4.3   Photomicrograph of a partially dissolved microcline grain and an undifferentiated silicic grain (top, center). Hematite and kaolinite/illite have precipitated within the voids and have subsequently undergone dissolution during late diagenesis. The hematite that precipitated within the voids of this grain kept it recognizably intact during late episodes of dissolution and grain rearrangement (image width = 1.3 mm).

36
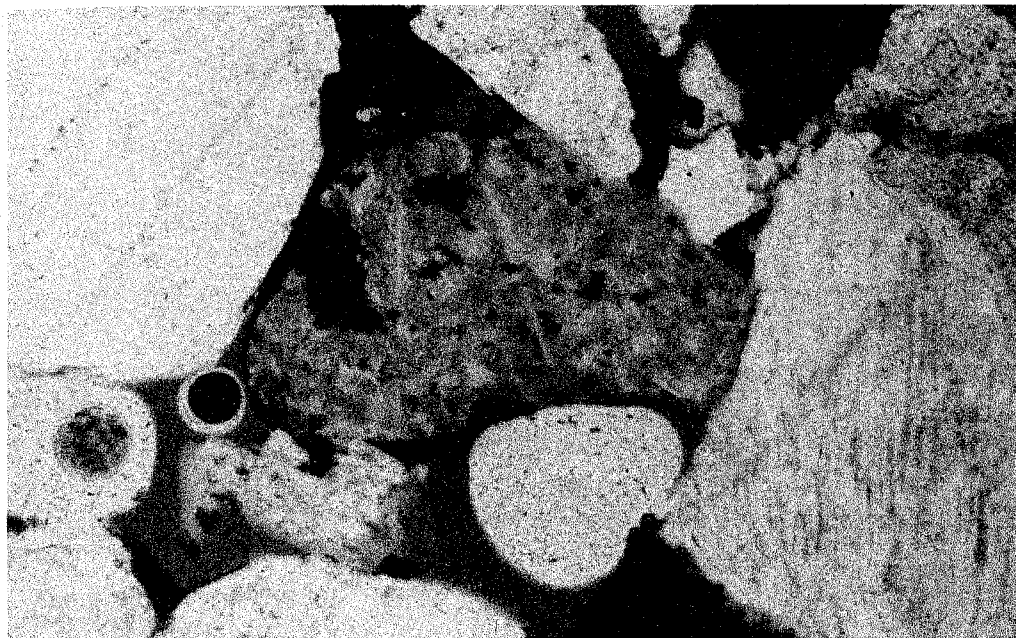
Figure 4.4 Photomicrograph of a replaced lithic grain. The translucent blue hue of this grain is intragranular dissolution microporosity and microscopic pores within authigenic kaolinite. The replaced grain is composed of hematite, potassium rich alumino-silicates, quartz fragments, kaolinite and illite. This is the composition of many of the diagenetically altered and replaced, ductile lithic grains (image width = 1.3 mm).

primarily phyllitic and schistosic, whereas sedimentary components are principally

aggregates of siltstones and claystones.

The primary cements observed include hematite, ferroan dolomite and authigenic

quartz (mean = 14 vol %). The first-order structure exhibits the greatest amount of

cement (mean = 19 vol %), followed by second and third-order structures (mean = 17 and

13 vol %, respectively). Ferroan cements include hematite and ferroan dolomite, and

make up the greatest percentage of total cements (mean = 11 vol %; Figure 4.5). Of this

11%, ferroan dolomite is present as rhombic crystal forms (small tooth-like individuals

and clusters) and comprise an average of 3% of the entire sandstone block. The first-

order structure contains the greatest percentage of ferroan cements (mean = 17 vol %:

hematite, 12%; ferroan dolomite, 5%). Ferroan cements present within the second-order

structures have a mean of 14 vol %; hematite, 10%, ferroan dolomite, 4%, and third-order

structures, 10% (hematite, 8%; ferroan dolomite, 2%).

Authigenic quartz cement (mean = 3 vol %) is less prevalent in the Massillon than

ferroan cements (mean = 11 vol %; Figures 4.6 and 4.7). Authigenic quartz is present as

euhedral and partial overgrowths, predominately rimming monocrystalline quartz grains

and rarely pore-occluding (Figure 4.8). The first-order structure contains slightly less

authigenic quartz cement than the second and third-order structures, which exhibit means

of 1 and 3 vol %, respectively). The first-order structure has the lowest percentage of

authigenic quartz, as well as the lowest measured porosities and permeabilities. Visual

examination of cathodoluminescence images confirms this data (Figures 4.9 and 4.10).

Scanning electron and back scattered images using both the Cameca SX-100 electron

microprobe and the JEOL JSM-5900 LV scanning electron microscope appear to
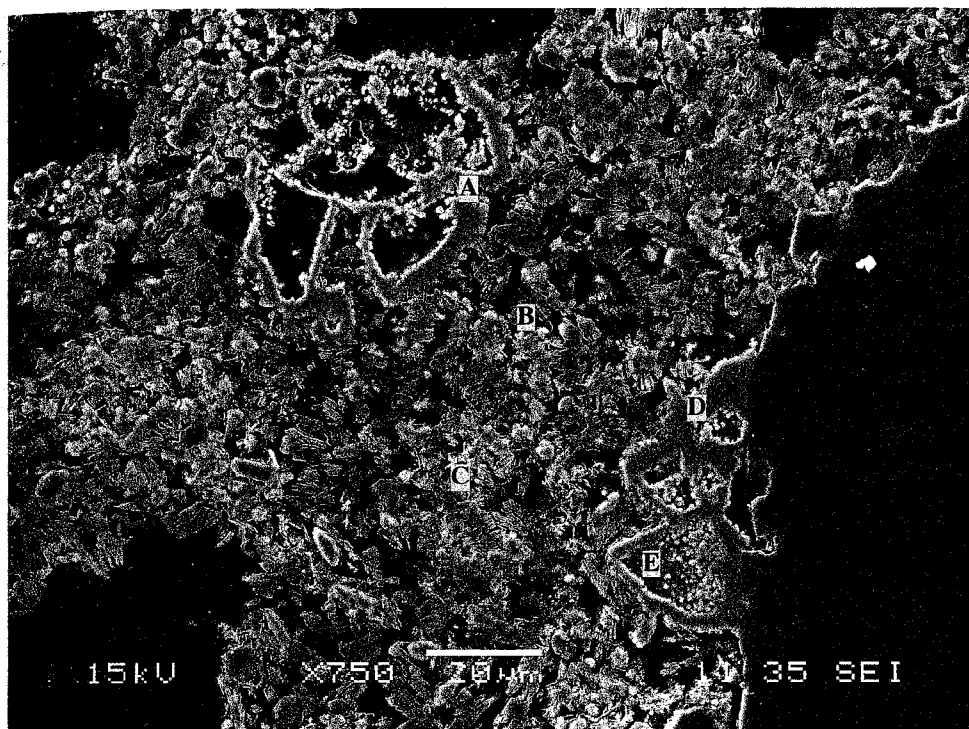
Figure 4.5   BSE photomicrograph showing authigenic hematite, kaolinite and partially dissolved ferroan dolomite clusters occluding pore space between quartz grains. Hematite has precipitated within many partially dissolved dolomite rhombs (E), equilibrating the positive effects of dissolution on the permeability. Secondary porosity created within other partially dissolved clusters (A) will possibly increase the effective porosity and the permeability.

Mineral Phases Investigated:

A: Fe, O, Si, Al (hematite)
B: Fe, O, Si, Al (hematite)
C: Si, Al, O (kaolinite)
D: Fe, O, Si, Al (hematite)
E: Fe, O, Si, Al (hematite)
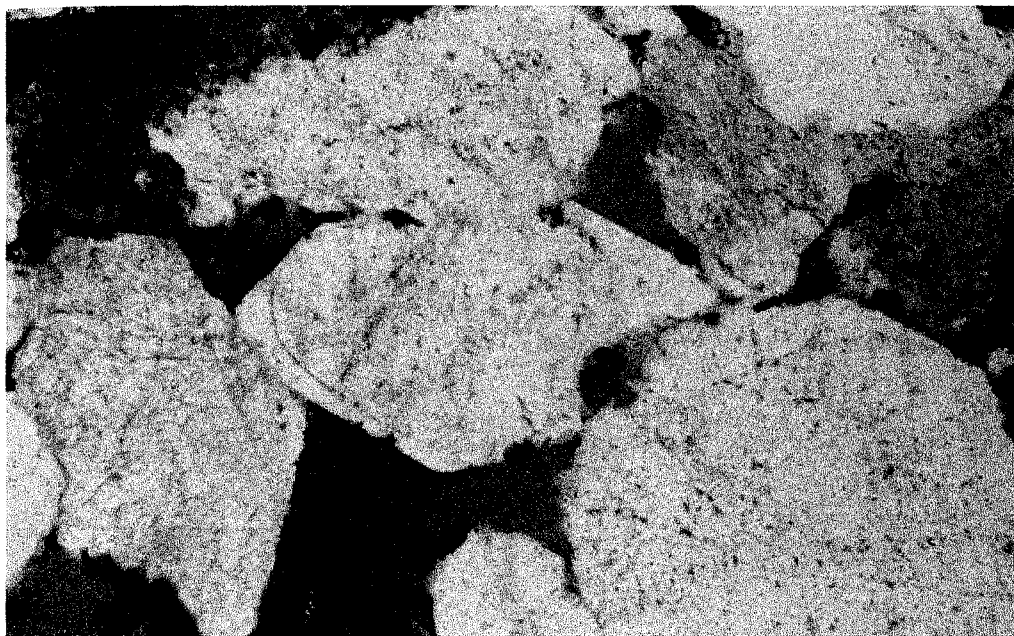
Figure 4.6   Photomicrograph showing a conspicuous framework quartz grain (center), that has precipitated authigenic quartz along most of it's margin. A dust rim of iron oxide separates the euhedral overgrowth from the original detrital grain. Authigenic quartz has replaced the dolomite clusters to the right of the grain, but has not fully engulfed the rhombohedral mineral cluster (image width = 1.3 mm).
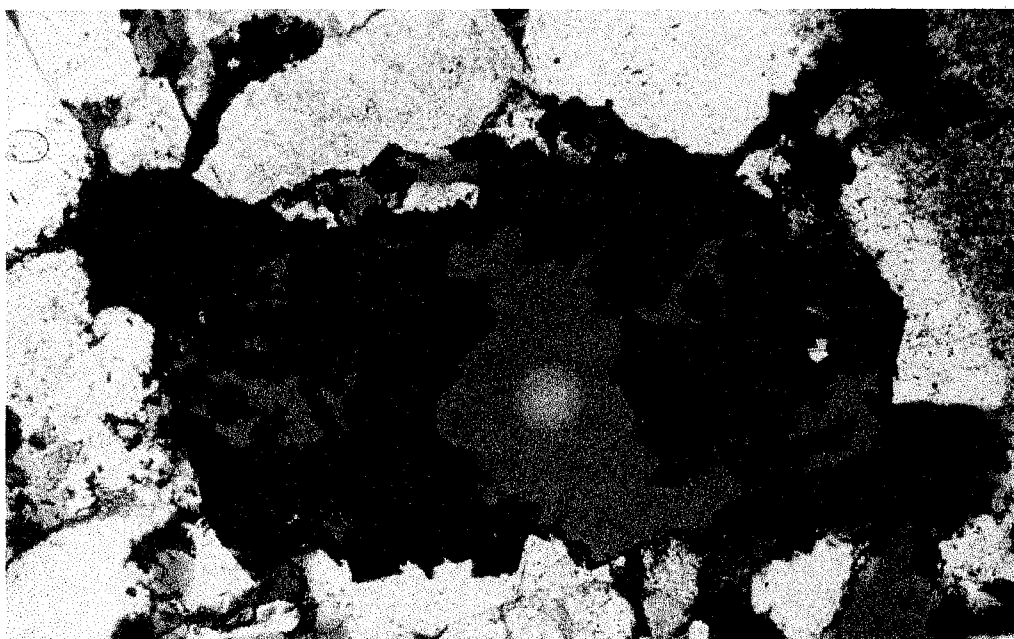
Figure 4.7   Photomicrograph of ferroan dolomite rhombohedral clusters and authigenic hematite surrounded by framework quartz. These iron and silica replaced dolomite rhombs are widespread and ubiquitous, and their partial and complete dissolution has possibly increased the effective porosity and the permeability in the Massillon (image width = 1.3 mm).

40
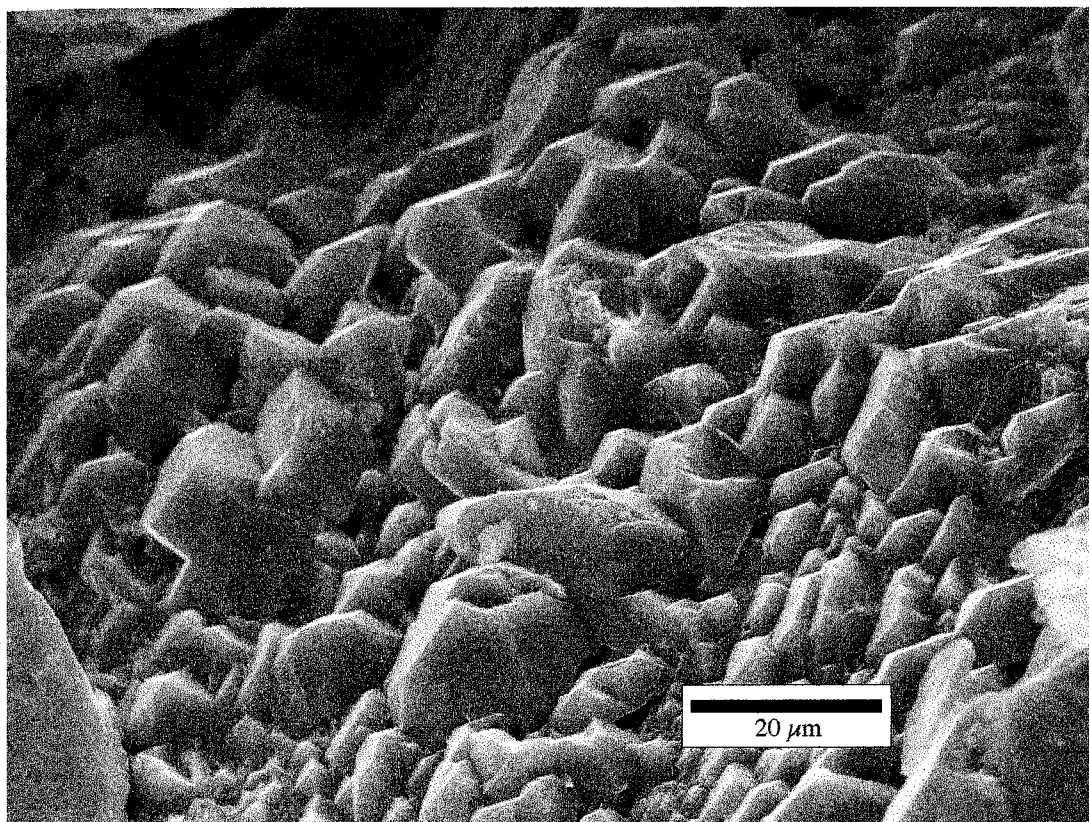
Figure 4.8

SEM photomicrograph of authigenic, euhedral microquartz and megaquartz. Although easily discerned using the electron microprobe, these quartz overgrowths are difficult to recognize using the petrographic microscope.
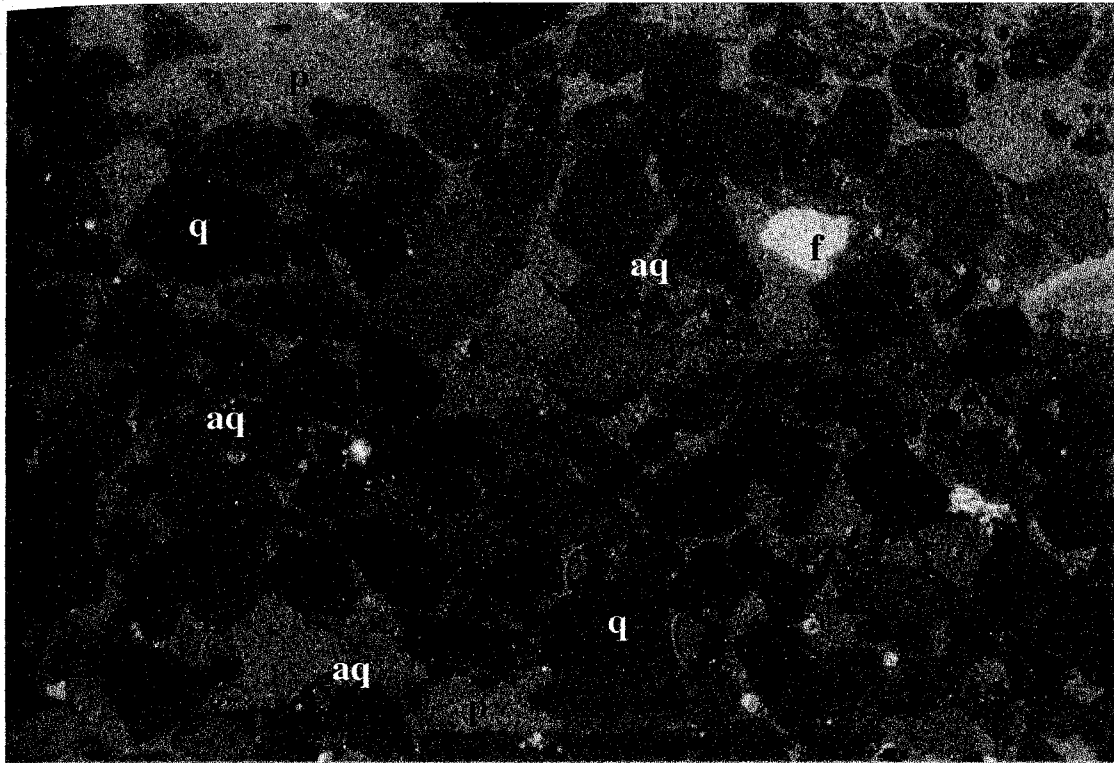
Figure 4.9

Cathodoluminescence photomicrograph taken from a portion of subsection 7G1z.4. The complete subsection image contains approximately 0.5 vol % authigenic quartz, determined from modal analysis. Thin, grain-rimming authigenic quartz (aq) is observed along the margins of detrital framework quartz grains (q; seen here as reddish-brown, reddish-orange and pink). The authigenic quartz overgrowths, when observed using the luminoscope, are darker than the host grains they surround, fascilitating their recognition. The bright, bluish-white grains are feldspars (f) and the green matrix between framework grains is porosity (p). This image was captured using a voltage of 21 kV, a current of 0.5 mA, and an exposure time of 15 minutes (mean framework grain size in this image is 1.09 phi, or 0.47 mm).
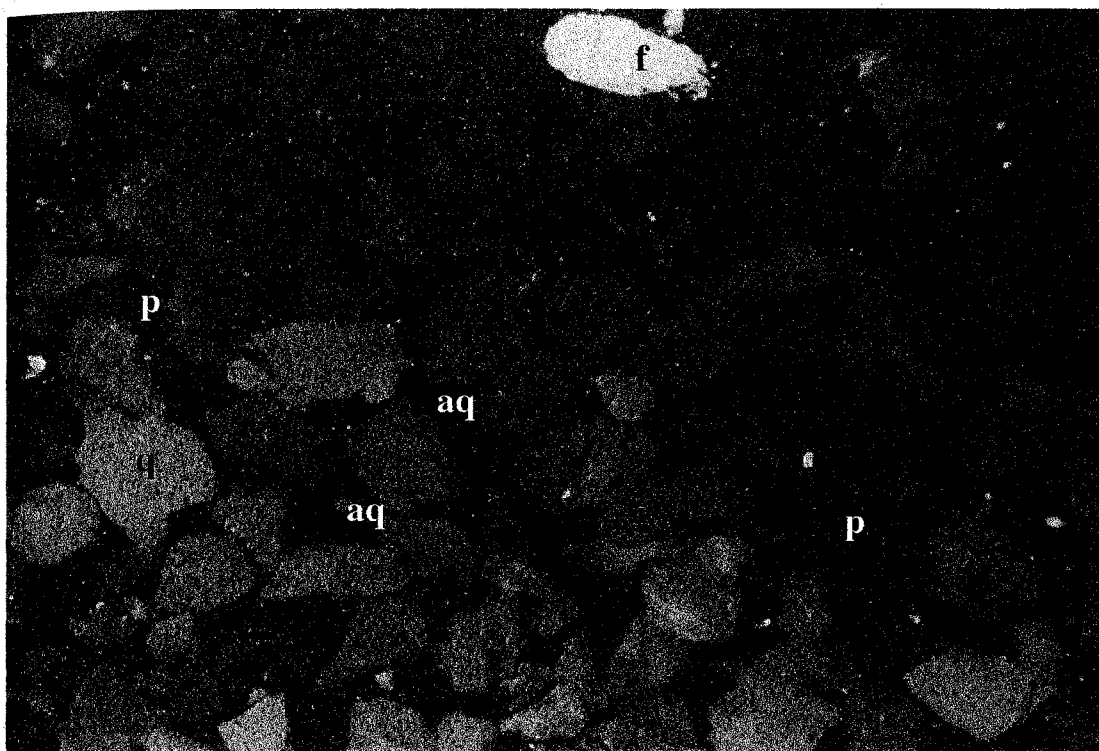
Figure 4.10

Cathodoluminescence photomicrograph taken from a portion of subsection 7B3z.3. The complete subsection image contains approximately 5.5 vol % authigenic quartz, determined from modal analysis. Thin, grain-rimming authigenic quartz (aq) is observed around the margins of detrital framework quartz grains (q; seen here as light brown, reddish-orange and tannish-rose). The authigenic quartz overgrowths are darker, or approximately the same color as the host grains they surround. The bright, bluish-white grain is a feldspar (f) and the green and dark brown matrix between framework grains is porosity (p). This image was captured using a voltage of 21 kV, a current of 0.5 mA and an exposure time of 15 minutes (mean framework grain size in this image is 0.74 phi, or 0.60 mm).

contradict this observation, and suggest that authigenic quartz is rather ubiquitous (Figure 4.11). However, visual examination of grain surfaces using the SEM often exaggerates the abundance of cements and matrix material rimming and coating grains, because the SEM preferentially examines grain surfaces, which is where such components are concentrated (Mozley, 2001; personal communication). The point count values for authigenic quartz are the only quantitative data used in this thesis.

Allogenic and authigenic, pore filling and pore lining clay minerals make up 6% of the whole rock. The first-order erosional structure has a mean of 3 vol % clay (2% pore filling; 1% pore lining), whereas second-order structures average 5% clay (3% pore filling; 2% pore lining) and third-order structures are comprised of an average of 6% clay (4% pore filling; 2% pore lining clay). Kaolinite is the most abundant authigenic clay in the Massillon Sandstone and may represent neomorphic replacement of preexisting detrital feldspar and/or lithic grains. Three textural varieties of kaolinite are present: 1) fine-grained vermicules; 2) coarse-grained vermicules; and 3) blocky crystals (Figure 4.12). Illite, sericite and paragonite are also present as platy sheets.

Matrix material (mean = 20 vol %) is the intergranular volume excluding intergranular porosity, and includes ferroan cements (hematite and ferroan dolomite), authigenic quartz cement, allogenic clay and authigenic clay. Matrix material contributes more to the intergranular volume than does porosity, with the maximum equaling 31% and a minimum of 13%, with first and second-order structures averaging 22% and third-order structures averaging 19%.
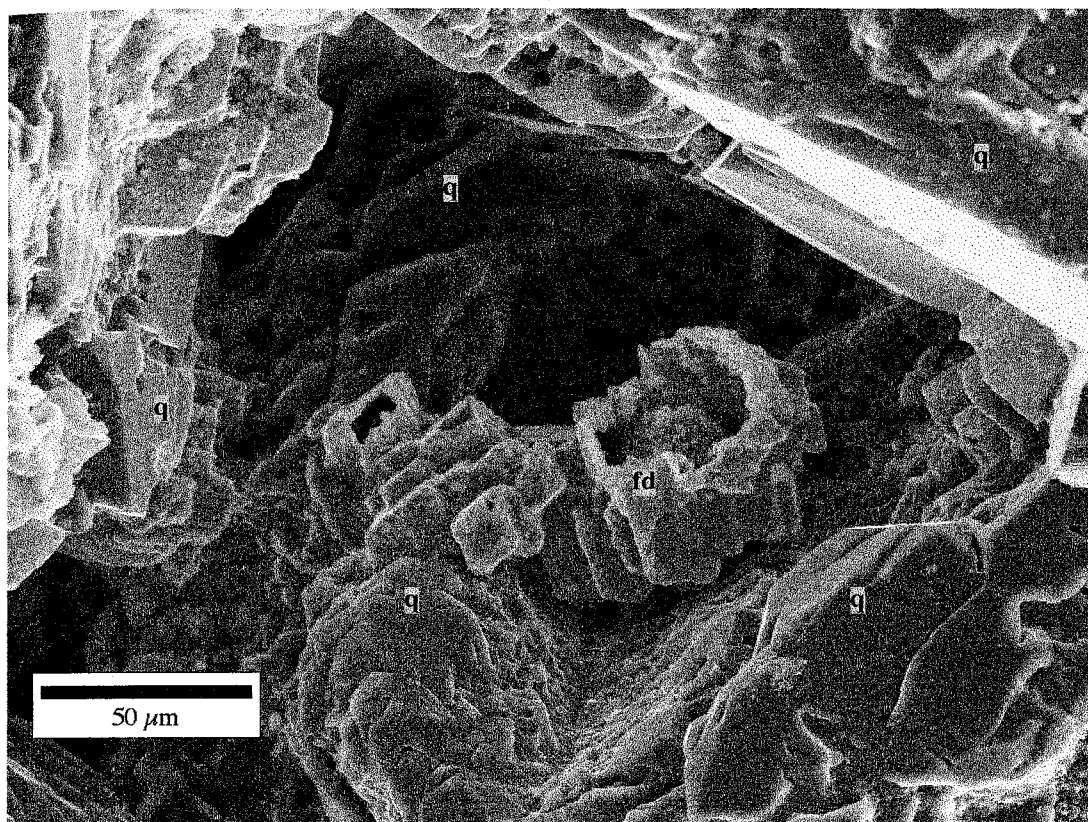
Figure 4.11

SEM photomicrograph of a large, partially open pore in the Massillon Sandstone. Euhedral, authigenic quartz has replaced the oxidized rhombohedral dolomite clusters. Authigenic megaquartz (q) keeps the clusters in place, restricting flow along the pore walls. The outline of previously attached dolomite rhombs can be seen on and around the surface of the varigated quartz overgrowths. The predissolution volume percentage of dolomite was apparently considerably higher; their subsequent dissolution has apparently increased the effective pore network in this sandstone. Within the relatively large, dissolved, rhombohedral calyx (fd), authigenic hematite has precipitated.
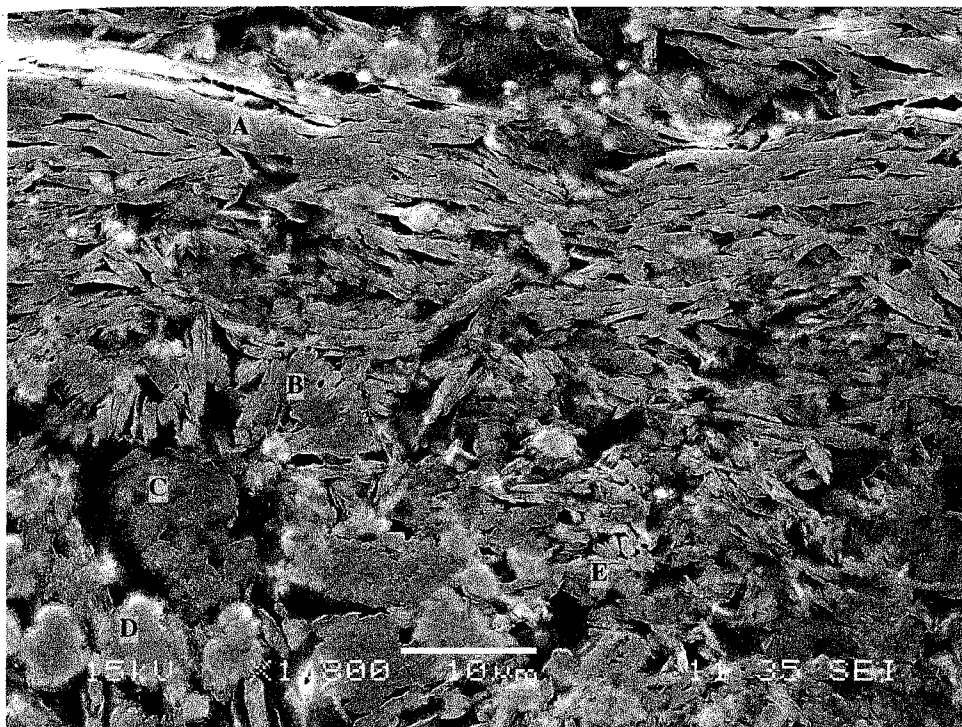
Figure 4.12   BSE photomicrograph of detrital and authigenic clay (A), blocky and vermicular, authigenic kaolinite (B,C), hematite (D) and remnants of a potassic feldspar that may have altered to sericite or illite (E). Kaolinite, sericite, illite and paragonite will precipitate as a result of the dissolution and alteration of feldspars, such as microcline, in this and similar sandstones.

Mineral Phases Investigated:

A: Si, Al, K, O, Na (paragonite:sericite:illite)
B: Si, Al, O (kaolinite)
C: Si, Al, O (kaolinite)
D: Fe, O, Si, Al (hematite)
E: Al, Si, O, K (sericite:illite)

4.2.2. Porosity and Pore Structure

Porosity was examined both by point counting thin sections and using image analysis applied to rendered and binarized, thin section subsection photomicrographs. Average total porosity determined by point counting is 16%. Of this, less than 0.5% is microporosity (primarily in replaced, fine-grained silicic lithics). Third-order structures have the highest porosities (mean = 17 vol %), followed by second-order structures (mean = 15 vol %) and then the first-order structure (mean = 12 vol %; Figure 4.13). Intergranular macroporosity, whether preserved primary or diagenetic secondary, makes up 99.5% of the total porosity within all erosional, bounding surface and depositional, cross-stratified structures.

Two-dimensional intergranular pore widths were measured during point counting. Measurements were made from the centers of pores (not the pore throats). The widest intergranular pores are observed in the second and third-order structures (whole rock mean width = 0.12 mm), with the widest measuring 0.20 mm and the narrowest measuring 0.06 mm. First-order subsections have the narrowest pores (mean = 0.09 mm), the widest reaching 0.15 mm and the narrowest measuring 0.07 mm.

Porosity was also quantified using IP Lab Software and binarized subsection images. Whole rock mean porosity determined by image analysis is 14% (minimum = 4%; maximum = 23%). Third-order structures have the highest image analysis derived porosities (mean = 15 vol %), followed by second-order structures (mean = 12 vol %) and finally, the first-order structure (mean = 8 vol %).

47

Distribution of Micro- and Macro- Point Count Porosity
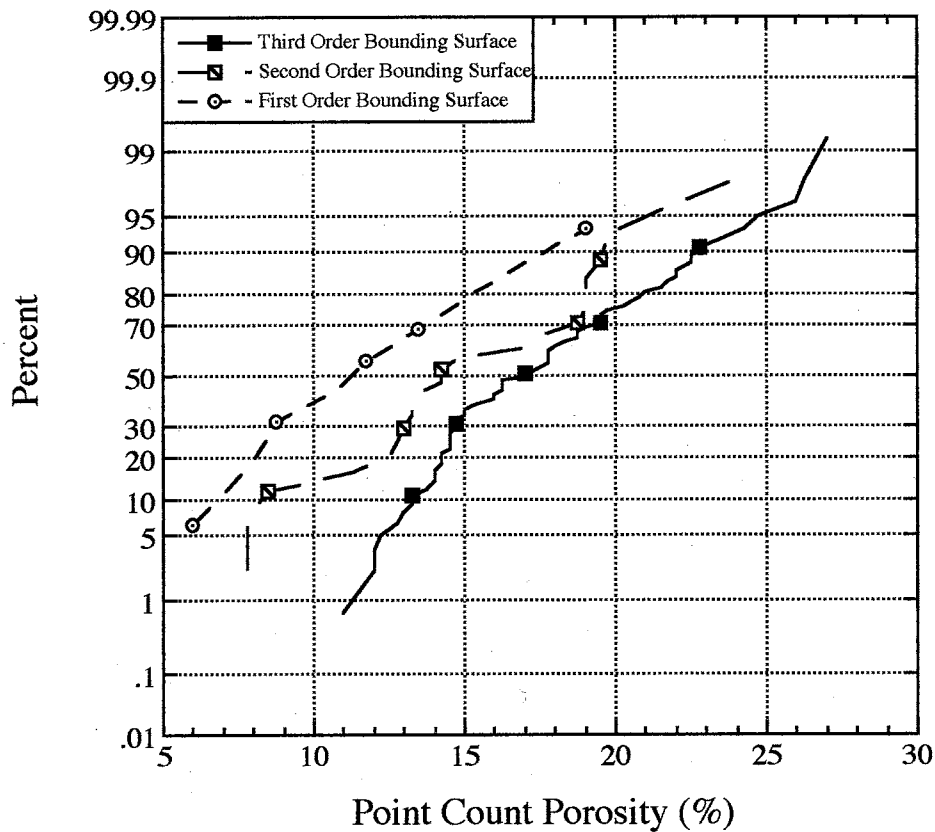
Figure 4.13

Distribution plot showing the volume percentages of micro- and macroporosity determined from modal analysis of all thin section subsections. Third-order structures have the highest total porosities (mean = 17.48%; max. = 27.00%; min. = 11.00%), second-order structures have the second highest total porosities (mean = 15.00%; max. = 23.75%; min. = 7.75%), and the first-order structure has the lowest determined point count porosities (mean = 11.65%; max. = 19.00%; min. = 6.00%).

4.3. Diagenesis

Detailed petrographic inspection of thin sections and core samples reveals that the Massillon has undergone a complex diagenetic history involving initial grain rearrangement and early cementation, as well as continued grain rearrangement, fracturing, mineral precipitation, mineral replacement and mineral dissolution during burial and uplift.

4.3.1. Compaction and Grain Rearrangement

Floating grains (with no grain-to-grain contacts), as well as tangential, long, concavo-convex and sutured contacts are observed in Massillon Sandstone (Figures 4.14 and 4.15). Concavo-convex, long and tangential grain contacts are numerous, whereas the occurrence of floating grains is due to a high degree of grain and mineral dissolution, evident by the numerous oversized pores. Sutured framework quartz grains are prolific, an indication that this sandstone has undergone extensive compaction. Suturing can generate, and subsequently liberate, siliceous fluids into the system by pressure solution, a process that contributes to authigenic quartz precipitation. Petrographic and SEM analysis reveals that authigenic quartz overgrowths occur in close proximity to sutured contacts.

In addition, grain bending, as with muscovite flakes, grain fracturing (Figures 4.16 and 4.17) and ductile deformation of labile grains (Figures 4.18 and 4.19) are also commonly observed. Almost all of the deformed lithics have been replaced by authigenic hematite, kaolinite, illite and other undifferentiated authigenic clays (Figure 4.20). Fractured grains contribute 0.2% of the whole rock porosity attributed to Face 7.

49
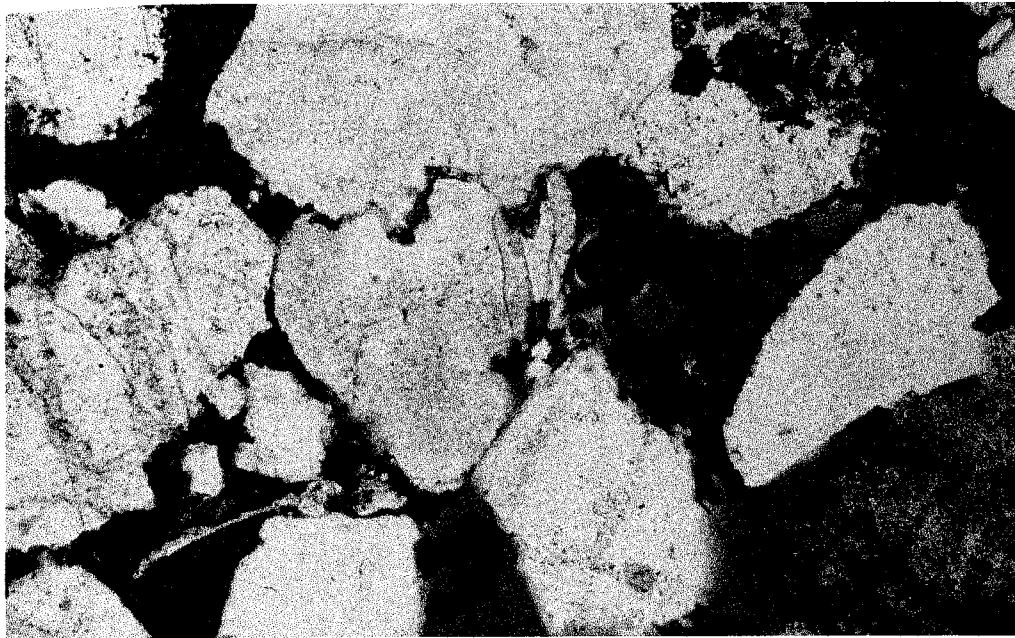
Figure 4.14   Photomicrograph of authigenic iron oxide replaced alumino-silicate minerals and ferroan dolomite compacted between two quartz grains (center of this photomicrograph). Many quartz grains have heavily corroded margins, due in part to the stresses induced from pressure solution. The ubiquitous precipitation of, and replacement by authigenic hematite is observed throughout this sandstone (image width = 1.3 mm).
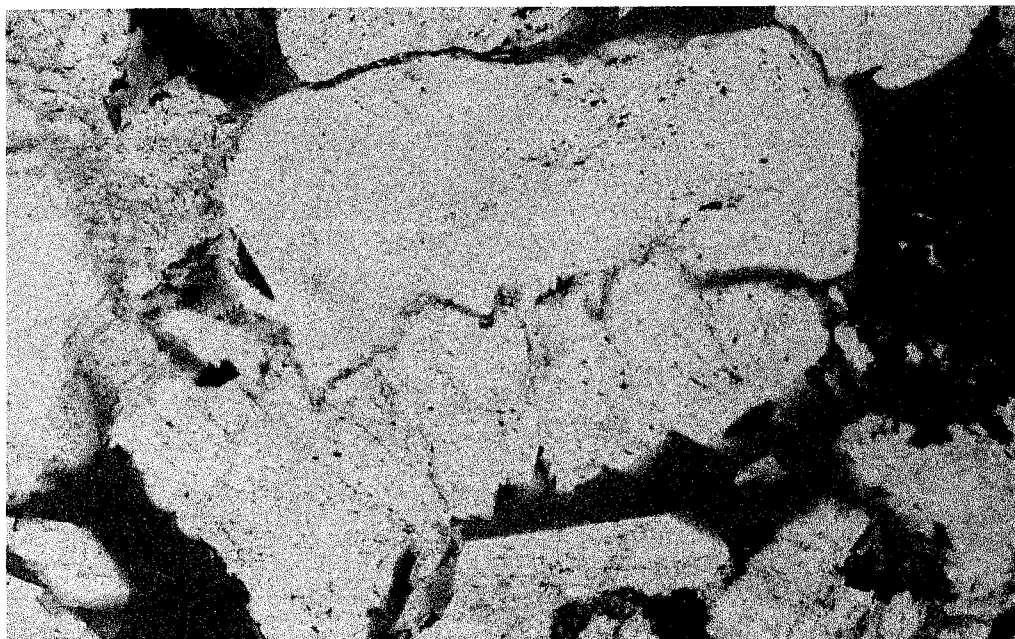
Figure 4.15   Photomicrograph of two sutured quartz grains. The margin of the central grain is highly irregular and corroded, most likely due to authigenic quartz precipitation into now dissolved ferroan dolomite assemblages. Authigenic quartz has precipitated on the margin of a quartz grain at the bottom of the image (image width = 1.3 mm).
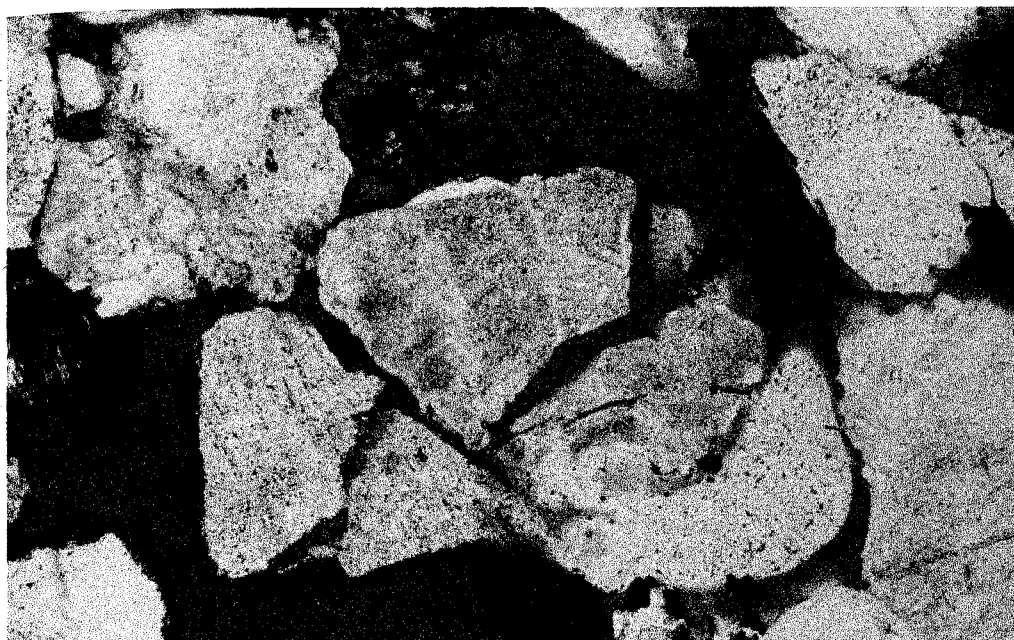
Figure 4.16   Photomicrograph of two fractured quartz grains; the fractures are relatively hematite free. Enhanced secondary porosity created by intragranular fracturing does not appear to significantly increase the effective porosity or permeability of the Massillon Sandstone (image width = 1.3 mm).
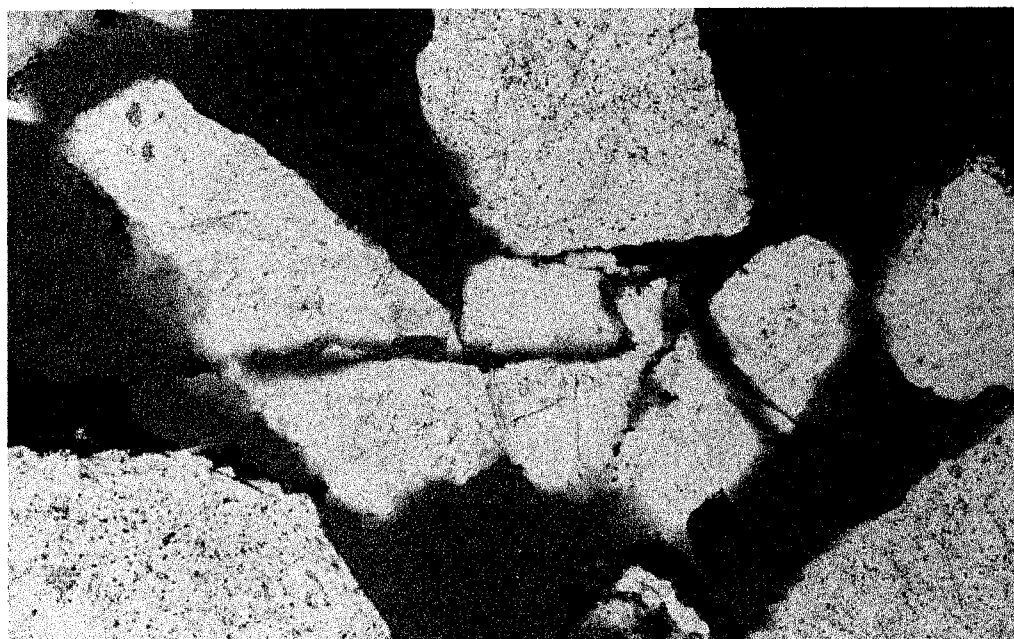
Figure 4.17   Photomicrograph of three fractured quartz grains. The grains are slightly off-set (bottoms moved to the right), an indication of limited movement during the fracture event. These grains, as well as their fractures are relatively clean, which is uncommon in this sandstone (image width = 1.3 mm).

Figure 4.18   Photomicrograph exhibiting the compaction of a fine-grained, undifferentiated silicic lithic grain composed of hematite, kaolinite and potassic and sodic alumino-silicate minerals. Framework quartz grains and a smaller microcline grain have enclosed this ductile grain (image width = 1.3 mm).

Figure 4.19   Photomicrograph of quartz grains surrounding a pore occluding, iron oxide replaced, fine-grained silicic lithic. Dissolution has occurred within the replaced, hematitic matrix and at the grain's margins. Hematite has also precipitated within fractures in several quartz grains. Compaction and the precipitation of authigenic cements, such as authigenic hematite, are responsible for the majority of diagenetically induced pore occlusion in this sandstone (image width = 1.3 mm).
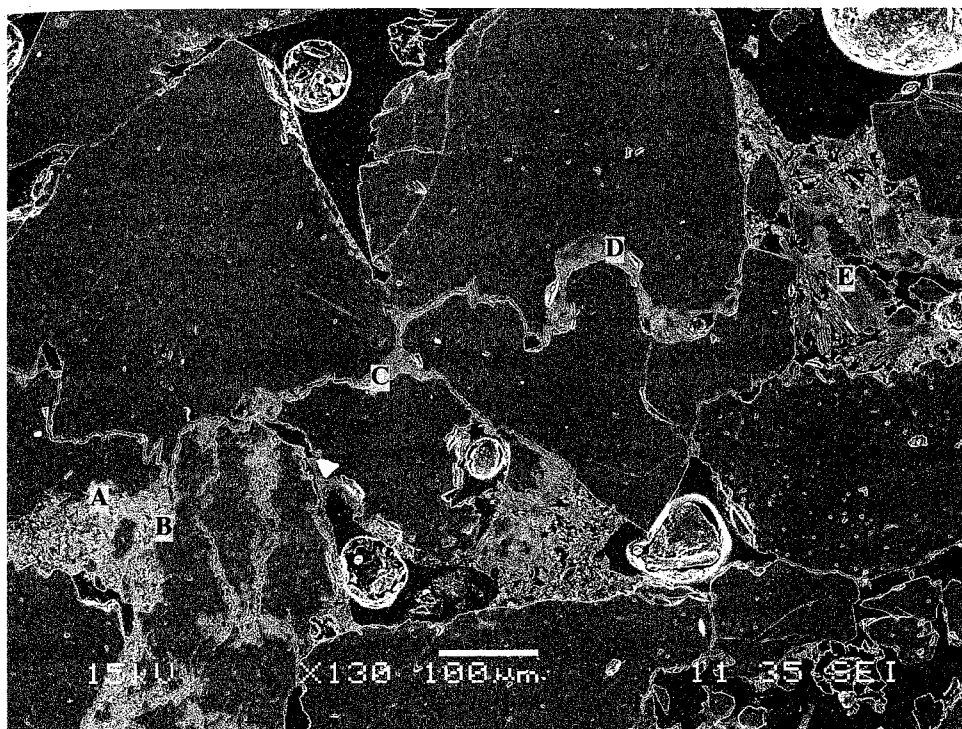
Figure 4.20 BSE photomicrograph showing authigenic iron oxide replaced alumino-silicate minerals and hematite compacted between quartz and feldspar grains. Many quartz grains have heavily corroded margins due in part to pressure solution. Almost all feldspars are partially dissolved and replaced, or have authigenic minerals precipitated within their dissolved twin and cleavage planes.

Mineral Phases Investigated:

A: Fe, Si, O, Al (hematite)
B: Si, Al, K, O (k-feldspar)
C: Al, Si, O (kaolinite)
D: Si, Al, K, O (k-feldspar)
E: Si, Al, K, O (k-feldspar)

4.3.2. Cementation and Replacement

Matrix material makes up an average of 20% of the Massillon Sandstone. Cements comprise 14% (hematite 8%; ferroan dolomite 3%; authigenic quartz 3%) and clay minerals comprise 6% of the whole rock volume (4% pore filling clay; 2% pore lining clay). Authigenic clay includes scalloped and vermicular kaolinite (occurring as pore filling and pore lining clay or as replacement phase minerals within lithic and feldspar grains), sheeted and platy illite, and undifferentiated authigenic clay. Hematite replaces labile lithics and feldspars, precipitated within fractures and partially dissolved framework grains and coats framework grains (Figures 4.21 and 4.22). Ferroan dolomite is present as individual rhombs and as intact or partially dissolved bound assemblages or clusters. The dolomite is ubiquitous and microscopic (typical length is 10-50 μm) and has been automorphically penetrated by authigenic quartz along the sandstone pore walls (Figures 4.23 - 4.25). The ferroan dolomite and hematite also form bridges that span pore throats and individual pores (Figures 4.26 and 4.27).

Authigenic quartz occurs as both mega- and microquartz (< 20 μm) and also forms intergranular bridges (Figure 4.28). It appears to restrict, to some degree, the precipitation of clays on pore walls and the population of ferroan dolomite clusters that also occupy space on the pore walls.

4.3.3. Secondary Porosity

Secondary porosity in the Massillon Sandstone is derived from either: 1) the complete or partial dissolution of detrital, framework grains or non-framework constituents; 2) the dissolution of authigenic minerals; and 3) the fracturing of grains,

54

Figure 4.21 Photomicrograph of pore filling, authigenically precipitated and replaced ferroan cements (primarily authigenic hematite and ferroan dolomite clusters; image width = 1.3 mm).
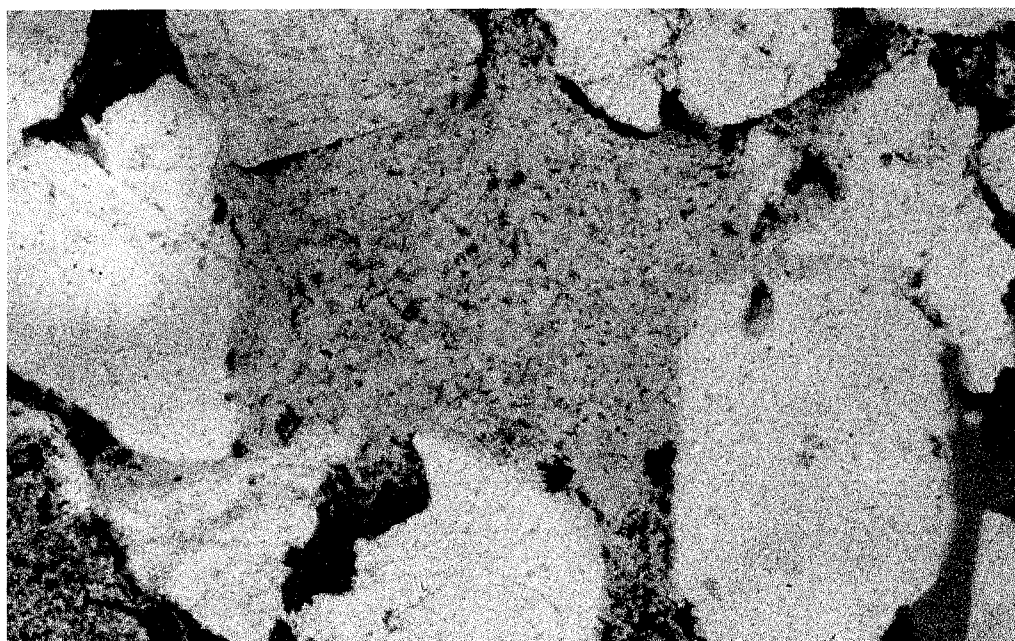
Figure 4.22 Photomicrograph of pore occluding authigenic kaolinite, hematite, intact and partially dissolved ferroan dolomite, authigenic quartz and potassium rich alumino-silicate minerals. This recycled plug of diagenetically precipitated minerals is the subsequent result of grain dissolution (feldspar grain, lithic grain or diagenetic clay; image width = 1.3 mm).
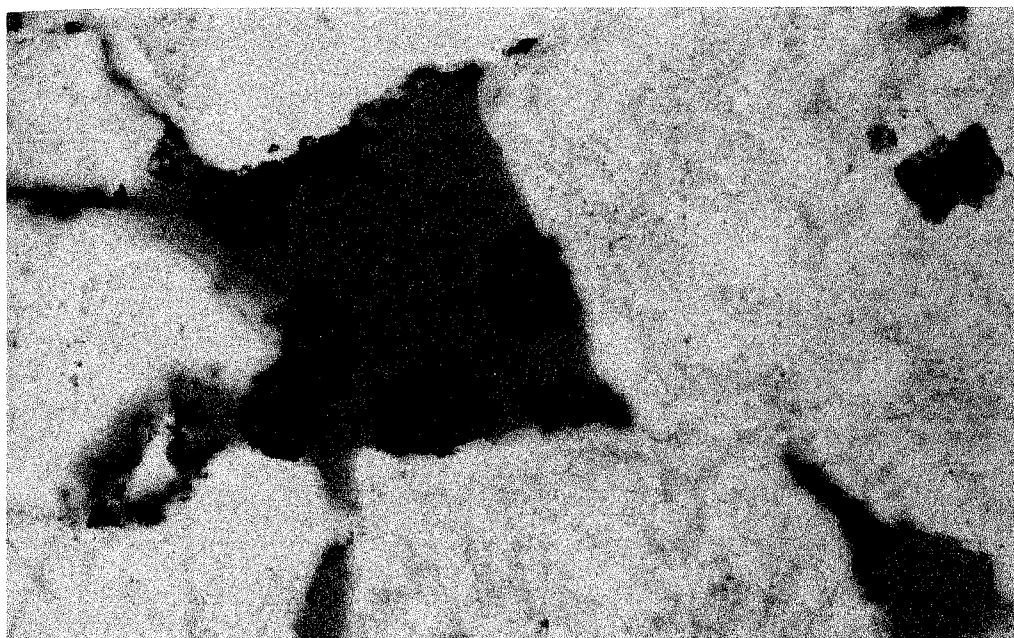
Figure 4.23   Photomicrograph of ferroan dolomite rhombohedral clusters clinging to the margins of quartz grains, engulfed by authigenic quartz and lining the small pore between the grains (image width = 0.65 mm).
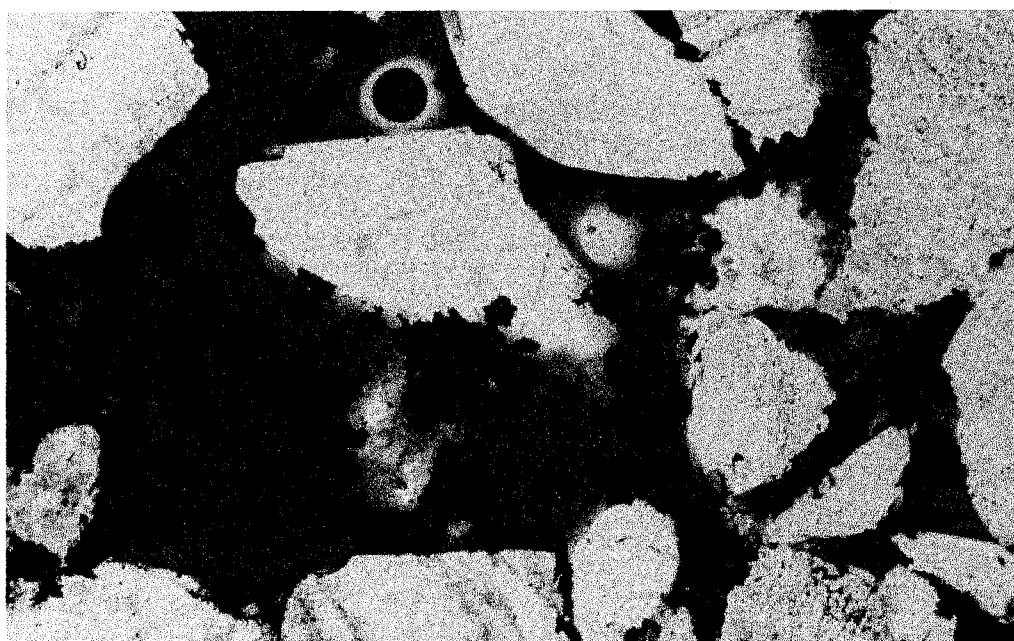
Figure 4.24   Photomicrograph of pore lining and pore filling ferroan dolomite individuals and clusters. These minerals occlude pore channels and pore throats and cling to the pore walls, automorphically penetrated by authigenic quartz. The rhombs' congested attitude and cluster arrangements are concentrated along grain margins, decreasing the intergranular macroporosity, as well as restricting flow through pores and pore throats (image width = 1.3 mm).
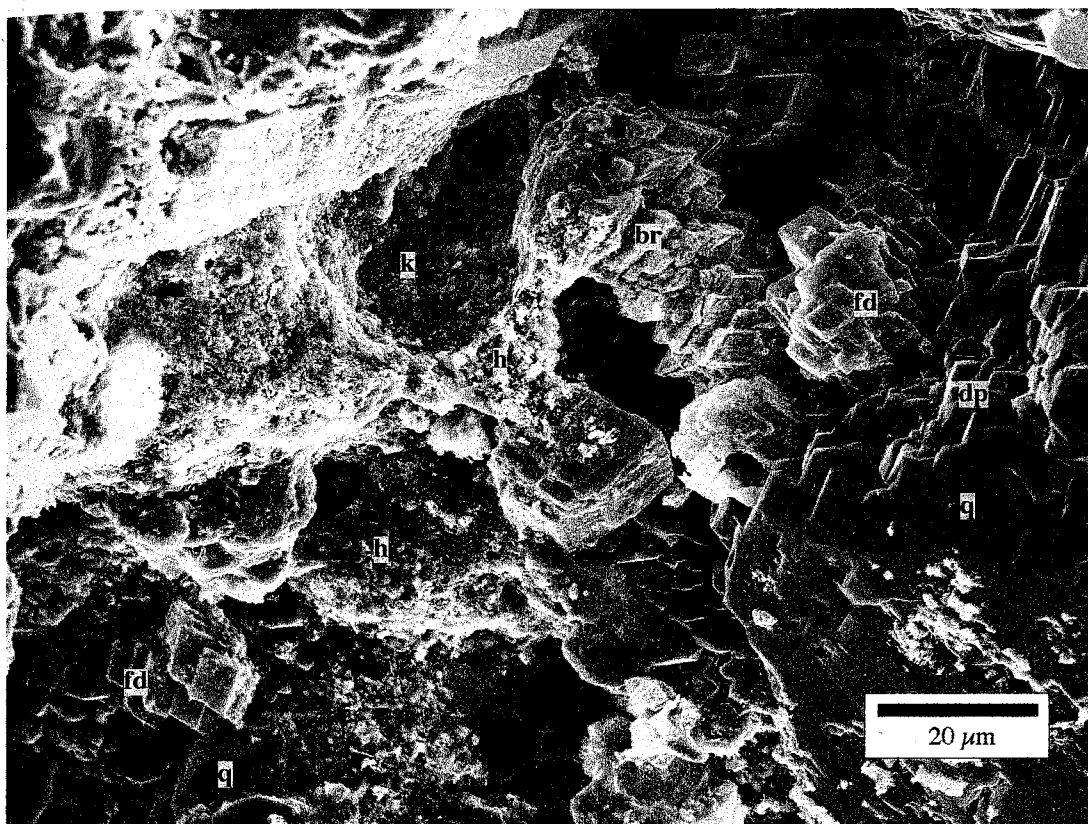
Figure 4.25

SEM photomicrograph of euhedral, micro- and megaquartz (q), fully intact ferroan dolomite clusters (fd), a ferroan dolomite bridge (br), authigenic iron oxide cement (hematite; h) and authigenic kaolinite (k) with other undifferentiated detrital and autochthonous clays. Complete dissolution of a ferroan dolomite cluster is revealed by the dissolution surface pits (dp) on the margin of the large quartz grain (far right at center).
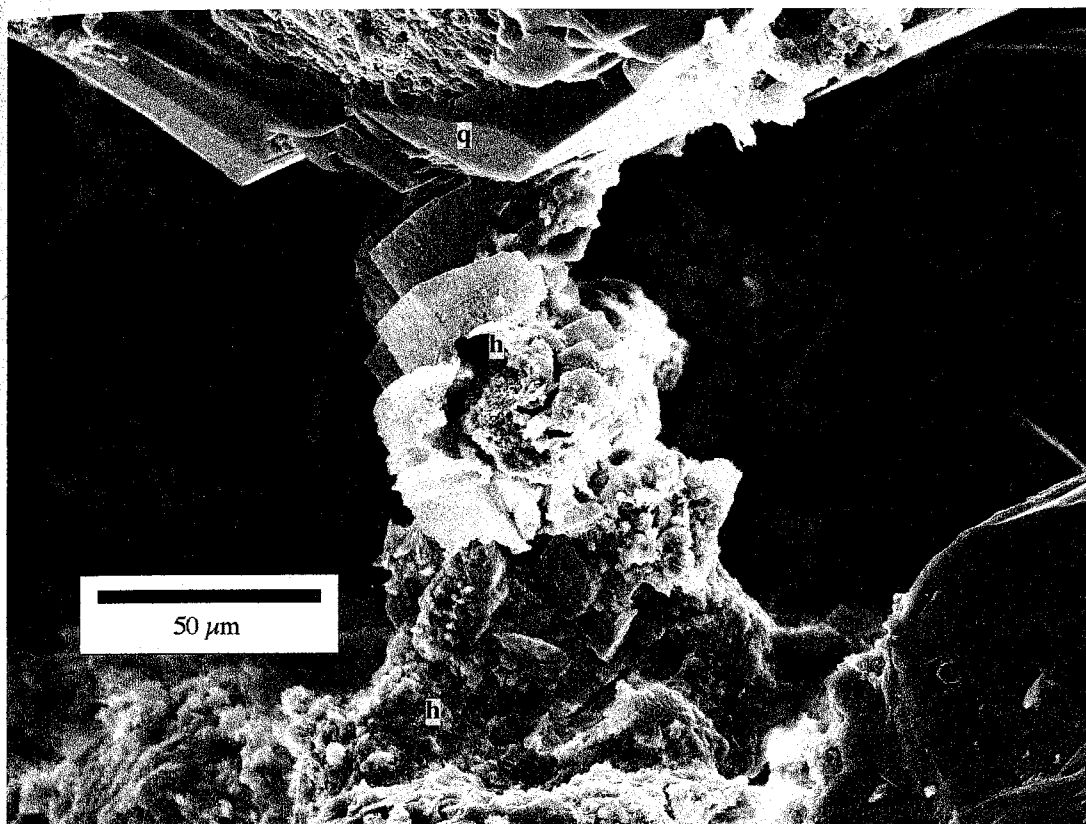
Figure 4.26

SEM photomicrograph of a ferroan dolomite bridge spanning a pore channel. The bridge is attached to the top pore wall by euhedral, authigenic megaquartz. As the authigenic quartz (q) precipitated, it automorphically penetrated the dolomite, replacing first the rhomb's margin, then subsequently the entire mineral aggregate. The center of the bridge is partially dissolved. Inside the partially dissolved rhomb authigenic iron oxides have precipitated (h), as well as at the base of the structure.
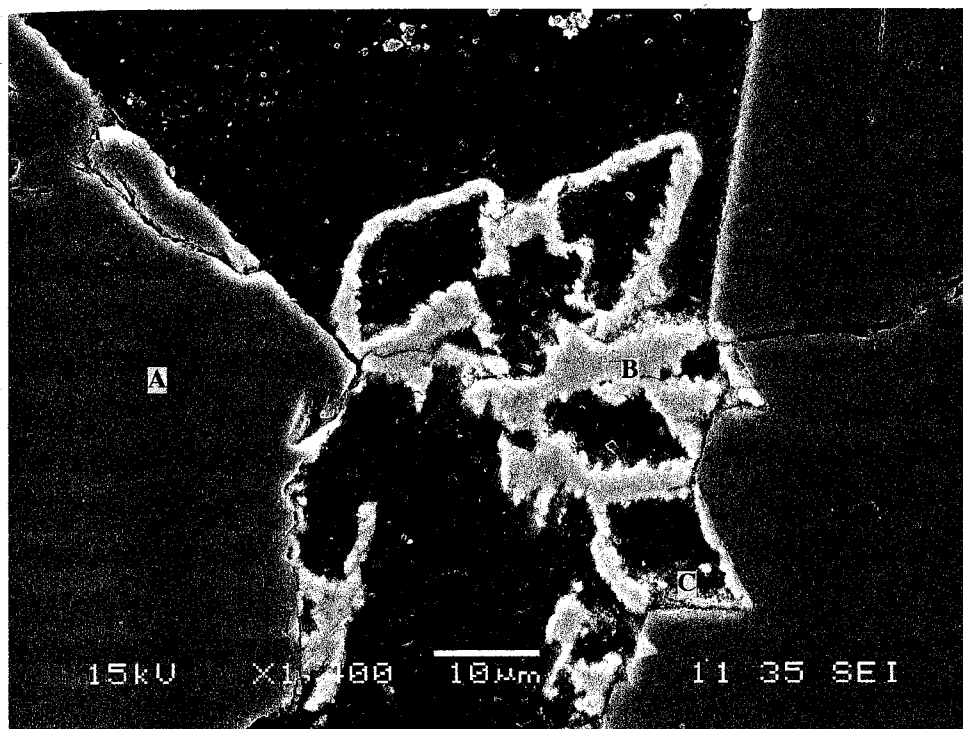
Figure 4.27   BSE photomicrograph of pore filling and pore lining, intact and partially dissolved ferroan dolomite clusters. These minerals restrict flow through pore throats such as this, decreasing the effective porosity and the permeability of the sandstone. Secondary porosity created from the partial dissolution of ferroan dolomite clusters also acts to increase the permeability.

Mineral Phases Investigated:

A: Si, O (quartz)
B: Fe, O, Si (hematite)
C: Si, Fe, O (hematite)
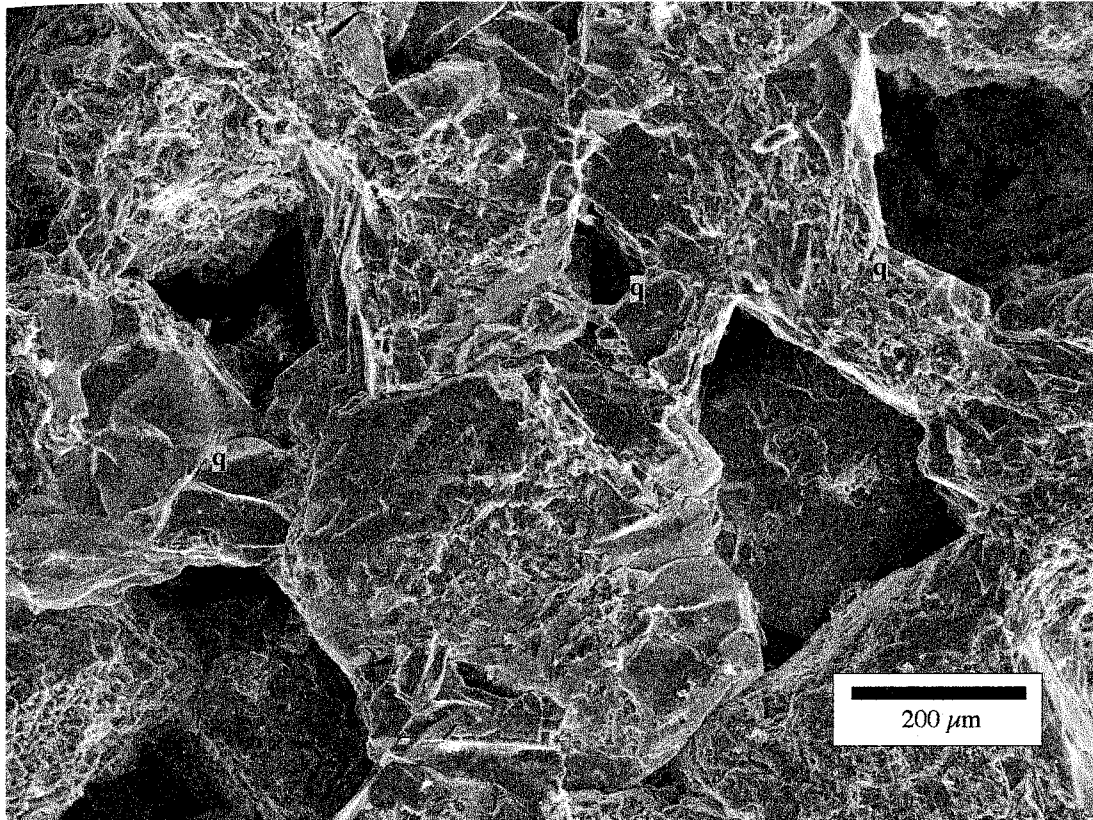
Figure 4.28

SEM photomicrograph of authigenic quartz bridges (q) adjoining relatively clean framework quartz grains. These bridges create a more tortuous path for fluids and obstruct movement through the pore network.

cements or matrix. Relatively unstable, detrital, sedimentary and metamorphic lithic grains and sericitized feldspars have undergone dissolution, particularly through the centers of the grains (Figures 4.29 and 4.30). Hematite that had once partially replaced and precipitated within the dissolved void spaces created within lithics, feldspars and detrital quartz, has subsequently undergone its own full or partial dissolution (Figure 4.31). Undifferentiated, fine-grained silicic framework grains contain secondary, dissolution, intragranular micro- and macroporosity (Figure 4.32). The original grains are frequently either framework lithic fragments or feldspar grains, initially replaced almost completely by kaolinite and other authigenic clay minerals, followed by replacement and precipitation of hematite. Subsequent dissolution produced the observed intragranular micro- and macroporosity found in such grains. Feldspars, in particular microcline, have undergone extensive dissolution and fracturing, increasing the porosity and possibly the effective permeability of the sandstone (Figures 4.33, 4.34 and 4.36).

The dissolution of ferroan dolomite also contributes to higher porosities in the Massillon (Figure 4.35). Although the rhombohedral minerals bridge and plug many pore throats, many of the rhombs are partially or almost completely dissolved. A dog-tooth-like texture is recognized on the authigenic quartz surface after once-engulfed dolomite minerals have dissolved. Many of these partially dissolved ferroan dolomite rhombs have been eroded into calyx type structures, within which hematite (0.5-1 μm flakes) and authigenic clays precipitated (Figure 4.11).

Dissolved and corroded grains (Figure 4.37) and oversized pores (Figure 4.38) indicate that the dissolution of either an original grain or a replaced pseudomorph has occurred. Feldspars and lithics are relatively unstable and thus are the most likely

61
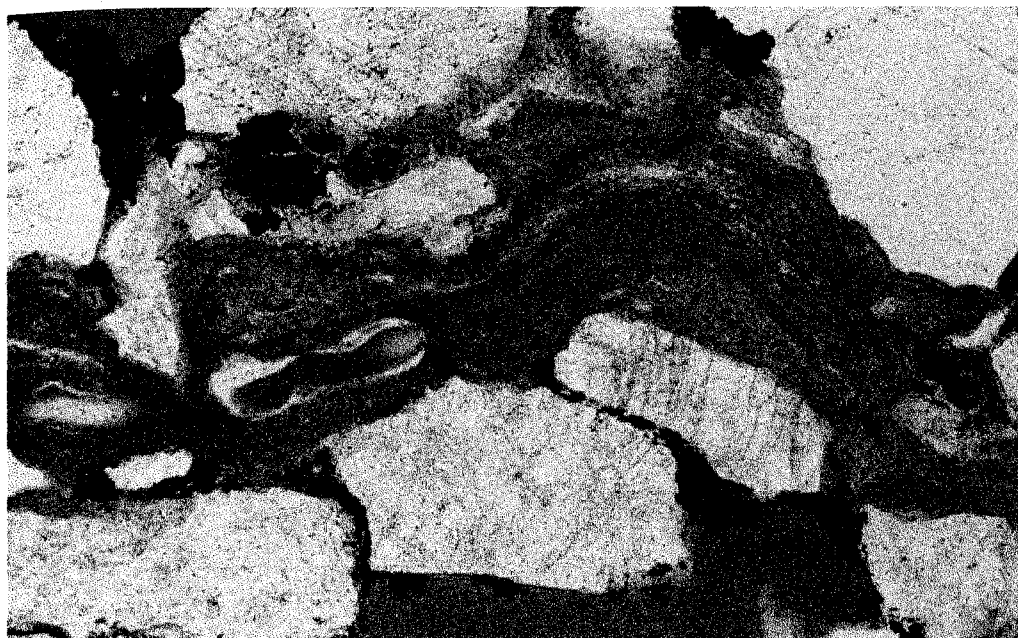
Figure 4.29 Photomicrograph of a partially dissolved, ductile, lithic grain. The rock fragment is a potassium and sodium rich alumino-silicate grain. Dissolution of grain centers, such as this, positively increases the porosity and permeability (image width = 1.3 mm).
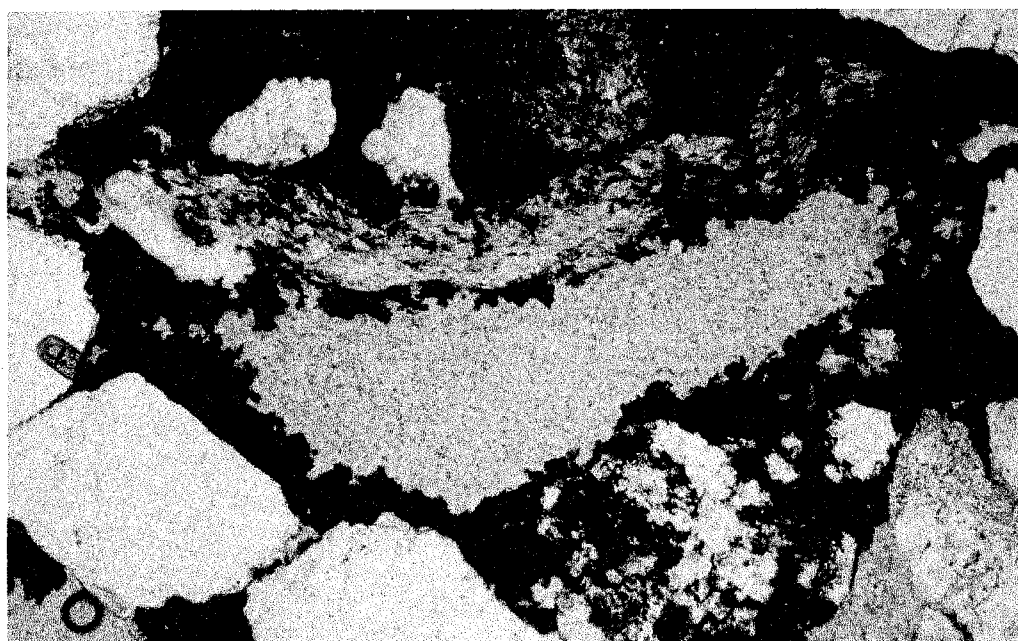
Figure 4.30 Photomicrograph showing the almost complete dissolution of an unstable, undifferentiated silicic grain. Hematite that has precipitated along the open pore margin was unable to precipitate within the entire pore after the initial dissolution event that created this secondary porosity (image width = 1.3 mm).
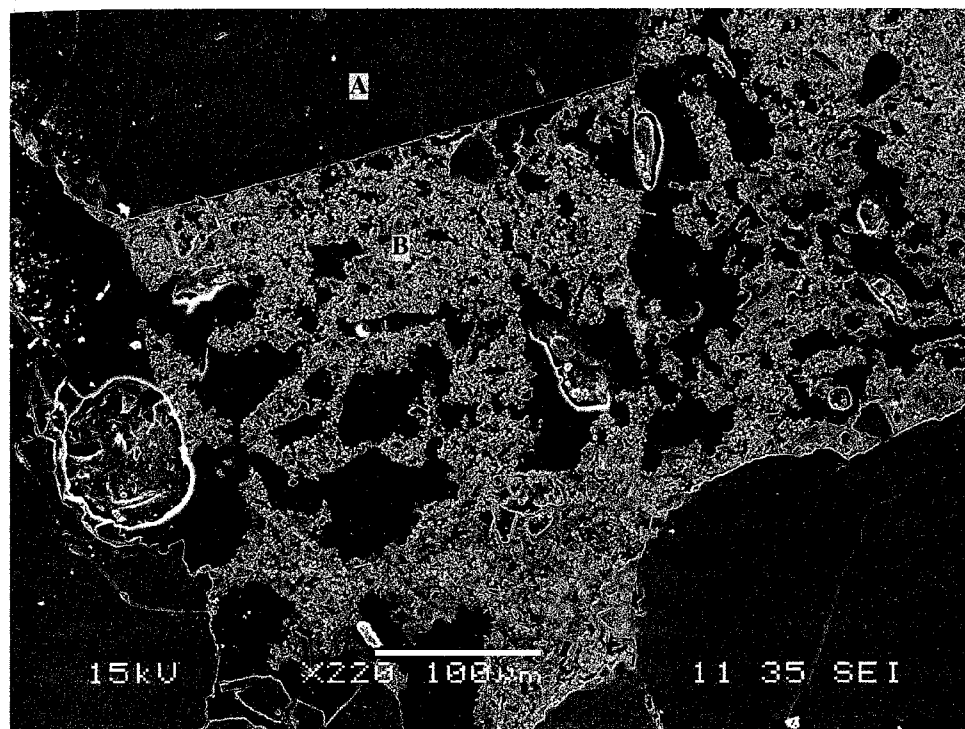
Figure 4.31   SEM photomicrograph showing a euhedral quartz overgrowth and authigenic hematite. The hematite has either been partially dissolved or failed to completely fill the pore.

Mineral Phases Investigated:

A: Si, O (quartz)
B: Fe, Si, AL, O (hematite)
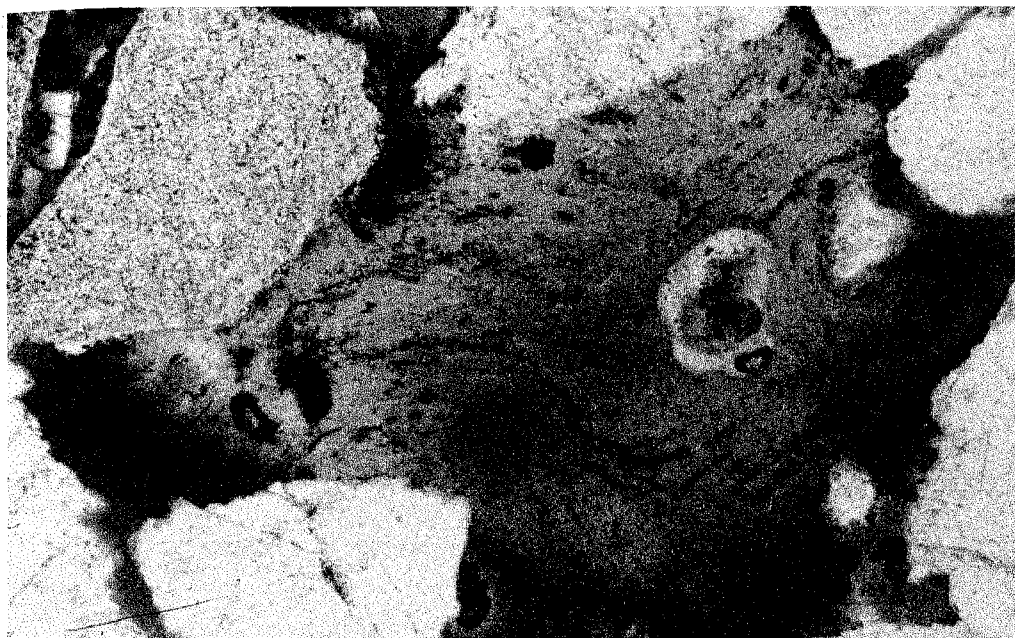
Figure 4.32 Photomicrograph of a partially dissolved, kaolinite, potassic, alumino-silicate and hematite replaced lithic grain(s). Secondary intragranular micro- and macroporosity is observed (image width = 1.3 mm).

Figure 4.33 Photomicrograph of a partially dissolved feldspar grain and intragranular microporosity in authigenic kaolinite and potassic alumino-silicates. Whole and partially dissolved ferroan dolomite rhombohedral clusters occlude pore pathways, reducing the effective porosity of the sandstone (image width = 1.3 mm).

64
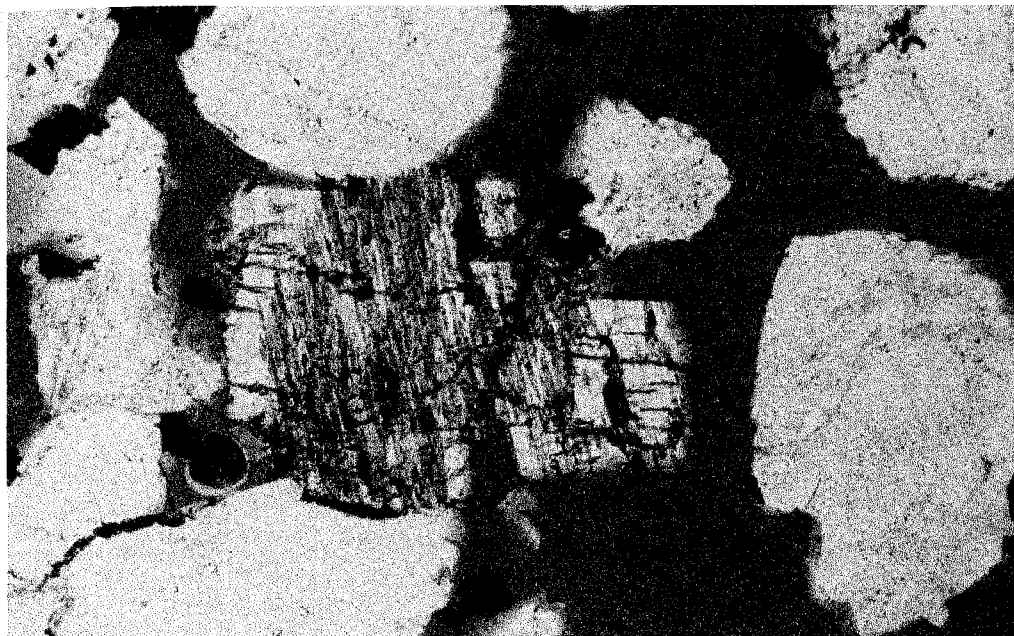
Figure 4.34   Photomicrograph of a partially dissolved microcline grain. Preferential dissolution has occurred along cross-hatched twin planes and authigenic hematite has precipitated within the open, intragranular porosity. Dissolution occurred post compaction, as evidenced by the grains position in this image (image width = 1.3 mm).
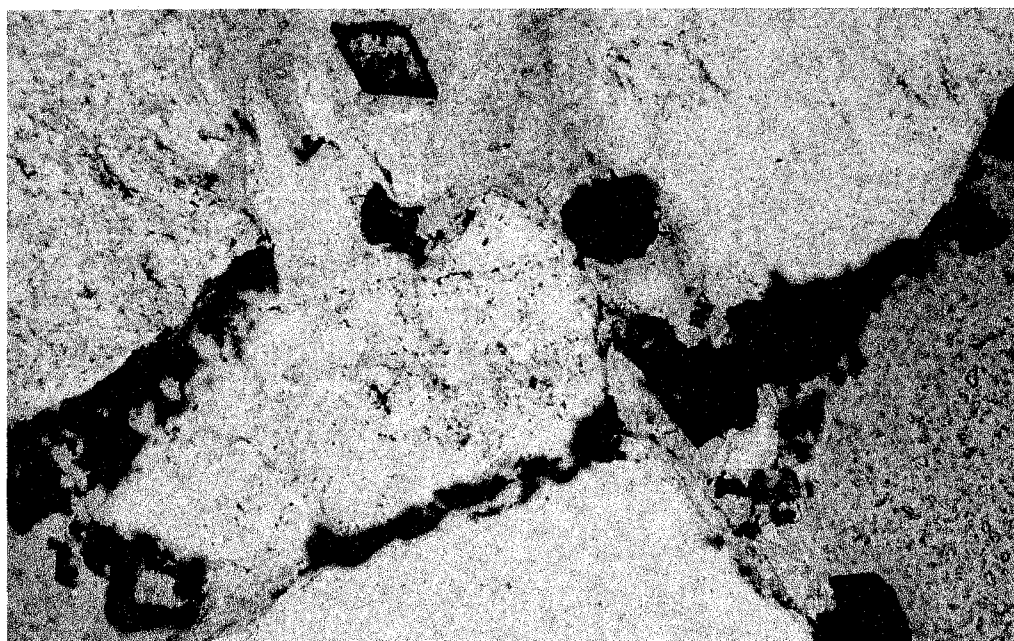
Figure 4.35   Photomicrograph showing secondary porosity created by the partial dissolution of ferroan dolomite rhombohedra. Partially dissolved clusters of these microscopic minerals may increase the effective porosity and the permeability of the Massillon Sandstone, whereas other whole individuals and pore lining and pore bridging clusters occlude the movement of fluids and gases through intragranular conduits and the intergranular pore network (image width = 0.65 mm).
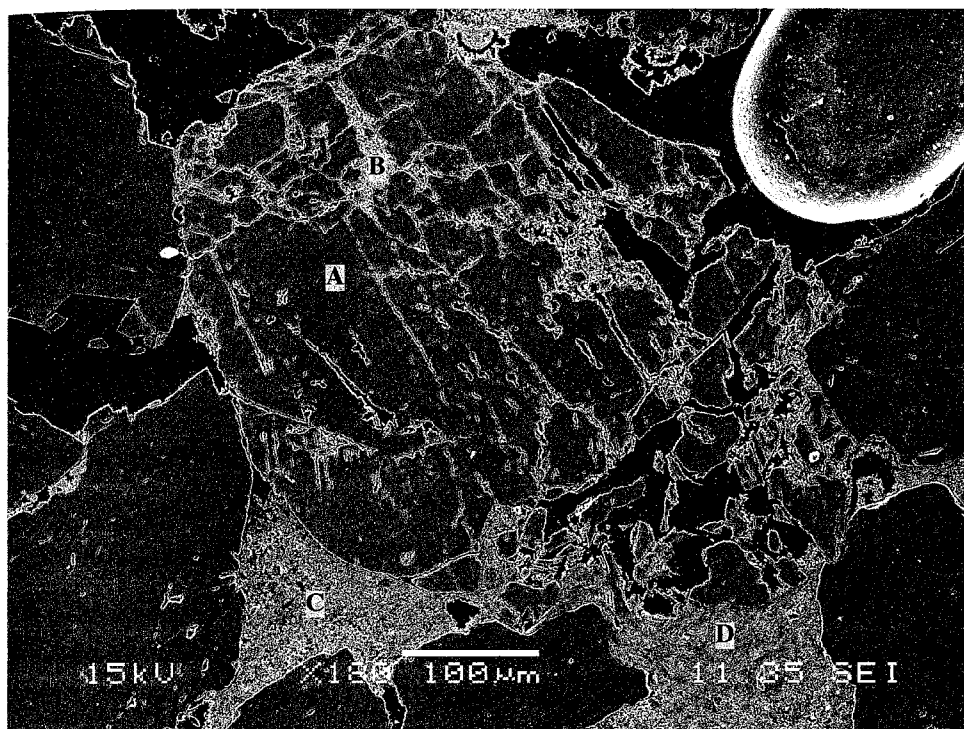
Figure 4.36 BSE photomicrograph of a partially and preferentially dissolved potassium feldspar grain, most likely orthoclase or microcline. Cross-hatched twinning is not particularly obvious, therefore, this is most likely an altered orthoclase grain. Intragranular dissolution porosity within almost all of the framework feldspar grains is almost always offset by the precipitation of authigenic hematite, kaolinite, sericite and/or illite.

Mineral Phases Investigated:

A: Si, Al, K, O (k-feldspar:orthoclase:microcline)
B: Fe, O, Si, Al (hematite)
C: Si, Al, K, O (sericite:illite:fine-grained muscovite)
D: Si, Al, K, O (sericite:illite:fine-grained muscovite)

Figure 4.37 Photomicrograph showing late stage, secondary macroporosity created by the almost complete dissolution of a feldspar grain. Observe the large, euhedral, authigenic quartz overgrowths rimming the margins of framework grains in the lower left and middle right of the image. Authigenic quartz appears to be a more important diagenetic phase than modal analysis indicates (image width = 1.3 mm).
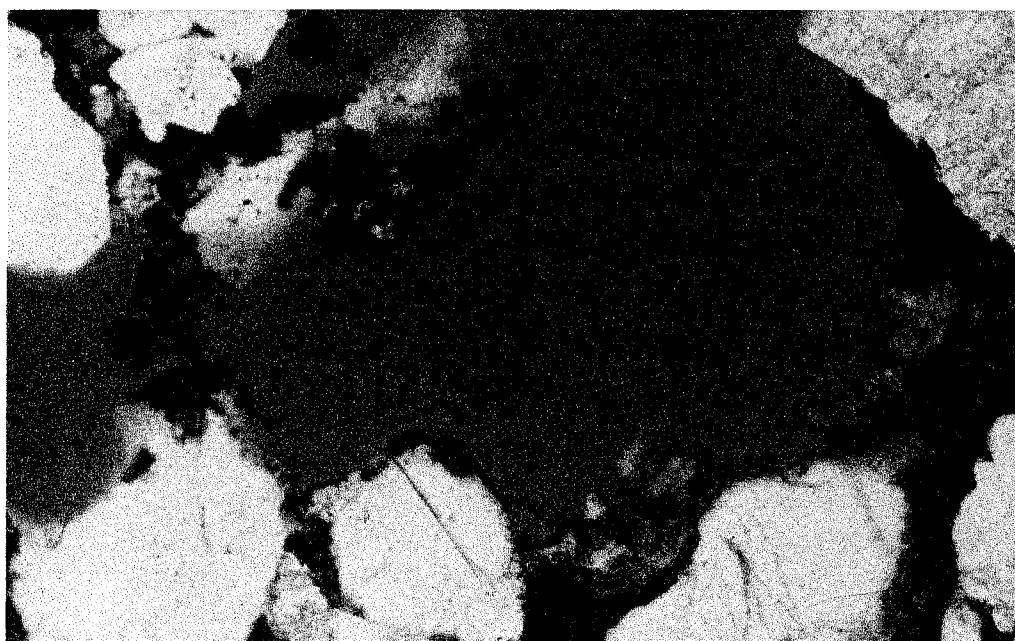
Figure 4.38 Photomicrograph showing secondary microporosity created by the almost complete dissolution of a previously replaced framework grain. This oversized pore, although not uncommon, is considerably larger than most pores found in the Massillon Sandstone. The original grain was diagenetically replaced by kaolinite, hematite and another alumino-silicate minerals before its eradication (notice remnants within the pore at bottom right; image width = 1.3 mm).

67

precursor grains. However, in places, even detrital quartz grains appear to have undergone partial dissolution (Figure 4.39).

Secondary dissolution porosity in the form of intragranular micropores (approximately 20 μm in diameter) in hematite, ferroan dolomite clusters, allogenic clay and authigenic clay increased the porosity of this sandstone (Figure 4.40).

4.4. Permeability Data

A ranking of measured permeability data along with porosity data is presented in Table 4.1. The multi-support gas permeameter (MSP) generated permeabilities from subsections of all three structures using the 0.15 cm r_i tip seal. Third-order structures have the highest mean permeabilities (mean ln k = -27.042 m^2; maximum ln k = -25.876 m^2; minimum ln k = -28.758 m^2), second-order structures have the second highest mean permeabilities (mean ln k = -27.586 m^2; maximum ln k = -25.721 m^2; minimum ln k = -29.607 m^2), and sub-sections measured from the first-order structure have the lowest mean permeabilities (mean ln k = -27.864 m^2; maximum ln k = -27.011 m^2; minimum ln k = -28.979 m^2; Figure 4.41). Although the mean measurements of the second-order structures have the second highest permeabilities, the lowest 25% of these second-order structures have the overall lowest permeabilities and the highest 15% have the highest permeabilities (Figure 4.41).

A summary of measured permeability data collected across the Face 7 transect within the area investigated by the MSP (Figure 3.3) is presented in Table 4.2. Permeability was measured directly on the precored, sandstone face using the five
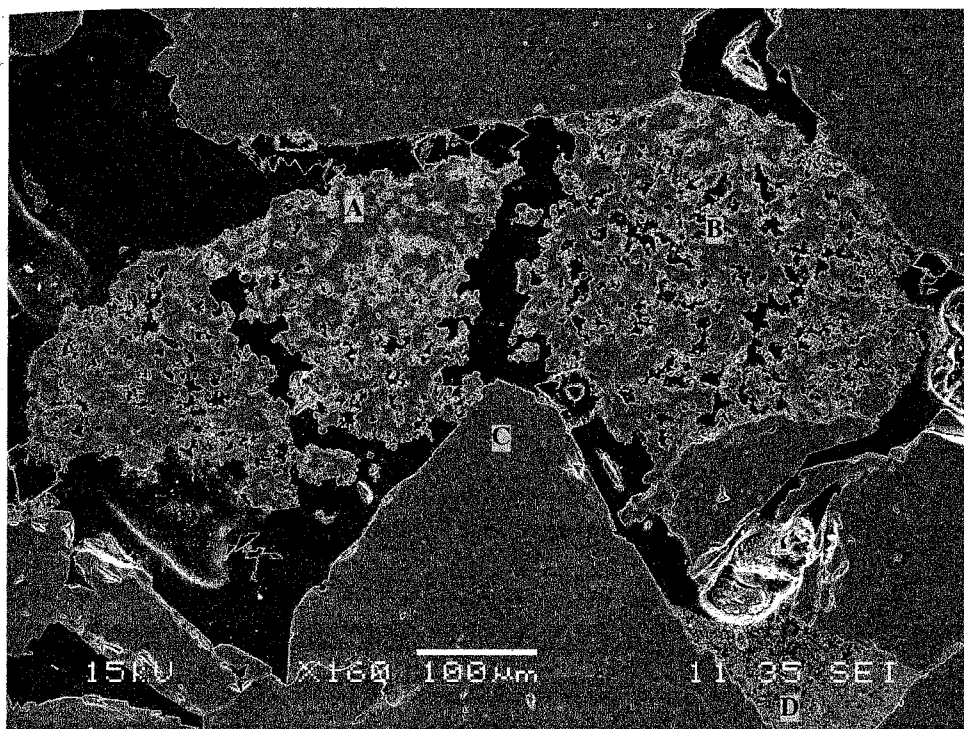
Figure 4.39 BSE photomicrograph showing late-stage, secondary intragranular macroporosity created by the alteration and dissolution of a detrital quartz grain and ferroan dolomite clusters. The dissolution of quartz grains such as this is uncommon in the Massillon.

Mineral Phases Investigated:

A: Si, O (quartz)
B: Si, O (quartz)
C: Si, O (quartz)
D: Si, Al, O (kaolinite)
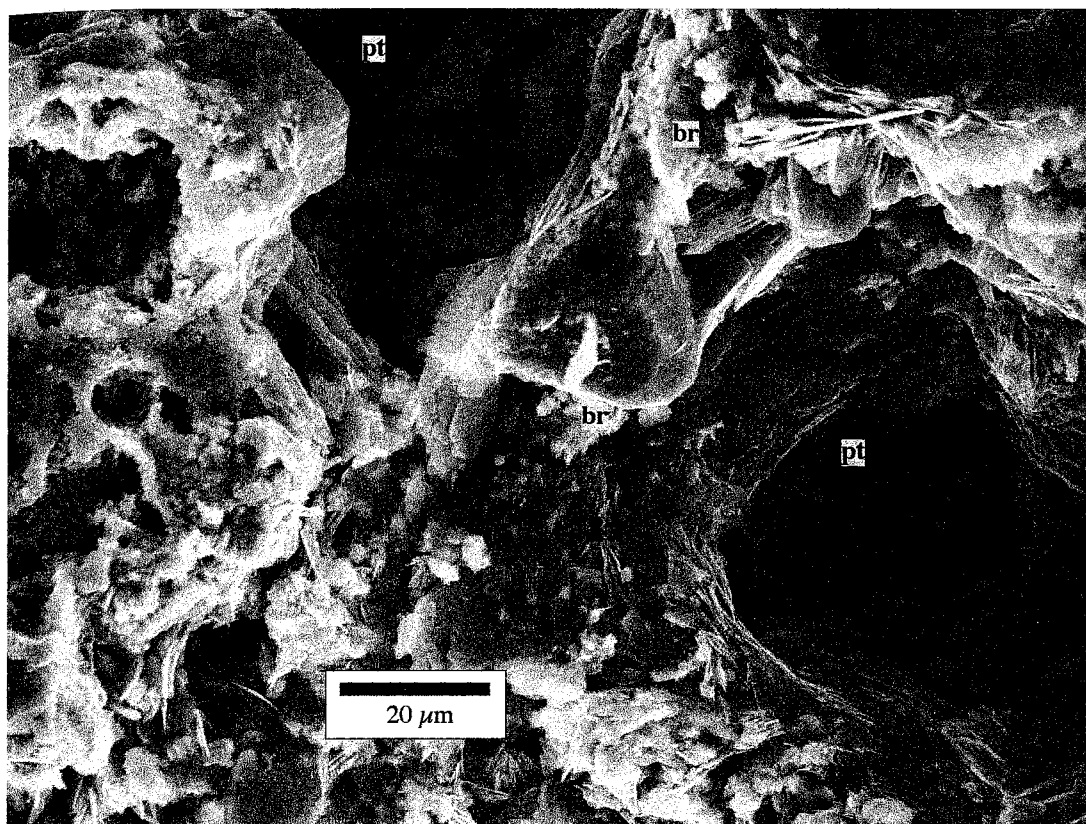
Figure 4.40

SEM photomicrograph of a microscopic pore channel in the Massillon Sandstone. Fluids passing through this sandstone late in it's diagenetic history have created both macroscopic and microscopic pore channels or throats (pt) by dissolving detrital and authigenic clays, hematite and the ferroan dolomite mineral assemblages that have coalesced with authigenic quartz to create this bridge (br) across the pore channel.

Table 4.1: A rank order summary of measured permeability and point count porosity data observed in the Massillon Sandstone.

Rank Order	Fourier Face	Sub-Section	Permeability (m^2)	Permeability ln (m^2)	Permeability (darcies)	Permeability (md)	Rank Order	Sub-Section	Porosity (pc) (%)
1	11	7C2z.4	6.8E-12	-25.7213	6.83891	6838.91	1	7B3z.3	27
2	12	7C2x.2	6.5E-12	-25.7599	6.58561	6585.61	2	7N3z.1	26.25
3	13	7N3z.1	5.8E-12	-25.8765	5.85613	5856.13	3	7H3z.2	26
4	14	7C2x.1	5.3E-12	-25.9723	5.31915	5319.15	4	7N3z.6	24.75
5	15	7N3z.4	5E-12	-26.0227	5.05572	5055.72	5	7N3z.3	24.25
6	16	7I3z.3	4.7E-12	-26.0883	4.74164	4741.64	6	7C2x.1	23.75
7	17	7N3z.3	4.6E-12	-26.113	4.62006	4620.06	7	7D3z.5	23.5
8	18	7N3z.6	4.5E-12	-26.1306	4.53901	4539.01	8	7H3z.5	22.75
9	19	7O3x.2	4.4E-12	-26.1401	4.49848	4498.48	9	7N3z.2	22.5
10		7D3z.5	4.2E-12	-26.1939	4.26545	4265.45	9	7N3z.4	22.5
11	21	7O3z.3	4.1E-12	-26.2145	4.17427	4174.27	10	7H3z.3	22
12	22	7O3x.1	3.4E-12	-26.3941	3.48531	3485.31	10	7N3z.5	22
13	23	7D3z.2	3.4E-12	-26.4111	3.43465	3434.65	11	7O3z.6	21.75
14	24	7D3z.1	3.3E-12	-26.4236	3.38399	3383.99	12	7B3z.5	21.5
15	25	7D3z.3	3.3E-12	-26.4461	3.31307	3313.07	13	7O3z.5	21
16	26	7N3z.5	3.2E-12	-26.4793	3.20162	3201.62	14	7D3z.1	20.75
17	27	7J3z.5	3E-12	-26.5269	3.05978	3059.78	15	7H3z.6	20.5
18	28	7D3z.6	3E-12	-26.5398	3.01925	3019.25	16	7H3z.1	20.25
19	29	7J3z.2	2.9E-12	-26.552	2.97872	2978.72	17	7M3z.1	19.75
20		7C2z.6	2.9E-12	-26.5526	2.97872	2978.72	17	7C2z.5	19.75
21	31	7J3z.1	2.8E-12	-26.621	2.78622	2786.22	18	7B3z.6	19.5
22	32	7H3z.1	2.7E-12	-26.6286	2.76596	2765.96	18	7E3z.6	19.5
23	33	7J3z.6	2.7E-12	-26.653	2.69504	2695.04	18	7K3z.6	19.5
24	34	7C2z.2	2.7E-12	-26.657	2.6849	2684.9	18	7C2z.6	19.5
25	35	7D3z.4	2.6E-12	-26.6599	2.67477	2674.77	19	7O3z.3	19
26	36	7N3z.2	2.4E-12	-26.7522	2.44174	2441.74	19	7C2z.2	19
27	37	7K3z.2	2.4E-12	-26.7748	2.38095	2380.95	19	7C2z.4	19
28	38	7K3z.4	2.3E-12	-26.7913	2.35056	2350.56	19	7L2x.1	19
29	39	7O3z.4	2.3E-12	-26.8027	2.32016	2320.16	19	7G1z.6	19
30		7K3z.3	2.3E-12	-26.8071	2.31003	2310.03	20	7F3z.4	18.75
31	41	7E3z.5	2.2E-12	-26.832	2.24924	2249.24	20	7I3z.3	18.75

71

Rank Order	Fourier Face	Sub-Section	Permeability (m^2)	Permeability ln (m^2)	Permeability (darcies)	Permeability (md)	Rank Order	Sub-Section	Porosity (pc) (%)
32	42	7C2z.1	2.2E-12	-26.854	2.19858	2198.58	20	7O3x.2	18.75
33	43	7H3z.2	2.1E-12	-26.8771	2.15805	2158.05	20	7C2x.2	18.75
34	44	7M3z.1	2.1E-12	-26.8816	2.14792	2147.92	21	7D3z.4	18.25
35	45	7J3z.3	2.1E-12	-26.8971	2.1074	2107.4	22	7E3z.3	18
36		7K3z.1	2.1E-12	-26.8979	2.1074	2107.4	23	7B3z.4	17.75
37		7B3z.2	2.1E-12	-26.9003	2.1074	2107.4	23	7D3z.2	17.75
38		7K3z.5	2E-12	-26.9281	2.04661	2046.61	23	7E3z.5	17.75
39		7F3z.6	2E-12	-26.9504	2.00608	2006.08	23	7K3z.1	17.75
40		7M3z.4	2E-12	-26.9618	1.97568	1975.68	23	7O3z.4	17.75
41		7O3z.2	2E-12	-26.9623	1.97568	1975.68	24	7J3z.2	17.5
42		7I3x.1	1.9E-12	-26.994	1.91489	1914.89	24	7C2z.1	17.5
43		7M3z.5	1.9E-12	-27.0073	1.89463	1894.63	25	7J3z.1	17.25
44		7G1x.1	1.9E-12	-27.0115	1.8845	1884.5	26	7D3z.6	17
45		7K3z.6	1.9E-12	-27.0133	1.87437	1874.37	26	7A2z.1	17
46	46	7M3z.6	1.7E-12	-27.0853	1.75279	1752.79	27	7O3x.1	16.75
47	47	7M3z.2	1.7E-12	-27.0854	1.75279	1752.79	28	7F3z.1	16.25
48	48	7H3z.4	1.7E-12	-27.0991	1.72239	1722.39	28	7F3z.6	16.25
49	49	7H3z.3	1.7E-12	-27.1013	1.72239	1722.39	28	7K3z.2	16.25
50		7H3z.5	1.7E-12	-27.1127	1.70213	1702.13	28	7K3z.4	16.25
51	51	7G1z.5	1.7E-12	-27.1139	1.70213	1702.13	29	7J3z.5	16
52	52	7C2z.3	1.7E-12	-27.1167	1.692	1692	29	7O3z.2	16
53	53	7O3z.6	1.7E-12	-27.1172	1.692	1692	30	7J3z.6	15.75
54	54	7J3z.4	1.6E-12	-27.1396	1.6616	1661.6	31	7G1z.5	15.5
55	55	7M3z.3	1.5E-12	-27.2269	1.51976	1519.76	32	7B3z.2	15.25
56	56	7L2z.5	1.5E-12	-27.2388	1.49949	1499.49	33	7H3z.4	15
57	57	7E3z.6	1.4E-12	-27.263	1.45897	1458.97	33	7I3z.5	15
58	58	7C2z.5	1.4E-12	-27.2886	1.42857	1428.57	33	7M3z.5	15
59	59	7I3z.2	1.4E-12	-27.3136	1.38804	1388.04	34	7I3x.2	14.75
60		7G1z.6	1.3E-12	-27.3767	1.30699	1306.99	34	7J3z.3	14.75
61	61	7L2x.2	1.3E-12	-27.3892	1.28673	1286.73	34	7J3z.4	14.75
62	62	7I3x.2	1.2E-12	-27.4205	1.2462	1246.2	34	7L2z.2	14.75

72

Rank Order	Fourier Face	Sub-Section	Permeability (m^2)	Permeability ln (m^2)	Permeability (darcies)	Permeability (md)	Rank Order	Sub-Section	Porosity (pc) (%)
63	63	7E3z.1	1.2E-12	-27.4317	1.23607	1236.07	35	7B3z.1	14.5
64	64	7F3z.5	1.2E-12	-27.4466	1.21581	1215.81	35	7D3z.3	14.5
65	65	7L2z.1	1.2E-12	-27.4626	1.19554	1195.54	35	7I3x.1	14.5
66	66	7B3z.5	1.1E-12	-27.5095	1.14488	1144.88	35	7M3z.3	14.5
67	67	7E3z.3	1.1E-12	-27.5172	1.13475	1134.75	35	7M3z.6	14.5
68	68	7L2x.1	1.1E-12	-27.543	1.10436	1104.36	36	7I3z.2	14.25
69	69	7B3z.1	1E-12	-27.6002	1.04458	1044.58	36	7K3z.5	14.25
70		7F3z.4	1E-12	-27.6124	1.03343	1033.43	36	7M3z.2	14.25
71	71	7G1z.4	9.8E-13	-27.6513	0.99291	992.908	36	7C2z.3	14.25
72	72	7E3z.4	9.5E-13	-27.6868	0.95846	958.46	36	7L2x.2	14.25
73	73	7E3z.2	9.5E-13	-27.6874	0.95745	957.447	37	7E3z.4	14
74	74	7H3z.6	9.3E-13	-27.702	0.94326	943.262	37	7I3z.6	14
75	75	7L2z.2	9.2E-13	-27.7115	0.93516	935.157	37	7O3z.1	14
76	76	7O3z.5	9.2E-12	-27.7119	9.34144	9341.44	38	7F3z.2	13.75
77	77	7L2z.4	9.2E-13	-27.7182	0.92806	928.065	39	7A2z.5	13.5
78	78	7B3z.4	8.9E-13	-27.744	0.90476	904.762	39	7G1x.1	13.5
79	79	7L2z.6	8.8E-13	-27.7548	0.89564	895.643	40	7F3z.5	13.25
80		7O3z.1	8.6E-13	-27.7786	0.87437	874.367	40	7I3z.1	13.25
81	81	7F3z.1	7.9E-13	-27.8659	0.80142	801.418	40	7A2z.3	13.25
82	82	7F3z.3	7.8E-13	-27.8797	0.79027	790.274	40	7A2z.6	13.25
83	83	7I3z.5	7.8E-13	-27.8835	0.78723	787.234	41	7K3z.3	13
84	84	7B3z.3	7.7E-13	-27.8892	0.78217	782.168	41	7L2z.3	13
85	85	7I3z.4	7.1E-13	-27.9738	0.71935	719.352	42	7F3z.3	12.75
86	86	7G1x.2	7.1E-13	-27.9771	0.71631	716.312	42	7A2z.4	12.75
87	87	7F3z.2	7E-13	-27.9925	0.70618	706.18	43	7L2z.1	12.5
88	88	7L2z.3	6.7E-13	-28.0385	0.67376	673.759	44	7I3z.4	12.25
89	89	7I3z.1	6.2E-13	-28.1085	0.62817	628.166	45	7E3z.1	12
90		7A2z.1	6E-13	-28.1454	0.60588	605.876	45	7E3z.2	12
91	91	7G1z.1	5.2E-13	-28.2928	0.5228	522.796	46	7G1z.4	11.75
92	92	7G1z.3	4.2E-13	-28.5091	0.42148	421.479	47	7A2z.2	11.25
93	93	7B3z.6	3.2E-13	-28.7577	0.32827	328.267	48	7M3z.4	11

Rank Order	Fourier Face	Sub-Section	Permeability (m^2)	Permeability ln (m^2)	Permeability (darcies)	Permeability (md)	Rank Order	Sub-Section	Porosity (pc) (%)
94	94	**7A2z.4**	3.1E-13	-28.8018	0.31408	314.083	49	**7G1x.2**	10.75
95	95	**7A2z.5**	2.7E-13	-28.94	0.27356	273.556	50	**7G1z.2**	8.75
96	96	**7G1z.2**	2.6E-13	-28.979	0.26342	263.425	51	**7L2z.4**	8.5
97	97	**7A2z.3**	2.4E-13	-29.0608	0.24215	242.148	52	**7G1z.3**	8
98	98	**7A2z.6**	1.5E-13	-29.557	0.14792	147.923	53	**7L2z.5**	7.75
99	99	**7A2z.2**	1.4E-13	-29.607	0.14083	140.831	53	**7L2z.6**	7.75
							54	**7G1z.1**	6
		Whole Rock Mean	**1.9E-12**	**-27.229**	**2.067**	**2067**			**16.47**

Distribution of the MSP Measured Permeability using the 0.15 cm r_i tip seal
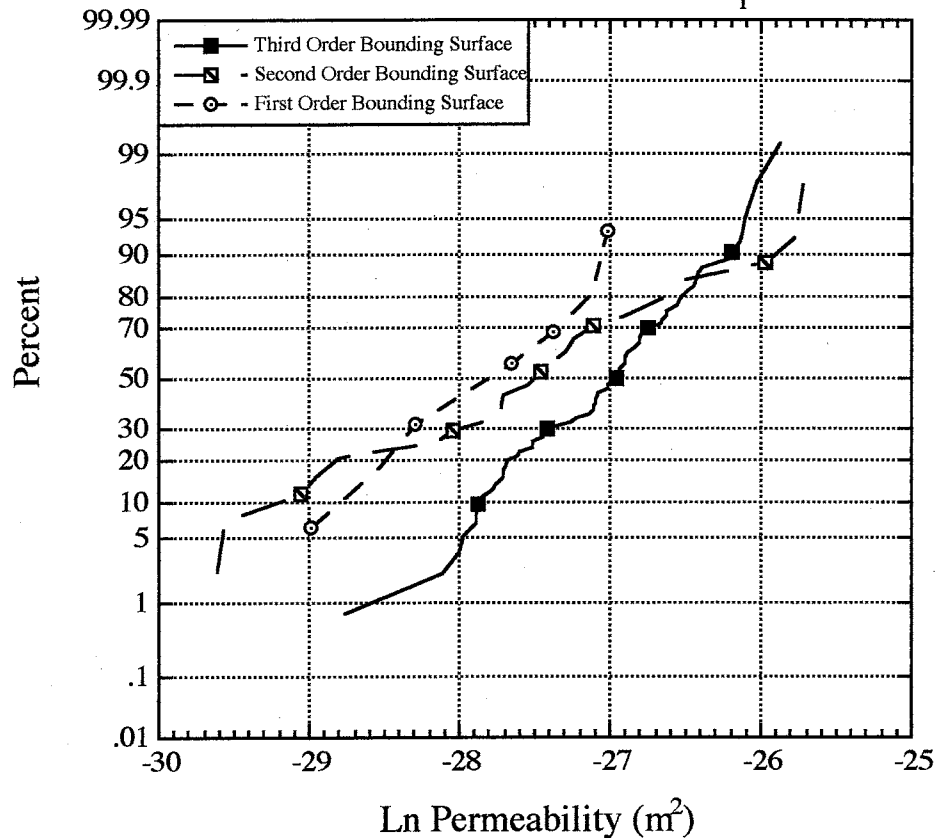
Figure 4.41

Distribution plot showing the MSP generated permeabilities from all billet surfaces employing the 0.15 cm r_i tip seal. Third-order structures record the highest permeabilities (mean ln k = -27.042 m^2; max. ln k = -25.876 m^2; min. ln k = -28.758 m^2), second-order structures record the second highest permeabilities (mean ln k = -27.586 m^2; max. ln k = -25.721 m^2; min. ln k = -29.607 m^2), and the first-order structure records the lowest MSP measured permeability (mean ln k = -27.864 m^2; max. ln k = -27.011 m^2; min. ln k = -28.979 m^2). Although the second-order structures have the second highest mean permeabilities, the lowest 25% of these measured sub-sections record the lowest of all bounding structures, whereas the highest 15% record the highest permeabilities of all investigated sub-sections.

Table 4.2: Permeability data collected across the Face 7 transect within the area investigated by the MSP (see Figure 3.3). Measurements were made prior to coring. Each tip seal measurement correlates with the centered coordinates of the 15 plugs cored across the transect.

Permeability Measurements: ln k; k in m^2.

Core	y-coord (cm)	x-coord (cm)	0.15 cm tip seal (m^2)	0.31 cm tip seal (m^2)	0.63 cm tip seal (m^2)	1.27 cm tip seal (m^2)	2.54 cm tip seal (m^2)
A	0.2	6.05	-26.7452	-26.9728	-27.1994	-27.0219	-26.6226
B	3.7	6.6	-26.7008	-26.4817	-26.0938	-25.7857	-25.7979
C	8.2	7	-25.9732	-26.1654	-26.0351	-25.981	-25.8244
D	15.2	6.6	-26.6682	-26.5656	-26.0802	-25.8069	-25.7748
E	18.9	6.7	-27.2289	-27.2385	-27.0254	-26.3731	-26.1414
F	22.8	6.55	-27.0917	-27.1746	-27.0797	-26.5623	-26.2392
G	26.7	6.45	-28.5665	-28.1718	-27.5721	-26.9623	-26.4966
H	31.2	6	-27.2161	-27.2265	-27.2729	-26.9601	-26.7032
I	34.7	6.1	-27.1641	-27.2393	-27.1349	-26.8838	-26.6166
J	38.2	5.7	-27.4249	-27.6301	-27.2356	-26.7927	-26.5768
K	41.5	5.7	-27.4444	-27.3892	-27.1181	-26.8061	-26.7794
L	44.5	5.7	-27.9319	-27.8549	-27.7484	-27.1198	-26.6309
M	48.2	5.95	-26.8243	-26.6943	-26.5509	-26.2081	-25.9374
N	52	6.3	-27.0298	-26.9409	-26.3755	-25.9163	-25.7307
O	57.9	6.6	-28.0852	-27.8813	-27.27789	-26.7465	-26.2295

different tip seals within a measured area of 60.325 cm x 12.065 cm. The whole rock face averages were compiled using 728 MSP measurements from each tip seal.

A comparison of the permeability fields (Appendix B) and permeability plots created across the Face 7 cored transect reveal an increase in permeability between the first and second-order bounding surfaces (within the low-angle, depositional third-order cross-stratification structures). In addition, a distinct 'smoothing' in the permeability data is observed across the cored transect as the tip seal size increases (Figure 4.42). This noticeable 'smoothing' reflects the preferential filtering of the thinner, third-order depositional structure (Tidwell and Wilson, 2000; Appendix B). As third-order structures are filtered, the large-scale features associated with the first and second-order bounding structures become more apparent.

Mean permeability measured along the Face 7, precored transect using the 0.63 cm r_i tip seal best correlates with the mean, billet permeability using the 0.15 cm r_i tip seal. Point count porosity and porosity derived from image analysis appear to correlate better with permeability measurements taken from the precored, Face 7 transect, as opposed to billet measurements, using the 0.15 cm r_i tip seal (Figure 4.42).

The mean permeability of billets oriented normal to bedding is ln k = -27.229 m^2, whereas the mean permeability of billets oriented parallel to cross-stratification is ln k = -26.860 m^2. Overall, the mean differences between measured permeability using the 0.15 cm r_i tip seal are small. Only measurements taken normal to cross-stratification (z-direction) were used for correlative purposes.
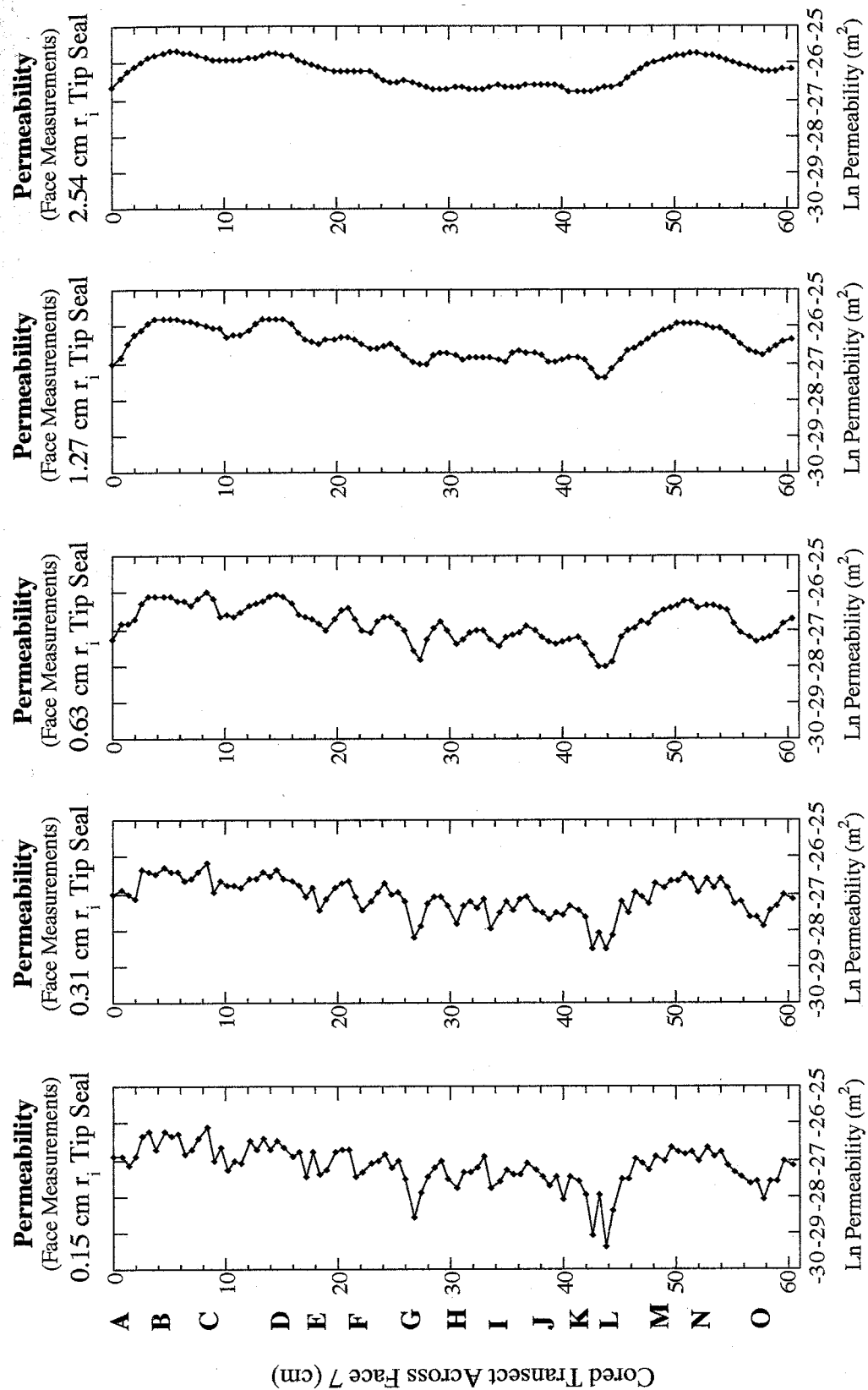
Figure 4.42: Permeability and porosity plots produced from data acquired from measurements across the Face 7 transect. Face permeability measurements were taken prior to coring the transect for modal and image analysis.

Permeability
(Face Measurements)
2.54 cm r_i Tip Seal

Permeability
(Face Measurements)
1.27 cm r_i Tip Seal

Permeability
(Face Measurements)
0.63 cm r_i Tip Seal

Permeability
(Face Measurements)
0.31 cm r_i Tip Seal

Permeability
(Face Measurements)
0.15 cm r_i Tip Seal

Ln Permeability (m^2)

Cored Transect Across Face 7 (cm)
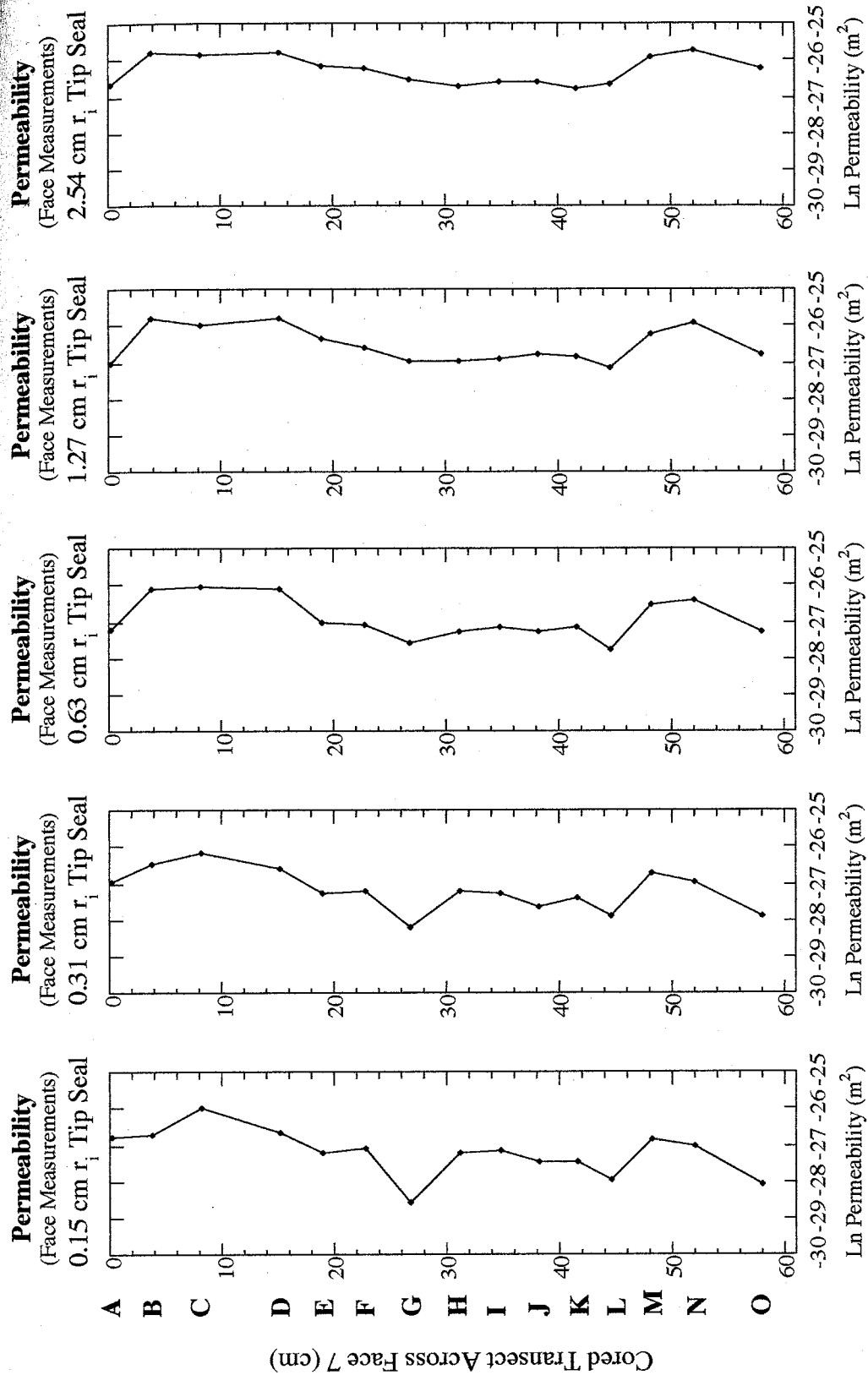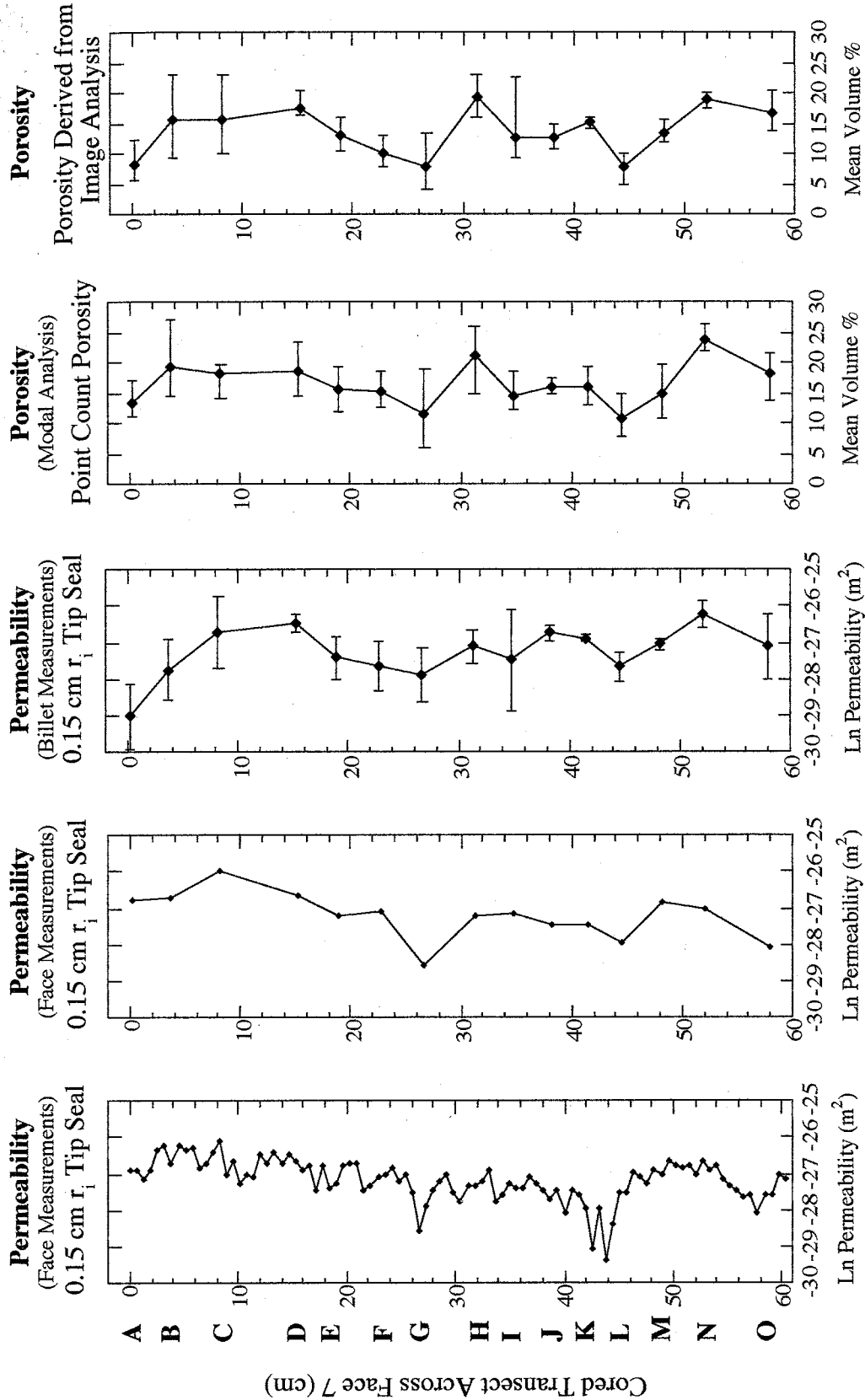
4.4.1. The Correlation Coefficient

The correlation coefficient (R) was used to determine the extent to which two variables are related. The correlation coefficient is the ratio of the covariance of two variables (σ_{ij}) to the product of their two standard deviations (σ_i and σ_j):

$$R = \sigma_{ij} / [(\sigma_i)(\sigma_j)]$$

The squared correlation coefficient, R^2, describes the proportion of variance in common between two variables. Variables and processes indicating a strong, positive or negative correlation with measured permeability will exhibit R values ≥ 0.90, which in turn translate into R^2 values $\geq 81\%$. Relationships indicating a good covariance with permeability exhibit an $90 > R > 0.71$ ($81 > R^2 \geq 50\%$). Weak or insignificant relationships have R values ≤ 0.70 ($R^2 < 50\%$; Davis, 1986).

4.4.2. Relationship Between Permeability and Compositional Variables

MSP generated permeability measurements were plotted against: 1) point count porosity (R = 0.53, n = 99; Figure 4.43); 2) mean, billet aggregate, point count porosity (Figure 4.44); 3) intergranular point count porosity (R = 0.63, n = 99; Appendix E, Figure E1); 4) intragranular point count porosity (R = 0.28, n =99; Appendix E, Figure E); and 5) lithic content (R = 0.34, n = 99; Appendix E, Figure E3). All cumulative expressions exhibit a weak, positive or negative correlation with measured permeability. First and second-order structures exhibit stronger, positive correlations with permeability than third-order structures for total point count porosity and intergranular point count porosity. Intergranular macroporosity is the most prevalent and the dissolution of framework grains, allogenic clays and authigenic minerals show the best positive correlation with

Permeability vs. Point Count Porosity

Legend:
— ■ — Third Order Bounding Surface
- - ▧ - - Second Order Bounding Surface
- - ⊙ - - First Order Bounding Surface

X-axis: Point Count Porosity (%)
Y-axis: Ln Permeability (m^2)

$y = -28.039 + 0.056884x$ R= 0.36144

$y = -29.854 + 0.15121x$ R= 0.57215

$y = -29.352 + 0.12767x$ R= 0.77625
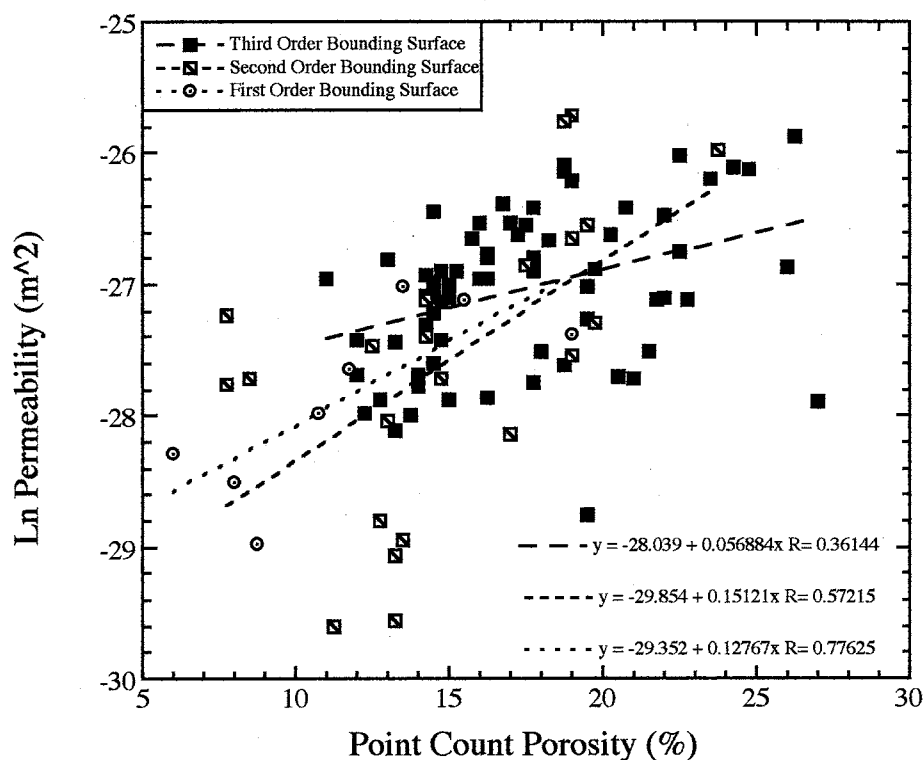
Figure 4.43

Diagram showing the correlation between permeability and micro- and macroporosity derived from MSP measurements and point counts of thin section subsections fabricated from billets cut from cored first, second and third-order structures. The plot shows a weak, positive correlation between permeability and point count porosity (R= 0.53, n= 99) for cumulative measurements. The first order-structure exhibits a good, positive correlation with permeability (R= 0.78, n= 8), whereas second and third-order structures exhibit weak, positive correlations between permeability and point count porosity (R= 0.57, n= 22; R= 0.36, n= 69, respectively). Assessed correlation coefficients: strong [R ≥ 0.90], good [0.90 > R > 0.71], weak or insignificant [R ≤ 0.70].

Permeability vs. Billet Aggregate Porosity
using the 0.15 cm r_i tip seal
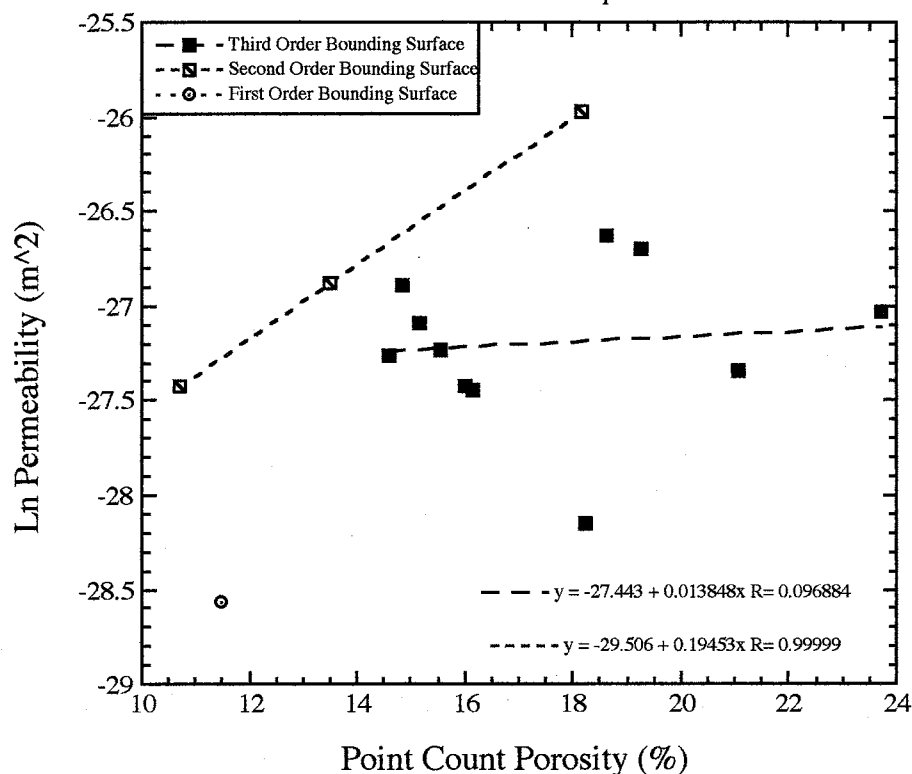
Figure 4.44

Diagram showing the correlation between permeability and mean, point count micro-
and macroporosity values. MSP measurements were taken from billets oriented normal
to cross-stratification and cut from cored first, second and third-order structures. For
these measurements, the 0.15 cm r_i tip seal was employed. Porosity values are mean,
point count accumulations compiled from modal analysis of thin section subsections
made from the same oriented billets. The plot shows that mean, first-order, point count
porosity measurements are the lowest of all subsections. Individual second-order
porosity measurements are the lowest, yet one of the three second-order subsections
records the highest permeability. Subsections from third-order structures have the
highest point count porosities, although their permeability's fall between those of first
and second-order structures.

83

permeability. A weak, negative correlation is observed between permeability and lithic content (R = 0.34, n = 99; Appendix E, Figure E3). Second-order bounding structures control this correlation, whereas first and third-order structures do not.

Increasing mean volume percentages of framework grains (detrital quartz, feldspar and lithic fragments) do not positively correlate with measured permeability.

4.4.3. Relationship Between Permeability and Textural Variables

A weak, positive correlation is observed between permeability and mean grain size (R = 0.34, n = 99 Figure 4.45) and between permeability and degree of sorting (R = 0.28, n = 99; Figure 4.46). Mean grain sizes of the first-order structure exhibit a strong, positive correlation with permeability (R = 0.94, n = 8). Second-order structures exhibit a good, positive correlation between permeability and grain sorting (R = 0.73, n = 22). Third-order structures exhibit a weak or insignificant, positive, correlation with permeability for both mean grain size and grain sorting.

4.4.4. Relationship Between Permeability and Diagenetic Alterations

There are weak or insignificant, positive correlations between permeability and: 1) matrix material (R = 0.64, n = 99; Figure 4.47); 2) authigenic quartz and ferroan cements (hematite and ferroan dolomite: R = 0.64, n = 99; Appendix E, Figure E4); and 3) isolated ferroan cements (R = 0.63, n = 99; Figure 4.48). Increasing permeability with decreasing matrix material and cements is considered a positive relationship. First and second-order structures exhibit stronger, positive correlations with permeability as compared to third-order structures for all three correlations. The distribution of ferroan

84

Permeability vs. Mean Framework Grain Size

Legend:
- Third Order Bounding Surface
- Second Order Bounding Surface
- First Order Bounding Surface

$y = -26.349 - 0.70806x \quad R = 0.1798$

$y = -25.151 - 2.6581x \quad R = 0.56378$

$y = -13.829 - 12.73x \quad R = 0.93983$

Y-axis: Ln Permeability (m^2)

X-axis: Mean Framework Grain Size (phi)
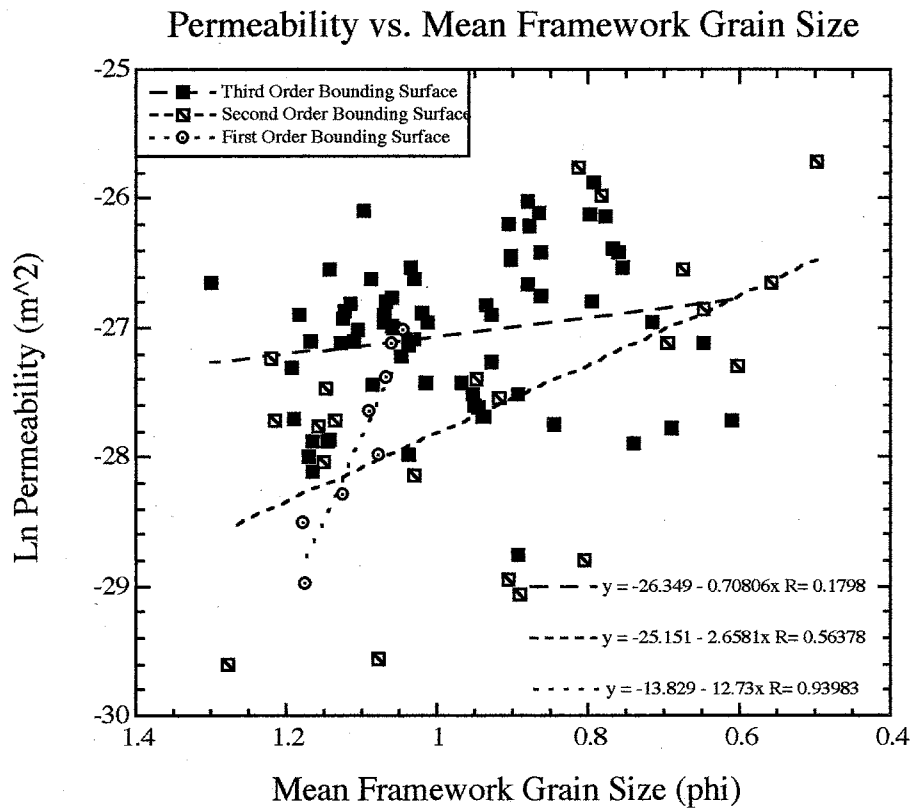
Figure 4.45

Diagram showing the correlation between permeability and mean framework grain size derived from MSP measurements and point counts of thin section subsections produced from billets cut from cored first, second and third-order structures. The plot shows a weak, positive correlation between permeability and mean grain size (R= 0.34, n= 99) for cumulative measurements. Collectively, the first-order bounding structure exhibits a strong, positive correlation with permeability (R= 0.94, n= 8), whereas second and third-order structures exhibit weak, positive relationships (R= 0.56, n= 22; R= 0.18, n= 69, respectively). Assessed correlation coefficients: strong [R ≥ 0.90], good [0.90 > R > 0.71], weak or insignificant [R ≤ 0.70].

Permeability vs. Framework Grain Sorting

y = -26.827 - 0.56151x R= 0.054633

y = -22.392 - 12.584x R= 0.7258

y = -30.265 + 6.6707x R= 0.31408

Ln Permeability (m^2)

Third Order Bounding Surface
Second Order Bounding Surface
First Order Bounding Surface

Degree of Framework Grain Sorting (phi)
(Inclusive Graphic Standard Deviation, Folk, 1974)
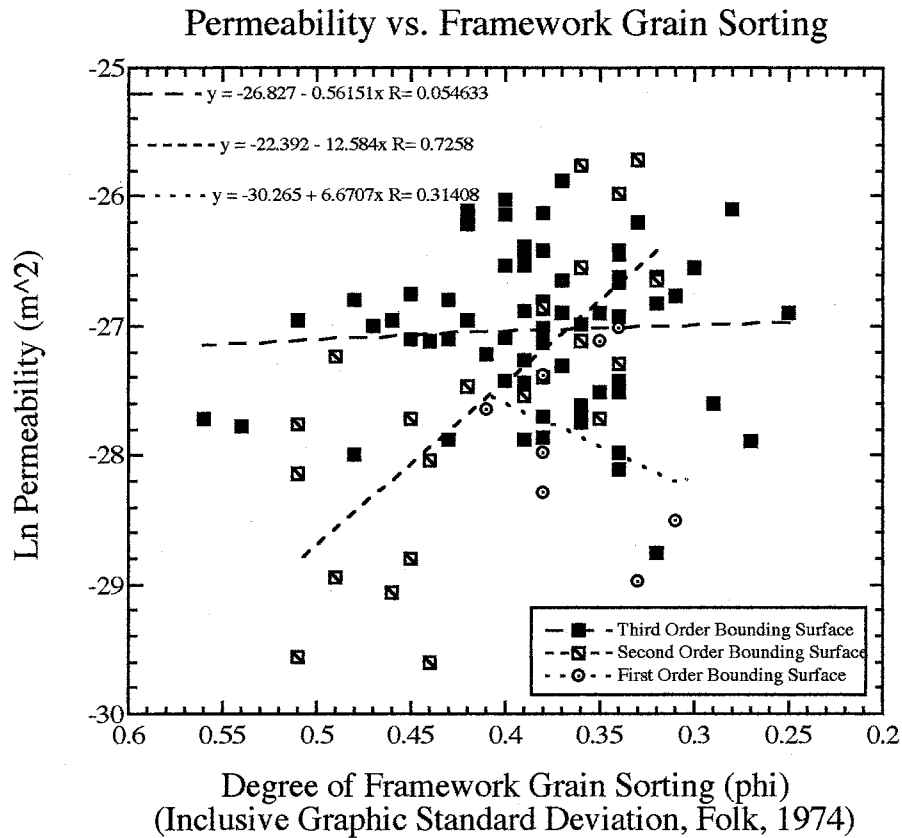
Figure 4.46

Diagram showing the correlation between permeability and the degree of framework grain sorting (phi units) derived from MSP measurements and point counts of thin section subsections made from billets cut from cored first, second and third-order sedimentary structures. Grain sorting was determined using the inclusive graphic standard deviation taken from Folk, 1974. The plot shows a weak, positive correlation between permeability and the degree of grain sorting (R= 0.28, n= 99) for cumulative measurements. Collectively, the first-order structure exhibits a weak, negative correlation (R= 0.31, n= 8). Conversely, second-order structures exhibit a good, positive correlation (R= 0.73, n= 22), and third-order structures exhibit a weak, positive correlation (R= 0.05, n= 69). Assessed correlation coefficients: strong [R ≥ 0.90], good [0.90 > R > 0.71], weak or insignificant [R ≤ 0.70].

Permeability vs. Matrix Material and Cements
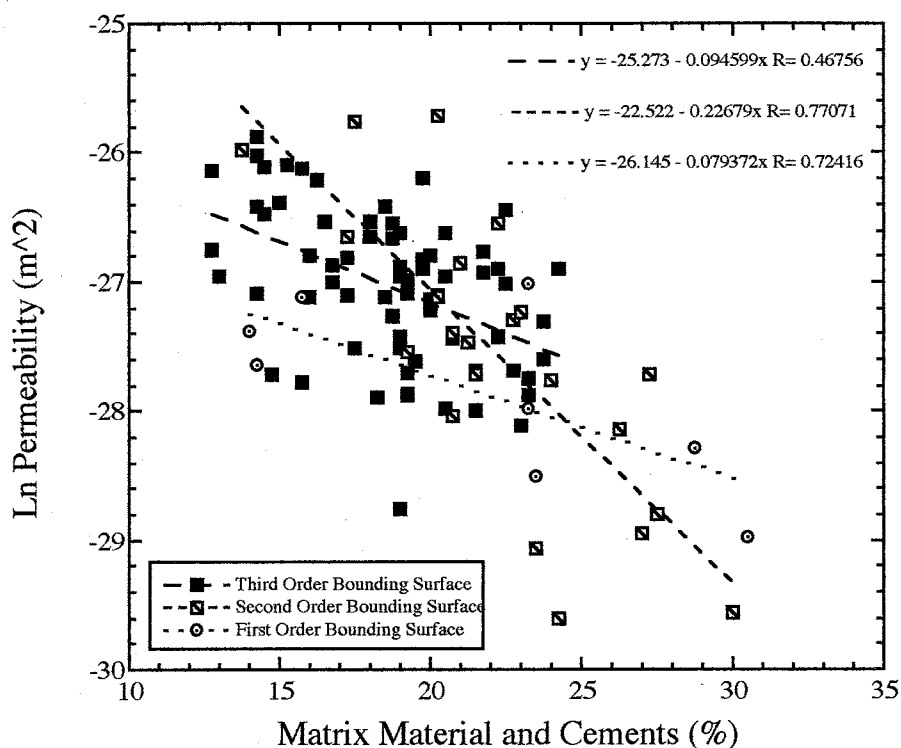
Figure 4.47

Diagram showing the correlation between permeability and all matrix material and cements (ferroan cements, authigenic quartz, and allogenic and authigenic clay minerals), derived from MSP measurements and point counts of thin section subsections produced from billets cut from cored first, second and third-order structures. This plot shows a weak, positive correlation between permeability and aggregate matrix material (R= 0.64, n= 99) for cumulative measurements. Collectively, first and second-order bounding structures exhibit good, positive correlations (R= 0.72, n= 8; R= 0.77, n= 22, respectively), whereas, third-order structures exhibit a weak, positive correlation (R= 0.47, n= 69). Increasing permeability with decreasing matrix volume percentages is considered a positive relationship. Assessed correlation coefficients: strong [R ≥ 0.90], good [0.90 > R > 0.71], weak or insignificant [R ≤ 0.70].

87

Permeability vs. Ferroan Cements
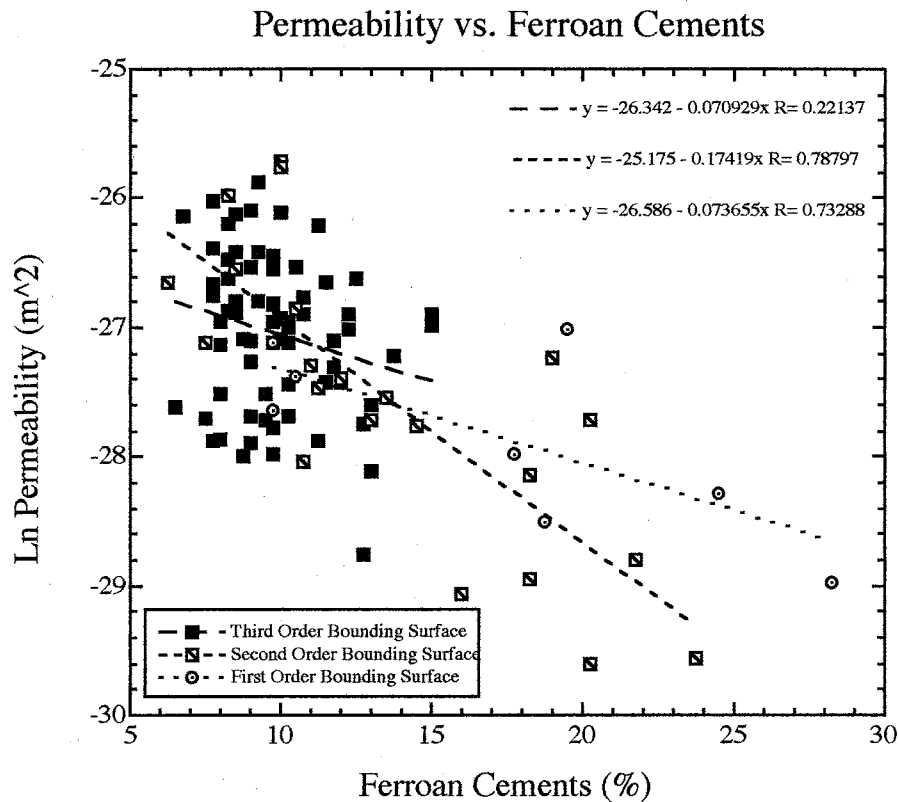
Figure 4.48

Diagram showing the correlation between permeability and ferroan cements (hematite and ferroan dolomite) derived from MSP measurements and point counts of thin section subsections made from billets cut from cored first, second and third-order structures. The plot shows a weak, positive correlation between permeability and ferroan cements (R= 0.63, n= 99) for cumulative measurements. Collectively, first and second-order bounding surface structures exhibit good, positive correlations (R= 0.73, n= 8 and R= 0.79, n= 22, respectively), whereas third-order structures exhibit a weak, positive correlation (R= 0.22, n= 69). Increasing permeability with decreasing ferroan cement volume percentages is considered a positive relationship. Assessed correlation coefficients: strong [R $\geq$ 0.90], good [0.90 > R > 0.71], weak or insignificant [R $\leq$ 0.70].

cements is evident upon outcrop observation of the sandstone (i.e., the first-order structure is cemented more completely by ferroan cements, whereas quartz cement is more abundant in third-order depositional structures). Although the relationship is statistically weak, an increase in the volume percentage of hematite and ferroan dolomite anywhere in this sandstone correlates with a decrease in the porosity and the measured permeability. Third-order structures have the highest permeabilities and the positive correlation between permeability and matrix material for first and second-order structures are the best correlations observed (Figure 4.47). The first-order structure contains the greatest volume of framework grains and total cement, as well as the lowest measured porosity and permeability values. A less convincing, positive correlation is observed between permeability and ferroan dolomite ($R = 0.34$, $n = 99$; Appendix E, Figure E5). The positive relationship between permeability and ferroan dolomite for the first-order structure ($R = 0.88$, $n = 8$; Appendix E, Figure E5), shows the best correlation of all four plots (Figures 4.47 and 4.48; Appendix E, Figures E4 and E5).

Other diagenetic alterations that illustrate an overall weak or insignificant correlation with MSP measured permeability (all three structures correlated collectively), are: 1) authigenic quartz overgrowth cement ($R = 0.06$, $n = 99$; Appendix E, Figure E6); 2) allogenic and authigenic clay minerals ($R = 0.09$, $n = 99$; Appendix E, Figure E7); 3) pore filling clay ($R = 0.02$, $n = 99$; Appendix E, Figure E8); and 4) pore lining clay ($R = 0.21$, $n = 99$; Appendix E, Figure E9). In some cases, however, individual subsections measured within each structure, as opposed to the collective, will exhibit good and even strong correlations with permeability. Measurements of second-order structures indicate that permeability increases with increasing total clay (Appendix E, Figure E7).

structures containing the highest percentages of clay also contain lesser amounts of ferroan cement, have more authigenic quartz cement, higher porosities and higher permeabilities.

A summary comparison of: 1) porosity types (point count porosity, porosity derived from image analysis, and intergranular porosity); 2) matrix material and ferroan cement volume percentages; and 3) textural data (mean framework grain size and degree of sorting) determined from modal analysis and Face 7 transect and billet permeability measurements is presented in Figure 4.49.

4.5. Structural Image Analysis

Rendered (Photoshop® 5.0) three-phase images of first, second and third-order structures depict graphically the various volume percentages of framework grains (white), porosities (blue) and matrix material (black) in each subsection (Figures 4.50 - 4.52; Appendix F, Figures F1 - F24). Subsection 7N3z.1 has the 3rd highest measured permeability in this investigation (ln k = -25.8765 m^2; Figure 4.50). Two-phase images isolating macroporosity (Figure 4.51; Appendix F) and matrix material (ferroan cements and total clay minerals excluding authigenic quartz cement; Figure 4.52; Appendix F) for the same three-phase photomicrograph shown in Figure 4.50, display graphically, the spatial coordination of macroporosity and matrix material.

A weak, positive correlation exists between MSP measured permeability and the porosities derived from image analysis (Figure 4.53). The same relationship exists between permeability and point count porosity (Figures 4.43 and 4.44). Mean point count porosity for all thin sections is 16.5%, whereas the porosity derived from image
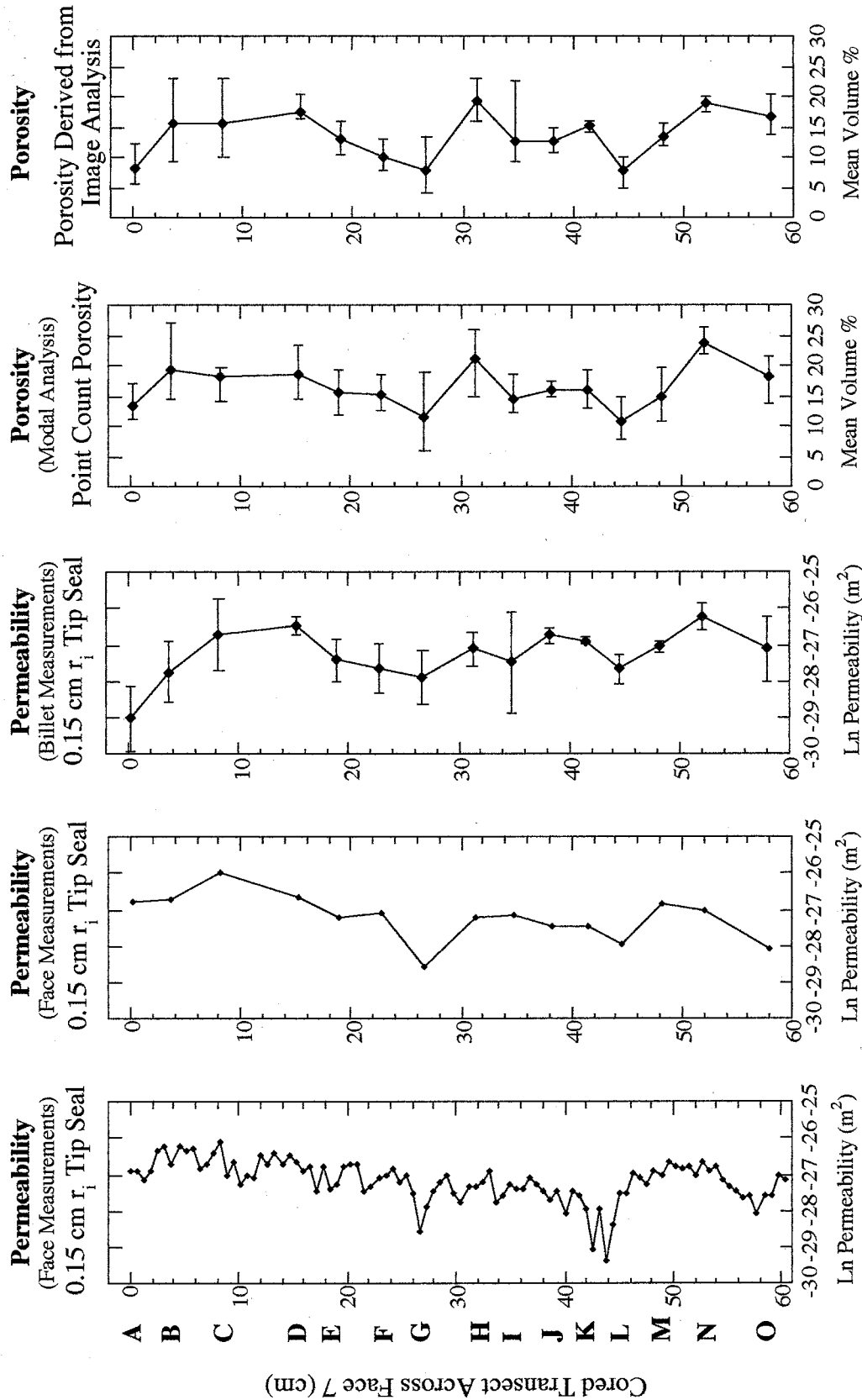
Figure 4.49: Permeability, porosity, matrix material and cements, ferroan cements, mean grain size and sorting plots produced from data acquired from measurements across the Face 7 transect.

91
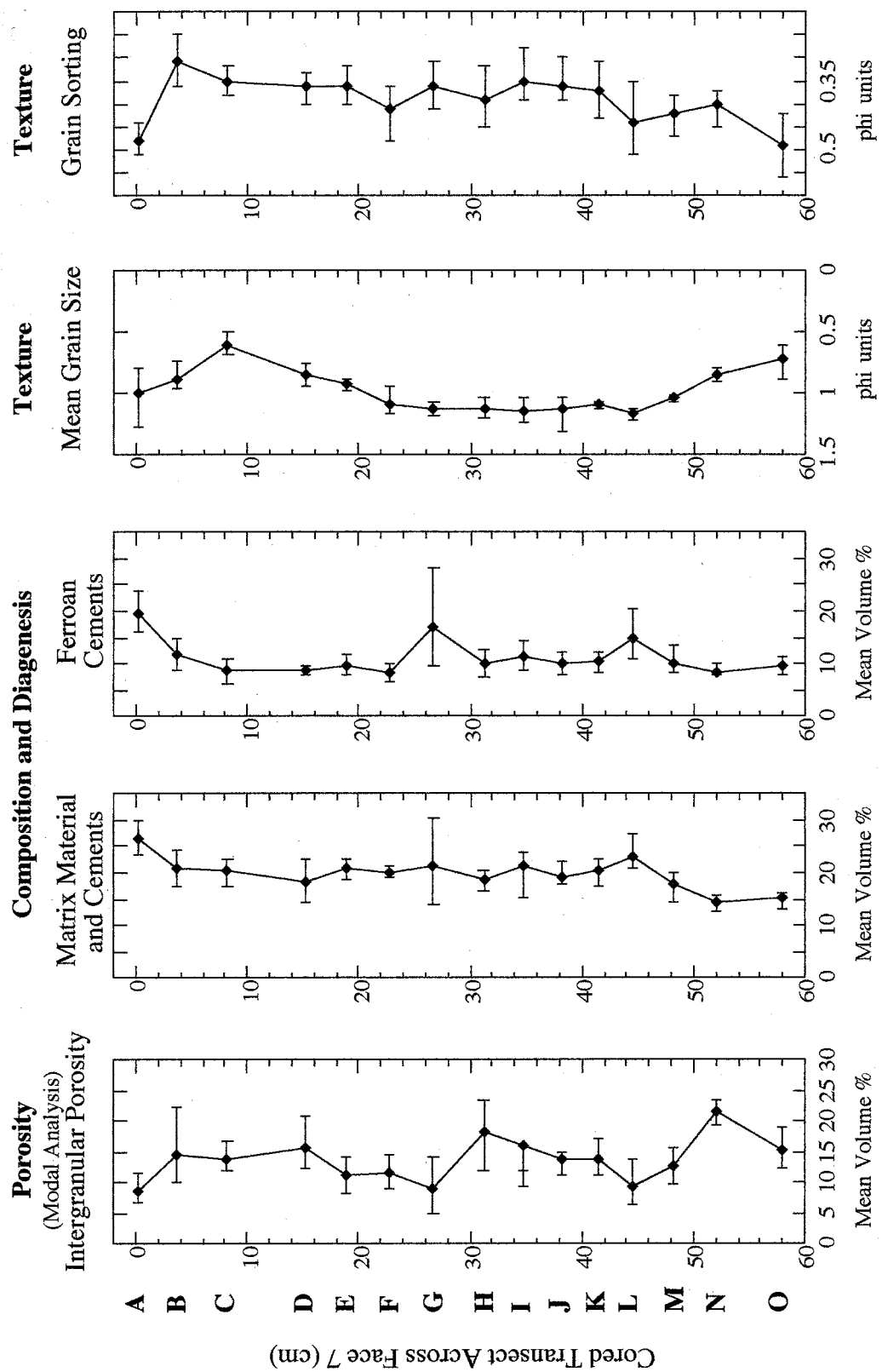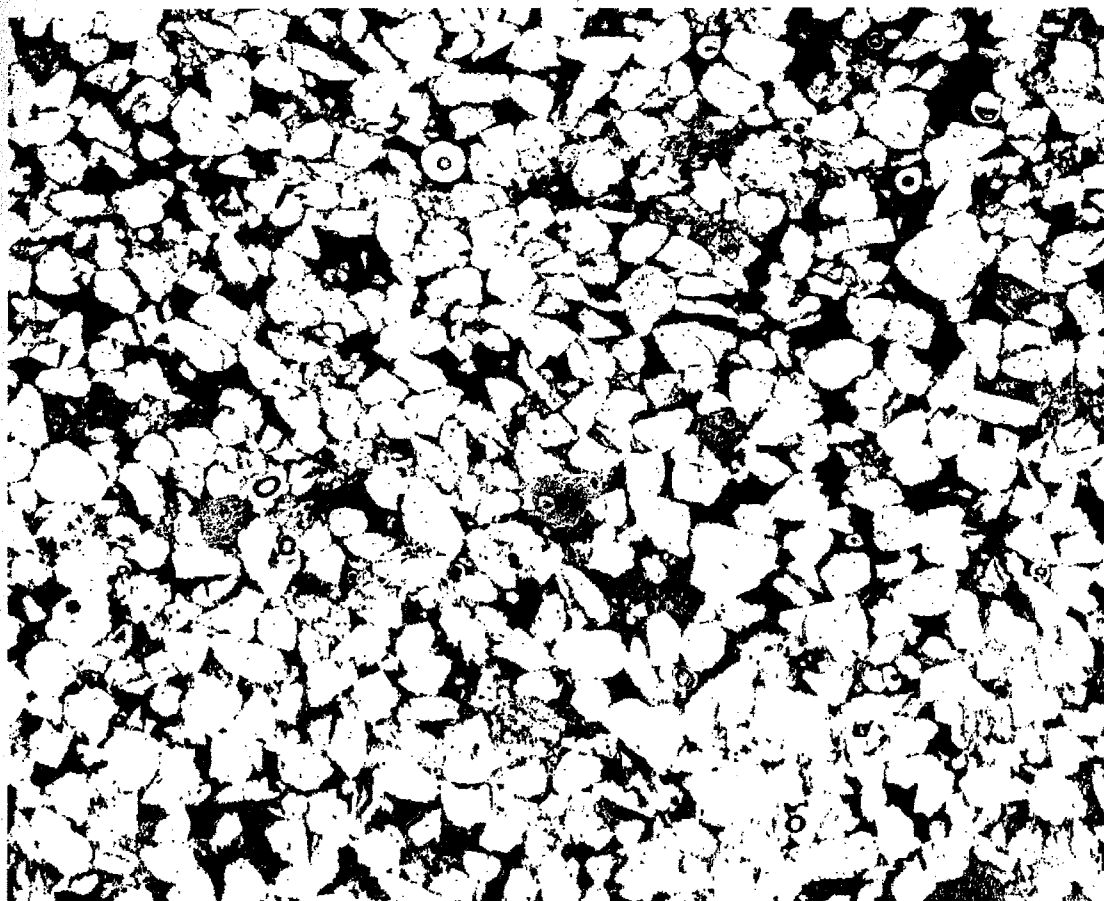
Figure 4.50

Rendered three-phase photomicrograph of subsection 7N3z.1. White pixels are detrital, framework grains including authigenic micro- and megaquartz. Black pixels are matrix material, including authigenic iron oxide minerals, ferroan dolomite rhombohedra and allogenic and authigenic clay minerals. Blue pixels are intergranular and intragranular macroporosity. This thin section subsection was prepared from 2.5 cm core drilled from a third-order, depositional structure and has the 3rd highest permeability of all measured subsections. The permeability was measured using the MSP equipped with the 0.15 cm ri tip seal: $k = 5.78E-12$ m^2; ln $k = -25.88$ m^2, $k = 5856$ millidarcies. Point count porosity derived from modal analysis is 26.25%, porosity derived from image analysis is 20.23% and matrix material consumes 12.75% of the subsection. The mean grain size is 0.793 phi (coarse-lower sand). The sorting is 0.37 phi (well-sorted sand) and was determined by applying the inclusive graphic standard deviation to the measured major axes of 237 framework grains (Folk, 1974). Image dimensions are 10.170 mm x 8.199 mm.
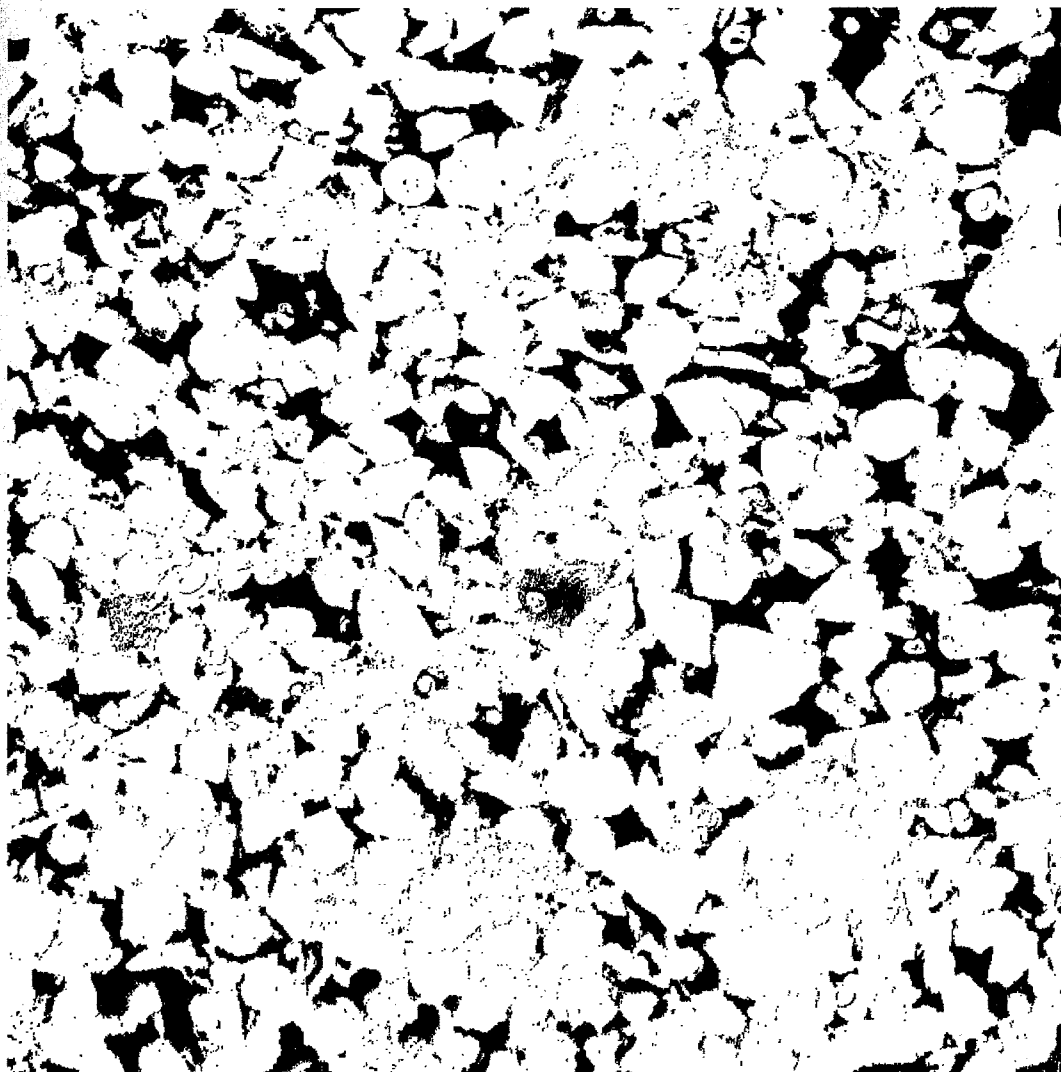
Figure 4.51

Rendered two-phase photomicrograph of subsection 7N3z.1. White pixels are detrital, framework grains including authigenic micro- and megaquartz and matrix material, including authigenic iron oxide minerals, ferroan dolomite rhombohedra and allogenic and authigenic clay minerals. Black pixels are intergranular and intragranular macroporosity. This thin section subsection was prepared from 2.5 cm core drilled from a third-order, depositional structure and has the 3rd highest permeability of all measured subsections. The permeability was measured using the MSP equipped with the 0.15 cm ri tip seal: $k = 5.78E-12$ m^2; $\ln k = -25.8765$ m^2; $k = 5856$ millidarcies. Point count porosity determined from modal analysis is 26.25%, porosity derived from image analysis is 20.23% and matrix material consumes 12.75% of the subsection. Image dimensions are 7.929 mm x 7.929 mm: magnification is 850X.

Figure 4.52

Rendered two-phase photomicrograph of subsection 7N3z.1. White pixels are detrital, framework grains including authigenic micro- and megaquartz and intergranular and intragranular macroporosity. Black pixels are matrix material, including authigenic iron oxide minerals, ferroan dolomite rhombohedra and allogenic and authigenic clay minerals. This thin section subsection was prepared from 2.5 cm core drilled from a third-order, depositional structure and has the 3rd highest permeability of all measured subsections. The permeability was measured using the MSP equipped with the 0.15 cm ri tip seal: $k = 5.78E-12 \ m^2$; $\ln k = -25.8765 \ m^2$; $k = 5856$ millidarcies. Matrix material consumes 12.75% of the subsection. Image dimensions are 7.929 mm x 7.929 mm: magnification is 850X.

Permeability vs. Porosity Derived from Image Analysis

Legend:
- ■ Third Order Bounding Surface
- ◩ Second Order Bounding Surface
- ⊙ First Order Bounding Surface

$y = -28.179 + 0.076787x$ $R = 0.46011$

$y = -29.425 + 0.14373x$ $R = 0.73989$

$y = -29.672 + 0.21869x$ $R = 0.74101$

X-axis: Porosity Derived from Image Analysis (%)
Y-axis: Ln Permeability (m^2)
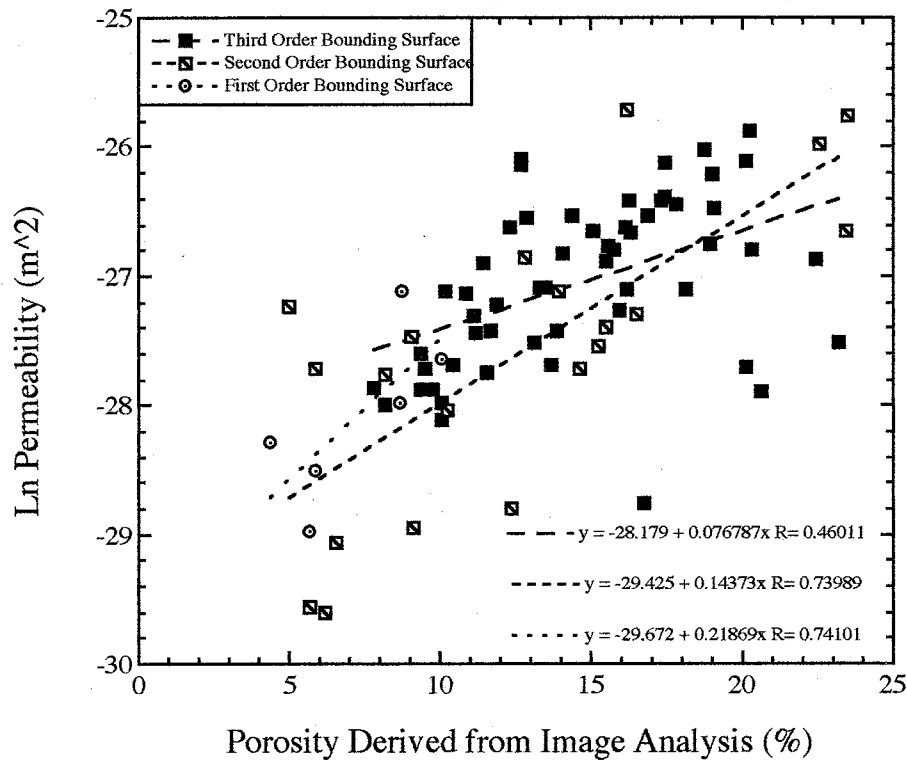
Figure 4.53

Diagram showing the correlation between permeability and porosity derived from image analysis. Permeability was obtained from MSP measurements and porosity was derived from the application of IP Lab to scanned, rendered and binarized subpsections of billets cut from cored first, second and third-order structures. The plot shows an overall, weak, positive correlation between permeability and image derived porosity (R= 0.63, n= 99) for cumulative measurements. First and second-order bounding structures exhibit a good, positive correlation (R= 0.74, n= 22 and n= 8, respectively), whereas third-order structures exhibit a weak, positive relationship (R= 0.46, n= 69). Assessed correlation coefficients: strong [R ≥ 0.90], good [0.90 > R > 0.70], weak or insignificant [R ≤ 0.70].

analysis was determined to be 13.8% (R = 0.78; R^2 = 0.61; Figures 4.49 and 4.54; Appendix D).

Average measurements derived from image analysis for both macroporosity and matrix material are lower than those determined from modal analysis because: 1) microporosity is not included; 2) certain portions of each rendered subsection image are too small to resolve; 3) boundaries between framework grains, macroporosity and matrix are sometimes difficult to discern; or 4) cropped, binarized images may be areally smaller than the point counted subsection. Usually, the porosity derived from image analysis is associated with the effective porosity (i.e., those pores containing mobile fluids and or hydrocarbons; Ehrlich et al., 1991).

Good correlations do exist between permeability measurements and aggregate point count and image analysis porosities of the highest permeability billets cut from each structure (aggregate measurements include all six individual subsection measurements; Figure 4.55). Typically, the first and second-order structures have lower porosities and permeabilities when compared to third-order structures. Measured subsections from second-order structures record the highest porosities, as well as the highest and lowest permeabilities (Figure 4.55).

The radial power spectra was plotted against frequency for binarized images of intergranular and intragranular macroporosity (Figure 4.56). Subsections having the greatest variance (highest porosities) also exhibit the highest permeability measurements (the 14th, 18th, 26th and 38th highest measured permeability subsections). Variances are generally lower for the lowest permeability images (the 79th, 88th, 96th, and 99th highest permeability subsections).

Point Count Porosity vs. Porosity Derived from Image Analysis

Figure showing a scatter plot with axis "Point Count Porosity (%)" on the y-axis (from 5 to 30) and "Porosity Derived from Image Analysis (%)" on the x-axis (from 0 to 25). Legend:
- Third Order Bounding Surface
- Second Order Bounding Surface
- First Order Bounding Surface

Regression equations:
$$y = 6.7603 + 0.71162x \quad R = 0.69523$$
$$y = 7.3649 + 0.62911x \quad R = 0.8285$$
$$y = 3.8577 + 1.0171x \quad R = 0.75376$$
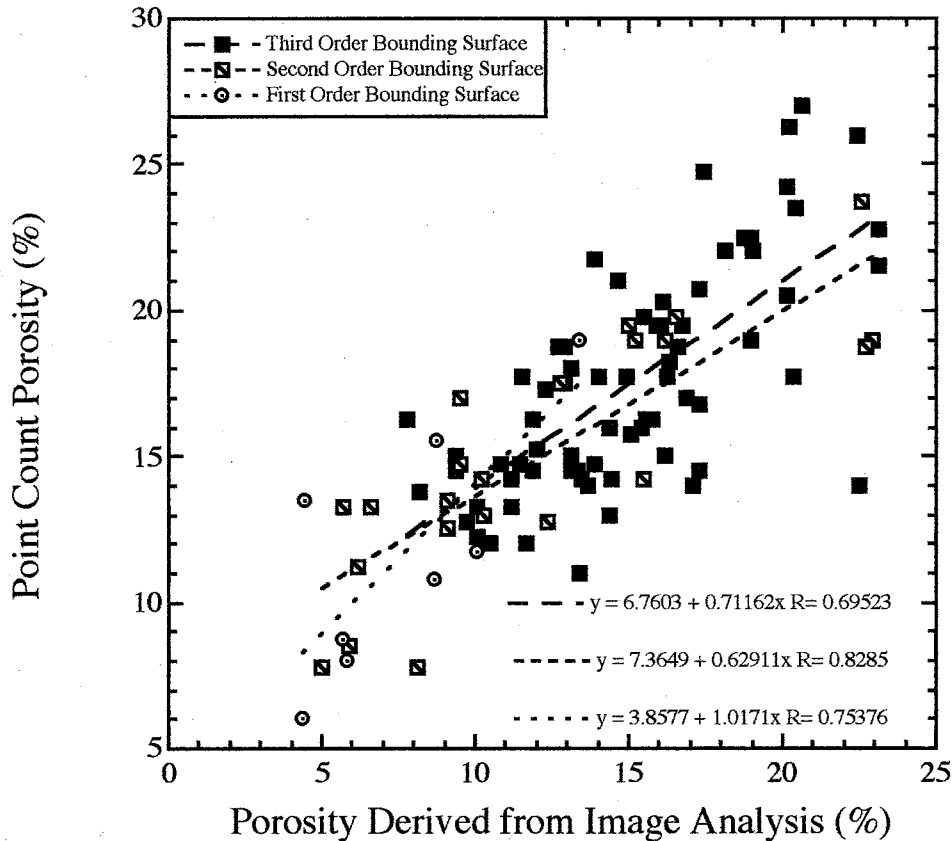
Figure 4.54

Diagram showing the correlation between point count porosity and porosity derived from image analysis. All measurements were produced from thin section subsections of billets cut from cored first, second and third-order structures and the binarized photomicrographs of the same thin sections subsections. Overall, the plot shows a good correlation between both porosity measurements for all structures (R= 0.78, n= 100). The plot shows a good, positive correlation between both porosity measurements for first and second-order structures (R= 0.75, n= 8; R= 0.83, n= 22, respectively), whereas the correlation between point count porosity and porosity derived from image analysis for third-order structures is weaker (R= 0.70, n= 70). Assessed correlation coefficients: strong [R ≥ 0.90], good [0.90 > R > 0.70], weak or insignificant [R ≤ 0.70].

Permeability vs. Image Analysis Porosity for the Highest Permeability Thin Sections from each Structure
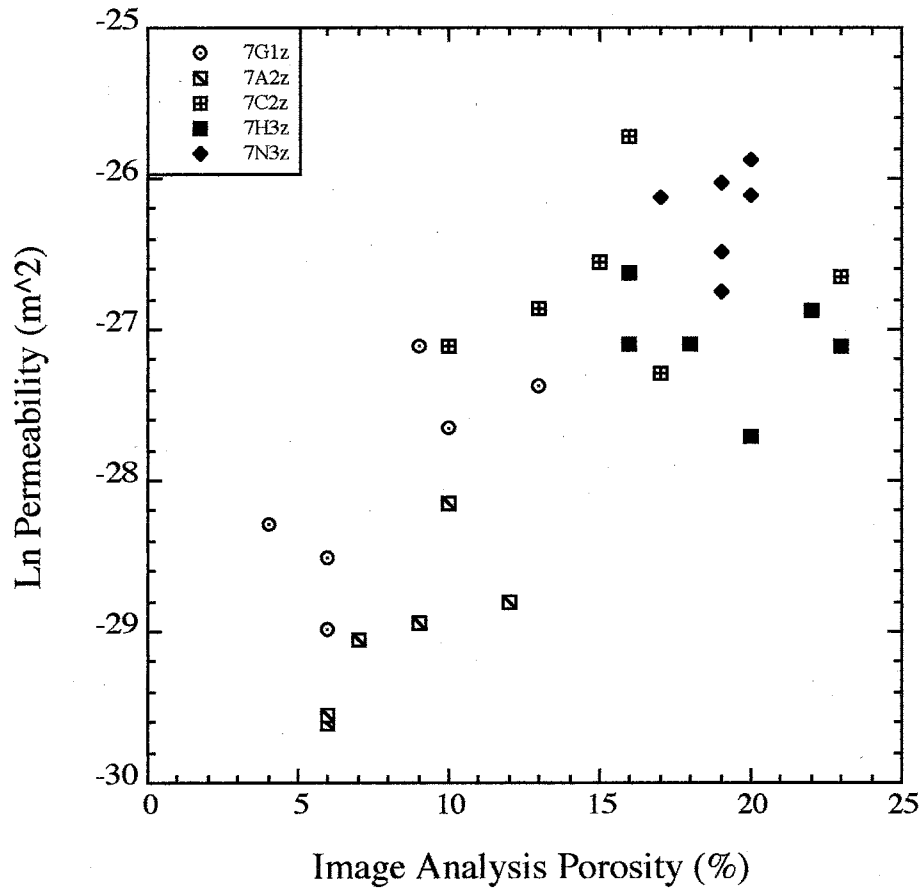
Figure 4.55

Diagram showing the correlation between permeability and the individual subsection porosities derived from image analysis for the highest permeability billets measured from each of the three different structures. Permeability was measured using the MSP, employing the 0.15 cm r_i tip seal and porosity was determined using IP Lab Software on binarized subsection images. Overall, the plot shows a good, positive correlation between permeability and porosity (R= 0.76). The thin section 7G1z is represented by circles. The two aggregate thin section subsections of the second-order structure, 7A2z and 7C2z, are represented by open, cross-hatched squares. The third-order subsections, 7H3z and 7N3z, are represented by a filled square and a filled diamond. Measurements from the third-order structure have the tightest grouping; these samples have the highest overall laboratory measured permeabilities and porosities. Second-order structures record the highest and the lowest individual permeability measurements.

2D Radial Power Spectra vs. Frequency for Porosity Derived from Image Analysis
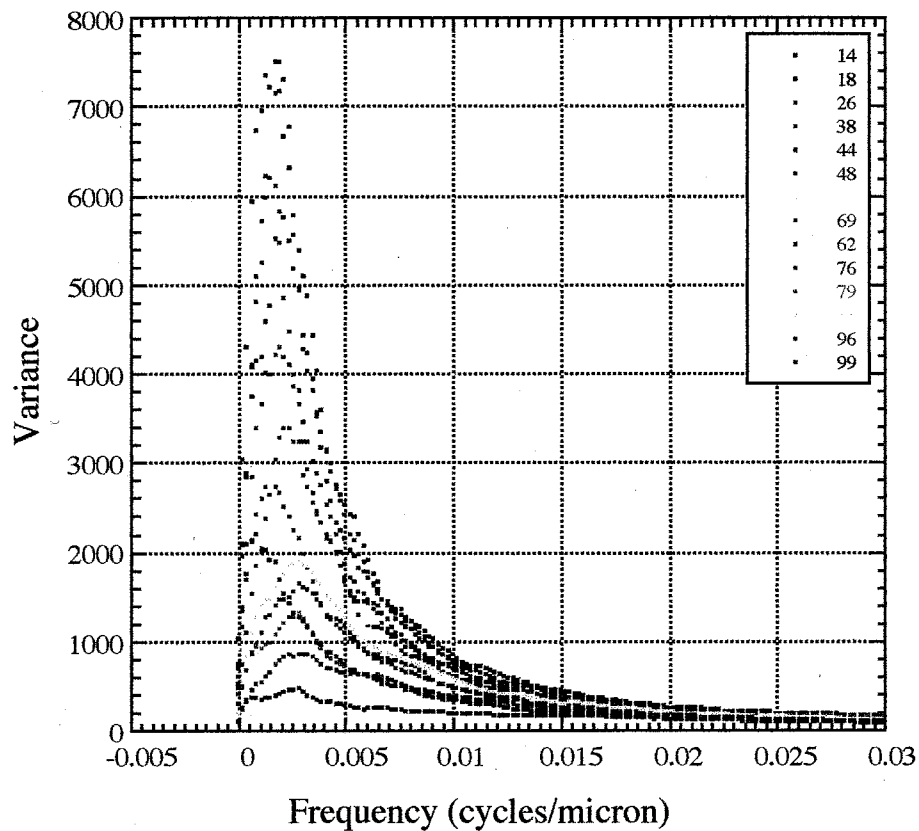
Figure 4.56

Diagram showing the power spectra (variance or porosity) plotted against the frequency for binarized images isolating porosity. The radial power spectra density function is used to determine a correlation length scale for pore populations.

Permeability values measured parallel to stratification (x-axis) appear to increase as the distance between pore voids increases (Figure 4.57). This would indicate that permeability in the Massillon is higher in areas with smaller, more numerous and isolated structures, than in areas with more continuous (two-dimensions) and larger pores in the direction of paleoflow. Measured permeability differences normal to cross-stratification (y-axis) are independent of the correlation length (Figure 4.58). Porosity is spatially correlated at an interval of 74 microns parallel to cross-stratification (Figure 4.57) and 70 microns normal to cross-stratification (Figure 4.58).

A weak, positive correlation is observed between permeability and the fractal dimension for binarized porosity subsection images parallel to cross-stratification (R = 0.30; Figure 4.59) and normal to cross-stratification (R = 0.22; Figure 4.60). As the fractal dimension approaches the value of '2', the less linear and continuous, or more tortuous the path between similar points. The mean fractal dimension between isolated pore voids in both directions is 1.65, indicating that porous voids are not particularly continuous, explaining the poor correlation with permeability. There is no preferential direction of spatial correlation between porosity populations; mean fractal dimension parallel to bedding = 1.6 and normal to bedding = 1.7, therefore, the system is assumed to be isotropic (directionally invariant).

A weak, negative correlation exists between permeability and the fractal dimension for matrix material parallel to cross-stratification (R = 0.62; Figure 4.61) and normal to bedding (R = 0.54; Figure 4.62). As matrix material becomes more continuous, possibly in lenses and thin, linear structures, the permeability appears to increase. The mean fractal dimension is lower than that for porosity, possibly explaining the better correlation

101

Permeability vs. Correlation Length Scale for Porosity (parallel to cross-stratification)

Legend:
- Third Order Bounding Surface
- Second Order Bounding Surface
- First Order Bounding Surface

$y = -26.426 - 0.0087246x \quad R = 0.22583$

$y = -22.79 - 0.064572x \quad R = 0.62723$

$y = -27.816 - 0.0028612x \quad R = 0.066537$

X-axis: Correlation Length Scale (microns)
Y-axis: Ln Permeability (m^2)
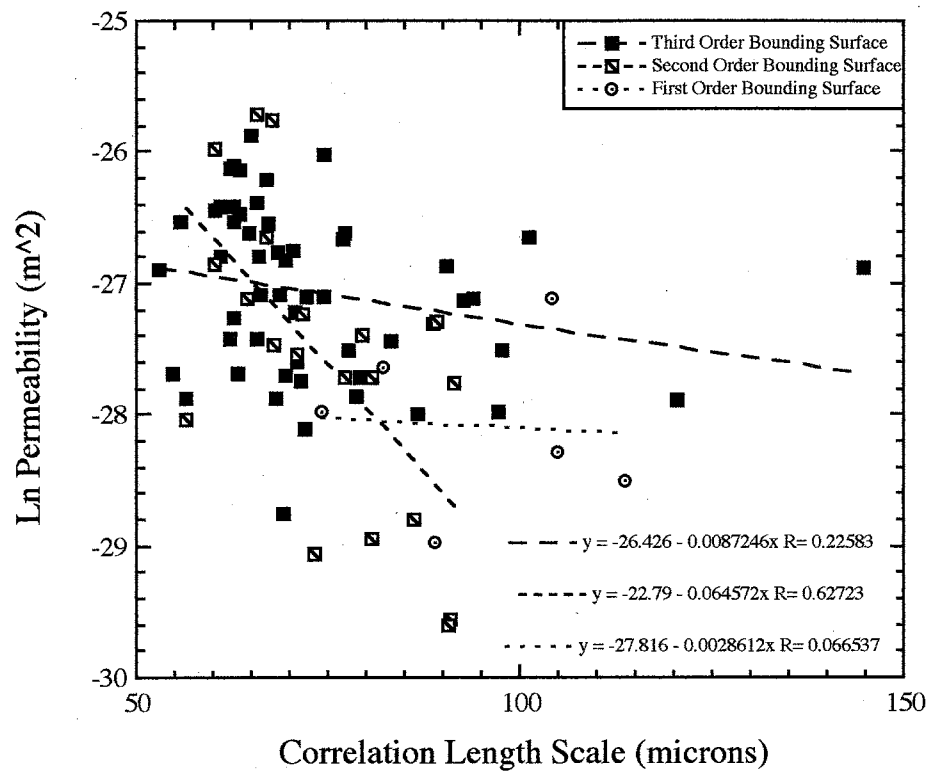
Figure 4.57

Diagram showing permeability plotted against the correlation length scale measured parallel to cross-stratification on binarized, subsection images that isolate porosity (predominately intergranular macroporosity; data derived from image analysis). Porosity is spatially correlated at an interval of 74 microns parallel to cross-stratification (x-axis).

Permeability vs. Correlation Length Scale for Porosity (normal to cross-stratification)

Legend:
- Third Order Bounding Surface
- Second Order Bounding Surface
- First Order Bounding Surface

$y = -27.252 + 0.0028961x$ R= 0.084782

$y = -26.092 - 0.019629x$ R= 0.27152

$y = -24.667 - 0.043195x$ R= 0.94299

Y-axis: Ln Permeability (m^2)

X-axis: Correlation Length Scale (microns)
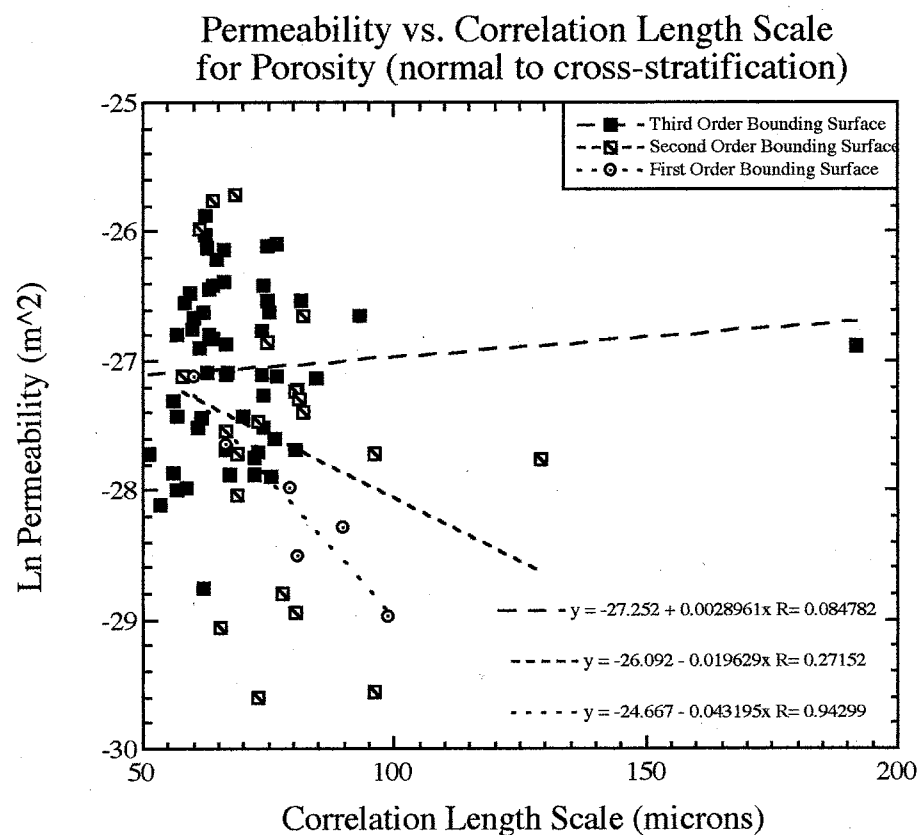
Figure 4.58

Diagram showing permeability plotted against the correlation length scale measured normal to cross-stratification on binarized, subsection images that isolate porosity (predominately intergranular macroporosity; data derived from image analysis). Porosity is spatially correlated at an interval of 70 microns normal to cross-stratification (y-axis).

Permeability vs. Fractal Dimension
for Porosity (parallel to cross-stratification)
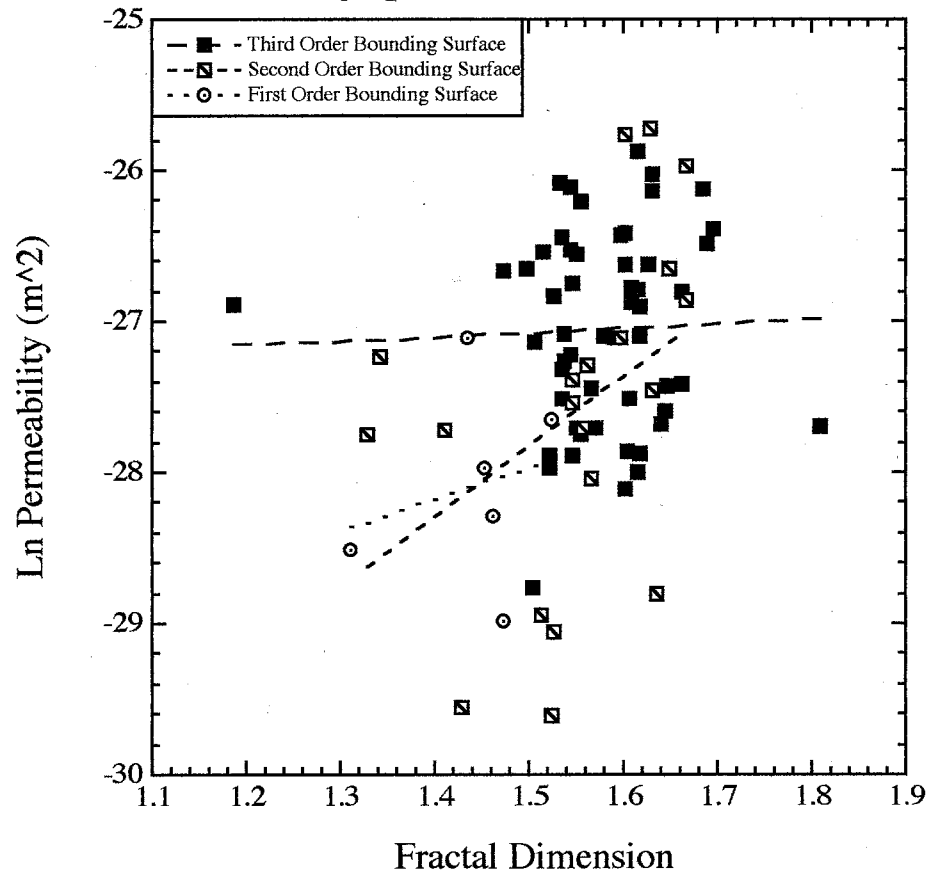
Figure 4.59

Diagram showing the correlation between permeability and the fractal dimension for porosity measured parallel to cross-stratification. The fractal dimension is derived using the slope of the power spectra applied to binarized images of thin section subsections that isolate the sandstone's intergranular and intragranular macroporosity. This plot displays a weak, negative, combined structural correlation between permeability and the fractal dimension (linear correlation or an increase in the spatial variability of macroporosity populations; R= 0.30). The mean fractal dimension is 1.6 along the x-axis (parallel to cross-stratification).

Permeability vs. Fractal Dimension for Porosity (normal to cross-stratification)

Legend:
- ■ - Third Order Bounding Surface
- ◩ - Second Order Bounding Surface
- ⊙ - First Order Bounding Surface

$y = -24.974 - 1.2526x \quad R= 0.12633$

$y = -36.404 + 5.3558x \quad R= 0.38291$

$y = -38.966 + 6.9392x \quad R= 0.61716$

X-axis: Fractal Dimension
Y-axis: Ln Permeability (m^2)
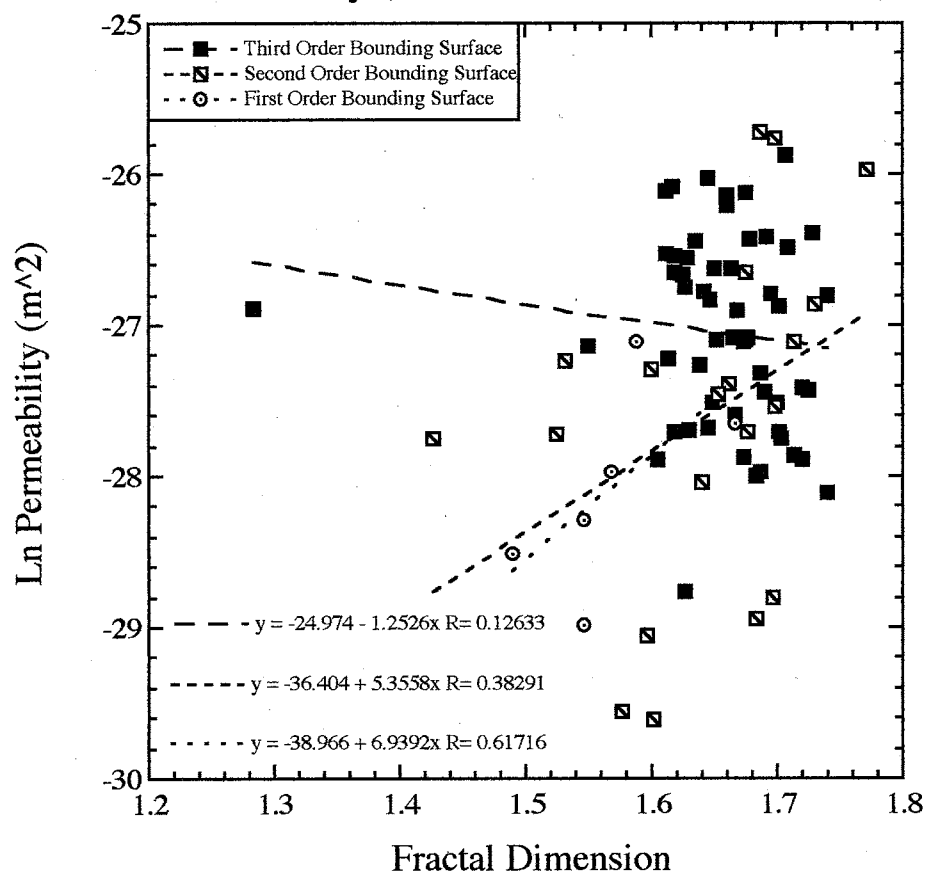
Figure 4.60

Diagram showing the correlation between permeability and the fractal dimension for porosity measured normal to cross-stratification. The fractal dimension is derived using the slope of the power spectra applied to binarized images of thin section subsections that isolate the sandstone's intergranular and intragranular macroporosity. This plot displays a weak, negative, combined structural correlation between permeability and the fractal dimension (linear correlation or an increase in the spatial variability of macroporosity populations; R= 0.22). The mean fractal dimension is 1.7 along the y-axis (normal to cross-stratification).

Permeability vs. Fractal Dimension for Matrix Material (parallel to cross-stratification)

Legend:
- ■ Third Order Bounding Surface
- ◩ Second Order Bounding Surface
- ⊙ First Order Bounding Surface

$y = -20.531 - 4.3801x$ R= 0.41652

$y = -8.3833 - 12.939x$ R= 0.79487

$y = -23.044 - 3.3244x$ R= 0.80238

X-axis: Fractal Dimension
Y-axis: Ln Permeability (m^2)
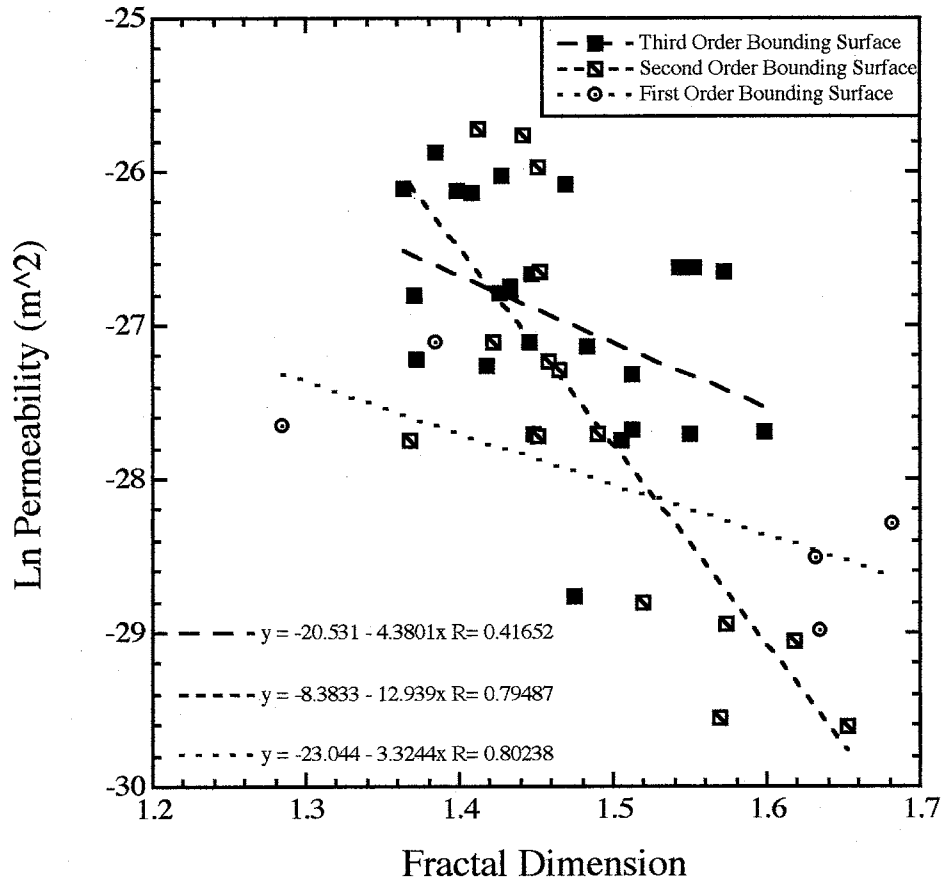
Figure 4.61

Diagram showing the correlation between permeability and the fractal dimension for matrix material measured parallel to cross-stratification. The fractal dimension is derived using the slope of the power spectra applied to binarized images of thin section subsections that isolate the sandstone's matrix material. This plot displays a weak, negative, combined structural correlation between permeability and the fractal dimension (linear correlation or a decrease in the spatial variability of matrix populations; R= 0.62). The mean fractal dimension is 1.5 along the x-axis (parallel to cross-stratification).

Permeability vs. Fractal Dimension for Matrix Material (normal to cross-stratification)

Legend on chart:
- — — y = -15.501 - 7.4817x R= 0.56056
- ----- y = -9.324 - 11.802x R= 0.56895
- ······ y = -12.727 - 10.098x R= 0.6949

Axis labels: Ln Permeability (m^2) vs. Fractal Dimension

Legend box:
- Third Order Bounding Surface
- Second Order Bounding Surface
- First Order Bounding Surface
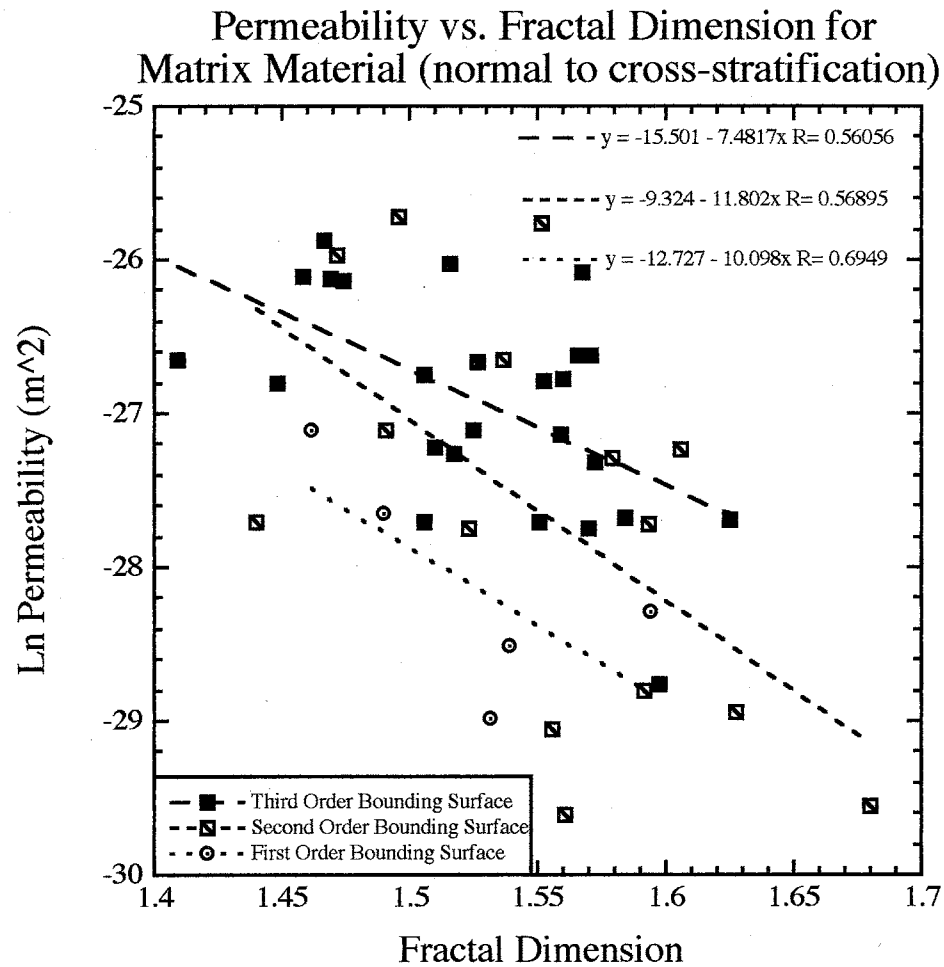
Figure 4.62

Diagram showing the correlation between permeability and the fractal dimension for matrix material measured normal to cross-stratification. The fractal dimension is derived using the slope of the power spectra applied to binarized images of thin section subsections that isolate the sandstone's matrix material. This plot displays a weak, negative combined structural correlation between permeability and the fractal dimension (linear correlation or a decrease in the spatial variability of matrix populations; R= 0.54). The mean fractal dimension is 1.5 along the y-axis (normal to paleoflow).

between matrix material and cements with permeability. There is no preferential direction of spatial correlation between matrix populations; mean fractal dimension parallel and normal to cross-stratification = 1.5, therefore, the system is assumed to be isotropic (directionally invariant).

The two-dimensional radial power spectra plotted against frequency for binarized subsection images of matrix material indicates that at a frequency below 4 cycles/micron, the variance between matrix is much greater than at frequencies greater than 4 cycles/micron (Figure 4.63). At higher frequencies, higher permeability subsection images exhibit higher variances (greater matrix material volume percentages; Figure 4.63). Binarized images of subsections having the highest permeabilities (the 4th, 8th, 16th, 28th and 34th highest permeability subsection images) also have the greatest variance at frequencies lower than 4 cycles/micron.

A very weak, positive correlation between permeability and the correlation length (microns) exists for binarized matrix material images both parallel and normal to stratification. Matrix material is spatially correlated at an interval of 125 microns along the x-axis (parallel to cross-stratification; Figure 4.64) and at 108 microns along the y-axis (normal to cross-stratification; Figure 4.65).

2D Radial Power Spectra vs. Frequency for Matrix Material
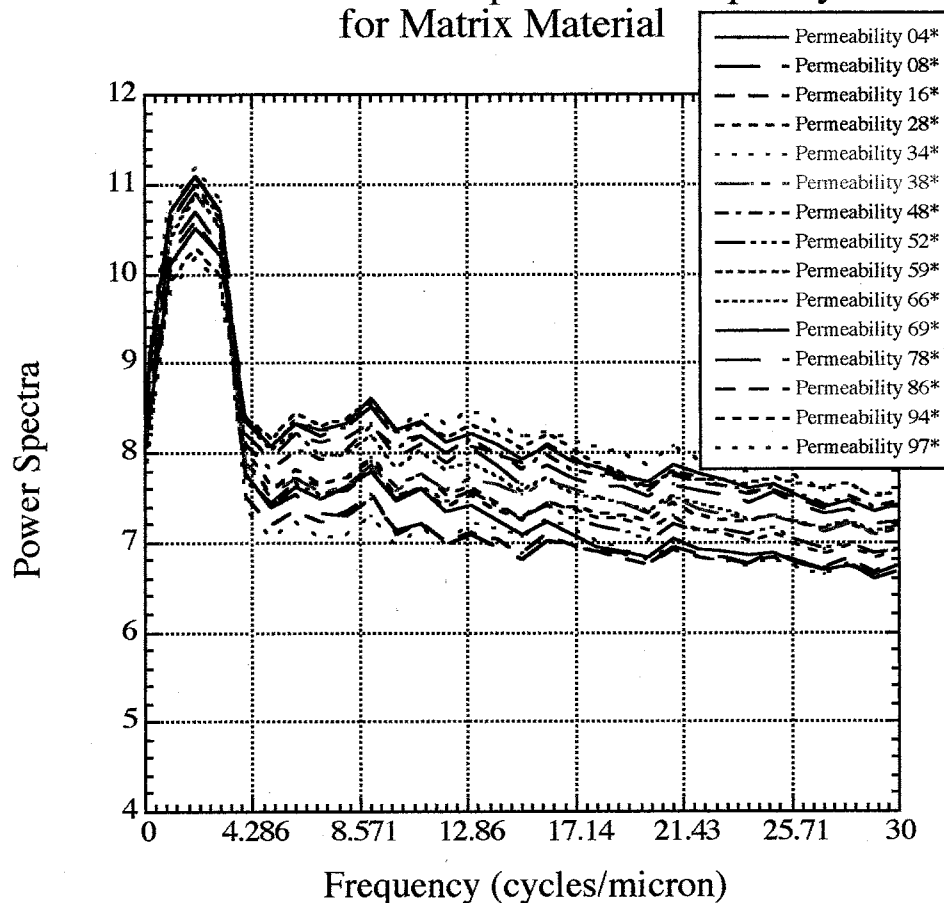
Figure 4.63

Diagram showing the radial power spectra (variance or matrix material) plotted against the frequency for binarized subsection images that isolate the matrix material (ferroan cements and all clay minerals). The radial power spectra density function is employed to determine a correlation length scale for the matrix material.

Permeability vs. Correlation Length Scale for Matrix Material (parallel to cross-stratification)

Legend:
- Third Order Bounding Surface
- Second Order Bounding Surface
- First Order Bounding Surface

$y = -28.015 + 0.008662x$ R= 0.51353

$y = -28.082 + 0.0041572x$ R= 0.1187

$y = -29.424 + 0.011197x$ R= 0.80104

Y-axis: Ln Permeability (m^2)
X-axis: Correlation Length Scale (microns)
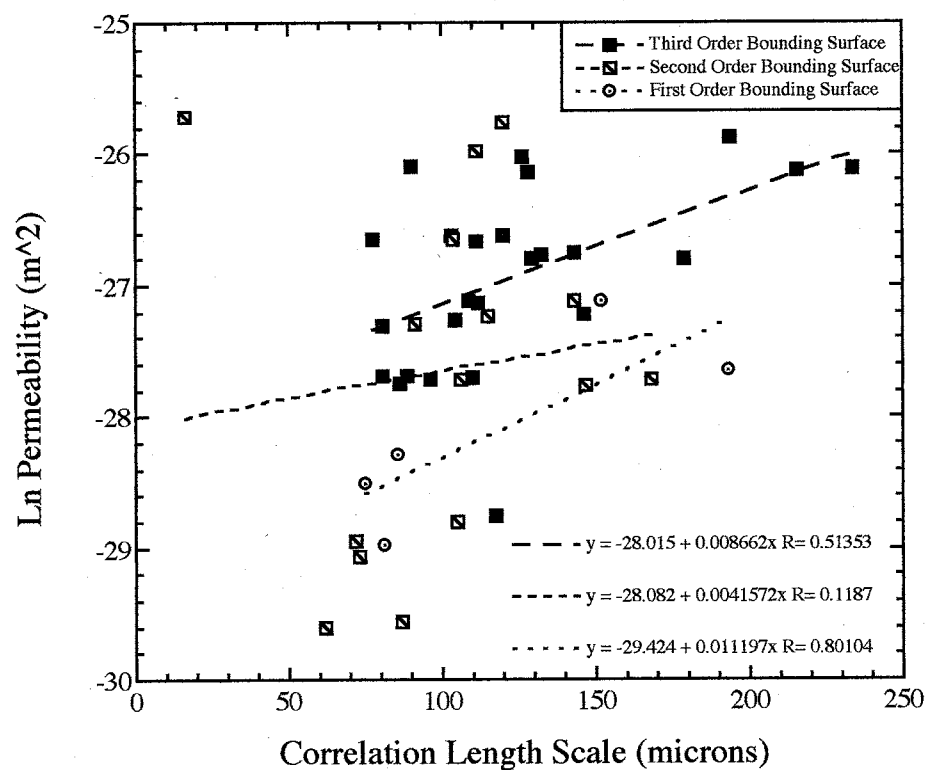
Figure 4.64

Diagram showing permeability plotted against the correlation length scale measured parallel to cross-stratification on binarized subsection images that isolate matrix material. Matrix material is spatially correlated at an interval of 125 microns parallel to cross-stratification (x-axis).

Figure 4.65

Diagram showing permeability plotted against the correlation length scale measured normal to cross-stratification on binarized subsection images that isolate matrix material. Matrix material is spatially correlated at an interval of 108 microns normal to cross-stratification (y-axis).

CHAPTER 5: DISCUSSION

5.1. Introduction

To gain a better understanding of the controls on permeability, this discussion addresses the following topics: 1) porosity evolution within the Massillon Sandstone, beginning with an estimate of the original porosity and continuing through the diagenetic alterations that have produced the present structure of the sandstone's pore network; 2) expected and observed depositional, diagenetic and spatial controls on the permeability distribution and an examination of the relationships, if any, that positively control fluid movement through the pore structure; 3) problems related to the method of analysis, in particular, issues concerning: a) the rendering of thin section subsections into binarized, digital images; b) the lack of correlation between two-dimensional thin section data and three-dimensional measured permeability data; and c) the relationship between measurement scale and the scale of heterogeneity.

In addition, this thesis was undertaken to evaluate the controls on the laboratory measured permeability distribution in the cross-stratified Massillon Sandstone. As noted in the previous sections, a number of variables appear to influence permeability in the unit, including mineralogy, texture, structure, diagenetic alterations, porosity types, as well as the spatial continuity of pores and matrix. However, these variables alone do not reveal a great deal about the pore connectivity or the transmissivity pathways of fluids within the sandstone's open network. One reason for this is that petrographic modal and scanning electron analyses were performed using thin sections and freshly broken surfaces of cored sandstone, which provide information in only two-dimensions, and thus can not be directly related to fluid movement in three-dimensions. Other concerns relate

to: 1) the sample support, or scale, as well as the method upon which the analysis was performed; 2) the paucity of cored material procured from first and second-order bounding structures; and 3) the sheer absence of pore throat distribution and size analysis. Because of the poor correlations between the point count component volume percentages and permeability, structural image analysis was performed on rendered and binarized thin sections to ascertain viable controls on the measured permeability.

5.2. Paragenetic Sequence

The paragenetic sequence was determined from textural relationships observed from analysis employing petrographic and scanning electron microscopy (Figure 5.1).

5.2.1. Early Diagenesis

Compaction and grain rearrangement appear to have occurred early in diagenesis (Figures 4.14 and 4.15). Sutured quartz grains are observed in contact solely with each other and with highly deformed ductile, framework lithics between them. Early dolomitization occurred after early compaction and prior to the precipitation and replacement of iron oxides, principally hematite (Figure 4.24). There are no conspicuously crushed, folded, bent, contorted or dilated ferroan dolomite minerals and all rhombohedra have been replaced by iron oxides (Figure 4.27). Iron oxide precipitation and replacement occurred early in the diagenetic process, partially or fully replacing the dolomite, allogenic pore lining and pore filling clay minerals, labile and ductile lithics and feldspars (Figure 4.7). Hematite predates authigenic quartz as indicated by its coating many quartz grains prior to euhedral, authigenic quartz cement

113

Diagenetic Alteration

	EARLY	MIDDLE	LATE
Compaction and Grain Rearrangement	—		
Dolomitization	—		
Iron Oxide Precipitation and Ferroan Dolomite	—		
Authigenic Quartz and Replacement by Silica	—		
Grain and Mineral Dissolution, Alteration and Replacement		—	
Authigenic Hematite		—	
Authigenic Kaolinite		—	
Authigenic Pore Lining and Pore Filling Clay Minerals		—	
Grain and Mineral Dissolution		—	
Authigenic Iron Oxide and Clay Minerals			—
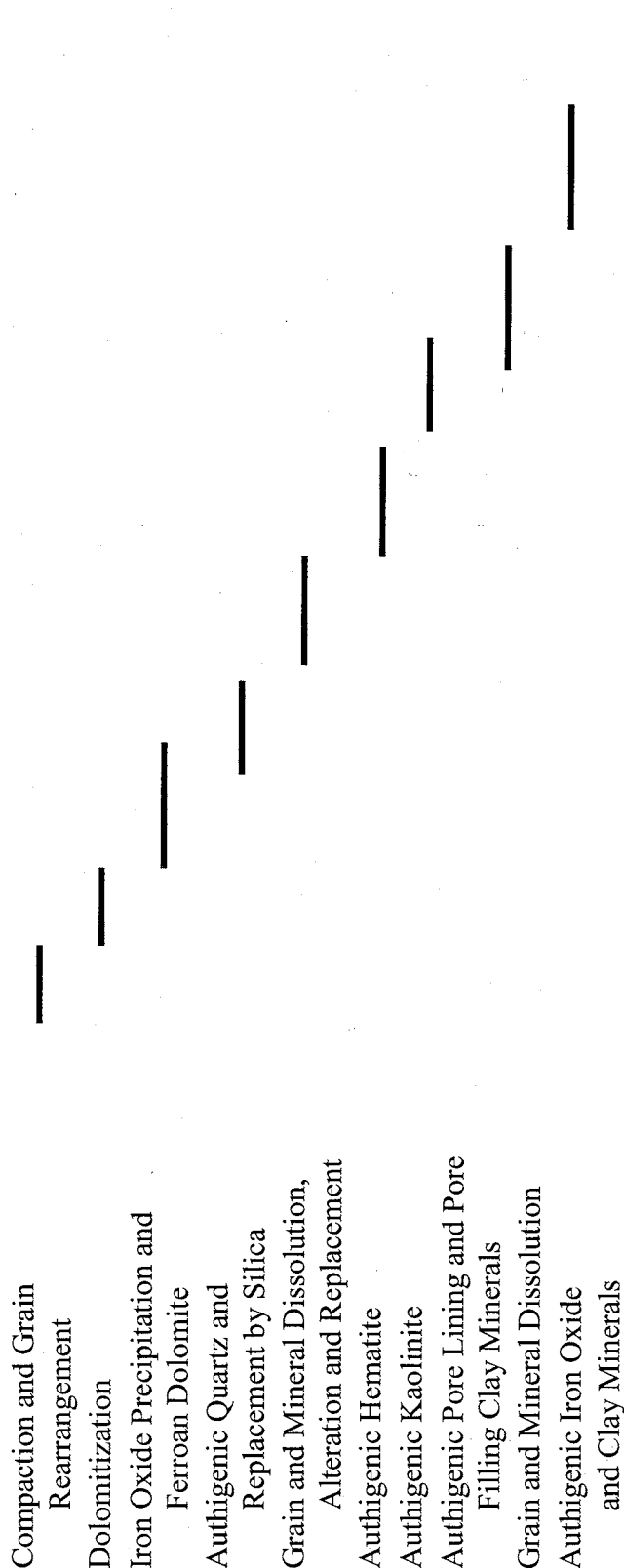
Figure 5.1: Observed paragenetic sequence for the Massillon Sandstone.

114

precipitation (Figure 4.6). Authigenic quartz precipitation followed, automorphically penetrating the dolomitic rhombohedra minerals and growing into primary pore voids not closed during early compaction or occupied by early dolomite, iron oxide cements and foliated detrital clay (Figure 5.2).

5.2.2. Middle Diagenesis

Grain and mineral dissolution, alteration and replacement processes occurred during middle diagenesis. Feldspar grains have been preferentially and partially dissolved along twin planes and have subsequently precipitated authigenic clays and hematite occupying their interiors (Figures 4.2 and 4.3). Hematite fully replaced all rhombohedral minerals that had not been fully affected. Hematite also replaced framework and non-framework constituents for a second time. Authigenic kaolinite precipitated after the dissolution event and the second iron oxide precipitation episode. Kaolinite is present as fine-grained vermicules and blocky crystals that appear to have precipitated post any compaction event and have not been substantially (or even minimally) replaced by hematite (Figure 4.12). Other authigenic pore lining and pore filling clay minerals, such as illite, sericite, and possibly paragonite, also precipitated (Figure 4.22), the result of dissolution and replacement of unstable feldspars and undifferentiated silicic lithic fragments and the influx of silicic rich meteoric fluids.

5.2.3. Late Diagenesis

Secondary dissolution porosity in the form of intergranular and intragranular micro- and macroporosity occurred late in the diagenetic evolution of this sandstone. The
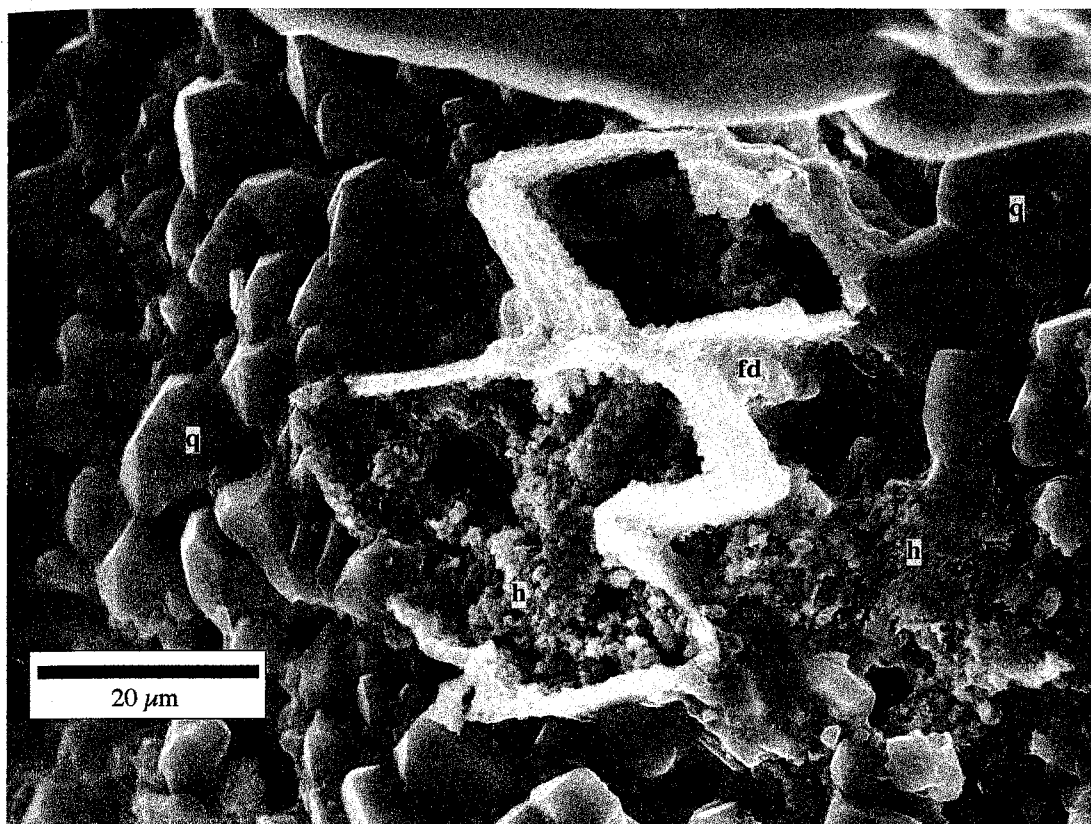
Figure 5.2

SEM photomicrograph of euhedral microquartz (q), a partially dissolved ferroan dolomite cluster (fd), and authigenically precipitated iron oxide cement (h). The dissolution and precipitation of diagenetic, autochthonous minerals and cements both positively and negatively affect the effective porosity and permeability in the Massillon Sandstone.

continued dissolution replaced framework grains and authigenic matrix material produced the dominant portion of porosity and permeability in the present day sandstone (Figures 4.32, 4.37 and 4.38). Latest stage iron oxide and authigenic clay precipitation can be seen in the last vestiges of dissolved rhombohedral assemblages (Figures 4.5 and 4.26)

5.3. Evolution of Porosity in the Massillon Sandstone

Permeability of reservoir rocks is a function of the pore network (the medium within which intragranular and intergranular pores are connected via pore throats) and it's framework architecture or structure, and is the result of original composition and texture, as well as diagenetic alterations that have affected the sandstone from the time of burial and initial consolidation to the present. An understanding of the evolution of this pore network as a function of diagenesis (cement precipitation, compaction and dissolution of framework and non-framework constituents) is key to evaluating the intrinsic permeability of any reservoir formation.

Today, the Massillon Sandstone is a sublitharenite, composed primarily of sub-rounded, monocrystalline quartz grains, ferroan cements and authigenic kaolinite. The original composition of the sandstone included higher percentages of lithic fragments and feldspars, whose subsequent dissolution and alteration produced authigenic matrix phases that presently occlude the open pore volume and negatively correlate with point count porosity values and laboratory measured permeability. Ferroan dolomite cement was also more prevalent earlier in the sandstone's history, possibly reducing the effective porosity of a younger, reservoir rock.

Grain size and sorting are the most significant textural parameters affecting the original porosity and permeability of unconsolidated sand (Beard and Weyl, 1973). Using their tables, the depositional (i.e., pre-diagenesis) porosity for the Massillon Sandstone block studied was most likely, approximately 39% (Appendix C). This porosity is supported by an observed, mean framework grain size of 0.98ϕ (coarse-lower sand) and a mean degree of sorting equal to 0.39ϕ (well-sorted sand; Appendix D). The present porosity determined by modal analysis is 16% (14% when derived from image analysis). This loss of approximately 24% porosity is principally due to chemical diagenesis. The majority of microcline, orthoclase and plagioclase grains, as well as almost all sedimentary and metamorphic lithic grains have been replaced by authigenic hematite and clay minerals, which in turn have precipitated into areas surrounding these grains and into adjacent, primary (preserved depositional) and secondary (dissolution) pore spaces. Pore-occluding matrix material, including hematite, ferroan dolomite, kaolinite, illite, sericite and undifferentiated allogenic clays choke pore throats, heavily line pore walls, form bridges across open pores, coat and rim framework grains and fill intragranular fractures. Although a high degree of mechanical diagenesis is observed (concavo-convex and sutured framework grain contacts), the negative effects due to compaction on the overall porosity of the rock are overshadowed by the abundant authigenic mineral precipitation.

Late-stage, dissolution porosity (i.e., grain and mineral dissolution) increased intragranular and intergranular porosity, and was the principal diagenetic process to enhance the porosity and permeability of the Massillon Sandstone. All micro- and macroporosity within cemented, compacted and mineral replaced regions is secondary,

118

dissolution porosity. The larger, oversized pores and dissolved shells of framework components are predominately isolated features, whereas thinner lenses of dissolved clays and ferroan cements between the predominant quartz grains are more continuous lineaments (Appendix F).

5.4. Depositional Controls on Permeability

Expected depositional (primary) controls affecting the permeability distribution in the Massillon include compositional (detrital framework and non-framework components and mineralogy), textural (the mean framework grain size and the degree of grain sorting), and structural (sedimentary structures, i.e., erosional bounding surfaces and depositional, cross-stratification) features inherent to the sandstone. All were analyzed to determine which, if any, independently control the sandstone's permeability distribution.

Increasing mean volume percentages of detrital quartz and lithic fragments do not positively correlate with permeability measurements (R values = 0.15 and 0.34, respectively) made using the 0.15 cm r_i tip seal. Mean feldspar abundance does not correlate well with permeability measurements either (R = 0.07). The paucity of feldspar grains (mean = 3 vol %) is attributed to both a limited source supply and to the diagenetic processes of dissolution and alteration to the authigenic clays kaolinite, illite, and possibly paragonite, to undifferentiated pore filling and lining clays and to sericite. It appears that the independent and whole rock distribution of detrital framework grains (composition and mean volume %), within the Massillon Sandstone block does not control the measured permeability at the sample support investigated (R = 0.04; plotted permeability against total detrital framework grain percentages).

119

The mean grain size of detrital framework grains correlates poorly with permeability (R = 0.34), although the correlation is a positive one, indicating that with increasing mean grain sizes, the measured permeability does appear to increase. Weak, positive relationships with permeability are also observed between both the degree of sorting (R = 0.28) and the mean pore width (R = 0.37). Therefore, expected textural controls on permeability fail to fully explain the measured permeability distribution.

An attempt to quantify differences between first, second and third-order structures was another task undertaken in this investigation. Only one of the 15 core samples was characterized as a first-order structure; the eight subsections investigated from this first-order structure are possibly an insufficiently small subset for producing meaningful correlations between permeability and porosity types, pore structure and diagenetic alterations. Standard deviations of the major petrographic element percentages observed in the sandstone (permeability, porosity, mineralogy and textural characteristics) are the lowest in almost every category within the first-order structure. Although it appears that this structure is the most homogeneous of the three, this is probably a response to the small number of subsections sampled from the first-order structure. An interesting statistical point is that the percentages of matrix material and total cements in this first-order structure are the most variable. The reason for this is that core G was taken from Face 7 at the transition zone between a third-order structure and the only first-order structure on the face. Permeability, porosity and textural variations are small, only the difference in percentages of matrix and total cements is considered significant. Outcrop observations clearly reveal this problem (Figure 3.3). Therefore, all described first-order structural subsections throughout this treatise are actually hybrid samples.

With this in mind, it would be expected that relationships involving third-order structures (69 measured subsections) would correlate more convincingly, either positively or negatively, with permeability. This is not the case, however, for the third-order structural relationships have the overall weakest correlations with permeability.

Measurements taken from second-order structures prove to contain the most variable elements observed from modal analysis, scanning electron and permeability analysis. Subsections of these structures record the highest and the lowest permeabilities of all the samples.

5.5. Diagenetic Controls on Permeability

Diagenetic (secondary) controls on permeability include: 1) processes that create resistance to fluid flow and introduce pore occluding materials, and 2) alterations that increase the effective porosity of a reservoir rock and ultimately the permeability. It is expected that the precipitation of authigenic minerals within pores and the negative effects of compaction will cause a decrease in permeability, whereas the processes of mineral dissolution and fracturing will increase permeability.

The precipitation of ferroan cements (hematite and ferroan dolomite), as well as their replacement of framework and non-framework constituents, appears to have the greatest impact on effective porosity and the permeability in the Massillon. Ferroan dolomite (mean = 3 vol %), although microscopic, is an ubiquitous intergranular pore occluding agent; clogging pore throats, bridging pore voids and coating grain margins in distinct clusters. Hematite, due to it's abundance (mean = 9 vol %), is the most important cementing phase negatively affecting the reservoir quality of this sandstone. Authigenic clay minerals, particularly kaolinite and illite, have precipitated as pore filling (primarily

121

within unstable, detrital grains) and pore lining types. These clay minerals can produce significant reductions in the permeability when evenly distributed throughout the pore matrix. In areas where the clays are not continuously distributed (where they exist as isolated clots within replaced framework grains), reservoir fluids can readily bypass them, nominally affecting the reservoir quality and permeability of the sandstone (Wilson and Stanton, 1994).

Various degrees of compaction are observed, as well as sutured grains with associated quartz overgrowths. The high density of sutured grains indicates that this sandstone has undergone a high degree of compaction, negatively affecting the permeability. Silica introduced to the pores, in part by pressure solution of abundant framework quartz grains, reprecipitated along some quartz grain margins. Although frequently observed in SEM images, authigenic quartz was seldom encountered during the point count analysis. Cathodoluminescence analysis supports the paucity of quartz overgrowths. Sandstones having a majority of monocrystalline quartz grains tend to precipitate authigenic quartz more prevalently when mean grain sizes are smaller (Heald and Renton, 1966). The Massillon's mean grain size is coarse-lower sand, possibly explaining the lack of observed authigenic quartz overgrowths. Therefore, quartz overgrowth cement appears to be an insignificant fluid inhibiting authigenic phase.

Although the presence of secondary porosity does not always result in a net increase in total porosity and permeability (Bloch, 1994), in the Massillon, dissolution porosity appears to be an important control on the porosity and consequently the permeability. Evidence for the enhancement of porosity due to late-stage dissolution is supported by: 1) the abundance of oversize pores; 2) the complete and partial dissolution

of feldspars, lithics, allogenic and authigenic clay minerals, hematite and ferroan dolomite; 3) etched quartz overgrowth margins; 4) the abundance of corroded grains; 5) the partial dissolution of some quartz grains; and 6) open, intragranular fractures. Two-dimensional observations reveal that many of the oversized pores and dissolved framework grains are isolated features, yet they may be spatially continuous in three-dimensions, enhancing the effective porosity. This may explain, in part, the relatively poor correlation between permeability and porosity values. Intragranular micro- and macroporosity is only important with respect to the first-order bounding structure; interstitial micropores within authigenic kaolinite vermiforms and illite plates and contribute the majority of microporosity observed in the first-order structure. Microporosity does not appear to strongly enhance the reservoir quality of this sandstone.

Although almost all correlations of total point count porosity and porosity derived from image analysis with measured permeability are weak (R = 0.53 and 0.63, respectively), these relationships convey two of the strongest of all correlations. All investigated relationships are positive, indicating that with increasing permeability, an increase in either total porosity or more importantly, an increase in intergranular macroporosity is observed.

5.6. Spatial Controls on Permeability

Expected primary (depositional) and secondary (diagenetic) controls do not correlate well with permeability, therefore, structural image analysis was investigated in an attempt to quantify this lack of correlation and to ascertain whether or not the two-dimensional spatial architecture of pores and matrix material are qualitative controls on

123

laboratory based permeability measurements. The application of three spectral models was applied to the rendered, two-phase, subsection photomicrographs to increase the scope of the image analysis.

The spatial continuity of: 1) intergranular and intragranular macroporosity, and 2) non-framework allogenic and authigenic matrix material were investigated. Both were analyzed employing three different spectral analysis models: 1) the correlation length scale determined from the power spectral density function; 2) the fractal dimension, also obtained from analysis of the power spectral density function; and 3) the radial spectra (a measure of the pore space), which investigates the spectrum integrated over the full 360° of each binarized images.

The mean fractal dimension between macropores measured parallel and normal to cross-stratification is 1.65, indicating that these voids are not particularly continuous, possibly explaining the poor correlation between macroporosity and permeability. For two-dimensional data sets, a fractal dimension of (1) indicates a spatially continuous structure, a value of (2) indicates that the structure is not spatially continuous and more tortuous. Macroporosity is spatially correlated at an interval of 74 microns parallel to cross-stratification and at 70 microns normal to structure. The correlation length is even shorter than the measured, mean pore width of 116 microns, which is difficult to explain. The greater the correlation length for an investigated structure, the more continuous the entity is in space. It was expected that the correlation length between pores would closely approach the mean pore width of 116 microns. It appears that the interpore structure does not consistently repeat itself in a distinguishable pattern recognized by the spectral density function. The cause of the small correlation length is difficult to explain,

and may indicate that the method is flawed or that errors occurred in the data acquisition and results phases.

The mean fractal dimension between binarized images of matrix material (ferroan cements, allogenic and authigenic clay minerals) is lower than that for macroporosity, possibly explaining the stronger correlation between matrix material and permeability. There is no preferential direction of spatial correlation between matrix populations (mean fractal dimension parallel and normal to cross-stratification = 1.5), therefore, the system is assumed to be isotropic. Matrix material is spatially correlated at an interval of 125 microns parallel to structure and at 108 microns normal to structure, and appears to be more continuous spatially than the pore voids. This may explain why matrix material correlates better with measured permeability.

Application of the correlation length scale, the fractal dimension and the radial power spectra did not resolve the poor correlation expressed from modal analysis. The spatial continuity of both macroporosity and matrix material does not correlate well with laboratory measured permeability either (R = 0.53 and 0.64, respectively).

5.7. Reworking the Method

Specific analytical problems encountered in this investigation include issues that concern image rendering and acquisition, the application of two-dimensional textural and structural data to explain fluid movement in three-dimensions and the relationship between the measurement scale and the scale of heterogeneity.

There are several explanations for the lack of spatial correlations between measured permeability and image analysis data. First, operator error (difficulties

discerning between grain, matrix and pore margins), as well as limitations of the photomicrograph rendering and binarization process can create differences in the areal percentages of both macroporosity and total matrix material. Second, errors in the rendering process may have produced results that are not realistic or that have been compromised. Pixel based photomicrographs that are created for image based analysis represent an approximation of the continuous real scene selected for investigation. Because thresholding classifies each pixel as either part of the foreground or the background, there is only a certain level of accuracy that can be achieved during the rendering process. This is especially true, since human operators are usually not very good at setting threshold levels without bias (Russ, 1992). Thus, segmentation of gray scale images into regions for measurement (ROI's) is probably the most important single problem area while performing image analysis. In addition, correlations between any single pore parameter and individual reservoir properties, such as the permeability, tend to be rather poor (Clelland and Fens, 1991).

Alternative methods for acquiring quantitative descriptions of mineralogy, grain textures and pore structure in two-dimensions should be explored. The modal analysis and thin section rendering process used in this investigation are both tedious and time consuming. The ability to accurately render and binarize scanned thin sections in Adobe Photoshop® 5.0 is a challenging and labor intensive process, and may compromise the level of objectiveness needed for such and investigation. To increase the accuracy of data acquisition and to reduce the time required for analysis, several workers have employed alternative techniques to determine mineralogy, grain texture and pore structure from resin-impregnated and polished thin sections. Utilization of a scanning

126

electron microscope (SEM) equipped with an energy dispersive x-ray analyzer (EDX) and an integrated image processing system (IPS) is one such method (Clelland and Fens, 1991). Another approach is to integrate proton nuclear magnetic resonance (NMR) results with capillary pressure data taken from water saturated sandstones to more accurately determine pore and pore throat size distributions (Howard et al., 1993). A third approach is to incorporate mercury intrusion porosimetry (MIP) with image analysis to more accurately characterize the distribution of pore sizes in reservoir rocks (Abell et al., 1998).

The application of two-dimensional textural and pore structural data comprised from modal and image analysis to three-dimensional permeability data is an inherent problem. An investigation of pore connectivity, flow tortuosity pathways, pore throat architecture and the distribution of matrix and cements in three-dimensions in conjunction with measured permeability would produce more realistic controls on the actual permeability distribution in reservoir sands. Confocal scanning laser microscopy (CSLM) used in conjunction with two-dimensional image processing techniques may be employed to identify specific size distributions for pore bodies and pore throats in three-dimensions. This method uses image thresholding to reveal the pore volume structure to an approximate depth of 100 microns (Davidson et al., 1998).

Outcrop scale observations clearly show: 1) the different surface structures; 2) areas where hematite is prolific (particularly the first-order structure); and 3) areas that appear to incorporate more quartz cement and/or simply just clean quartz grains with little matrix (third-order structures). These same structures and differently cemented areas are also apparent in the rendered subsection images. In addition, the tip seals

127

reproduce, as revealed by the permeability field maps, the inherent erosional bounding surface and depositional, cross-stratification structures observed at the outcrop and pore scale (Appendix B). However, at the pore (thin section) and microscopic (scanning electron) scales, a paucity of statistically relevant mineralogical and textural heterogeneities between all three structures appears to exist (Appendix D).

5.8. Future Work

Comprehensive and detailed understanding of a sandstone's pore structure is a valuable tool used to identify geologic controls on porosity and permeability distributions. Various methods are used to investigate a reservoir rock's internal pore network. This thesis did not directly address the relationships between pore throats and permeability or the role of pore connectivity in two-dimensions as a primary control on measured permeability. High-pressure mercury injection porosimetry is one technique that could be employed to assess the influence that pore throats have in controlling the effective porosity and permeability of porous media.

Another viable method is to analyze the specific surface of a porous material. The specific surface is an expression of the fineness of pore voids; it is the ratio of the perimeter of pores to the cross-sectional area of porosity for a specified region of investigation (ROI). Various methods used to determine the specific surface are based on the adsorption of a gas by the internal surface of a porous medium. The larger the pores, the lower the specific surface. Both methods may be employed in the future to gain a greater understanding the relationship between porosity and permeability in two-dimensions.

The Kozeny-Carman theoretical model addresses possible correlations between porosity, the specific surface and pore area tortuosity with measured permeability values. Analysis by other workers has shown that permeability increases as the porosity increases and the specific surface and pore void tortuosity decreases (Ruzyla, 1986). Therefore, crossplots of porosity derived from image analysis and specific pore surface may be used to obtain a gross estimate of permeability in two-dimensions.

The MSP was created to investigate permeability upscaling in the laboratory. In this study, only the 0.15 r_i cm sample support was employed on billets prepared for thin section analysis. Yet, the 0.31 r_i cm and the 0.63 r_i cm tip seals were not employed to augment or support the measured data at the 0.15 r_i cm sample support. In the future, the permeability of each billet could be measured using the 0.31 r_i cm tip seal (two or three measurements per billet) and the 0.63 r_i cm tip seal (one or two measurements per billet) to determine which sample support depicts the true structure of the lithology and records the most accurate permeability.

CHAPTER 6: CONCLUSIONS

1. Pore-occluding matrix material, including; hematite, ferroan dolomite, kaolinite, illite, sericite and undifferentiated allogenic clays choke pore throats, heavily line pore walls, form bridges across open pores, coat and rim framework grains and fill intragranular fractures. Although a high degree of mechanical diagenesis is observed (concavo-convex and sutured framework grain contacts), the negative effects due to compaction on the overall porosity of the rock are overshadowed by the abundant early, middle and late-stage chemical diagenesis.

2. Petrographic and scanning electron analyses indicate that the principal diagenetic control on the permeability distribution is chemical diagenesis; in particular, the precipitation of ferroan cements (hematite and ferroan dolomite) and authigenic kaolinite, has significantly reduced permeability in the Massillon. Conversely, the development of late-stage, secondary intra- and intergranular macroporosity, as a result of grain and mineral dissolution and fracturing, significantly increased permeability.

3. First-order, erosional, bounding surface structures exhibit: a) the lowest mean permeability and point count and image analysis derived porosity values; b) the narrowest mean intergranular pore widths; c) the finest, mean framework grain sizes; d) the best overall, framework grain sorting; e) the highest, mean volume % of ferroan cements; f) the lowest, mean volume % of allogenic and authigenic clay minerals; and g) the lowest, mean volume % of authigenic quartz cement.

130

4. Second-order, erosional, bounding surface structures exhibit: a) the highest and lowest measured permeabilities for individual subsections; b) the coarsest framework grain sizes; c) the worst overall, framework grain sorting; d) the highest, mean volume % of matrix material including cements; and e) the highest, mean volume % of authigenic quartz overgrowth cement.

5. Third-order, depositional, cross-stratification structures exhibit: a) the highest mean permeability and point count and image analysis derived porosity values; b) the largest, mean intergranular pore widths; c) the lowest, mean volume % of matrix material including cements; and d) the highest, mean volume % of allogenic and authigenic clay minerals.

6. A comparison of the permeability fields and permeability plots created across the Face 7 cored transect reveal an overall increase in permeability within the low-angle, third-order cross-stratification structures.

7. A distinct 'smoothing' in the permeability data is observed across the Face 7 cored transect as the tip seal size increases.

8. The paucity of strong relationships between permeability and expected textural elements may, in part, be explained by the minor heterogeneities between mean grain sizes and the degree of grain sorting in each of the three sedimentary structures (i.e.,

131

the variation in grain size and sorting is too small to have caused significant porosity and permeability differences).

9. The positive correlation between permeability and matrix material for first and second-order structures are the best observed correlations. First and second-order structures exhibit stronger, positive correlations between permeability and total and intergranular, point count porosity compared to third-order structures. Intergranular macroporosity is the most prevalent porosity observed, principally created by the dissolution of framework grains, allogenic clays and authigenic minerals, and exhibits the second best positive correlation with permeability.

10. Sutured, detrital framework grains are prolific, an indication that this sandstone has undergone extensive compaction. Although the effects of mechanical compaction have decreased the original permeability of the sandstone, chemical diagenesis is a greater control on the effective pore network.

11. The structures and textures developed during deposition together with the multiple-stage secondary, diagenetic alterations of mineral precipitation and dissolution created the present, intricate pore architecture while controlling flow through the pore network. This tortuous pore structure along with the numerous alteration processes could very well explain the correlation problems observed between expected controls on subsurface fluid flow and laboratory measured permeability.

132

12. Image analysis reveals that large, oversized, intergranular and intragranular pores are predominately isolated features, whereas thinner lenses of dissolved clays and ferroan cements between the predominant quartz grains are more continuous lineaments.

13. The spatial continuity of both macroporosity and matrix material does not correlate well with laboratory measured permeability. The mean fractal dimension of matrix material is lower than that for macroporosity, possibly explaining the stronger correlation between matrix and permeability. Application of the radial spectra does not resolve the poor correlations between permeability and the expected or observed, primary and secondary controls investigated using modal analysis or the other image analysis models.

14. Operator error, in particular, difficulties differentiating between grains, matrix and pore margins, as well as limitations of the photomicrograph rendering and binarization process, most likely resulted in significant errors in the analysis.

15. Weak positive relationships between measured permeability and observed and expected primary, secondary and spatial controls reveal the complexity of diagenetic alterations affecting the sandstone and the inadequacy of relating two-dimensional modal and image analysis to three-dimensional permeability data.

APPENDIX A: Descriptions of three fining upwards geologic systems: 1) the Fire Island Inlet Sequence; 2) the Battery Point Sequence; and 3) the Old Red Sandstone Sequence, used as comparators to determine the Massillon Sandstone's depositional environment.

<u>The Fire Island Inlet Sequence</u>

The Fire Island Inlet Sequence is an overlap type of tidal inlet found off the coast of New York. Tidal inlets are corridors between barrier islands that permit tidal exchanges between the open ocean and brackish bays, lagoons and tidal marshes lying behind the islands (McCubbin, 1982). It is a modern example of a mesotidal channel deposit (2-4 m tidal range) and consists of five major units: 1) a channel floor; 2) a deep channel; 3) a shallow channel; 4) a channel margin platform; and 5) a spit beachface and spit berm. The conglomeratic channel floor is a gravel lag of large shells, shell hash and quartz pebbles. The deep channel deposits are characterized by high angle, ebb oriented, tabular and planar cross stratification. Reactivation surfaces formed by the erosional effects of flood oriented tidal currents. The channel margin or spit platform is characterized by small and large scale trough cross bedding at the top, high angle, longshore dipping strata in the middle and ebb oriented, planar-tabular and trough cross stratification below. The spit beachface and spit berm are characterized by sub-horizontal to low angle stratification (McCubbin, 1982, modified from Kumar and Sanders, 1974). Overall, this tidal sequence fines upward, although all facies, except the channel floor (gravel lag), are predominately composed of medium sand.

Three characteristics of the Fire Island Sequence are important in comparison to the Massillon Sequence. First, both sequences have a conglomeritic base, however, the compositions are very different; quartz pebbles and shells are prevalent in the Fire Island sequence, whereas coalspars and iron nodules are components of the Massillon Sequence.

Although large shells and shell hash are not observed in the Massillon, nonpreservation of marine tests may be explained by dissolution due to acidic or chilled meteoric waters. Secondly, the Ripple Coset Facies, the two Clayshale Facies and the sequence topping coal are not associated with the tidal inlet sequence. Thirdly, bi-directional and multidirectional crossbeds are diagnostic features of the tidal inlet sequence. The trough structures in the Massillon are observed to be unidirectional, not bi-directional. Therefore, the Massillon was most likely not wholly deposited in a tidal inlet.

The Battery Point Sequence

The Devonian Battery Point Sandstone, Quebec, is interpreted as a distal braided stream deposit. It resembles Miall's (1977) Donjek Sequence, a model consisting of fining upward cycles of variable scale reflecting deposition in braided rivers with mixed bedloads of sand and gravel. In this sequence, sedimentation occurs within channels or where channel aggradation is followed by channel shifting (Boggs, 1995). Distal braided stream sequences commonly consist of, from the base to the top, a sharp based, trough cross-stratified conglomerate, trough cross-stratified sand, mudshales and clayshales. Although this fining upward sequence is quite common, Miall's (1977) Scott Type and Bijou Creek Type braided river depositional profiles exhibit a paucity of fining or coarsening upward trends.

The Battery Point Sequence consists of eight major facies: 1) a scoured surface; 2) a poorly defined trough facies; 3) a well defined trough facies; 4) a planar-tabular crossbedded facies; 5) an asymmetric scour facies; 6) a small tabular facies; 7) a rippled mudstone and sandstone facies; and 8) a low angle stratified sandstone facies. This

136

sequence is believed to result from bar advance, sand flat formation and channel aggradation in a braided river (Cant, 1982). The conglomerates at the base of the Battery Point and Massillon Sandstones are similar, yet there are no coalspars, iron nodules or plant fossils in any of the Battery Point Facies. The large-scale trough and tabular beds are quite similar, yet the Massillon has an abundance of horizontal laminations associated with the bases of each bed, whereas the Battery Point basal contacts are more trough like. The small scale planar-tabular crossbeds at the top of the sandier portion of the Battery Point are most likely formed from the migration of two-dimensional sand waves, whereas, the Massillon Sandstone portion is topped by distinct ripples or troughs. The Massillon Sandstone is thus interpreted to be the end result of the migration of three-dimensional sand waves. Therefore, the Massillon may not have been deposited in a strictly braided stream complex.

The Old Red Sandstone Sequence

The Devonian Old Red Sandstone of Great Britain and Appalachia is a classic example of a meandering fluvial system. Lateral river migration deposited a fining upward sequence of lag gravel and intraclast conglomerate at the base, to trough crossbedded to parallel laminated sands, then finer rippled sands and finally overbank muds to create the Old Red Sequence (Cant, 1982). There are six major lithofacies associated with the Old Red Sandstone assemblage: 1) the conglomerate facies; 2) a cross-bedded sandstone facies; 3) a flat-bedded sandstone facies; 4) a cross-laminated sandstone facies; 5) an alternating bed facies; and 6) a siltstone facies. Similar features contained within the Massillon Sequence are the conglomerate base, the planar beds, the

137

trough crossbeds and the vertical accretionary deposits. The major differences are that the Old Red Sandstone has thinner intrachannel deposits and an overall decrease in sandstone thickness. The thinner intrachannel deposits may be due to a smaller main channel or more uniform flow conditions. The decrease in structural thickness is most probably due to a shift to a lower energy system or decreasing flow strength upward in the section.

APPENDIX B: Two-dimensional, natural log permeability field maps generated directly from Face 7 using tip seals with inner radii (r_i) of 0.15 cm, 0.31 cm, 0.63 cm, 1.27cm and 2.54 cm.

Ohio Sandstone; Face 7; 0.15 cm Tip Seal

X (cm)

Y (cm)

ln (k)
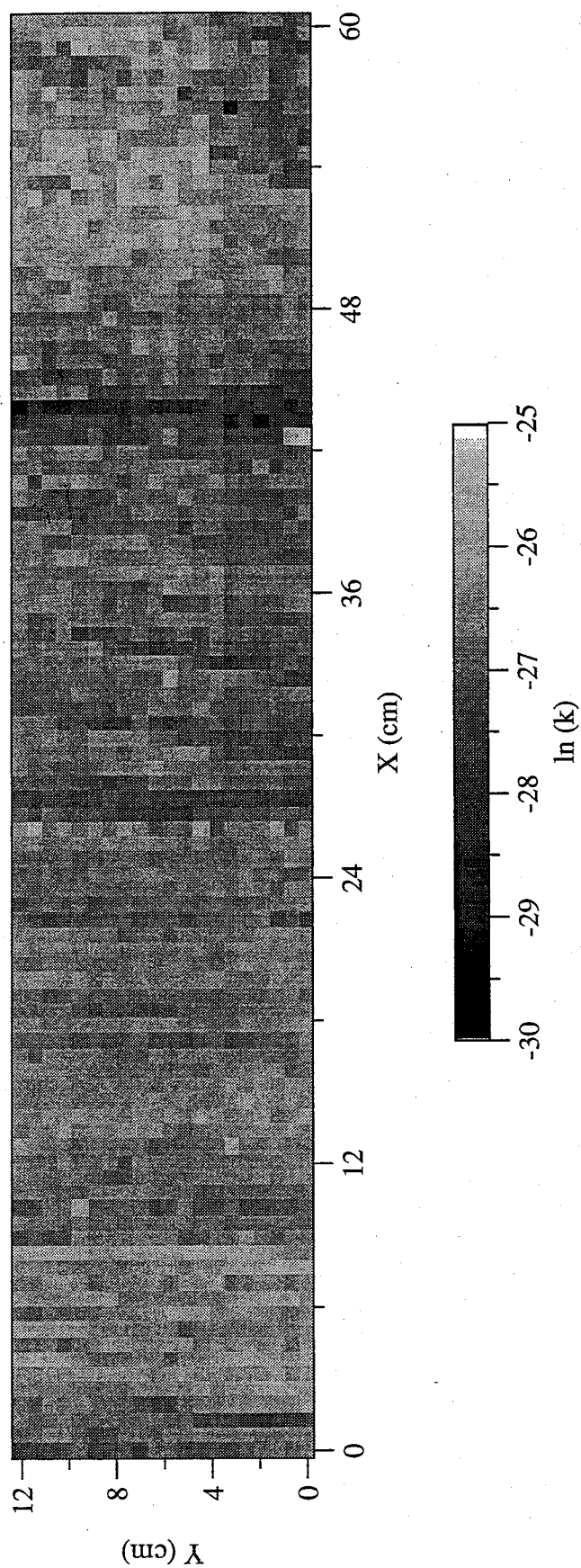
Ohio Sandstone; Face 7; 0.31cm Tip Seal

X (cm)

Y (cm)

ln (k)
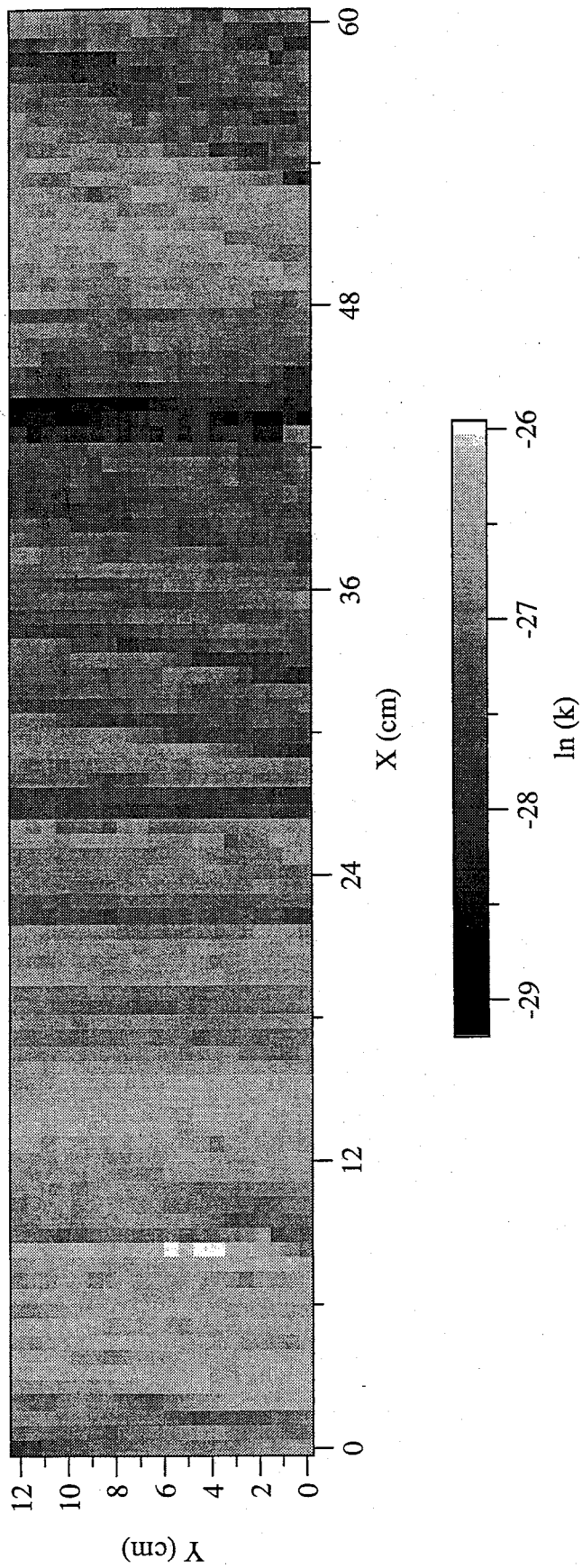
Ohio Sandstone; Face 7; 0.63 cm Tip Seal
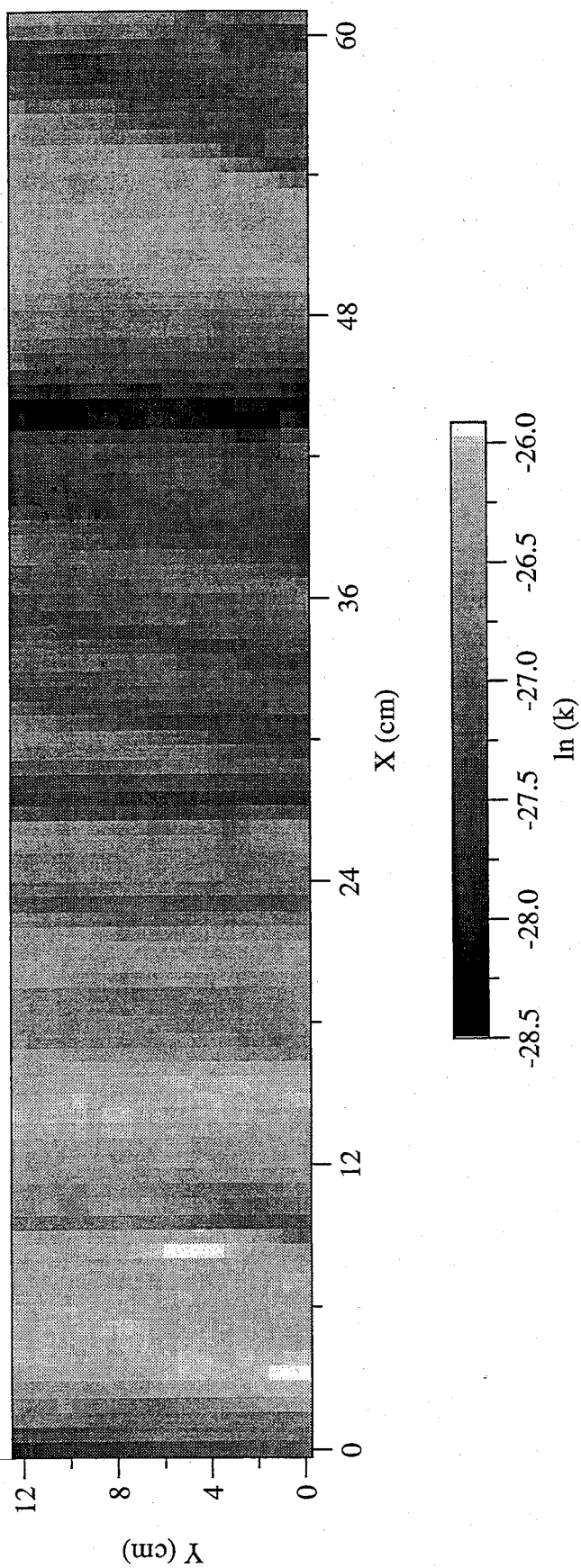
Ohio Sandstone; Face 7; 1.27 cm Tip Seal

X (cm)

Y (cm)

ln (k)

-27.5 -27.0 -26.5 -26.0

143
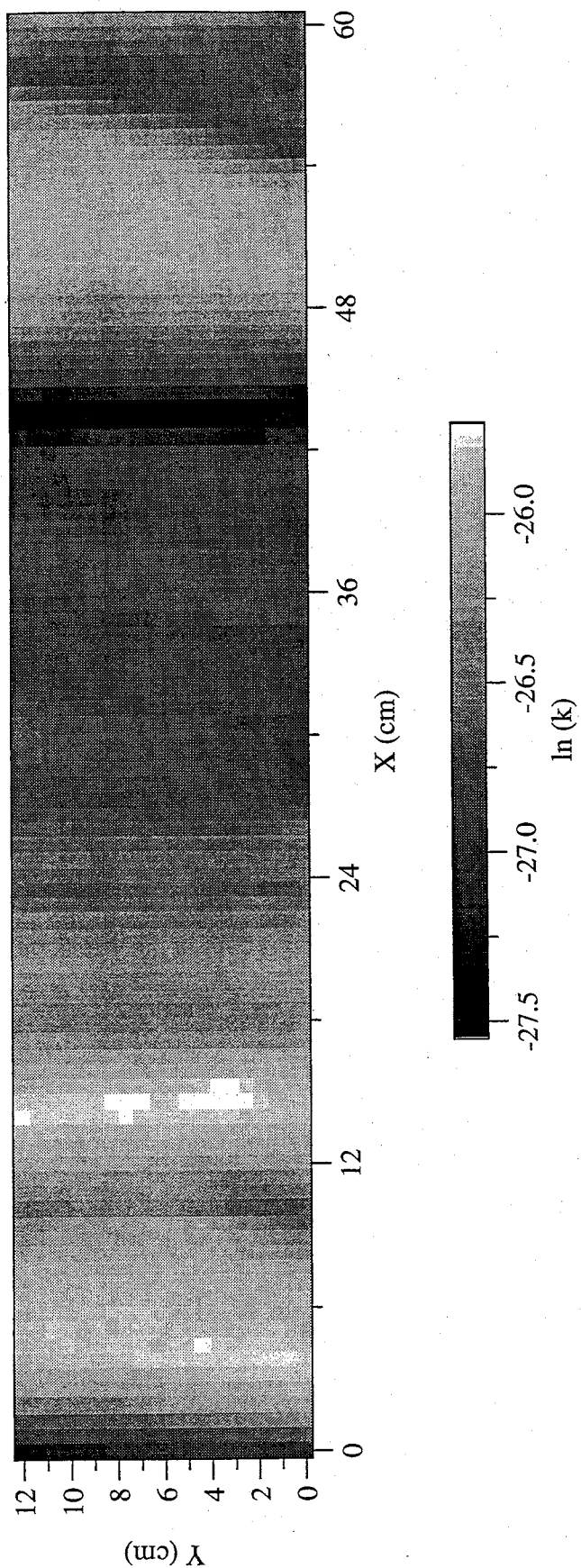
Ohio Sandstone; Face 7; 2.54 cm Tip Seal

X (cm)

Y (cm)

ln (k)

-25.75
-26.00
-26.25
-26.50
-26.75
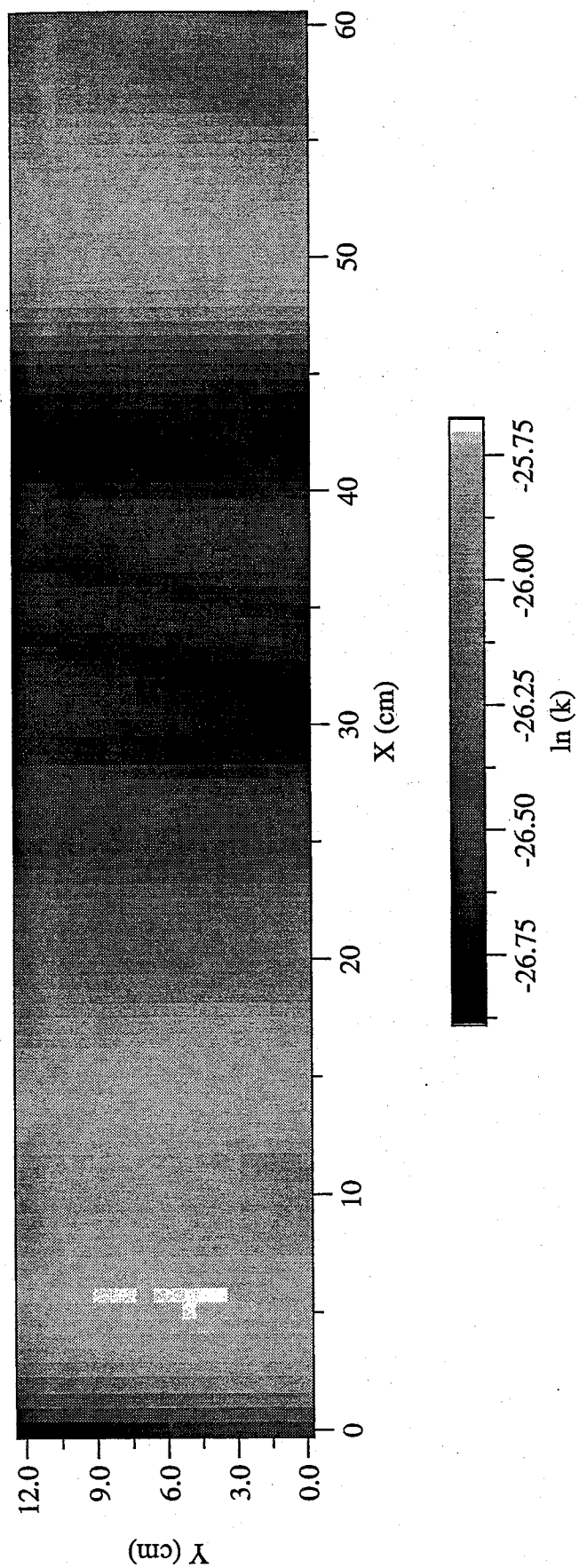
APPENDIX C: A petrographic index of nomenclature used during modal analysis and a summary table of petrographic elements observed in the Massillon Sandstone Formation, including: 1) permeability; 2) porosity; 3) mineralogy; and 4) textural data.

Sub-Section Nomenclature
Example for subsection 7B3z.1:

       7 – sample taken from Face 7 of the Massillon Sandstone Block.

       B – sample taken from core B (A-O).

       3 – sample is from a third-order structure (1st, 2nd or 3rd).

       z – sample is oriented normal to cross-stratification (x - oriented parallel to cross-stratification).

       1 – sample is from thin section subsection 1 (1-6).

Framework Grains and Components
Qm	monocrystalline quartz
Qp	polycrystalline quartz
Qrm	recrystallized metamorphic quartz (defined by triple junction contacts)
Qsm	stretched metamorphic quartz
Qv	vein quartz (contains vacuoles)
Flu	undifferentiated feldspar
Kf	potassium feldspar
Mc	microcline
Pl	plagioclase
Fs	sericitized feldspar
Lu	undifferentiated, fine-grained, silicic lithic
Ls	siltstone lithic
Lc	claystone lithic
Lps	metamorphic, phyllitic/schistosic lithic
Ch	chert and chalcedony
Mv	muscovite
Bt	biotite
Zr	zircon
Hb	hornblende

Non-Framework Components
Fe	ferroan cement (hematite and ferroan dolomite)
Rh	ferroan dolomite
Rd	partially dissolved ferroan dolomite
Py	pyrite
QOC	authigenic quartz
Kao	authigenic kaolinite
Kv	authigenic vermicular kaolinite
Clv	authigenic vermicular chlorite
Cpl	undifferentiated allogenic and authigenic pore lining clay
Cpf	undifferentiated allogenic and authigenic pore filling clay

Macroporosity
Intergranular Primary
Intergranular Secondary
Intergranular Fracture
Intragranular Grain
Intragranular Clay Mineral
Intragranular Matrix Material
Intragranular Cement

Microporosity
Intragranular Grain
Intragranular Clay Mineral
Intragranular Matrix Material
Intragranular Cement

Miscellaneous
WRM	whole rock mean
1OBS	first-order bounding structure
2OBS	second-order bounding structure
3OBS	third-order cross-stratification structure
PC	point count
IA	image analysis
QFL	quartz: feldspar: lithic fragment
MGS	mean grain size
MPW	mean pore width
IGSD	inclusive graphic standard deviation
Pi	original porosity
COPL	porosity loss due to compaction
CEPL	porosity loss due to cementation
IGV	intergranular volume
*	as a function of intergranular volume
**	as a function of matrix material and cements

Sub-Section	Permeability	Ln Permeability	Permeability	Permeability	Porosity [point count]	Porosity [image analysis]	Monocrystalline Quartz [Qm]	Mean Length [Qm]	Polycrystalline Quartz [Qp]	Mean Length [Qtz]
	m^2	m^2	darcies	mdarcies	%	%	%	mm	%	mm
7B3z.1	1.031E-12	-27.6002	1.045	1045	14.50	9.40	47.50	0.49	9.00	0.47
7B3z.2	2.08E-12	-26.9003	2.107	2107	15.25	11.99	45.75	0.51	10.25	0.49
7B3z.3	7.72E-13	-27.8892	0.782	782	27.00	20.65	40.25	0.54	12.00	0.53
7B3z.4	8.93E-13	-27.744	0.904	904	17.75	11.56	42.50	0.55	12.50	0.53
7B3z.5	1.13E-12	-27.5095	1.145	1145	21.50	23.16	47.00	0.49	10.50	0.52
7B3z.6	3.24E-13	-28.7577	0.328	328	19.50	16.77	45.50	0.51	11.25	0.54
Mean [B3z]	1.03833E-12	-27.7334833	1.051833	1051.833	19.25	15.59	44.75	0.52	10.92	0.51
7D3z.1	3.34E-12	-26.4236	3.384	3384	20.75	17.29	49.00	0.51	11.50	0.61
7D3z.2	3.39E-12	-26.4111	3.435	3435	17.75	16.24	48.00	0.55	11.25	0.61
7D3z.3	3.27E-12	-26.4461	3.313	3313	14.50	17.27	45.25	0.50	12.25	0.58
7D3z.4	2.64E-12	-26.6599	2.675	2675	18.25	16.29	44.25	0.51	15.00	57.60
7D3z.5	4.21E-12	-26.1939	4.265	4265	23.50	20.44	39.75	0.51	11.75	0.52
7D3z.6	2.98E-12	-26.5398	3.019	3019	17.00	16.85	46.75	0.55	13.25	0.59
Mean [D3z]	3.305E-12	-26.4457333	3.3485	3348.5	18.63	17.40	45.50	0.52	12.50	10.09
7E3z.1	1.22E-12	-27.4317	1.236	1236	12.00	11.66	42.25	0.49	15.25	0.51
7E3z.2	9.45E-13	-27.6874	0.957	957	12.00	10.46	47.50	0.50	11.00	0.52
7E3z.3	1.12E-12	-27.5172	1.135	1135	18.00	13.11	45.25	0.51	13.00	0.56
7E3z.4	9.46E-13	-27.6868	0.958	958	14.00	13.68	44.00	0.50	13.50	0.51
7E3z.5	2.22E-12	-26.832	2.249	2249	17.75	14.04	48.00	0.51	10.75	0.55
7E3z.6	1.44E-12	-27.263	1.459	1459	19.50	15.93	39.50	0.49	14.50	0.55
Mean [E3z]	1.31517E-12	-27.4030167	1.332333	1332.333	15.54	13.15	44.42	0.50	13.00	0.53
7F3z.1	7.91E-13	-27.8659	0.801	801	16.25	7.81	47.75	0.43	9.50	0.47
7F3z.2	6.97E-13	-27.9925	0.706	706	13.75	8.21	43.50	0.42	12.75	0.47
7F3z.3	7.8E-13	-27.8797	0.79	790	12.75	9.75	47.50	0.43	12.50	0.46
7F3z.4	1.02E-12	-27.6124	1.033	1033	18.75	12.94	44.00	0.49	10.50	0.52
7F3z.5	1.2E-12	-27.4466	1.216	1216	13.25	11.21	46.50	0.45	15.50	0.44
7F3z.6	1.98E-12	-26.9504	2.006	2006	16.25	11.85	39.75	0.47	15.75	0.51
Mean [F3z]	1.078E-12	-27.6245833	1.092	1092	15.17	10.30	44.83	0.45	12.75	0.48

148

Sub-Section	Permeability	Ln Permeability	Permeability	Permeability	Porosity [point count]	Porosity [image analysis]	Monocrystalline Quartz [Qm]	Mean Length [Qm]	Polycrystalline Quartz [Qp]	Mean Length [Qtz]
	m^2	m^2	darcies	mdarcies	%	%	%	mm	%	mm
7H3z.1	2.73E-12	-26.6286	2.766	2766	20.25	16.10	41.25	0.46	14.25	0.50
7H3z.2	2.13E-12	-26.8771	2.158	2158	26.00	22.41	43.75	0.44	9.50	0.43
7H3z.s	1.7E-12	-27.1013	1.722	1722	22.00	18.12	41.75	0.44	16.00	0.44
7H3z.4	1.7E-12	-27.0991	1.722	1722	15.00	16.19	49.00	0.47	13.00	0.46
7H3z.5	1.68E-12	-27.1127	1.702	1702	22.75	23.13	42.75	0.44	11.00	0.45
7H3z.6	9.31E-13	-27.702	0.949	949	20.50	20.11	47.00	0.42	9.75	0.45
Mean [H3z]	1.81183E-12	-27.0868	1.8365	1836.5	21.08	19.34	44.25	0.45	12.25	0.46
7I3z.1	6.2E-13	-28.1085	0.628	628	13.25	10.07	50.25	0.42	8.25	0.41
7I3z.2	1.37E-12	-27.3136	1.388	1388	14.25	11.15	47.00	0.42	8.25	0.46
7I3z.3	4.68E-12	-26.0883	4.742	4742	18.75	12.69	46.00	0.44	12.25	0.48
7I3z.4	7.1E-13	-27.9738	0.719	719	12.25	10.06	48.50	0.46	11.25	0.52
7I3z.5	7.77E-13	-27.8835	0.787	787	15.00	9.36	44.25	0.43	11.25	0.45
7I3z.6	N/A	N/A	N/A	N/A	14.00	22.50	46.75	0.40	10.75	0.45
Mean [I3z]	1.6314E-12	-27.47354	1.6528	1652.8	14.58	12.64	47.13	0.43	10.33	0.46
7I3x.1	1.89E-12	-26.994	1.915	1915	14.50	13.10	47.75	0.46	14.50	0.50
7I3x.2	1.23E-12	-27.4205	1.246	1246	14.75	13.87	50.75	0.47	11.25	0.53
Mean [I3x]	1.56E-12	-27.20725	1.5805	1580.5	14.63	13.49	49.25	0.47	12.88	0.52
7J3z.1	2.75E-12	-26.621	2.786	2786	17.25	12.32	46.00	0.45	10.25	0.48
7J3z.2	2.94E-12	-26.552	2.979	2979	17.50	12.90	44.00	0.43	12.25	0.46
7J3z.3	2.08E-12	-26.8971	2.107	2107	14.75	11.45	47.50	0.41	9.75	0.47
7J3z.4	1.64E-12	-27.1396	1.662	1662	14.75	10.85	47.25	0.46	12.50	0.45
7J3z.5	3.02E-12	-26.5269	3.06	3060	16.00	14.38	48.25	0.46	13.00	0.51
7J3z.6	2.66E-12	-26.653	2.695	2695	15.75	15.09	49.75	0.48	12.00	0.45
Mean [J3z]	2.515E-12	-26.7316	2.548167	2548.167	16.00	12.83	47.13	0.45	11.63	0.47
7K3z.1	2.08E-12	-26.8979	2.107	2107	17.75	14.94	45.75	0.46	10.50	0.46
7K3z.2	2.35E-12	-26.7748	2.381	2381	16.25	15.54	42.25	0.45	15.00	0.48
7K3z.3	2.28E-12	-26.8071	2.31	2310	13.00	14.35	53.25	0.44	11.75	0.42
7K3z.4	2.32E-12	-26.7913	2.351	2351	16.25	15.76	48.00	0.45	9.50	0.49
7K3z.5	2.02E-12	-26.9281	2.047	2047	14.25	14.48	46.00	0.44	13.50	0.46

149

Sub-Section	Permeability	Ln Permeability	Permeability	Permeability	Porosity [point count]	Porosity [image analysis]	Monocrystalline Quartz [Qm]	Mean Length [Qm]	Polycrystalline Quartz [Qp]	Mean Length [Qtz]
	m^2	m^2	darcies	mdarcies	%	%	%	mm	%	mm
7K3z.6	1.85E-12	-27.0133	1.874	1874	19.50	16.02	43.00	0.45	8.75	0.45
Mean [K3z]	2.15E-12	-26.86875	2.178333	2178.333	16.17	15.18	46.38	0.45	11.50	0.46
7M3z.1	2.12E-12	-26.8816	2.148	2148	19.75	15.50	46.25	0.47	9.25	0.53
7M3z.2	1.73E-12	-27.0854	1.753	1753	14.25	13.47	48.00	0.47	13.00	0.46
7M3z.3	1.5E-12	-27.2269	1.52	1520	14.50	11.89	45.25	0.45	12.00	0.50
7M3z.4	1.95E-12	-26.9618	1.976	1976	11.00	13.43	48.50	0.45	14.00	0.47
7M3z.5	1.87E-12	-27.0073	1.895	1895	15.00	13.16	47.25	0.46	12.00	0.48
7M3z.6	1.73E-12	-27.0853	1.753	1753	14.50	13.33	50.75	0.47	15.25	0.50
Mean [M3z]	1.81667E-12	-27.0413833	1.840833	1840.833	14.83	13.46	47.67	0.46	12.58	0.49
7N3z.1	5.78E-12	-25.8765	5.856	5856	26.25	20.23	43.25	0.55	11.25	0.58
7N3z.2	2.41E-12	-26.7522	2.442	2442	22.50	18.93	47.00	0.51	13.50	0.60
7N3z.3	4.56E-12	-26.113	4.62	4620	24.25	20.14	44.50	0.51	10.75	0.55
7N3z.4	4.99E-12	-26.0227	5.056	5056	22.50	18.73	44.50	0.52	13.00	0.53
7N3z.5	3.16E-12	-26.4793	3.202	3202	22.00	19.04	49.00	0.50	9.75	0.55
7N3z.6	4.48E-12	-26.1306	4.539	4539	24.75	17.41	42.00	0.53	13.25	0.60
Mean [N3z]	4.23E-12	-26.22905	4.285833	4285.833	23.71	19.08	45.04	0.52	11.92	0.57
7O3z.1	8.63E-13	-27.7786	0.874	874	14.00	17.12	54.00	0.58	10.25	0.69
7O3z.2	1.95E-12	-26.9623	1.976	1976	16.00	15.43	49.50	0.56	14.75	0.64
7O3z.3	4.12E-12	-26.2145	4.174	4174	19.00	18.98	49.00	0.51	11.75	0.55
7O3z.4	2.29E-12	-26.8027	2.32	2320	17.75	20.33	48.25	0.53	12.25	0.64
7O3z.5	9.22E-12	-27.7119	9.341	9341	21.00	14.63	47.25	0.60	11.25	0.70
7O3z.6	1.67E-12	-27.1172	1.692	1692	21.75	13.91	42.75	0.61	14.00	0.65
Mean [O3z]	3.35217E-12	-27.0978667	3.396167	3396.167	18.25	16.73	48.46	0.57	12.38	0.65
7O3x.1	3.44E-12	-26.3941	3.485	3485	16.75	17.28	49.00	0.56	12.00	0.59
7O3x.2	4.44E-12	-26.1401	4.498	4498	18.75	16.59	52.50	0.54	10.75	0.59
Mean [O3x]	3.94E-12	-26.2671	3.9915	3991.5	17.75	16.94	50.75	0.55	11.38	0.59
Mean [3OBS]	2.21E-12	-26.65557	2.24101	2241.01	17.49	15.07	46.19	0.48	11.99	1.33

150

Sub-Section	Permeability	Ln Permeability	Permeability	Permeability	Porosity [point count]	Porosity [image analysis]	Monocrystalline Quartz [Qm]	Mean Length [Qm]	Polycrystalline Quartz [Qp]	Mean Length [Qtz]
	m^2	m^2	darcies	mdarcies	%	%	%	mm	%	mm
7K3z.6	1.85E-12	-27.0133	1.874	1874	19.50	16.02	43.00	0.45	8.75	0.45
Mean [K3z]	2.15E-12	-26.86875	2.178333	2178.333	16.17	15.18	46.38	0.45	11.50	0.46
7M3z.1	2.12E-12	-26.8816	2.148	2148	19.75	15.50	46.25	0.47	9.25	0.53
7M3z.2	1.73E-12	-27.0854	1.753	1753	14.25	13.47	48.00	0.47	13.00	0.46
7M3z.3	1.5E-12	-27.2269	1.52	1520	14.50	11.89	45.25	0.45	12.00	0.50
7M3z.4	1.95E-12	-26.9618	1.976	1976	11.00	13.43	48.50	0.45	14.00	0.47
7M3z.5	1.87E-12	-27.0073	1.895	1895	15.00	13.16	47.25	0.46	12.00	0.48
7M3z.6	1.73E-12	-27.0853	1.753	1753	14.50	13.33	50.75	0.47	15.25	0.50
Mean [M3z]	1.81667E-12	-27.0413833	1.840833	1840.833	14.83	13.46	47.67	0.46	12.58	0.49
7N3z.1	5.78E-12	-25.8765	5.856	5856	26.25	20.23	43.25	0.55	11.25	0.58
7N3z.2	2.41E-12	-26.7522	2.442	2442	22.50	18.93	47.00	0.51	13.50	0.60
7N3z.3	4.56E-12	-26.113	4.62	4620	24.25	20.14	44.50	0.51	10.75	0.55
7N3z.4	4.99E-12	-26.0227	5.056	5056	22.50	18.73	44.50	0.52	13.00	0.53
7N3z.5	3.16E-12	-26.4793	3.202	3202	22.00	19.04	49.00	0.50	9.75	0.55
7N3z.6	4.48E-12	-26.1306	4.539	4539	24.75	17.41	42.00	0.53	13.25	0.60
Mean [N3z]	4.23E-12	-26.22905	4.285833	4285.833	23.71	19.08	45.04	0.52	11.92	0.57
7O3z.1	8.63E-13	-27.7786	0.874	874	14.00	17.12	54.00	0.58	10.25	0.69
7O3z.2	1.95E-12	-26.9623	1.976	1976	16.00	15.43	49.50	0.56	14.75	0.64
7O3z.3	4.12E-12	-26.2145	4.174	4174	19.00	18.98	49.00	0.51	11.75	0.55
7O3z.4	2.29E-12	-26.8027	2.32	2320	17.75	20.33	48.25	0.53	12.25	0.64
7O3z.5	9.22E-12	-27.7119	9.341	9341	21.00	14.63	47.25	0.60	11.25	0.70
7O3z.6	1.67E-12	-27.1172	1.692	1692	21.75	13.91	42.75	0.61	14.00	0.65
Mean [O3z]	3.35217E-12	-27.0978667	3.396167	3396.167	18.25	16.73	48.46	0.57	12.38	0.65
7O3x.1	3.44E-12	-26.3941	3.485	3485	16.75	17.28	49.00	0.56	12.00	0.59
7O3x.2	4.44E-12	-26.1401	4.498	4498	18.75	16.59	52.50	0.54	10.75	0.59
Mean [O3x]	3.94E-12	-26.2671	3.9915	3991.5	17.75	16.94	50.75	0.55	11.38	0.59
Mean [3OBS]	2.21E-12	-26.65557	2.24101	2241.01	17.49	15.07	46.19	0.48	11.99	1.33

Sub-Section	Permeability	Ln Permeability	Permeability	Permeability	Porosity [point count]	Porosity [image analysis]	Monocrystalline Quartz [Qm]	Mean Length [Qm]	Polycrystalline Quartz [Qp]	Mean Length [Qtz]
	m^2	m^2	darcies	mdarcies	%	%	%	mm	%	mm
7A2z.1	5.98E-13	-28.1454	0.606	606	17.00	9.55	38.25	0.46	13.00	0.54
7A2z.2	1.39E-13	-29.607	0.141	141	11.25	6.18	45.00	0.38	10.75	0.44
7A2z.3	2.39E-13	-29.0608	0.242	242	13.25	6.57	42.75	0.40	13.00	0.45
7A2z.4	3.1E-13	-28.8018	0.314	314	12.75	12.36	44.00	0.51	9.25	0.64
7A2z.5	2.7E-13	-28.94	0.274	274	13.50	9.13	41.75	0.51	9.50	0.53
7A2z.6	1.46E-13	-29.557	0.148	148	13.25	5.69	39.50	0.44	10.00	0.53
Mean [A2z]	2.83667E-13	-29.0186667	0.2875	287.5	13.50	8.25	41.88	0.45	10.92	0.52
7C2z.1	2.17E-12	-26.854	2.199	2199	17.50	12.79	41.00	0.63	11.50	0.60
7C2z.2	2.65E-12	-26.657	2.685	2685	19.00	22.93	43.25	0.63	12.00	0.67
7C2z.3	1.67E-12	-27.1167	1.692	1692	14.25	10.19	46.75	0.60	11.50	0.66
7C2z.4	6.75E-12	-25.7213	6.839	6839	19.00	16.21	42.50	0.69	11.75	0.64
7C2z.5	1.41E-12	-27.2886	1.429	1429	19.75	16.52	36.00	0.62	13.50	0.66
7C2z.6	2.94E-12	-26.5526	3.009	3009	19.50	15.01	36.00	0.60	10.75	0.59
Mean [C2z]	2.93167E-12	-26.6983667	2.9755	2975.5	18.17	15.61	40.92	0.63	11.83	0.64
7C2x.1	5.25E-12	-25.9723	5.319	5319	23.75	22.54	49.00	0.55	11.25	0.59
7C2x.2	6.5E-12	-25.7599	6.586	6586	18.75	22.74	46.50	0.55	13.75	0.60
Mean [C2x]	5.875E-12	-25.8661	5.9525	5952.5	21.25	22.64	47.75	0.55	12.50	0.60
7L2z.1	1.18E-12	-27.4626	1.196	1196	12.50	9.09	49.00	0.42	11.00	0.46
7L2z.2	9.23E-13	-27.7115	0.935	935	14.75	9.49	50.00	0.42	8.50	0.48
7L2z.3	6.65E-13	-28.0385	0.674	674	13.00	10.25	45.75	0.44	14.00	0.45
7L2z.4	9.16E-13	-27.7182	0.928	928	8.50	5.88	40.75	0.40	7.75	0.45
7L2z.5	1.48E-12	-27.2388	1.499	1499	7.75	5.01	52.50	0.41	10.50	0.42
7L2z.6	8.84E-13	-27.7548	0.896	896	7.75	8.16	45.75	0.43	14.00	0.42
Mean [L2z]	1.008E-12	-27.6540667	1.021333	1021.333	10.71	7.98	47.29	0.42	10.96	0.45
7L2x.1	1.09E-12	-27.543	1.104	1104	19.00	15.24	46.75	0.51	10.50	0.53
7L2x.2	1.27E-12	-27.3892	1.287	1287	14.25	15.47	45.00	0.49	14.25	0.54
Mean [L2x]	1.18E-12	-27.4661	1.1955	1195.5	16.63	15.36	45.88	0.50	12.38	0.54
Mean [2OBS]	1.79E-12	-27.58595	1.81827	1818.27	15.00	12.14	43.99	0.50	11.45	0.54

Sub-Section	Permeability	Ln Permeability	Permeability	Permeability	Porosity [point count]	Porosity [image analysis]	Monocrystalline Quartz [Qm]	Mean Length [Qm]	Polycrystalline Quartz [Qp]	Mean Length [Qtz]
	m^2	m^2	darcies	mdarcies	%	%	%	mm	%	mm
7G1z.1	5.16E-13	-28.2928	0.523	523	6.00	4.39	49.75	0.44	10.25	0.46
7G1z.2	2.6E-13	-28.979	0.263	263	8.75	5.69	48.00	0.43	9.50	0.43
7G1z.3	4.16E-13	-28.5091	0.421	421	8.00	5.86	52.75	0.43	8.50	0.43
7G1z.4	9.8E-13	-27.6513	0.993	993	11.75	10.05	53.75	0.44	12.50	0.49
7G1z.5	1.68E-12	-27.1139	1.702	1702	15.50	8.78	49.75	0.46	12.00	0.49
7G1z.6	1.29E-12	-27.3767	1.307	1307	19.00	13.43	50.25	0.46	11.00	0.47
Mean [G1z]	8.57E-13	-27.9871333	0.868167	868.1667	11.50	8.03	50.71	0.44	10.63	0.46
7G1x.1	1.86E-12	-27.0115	1.884	1884	13.50	4.43	51.00	0.47	10.00	0.45
7G1x.2	7.07E-13	-27.9771	0.716	716	10.75	8.71	51.00	0.45	11.00	0.48
Mean [G1x]	1.2835E-12	-27.4943	1.3	1300	12.13	6.57	51.00	0.46	10.50	0.47
Mean [1OBS]	9.64E-13	-27.86393	0.97613	976.125	11.66	7.67	50.78	0.45	10.59	0.46
WRM	2.04E-12	-27.22922	2.06749	2067.49	16.47	13.83	46.07	0.49	11.76	1.09

152

Sub-Section	Quartz Component [Qtz]	Feldspar Component [Flu]	Mean Length [Flu]	Lithic Component [Lith]	Accessory Minerals	Intergranular Volume [IGV]	Matrix Material and Cements	Framework Detrital Grains	Framework Detrital Grains	QFL Grains	Quartz [QFL]
	%	%	mm	%	%	%	%	%	total	total	%
7B3z.1	56.50	1.00	0.42	3.25	1.00	34.50	23.75	61.75	247.00	243.00	93.00
7B3z.2	56.00	1.75	0.48	1.75	1.00	34.50	24.25	60.50	242.00	238.00	94.00
7B3z.3	52.25	0.75	0.55	1.75	0.00	40.50	18.25	54.75	219.00	219.00	96.00
7B3z.4	55.00	0.50	0.37	3.00	0.50	36.00	23.25	59.00	236.00	234.00	94.00
7B3z.5	57.50	0.75	0.47	2.75	0.25	35.25	17.50	61.00	244.00	243.00	94.00
7B3z.6	56.75	0.50	0.48	1.00	0.50	33.00	19.00	61.50	246.00	244.00	93.00
Mean [B3z]	55.67	0.88	0.46	2.25	0.54	35.63	21.00	59.75	239.00	236.83	94.00
7D3z.1	60.50	2.25	0.50	2.25	0.00	32.00	14.25	65.00	260.00	260.00	92.00
7D3z.2	59.25	2.50	0.63	2.25	0.00	33.00	18.50	63.75	255.00	255.00	93.00
7D3z.3	57.50	3.25	0.51	2.50	0.00	35.00	22.50	63.00	252.00	252.00	91.00
7D3z.4	59.25	1.50	0.44	2.25	0.00	33.50	18.75	63.00	252.00	252.00	94.00
7D3z.5	51.50	4.00	0.52	1.25	0.00	40.50	19.75	56.75	227.00	227.00	91.00
7D3z.6	60.00	2.50	0.56	3.75	0.25	31.25	16.50	66.50	266.00	265.00	90.00
Mean [D3z]	58.00	2.67	0.53	2.38	0.04	34.21	18.38	63.00	252.00	251.83	91.83
7E3z.1	57.50	2.75	0.62	4.50	1.00	30.50	22.25	65.75	263.00	259.00	89.00
7E3z.2	58.50	2.75	0.52	5.25	0.00	30.50	21.50	66.50	266.00	266.00	88.00
7E3z.3	58.25	2.00	0.53	2.75	0.00	31.00	19.00	63.00	252.00	252.00	93.00
7E3z.4	57.50	1.75	0.53	3.75	0.25	31.75	22.75	63.25	253.00	252.00	91.00
7E3z.5	58.75	1.75	0.48	2.00	0.00	33.75	19.75	62.50	250.00	250.00	94.00
7E3z.6	54.00	3.25	0.52	4.25	0.00	33.00	18.75	61.75	247.00	247.00	88.00
Mean [E3z]	57.42	2.38	0.53	3.75	0.21	31.75	20.67	63.79	255.17	254.33	90.50
7F3z.1	57.25	1.25	0.47	5.75	0.25	31.50	19.25	64.50	258.00	257.00	89.00
7F3z.2	56.25	2.50	0.42	5.50	0.50	31.25	21.50	64.75	259.00	257.00	87.00
7F3z.3	60.00	3.50	0.41	4.00	0.50	28.25	19.25	68.00	272.00	270.00	89.00
7F3z.4	54.50	2.25	0.51	4.50	0.50	34.00	19.50	61.75	247.00	245.00	89.00
7F3z.5	62.00	1.75	0.46	2.25	0.00	31.00	20.75	66.00	264.00	264.00	94.00
7F3z.6	55.50	1.75	0.52	4.50	1.00	33.75	20.50	63.25	253.00	249.00	90.00
Mean [F3z]	57.58	2.17	0.47	4.42	0.46	31.63	20.13	64.71	258.83	257.00	89.67

153

Sub-Section	Quartz Component [Qtz]	Feldspar Component [Flu]	Mean Length [Flu]	Lithic Component [Lith]	Accessory Minerals	Intergranular Volume [IGV]	Matrix Material and Cements	Framework Detrital Grains	Framework Detrital Grains	QFL Grains	Quartz [QFL]
	%	%	mm	%	%	%	%	%	total	total	%
7H3z.1	55.50	1.50	0.47	2.00	0.25	37.75	20.50	59.25	237.00	236.00	94.00
7H3z.2	53.25	1.50	0.41	2.25	0.25	40.00	16.75	57.25	229.00	228.00	93.00
7H3z.s	57.75	0.00	0.00	2.00	0.00	37.50	17.25	60.75	243.00	243.00	97.00
7H3z.4	62.00	1.25	0.30	3.25	0.25	32.25	20.25	64.75	259.00	258.00	93.00
7H3z.5	53.75	2.00	0.41	3.00	0.00	39.00	18.50	58.75	235.00	235.00	92.00
7H3z.6	56.75	0.75	0.29	2.50	0.25	35.75	19.25	60.25	241.00	241.00	95.00
Mean [H3z]	56.50	1.17	0.31	2.50	0.17	37.04	18.75	60.17	240.67	240.17	94.00
7I3z.1	58.50	2.00	0.51	3.25	0.00	34.00	23.00	63.75	255.00	255.00	92.00
7I3z.2	55.25	2.75	0.39	4.00	0.00	35.50	23.75	62.00	248.00	248.00	89.00
7I3z.3	58.25	1.50	0.41	6.00	0.25	31.25	15.25	66.00	264.00	263.00	89.00
7I3z.4	59.75	1.25	0.41	6.00	0.25	29.75	20.50	67.25	269.00	268.00	89.00
7I3z.5	55.50	2.50	0.40	3.75	0.25	35.25	23.25	61.75	247.00	246.00	90.00
7I3z.6	57.50	1.25	0.43	4.75	0.00	34.50	22.50	63.50	254.00	254.00	90.00
Mean [I3z]	57.46	1.88	0.43	4.63	0.13	33.38	21.38	64.04	256.17	255.67	89.83
7I3x.1	62.25	0.75	0.41	2.50	0.25	32.00	19.25	66.25	265.00	264.00	94.00
7I3x.2	62.00	1.25	0.42	3.25	0.00	33.00	19.00	66.25	265.00	265.00	93.00
Mean [I3x]	62.13	1.00	0.42	2.88	0.13	32.50	19.13	66.25	265.00	264.50	93.50
7J3z.1	56.25	2.75	0.48	4.00	0.75	33.75	19.00	63.75	255.00	252.00	90.00
7J3z.2	56.25	3.00	0.40	4.50	0.00	33.75	18.75	63.75	255.00	255.00	88.00
7J3z.3	57.25	2.00	0.44	3.50	0.25	33.50	22.25	63.00	252.00	251.00	91.00
7J3z.4	59.75	1.50	0.39	3.75	0.25	32.25	20.00	65.25	261.00	260.00	92.00
7J3z.5	61.25	1.50	0.41	3.00	0.00	33.00	18.00	66.00	264.00	264.00	93.00
7J3z.6	61.75	1.75	0.32	2.75	0.00	32.00	18.00	66.25	265.00	265.00	93.00
Mean [J3z]	58.75	2.08	0.41	3.58	0.21	33.04	19.33	64.67	258.67	257.83	91.17
7K3z.1	56.25	2.50	0.46	3.50	0.25	34.25	19.75	62.50	250.00	249.00	90.00
7K3z.2	57.25	2.50	0.47	3.75	0.75	36.25	21.75	62.00	248.00	245.00	90.00
7K3z.3	65.00	0.50	0.54	3.50	0.00	28.50	17.25	69.75	279.00	279.00	94.00
7K3z.4	57.50	2.00	0.47	3.75	0.50	34.25	20.00	63.75	255.00	253.00	91.00
7K3z.5	59.50	1.25	0.43	2.75	0.50	33.50	21.75	64.00	256.00	254.00	94.00

Sub-Section	Quartz Component [Qtz]	Feldspar Component [Flu]	Mean Length [Flu]	Lithic Component [Lith]	Accessory Minerals	Intergranular Volume [IGV]	Matrix Material and Cements	Framework Detrital Grains	Framework Detrital Grains	QFL Grains	Quartz [QFL]
	%	%	mm	%	%	%	%	%	total	total	%
7K3z.6	51.75	1.75	0.43	4.25	0.25	39.50	22.50	58.00	232.00	231.00	90.00
Mean [K3z]	57.88	1.75	0.47	3.58	0.38	34.38	20.50	63.33	253.33	251.83	91.50
7M3z.1	55.50	1.00	0.52	4.50	0.25	34.50	19.00	61.25	245.00	244.00	91.00
7M3z.2	61.00	1.50	0.45	3.50	0.50	32.25	19.25	66.50	266.00	264.00	92.00
7M3z.3	57.25	2.75	0.50	5.50	0.00	33.50	20.00	65.50	262.00	262.00	89.00
7M3z.4	62.50	3.75	0.45	3.50	0.25	28.75	19.00	70.00	280.00	279.00	91.00
7M3z.5	59.25	3.50	0.43	5.50	0.00	29.75	16.75	68.25	273.00	273.00	87.00
7M3z.6	66.00	2.50	0.49	2.25	0.25	26.75	14.25	71.25	285.00	283.00	93.00
Mean [M3z]	60.25	2.50	0.47	4.13	0.21	30.92	18.04	67.13	268.50	267.50	90.50
7N3z.1	54.50	1.00	0.57	3.75	0.25	37.50	14.25	59.50	238.00	237.00	92.00
7N3z.2	60.50	1.25	0.48	3.00	0.00	32.00	12.75	64.75	259.00	259.00	93.00
7N3z.3	55.25	1.25	0.61	4.00	0.00	36.75	14.50	61.25	245.00	245.00	90.00
7N3z.4	57.50	2.75	0.60	2.75	0.25	34.50	14.25	63.25	253.00	252.00	92.00
7N3z.5	58.75	1.50	0.51	3.25	0.00	35.50	14.50	63.50	254.00	254.00	93.00
7N3z.6	55.25	1.25	0.53	3.00	0.00	39.25	15.75	59.50	238.00	238.00	93.00
Mean [N3z]	56.96	1.50	0.55	3.29	0.08	35.92	14.33	61.96	247.83	247.50	92.17
7O3z.1	64.25	1.50	0.45	4.50	0.00	28.25	15.75	70.25	281.00	281.00	92.00
7O3z.2	64.25	1.25	0.45	4.50	0.50	26.50	13.00	71.00	284.00	282.00	92.00
7O3z.3	60.75	1.75	0.54	2.00	0.25	32.00	16.25	64.75	259.00	258.00	94.00
7O3z.4	60.50	1.75	0.50	4.00	0.00	31.25	16.00	66.25	265.00	265.00	91.00
7O3z.5	58.50	1.00	0.77	4.75	0.00	33.75	14.75	64.25	257.00	257.00	91.00
7O3z.6	56.75	2.25	0.55	3.25	0.00	32.50	16.00	62.25	249.00	249.00	87.00
Mean [O3z]	60.83	1.58	0.54	3.83	0.13	30.71	15.29	66.46	265.83	265.33	91.17
7O3x.1	61.00	2.50	0.54	4.25	0.00	29.50	15.00	68.25	273.00	273.00	89.00
7O3x.2	63.25	2.00	0.58	3.00	0.25	28.75	12.75	68.50	274.00	273.00	93.00
Mean [O3x]	62.13	2.25	0.56	3.63	0.13	29.13	13.88	68.38	273.50	273.00	91.00
Mean [3OBS]	58.18	1.85	0.47	3.47	0.23	33.35	18.75	63.76	255.00	254.10	91.53

155

Sub-Section	Quartz Component [Qtz]	Feldspar Component [Flu]	Mean Length [Flu]	Lithic Component [Lith]	Accessory Minerals	Intergranular Volume [IGV]	Matrix Material and Cements	Framework Detrital Grains	Framework Detrital Grains	QFL Grains	Quartz [QFL]
	%	%	mm	%	%	%	%	%	total	total	%
7A2z.1	51.25	3.00	0.50	2.00	0.00	38.00	26.25	56.75	227.00	227.00	91.00
7A2z.2	55.75	2.50	0.41	6.25	0.50	31.00	24.25	64.50	258.00	256.00	87.00
7A2z.3	55.75	2.00	0.34	4.75	0.75	30.50	23.50	63.25	253.00	250.00	89.00
7A2z.4	53.25	1.25	0.44	4.75	0.50	38.00	27.50	59.75	239.00	237.00	90.00
7A2z.5	51.25	2.25	0.46	5.25	0.75	37.25	27.00	59.50	238.00	235.00	87.00
7A2z.6	49.50	1.00	0.33	5.50	0.75	36.75	30.00	56.75	227.00	224.00	89.00
Mean [A2z]	52.79	2.00	0.41	4.75	0.54	35.25	26.42	60.08	240.33	238.17	88.83
7C2z.1	52.50	3.00	0.62	5.50	0.50	33.50	21.00	61.50	246.00	244.00	86.00
7C2z.2	55.25	4.50	0.64	2.25	0.00	34.00	17.25	63.75	255.00	255.00	89.00
7C2z.3	58.25	2.50	0.66	4.50	0.25	32.25	20.25	65.50	262.00	261.00	89.00
7C2z.4	54.25	1.50	0.52	2.25	0.25	34.00	20.25	60.75	243.00	242.00	93.00
7C2z.5	49.50	2.75	0.60	3.50	0.75	36.50	22.75	57.50	230.00	227.00	89.00
7C2z.6	46.75	2.25	0.65	2.25	0.00	37.25	22.25	58.25	233.00	233.00	92.00
Mean [C2z]	52.75	2.75	0.62	3.38	0.29	34.58	20.63	61.21	244.83	243.67	89.67
7C2x.1	60.25	1.00	0.52	1.25	0.00	35.75	13.75	62.50	250.00	250.00	96.00
7C2x.2	60.25	0.75	0.31	2.75	0.00	35.00	17.50	63.75	255.00	255.00	95.00
Mean [C2x]	60.25	0.88	0.42	2.00	0.00	35.38	15.63	63.13	252.50	252.50	95.50
7L2z.1	60.00	1.75	0.47	4.25	0.00	32.25	21.25	66.25	265.00	265.00	91.00
7L2z.2	58.50	1.75	0.51	3.50	0.00	35.25	21.50	63.75	255.00	255.00	93.00
7L2z.3	59.75	2.75	0.45	3.50	0.25	31.75	20.75	66.25	265.00	264.00	91.00
7L2z.4	48.50	3.25	0.40	3.50	0.00	34.00	27.25	64.25	257.00	257.00	90.00
7L2z.5	63.00	2.00	0.40	3.75	0.50	29.50	23.00	69.25	277.00	275.00	92.00
7L2z.6	59.75	1.00	0.40	6.25	0.25	30.25	24.00	68.25	273.00	272.00	88.00
Mean [L2z]	58.25	2.08	0.44	4.13	0.17	32.17	22.96	66.33	265.33	264.67	90.83
7L2x.1	57.25	1.50	0.42	2.75	0.25	35.50	19.25	61.75	247.00	246.00	94.00
7L2x.2	59.25	2.25	0.54	3.75	0.00	33.00	20.75	65.00	260.00	260.00	91.00
Mean [L2x]	58.25	1.88	0.48	3.25	0.13	34.25	20.00	63.38	253.50	253.00	92.50
Mean [2OBS]	55.44	2.11	0.48	3.82	0.28	34.15	22.33	62.67	250.70	249.50	90.55

Sub-Section	Quartz Component [Qtz]	Feldspar Component [Flu]	Mean Length [Flu]	Lithic Component [Lith]	Accessory Minerals	Intergranular Volume [IGV]	Matrix Material and Cements	Framework Detrital Grains	Framework Detrital Grains	QFL Grains	Quartz [QFL]
	%	%	mm	%	%	%	%	%	total	total	%
7G1z.1	60.00	0.75	0.48	4.25	0.25	33.75	28.75	65.25	261.00	260.00	92.00
7G1z.2	57.50	1.00	0.36	2.25	0.00	37.50	30.50	60.75	243.00	243.00	94.00
7G1z.3	61.25	3.00	0.42	3.50	0.75	30.00	23.50	68.50	274.00	271.00	91.00
7G1z.4	66.25	1.75	0.43	5.75	0.25	23.25	14.25	74.00	296.00	295.00	90.00
7G1z.5	61.75	2.50	0.39	4.00	0.50	28.00	15.75	68.75	275.00	273.00	90.00
7G1z.6	61.25	2.25	0.49	3.00	0.50	28.25	14.00	67.00	268.00	266.00	92.00
Mean [G1z]	61.33	1.88	0.43	3.79	0.38	30.13	21.13	67.38	269.50	268.00	91.50
7G1x.1	61.00	0.50	0.43	1.50	0.25	33.75	23.25	63.25	253.00	252.00	97.00
7G1x.2	62.00	1.50	0.39	2.50	0.00	31.75	23.25	66.00	264.00	264.00	94.00
Mean [G1x]	61.50	1.00	0.41	2.00	0.13	32.75	23.25	64.63	258.50	258.00	95.50
Mean [1OBS]	61.38	1.66	0.42	3.34	0.31	30.78	21.66	66.69	266.80	265.50	92.50
WRM	57.83	1.90	0.47	3.54	0.25	33.32	19.77	63.76	255.00	254.00	91.39

Sub-Section	Feldspar [QFL]	Lithics [QFL]	Mean Grain Size	Mean Grain Size	Mean Grain Size [MGS]	Sorting [IGSD]	Sorting [IGSD]	Hematite	Ferroan Cements	Ferroan Cements**	Ferroan Cements*
	%	%	mm	phi	type	phi	type	%	%	%	%
7B3z.1	2.00	5.00	0.52	0.95	cL	0.29	vws	9.75	13.00	0.38	0.55
7B3z.2	3.00	3.00	0.53	0.93	cL	0.25	vws	9.00	15.00	0.43	0.62
7B3z.3	1.00	3.00	0.60	0.74	cL	0.27	vws	6.00	9.00	0.22	0.49
7B3z.4	1.00	5.00	0.56	0.84	cL	0.36	ws	8.50	12.75	0.35	0.55
7B3z.5	1.00	5.00	0.52	0.95	cL	0.35	ws	7.00	9.50	0.27	0.54
7B3z.6	1.00	6.00	0.54	0.89	cL	0.32	vws	8.50	12.75	0.39	0.67
Mean [B3z]	1.50	4.50	0.54	0.88	cL	0.31	vws	8.13	12.00	0.34	0.57
7D3z.1	4.00	4.00	0.55	0.86	cL	0.34	vws	8.25	9.25	0.29	0.65
7D3z.2	4.00	3.00	0.59	0.76	cL	0.38	ws	6.25	8.50	0.26	0.46
7D3z.3	5.00	4.00	0.54	0.90	cL	0.34	vws	6.50	9.75	0.28	0.43
7D3z.4	2.00	4.00	0.54	0.88	cL	0.34	vws	6.25	7.75	0.23	0.41
7D3z.5	7.00	2.00	0.53	0.90	cL	0.33	vws	6.75	8.25	0.20	0.42
7D3z.6	4.00	6.00	0.59	0.76	cL	0.40	ws	6.25	9.00	0.29	0.55
Mean [D3z]	4.33	3.83	0.56	0.84	cL	0.36	ws	6.71	8.75	0.26	0.49
7E3z.1	4.00	7.00	0.51	0.97	cL	0.40	ws	10.50	12.00	0.39	0.54
7E3z.2	4.00	8.00	0.52	0.94	cL	0.36	ws	9.50	10.25	0.34	0.48
7E3z.3	3.00	4.00	0.54	0.89	cL	0.34	vws	5.75	8.00	0.26	0.42
7E3z.4	3.00	6.00	0.52	0.94	cL	0.36	ws	8.00	9.00	0.28	0.40
7E3z.5	3.00	3.00	0.52	0.93	cL	0.32	vws	8.25	9.75	0.29	0.49
7E3z.6	5.00	7.00	0.53	0.93	cL	0.39	ws	7.00	9.00	0.27	0.48
Mean [E3z]	3.67	5.83	0.52	0.93	cL	0.36	ws	8.17	9.67	0.31	0.47
7F3z.1	2.00	9.00	0.45	1.14	mU	0.38	ws	7.50	8.00	0.25	0.42
7F3z.2	4.00	9.00	0.44	1.17	mU	0.48	ws	7.50	8.75	0.28	0.41
7F3z.3	5.00	6.00	0.45	1.15	mU	0.43	ws	6.50	7.75	0.27	0.40
7F3z.4	4.00	7.00	0.52	0.94	cL	0.36	ws	6.00	6.50	0.19	0.33
7F3z.5	3.00	3.00	0.47	1.09	mU	0.39	ws	9.50	10.25	0.33	0.49
7F3z.6	3.00	7.00	0.50	1.01	mU	0.42	ws	9.25	10.25	0.30	0.50
Mean [F3z]	3.50	6.83	0.47	1.08	mU	0.41	ws	7.71	8.58	0.27	0.43

Sub-Section	Feldspar [QFL]	Lithics [QFL]	Mean Grain Size	Mean Grain Size	Mean Grain Size [MGS]	Sorting [IGSD]	Sorting [IGSD]	Hematite	Ferroan Cements	Ferroan Cements**	Ferroan Cements*
	%	%	mm	phi	type	phi	type	%	%	%	%
7H3z.1	3.00	3.00	0.49	1.03	mU	0.32	vws	8.00	12.50	0.33	0.61
7H3z.2	3.00	4.00	0.46	1.12	mU	0.38	ws	6.25	8.25	0.21	0.49
7H3z.s	0.00	3.00	0.46	1.11	mU	0.43	ws	6.75	9.00	0.24	0.52
7H3z.4	2.00	5.00	0.45	1.17	mU	0.45	ws	8.75	11.75	0.36	0.58
7H3z.5	3.00	5.00	0.46	1.13	mU	0.38	ws	8.25	10.25	0.26	0.55
7H3z.6	1.00	4.00	0.44	1.19	mU	0.38	ws	6.75	7.50	0.21	0.39
Mean [H3z]	2.00	4.00	0.46	1.13	mU	0.39	ws	7.46	9.88	0.27	0.52
7I3z.1	3.00	5.00	0.45	1.17	mU	0.34	vws	9.25	13.00	0.38	0.57
7I3z.2	4.00	7.00	0.44	1.19	mU	0.37	ws	8.50	11.75	0.33	0.49
7I3z.3	2.00	9.00	0.47	1.10	mU	0.28	vws	6.50	9.00	0.29	0.59
7I3z.4	2.00	9.00	0.49	1.04	mU	0.34	vws	7.25	9.75	0.33	0.48
7I3z.5	4.00	6.00	0.45	1.17	mU	0.39	ws	10.00	11.25	0.32	0.48
7I3z.6	2.00	8.00	0.42	1.24	mU	0.39	ws	12.00	14.25	0.41	0.63
Mean [I3z]	2.83	7.33	0.45	1.15	mU	0.35	ws	8.92	11.50	0.34	0.54
7I3x.1	1.00	5.00	0.48	1.06	mU	0.36	ws	9.25	15.00	0.47	0.78
7I3x.2	2.00	5.00	0.50	1.01	mU	0.34	vws	7.75	11.50	0.35	0.61
Mean [I3x]	1.50	5.00	0.49	1.04	mU	0.35	ws	8.50	13.25	0.41	0.69
7J3z.1	4.00	6.00	0.47	1.09	mU	0.34	vws	6.25	8.25	0.24	0.43
7J3z.2	5.00	7.00	0.45	1.14	mU	0.30	vws	5.25	9.75	0.29	0.52
7J3z.3	3.00	6.00	0.44	1.18	mU	0.37	ws	8.50	12.25	0.37	0.55
7J3z.4	2.00	6.00	0.49	1.04	mU	0.38	ws	5.00	8.00	0.25	0.40
7J3z.5	2.00	5.00	0.49	1.03	mU	0.39	ws	6.25	10.50	0.32	0.58
7J3z.6	3.00	4.00	0.41	1.30	mU	0.37	ws	5.25	11.50	0.36	0.64
Mean [J3z]	3.17	5.67	0.46	1.13	mU	0.36	ws	6.08	10.04	0.30	0.52
7K3z.1	4.00	6.00	0.48	1.07	mU	0.35	ws	7.75	10.75	0.31	0.54
7K3z.2	4.00	6.00	0.48	1.06	mU	0.31	vws	8.25	10.75	0.30	0.49
7K3z.3	1.00	5.00	0.46	1.12	mU	0.38	ws	6.50	9.75	0.34	0.57
7K3z.4	3.00	6.00	0.48	1.07	mU	0.43	ws	7.00	8.50	0.25	0.43
7K3z.5	2.00	4.00	0.46	1.12	mU	0.34	vws	6.75	10.00	0.30	0.46

Sub-Section	Feldspar [QFL]	Lithics [QFL]	Mean Grain Size	Mean Grain Size	Mean Grain Size [MGS]	Sorting [IGSD]	Sorting [IGSD]	Hematite	Ferroan Cements	Ferroan Cements**	Ferroan Cements*
	%	%	mm	phi	type	phi	type	%	%	%	%
7K3z.6	3.00	7.00	0.46	1.11	mU	0.38	ws	9.25	12.25	0.31	0.54
Mean [K3z]	2.83	5.67	0.47	1.09	mU	0.37	ws	7.58	10.33	0.30	0.51
7M3z.1	2.00	7.00	0.49	1.02	mU	0.39	ws	6.75	8.50	0.25	0.45
7M3z.2	3.00	5.00	0.49	1.04	mU	0.38	ws	6.50	8.75	0.27	0.45
7M3z.3	3.00	8.00	0.48	1.05	mU	0.41	ws	11.75	13.75	0.41	0.69
7M3z.4	4.00	5.00	0.48	1.07	mU	0.46	ws	8.00	9.75	0.34	0.51
7M3z.5	5.00	8.00	0.48	1.06	mU	0.47	ws	7.75	10.25	0.34	0.61
7M3z.6	4.00	3.00	0.49	1.03	mU	0.40	ws	8.25	10.00	0.37	0.70
Mean [M3z]	3.50	6.00	0.49	1.04	mU	0.42	ws	8.17	10.17	0.33	0.57
7N3z.1	2.00	6.00	0.58	0.79	cL	0.37	ws	8.00	9.25	0.25	0.65
7N3z.2	2.00	5.00	0.55	0.86	cL	0.45	ws	6.25	7.75	0.24	0.61
7N3z.3	3.00	7.00	0.55	0.87	cL	0.42	ws	8.25	10.00	0.27	0.69
7N3z.4	4.00	4.00	0.54	0.88	cL	0.40	ws	6.25	7.75	0.22	0.54
7N3z.5	2.00	5.00	0.53	0.90	cL	0.39	ws	6.50	8.25	0.23	0.57
7N3z.6	2.00	5.00	0.57	0.80	cL	0.38	ws	7.00	8.50	0.22	0.54
Mean [N3z]	2.50	5.33	0.55	0.85	cL	0.40	ws	7.04	8.58	0.24	0.60
7O3z.1	2.00	6.00	0.62	0.69	cL	0.54	mws	8.00	9.75	0.35	0.62
7O3z.2	2.00	6.00	0.61	0.71	cL	0.51	mws	7.50	8.00	0.30	0.62
7O3z.3	3.00	3.00	0.54	0.88	cL	0.42	ws	9.75	11.25	0.35	0.69
7O3z.4	3.00	6.00	0.58	0.79	cL	0.48	ws	8.00	9.25	0.30	0.58
7O3z.5	2.00	7.00	0.66	0.61	cL	0.56	mws	8.75	9.50	0.28	0.64
7O3z.6	4.00	9.00	0.64	0.65	cL	0.44	ws	8.75	9.75	0.30	0.61
Mean [O3z]	2.67	6.17	0.61	0.72	cL	0.49	ws	8.46	9.58	0.31	0.63
7O3x.1	4.00	7.00	0.59	0.77	cL	0.39	ws	6.25	7.75	0.26	0.52
7O3x.2	3.00	4.00	0.58	0.78	cL	0.40	ws	5.00	6.75	0.23	0.53
Mean [O3x]	3.50	5.50	0.59	0.77	cL	0.40	ws	5.63	7.25	0.25	0.52
Mean [3OBS]	2.93	5.54	0.51	0.98	cL	0.38	ws	7.64	9.94	0.30	0.54

160

Sub-Section	Feldspar [QFL]	Lithics [QFL]	Mean Grain Size	Mean Grain Size	Mean Grain Size [MGS]	Sorting [IGSD]	Sorting [IGSD]	Hematite	Ferroan Cements	Ferroan Cements**	Ferroan Cements*
	%	%	mm	phi	type	phi	type	%	%	%	%
7A2z.1	5.00	4.00	0.49	1.03	mU	0.51	mws	13.25	18.25	0.48	0.70
7A2z.2	4.00	9.00	0.41	1.28	mU	0.44	ws	16.25	20.25	0.65	0.84
7A2z.3	3.00	8.00	0.54	0.89	cL	0.46	ws	13.75	16.00	0.52	0.68
7A2z.4	2.00	8.00	0.57	0.80	cL	0.45	ws	15.25	21.75	0.57	0.79
7A2z.5	4.00	9.00	0.53	0.91	cL	0.49	ws	13.00	18.25	0.49	0.68
7A2z.6	1.00	10.00	0.47	1.08	mU	0.51	mws	20.75	23.75	0.65	0.79
Mean [A2z]	3.17	8.00	0.50	1.00	cL	0.48	ws	15.38	19.71	0.56	0.74
7C2z.1	5.00	9.00	0.64	0.65	cL	0.38	ws	8.50	10.50	0.31	0.50
7C2z.2	7.00	4.00	0.68	0.56	cL	0.32	vws	3.50	6.25	0.18	0.36
7C2z.3	4.00	7.00	0.62	0.69	cL	0.36	ws	5.50	7.50	0.23	0.37
7C2z.4	3.00	4.00	0.71	0.50	cL	0.33	vws	6.00	10.00	0.29	0.49
7C2z.5	5.00	6.00	0.66	0.60	cL	0.34	vws	8.75	11.00	0.30	0.48
7C2z.6	4.00	4.00	0.63	0.68	cL	0.36	ws	6.75	8.50	0.23	0.38
Mean [C2z]	4.67	5.67	0.65	0.61	cL	0.35	vws	6.50	8.96	0.26	0.43
7C2x.1	2.00	2.00	0.58	0.78	cL	0.34	vws	6.00	8.25	0.23	0.60
7C2x.2	1.00	4.00	0.57	0.81	cL	0.36	ws	8.00	10.00	0.29	0.57
Mean [C2x]	1.50	3.00	0.58	0.80	cL	0.35	ws	7.00	9.13	0.26	0.59
7L2z.1	3.00	6.00	0.45	1.15	mU	0.42	ws	7.00	11.25	0.35	0.53
7L2z.2	2.00	5.00	0.46	1.13	mU	0.35	ws	8.25	13.00	0.37	0.60
7L2z.3	4.00	5.00	0.45	1.15	mU	0.44	ws	8.50	10.75	0.34	0.52
7L2z.4	5.00	5.00	0.43	1.21	mU	0.45	ws	16.75	20.25	0.60	0.74
7L2z.5	3.00	5.00	0.43	1.22	mU	0.49	ws	13.75	19.00	0.64	0.83
7L2z.6	3.00	9.00	0.45	1.16	mU	0.51	mws	11.25	14.50	0.48	0.60
Mean [L2z]	3.33	5.83	0.44	1.17	mU	0.44	ws	10.92	14.79	0.46	0.64
7L2x.1	2.00	4.00	0.53	0.92	cL	0.39	ws	10.50	13.50	0.38	0.70
7L2x.2	3.00	6.00	0.52	0.95	cL	0.38	ws	8.50	12.00	0.36	0.58
Mean [L2x]	2.50	5.00	0.52	0.93	cL	0.39	ws	9.50	12.75	0.37	0.64
Mean [2OBS]	3.41	6.05	0.54	0.92	cL	0.41	ws	10.44	13.84	0.41	0.61

Sub-Section	Feldspar [QFL]	Lithics [QFL]	Mean Grain Size	Mean Grain Size	Mean Grain Size [MGS]	Sorting [IGSD]	Sorting [IGSD]	Hematite	Ferroan Cements	Ferroan Cements**	Ferroan Cements*
	%	%	mm	phi	type	phi	type	%	%	%	%
7G1z.1	1.00	7.00	0.46	1.13	mU	0.38	ws	17.25	24.25	0.72	0.84
7G1z.2	2.00	4.00	0.44	1.18	mU	0.33	vws	21.25	28.25	0.75	0.93
7G1z.3	4.00	5.00	0.44	1.18	mU	0.31	vws	10.25	18.75	0.63	0.80
7G1z.4	2.00	8.00	0.47	1.09	mU	0.41	ws	7.75	9.75	0.42	0.68
7G1z.5	4.00	6.00	0.48	1.06	mU	0.35	ws	7.50	9.75	0.35	0.62
7G1z.6	3.00	5.00	0.48	1.07	mU	0.38	ws	7.25	10.50	0.37	0.75
Mean [G1z]	2.67	5.83	0.46	1.12	mU	0.36	ws	11.88	16.88	0.54	0.77
7G1x.1	1.00	2.00	0.49	1.04	mU	0.34	vws	17.25	19.50	0.58	0.84
7G1x.2	2.00	4.00	0.47	1.08	mU	0.38	ws	13.75	17.75	0.56	0.76
Mean [G1x]	1.50	3.00	0.48	1.06	mU	0.36	ws	15.50	18.63	0.57	0.80
Mean [1OBS]	2.38	5.13	0.47	1.10	mU	0.36	ws	12.78	17.31	0.55	0.78
WRM	2.99	5.62	0.51	0.98	cL	0.39	ws	8.67	11.39	0.34	0.57

Sub-Section	Authigenic Quartz	Authigenic Quartz**	Authigenic Quartz*	Total Cement	Pore Filling Clay	Pore Filling Clay*	Pore Filling Clay**	Pore Lining Clay	Pore Lining Clay*	Pore Lining Clay**	Undiss. Ferroan Dolomite [Rh]
	%	%	%	%	%	%	%	%	%	%	%
7B3z.1	3.00	0.09	0.13	16.00	6.50	0.27	0.19	1.25	0.05	0.04	2.75
7B3z.2	4.00	0.12	0.16	19.00	4.50	0.19	0.13	0.75	0.03	0.02	5.25
7B3z.3	5.50	0.14	0.30	14.50	2.25	0.12	0.06	1.50	0.08	0.04	3.00
7B3z.4	3.75	0.10	0.16	16.50	6.00	0.26	0.17	0.75	0.03	0.02	3.50
7B3z.5	2.25	0.06	0.13	11.75	4.50	0.26	0.13	1.25	0.07	0.04	2.00
7B3z.6	3.00	0.09	0.16	15.75	2.50	0.13	0.08	0.75	0.04	0.02	4.00
Mean [B3z]	3.58	0.10	0.17	15.58	4.38	0.20	0.12	1.04	0.05	0.03	3.42
7D3z.1	0.25	0.01	0.02	9.50	2.50	0.18	0.08	2.25	0.16	0.07	1.00
7D3z.2	2.50	0.08	0.14	11.00	4.50	0.24	0.14	3.00	0.16	0.09	1.75
7D3z.3	3.00	0.09	0.13	12.75	5.00	0.22	0.14	4.75	0.21	0.14	3.00
7D3z.4	2.75	0.08	0.15	10.50	3.50	0.19	0.10	4.75	0.25	0.14	0.75
7D3z.5	3.00	0.07	0.15	11.25	3.50	0.18	0.09	5.00	0.25	0.12	1.25
7D3z.6	1.75	0.06	0.11	10.75	2.00	0.12	0.06	3.75	0.23	0.12	2.75
Mean [D3z]	2.21	0.06	0.12	10.96	3.50	0.19	0.10	3.92	0.21	0.11	1.75
7E3z.1	1.25	0.04	0.06	13.25	6.75	0.30	0.22	2.25	0.10	0.07	0.75
7E3z.2	1.00	0.03	0.05	11.25	6.75	0.31	0.22	3.50	0.16	0.11	0.50
7E3z.3	1.75	0.06	0.09	9.75	4.75	0.25	0.15	4.50	0.24	0.15	1.75
7E3z.4	2.00	0.06	0.09	11.00	6.75	0.30	0.21	5.00	0.22	0.16	0.75
7E3z.5	2.50	0.07	0.13	12.25	4.00	0.20	0.12	3.50	0.18	0.10	1.25
7E3z.6	1.75	0.05	0.09	10.75	4.75	0.25	0.14	3.25	0.17	0.10	1.25
Mean [E3z]	1.71	0.05	0.08	11.38	5.63	0.27	0.18	3.67	0.18	0.12	1.04
7F3z.1	1.00	0.03	0.05	9.00	5.00	0.26	0.16	5.25	0.27	0.17	0.50
7F3z.2	3.00	0.10	0.14	11.75	7.00	0.33	0.22	2.75	0.13	0.09	0.75
7F3z.3	2.25	0.08	0.12	10.00	5.25	0.27	0.19	3.75	0.19	0.13	0.75
7F3z.4	2.00	0.06	0.10	8.50	6.75	0.35	0.20	4.25	0.22	0.13	0.00
7F3z.5	1.50	0.05	0.07	11.75	4.75	0.23	0.15	4.25	0.20	0.14	0.50
7F3z.6	3.75	0.11	0.18	14.00	4.00	0.20	0.12	2.50	0.12	0.07	0.75
Mean [F3z]	2.25	0.07	0.11	10.83	5.46	0.27	0.17	3.79	0.19	0.12	0.54

Sub-Section	Authigenic Quartz %	Authigenic Quartz** %	Authigenic Quartz* %	Total Cement %	Pore Filling Clay %	Pore Filling Clay* %	Pore Filling Clay** %	Pore Lining Clay %	Pore Lining Clay* %	Pore Lining Clay** %	Undiss. Ferroan Dolomite [Rh] %
7H3z.1	2.25	0.06	0.11	14.75	2.25	0.11	0.06	3.50	0.17	0.09	4.00
7H3z.2	2.50	0.06	0.15	10.75	4.00	0.24	0.10	2.00	0.12	0.05	1.50
7H3z.s	2.25	0.06	0.13	11.25	4.25	0.25	0.11	1.75	0.10	0.05	1.25
7H3z.4	2.50	0.08	0.12	14.25	4.25	0.21	0.13	1.75	0.09	0.05	3.00
7H3z.5	2.75	0.07	0.15	13.00	3.25	0.18	0.08	2.25	0.12	0.06	1.50
7H3z.6	3.50	0.10	0.18	11.00	5.25	0.27	0.15	3.00	0.16	0.08	0.50
Mean [H3z]	2.63	0.07	0.14	12.50	3.88	0.21	0.11	2.38	0.13	0.06	1.96
7I3z.1	4.00	0.12	0.17	17.00	3.50	0.15	0.10	2.50	0.11	0.07	3.25
7I3z.2	3.75	0.11	0.16	15.50	5.50	0.23	0.15	2.75	0.12	0.08	2.75
7I3z.3	2.00	0.06	0.13	11.00	3.00	0.20	0.10	1.25	0.08	0.04	2.00
7I3z.4	3.25	0.11	0.16	13.00	3.50	0.17	0.12	4.00	0.20	0.13	2.25
7I3z.5	3.50	0.10	0.15	14.75	6.25	0.27	0.18	2.25	0.10	0.06	1.00
7I3z.6	2.75	0.08	0.12	17.00	3.25	0.14	0.09	2.25	0.10	0.07	1.75
Mean [I3z]	3.21	0.10	0.15	14.71	4.17	0.19	0.12	2.50	0.12	0.08	2.17
7I3x.1	2.75	0.09	0.14	17.75	0.75	0.04	0.02	0.75	0.04	0.02	5.25
7I3x.2	3.75	0.11	0.20	15.25	2.00	0.11	0.06	1.75	0.09	0.05	3.75
Mean [I3x]	3.25	0.10	0.17	16.50	1.38	0.07	0.04	1.25	0.07	0.04	4.50
7J3z.1	2.50	0.07	0.13	10.75	5.25	0.28	0.16	3.00	0.16	0.09	1.50
7J3z.2	1.00	0.03	0.05	10.75	5.25	0.28	0.16	2.75	0.15	0.08	4.25
7J3z.3	2.25	0.07	0.10	14.50	5.50	0.25	0.16	2.25	0.10	0.07	3.00
7J3z.4	3.25	0.10	0.16	11.25	5.75	0.29	0.18	3.00	0.15	0.09	2.75
7J3z.5	1.75	0.05	0.10	12.25	3.00	0.17	0.09	2.75	0.15	0.08	4.00
7J3z.6	2.50	0.08	0.14	14.00	2.50	0.14	0.08	1.50	0.08	0.05	5.75
Mean [J3z]	2.21	0.07	0.11	12.25	4.54	0.23	0.14	2.54	0.13	0.08	3.54
7K3z.1	1.75	0.05	0.09	12.50	4.00	0.20	0.12	3.25	0.16	0.09	2.75
7K3z.2	3.75	0.10	0.17	14.50	3.75	0.17	0.10	3.50	0.16	0.10	1.25
7K3z.3	2.25	0.08	0.13	12.00	3.25	0.19	0.11	2.00	0.12	0.07	2.75
7K3z.4	4.50	0.13	0.23	13.00	4.00	0.20	0.12	3.00	0.15	0.09	1.25
7K3z.5	4.00	0.12	0.18	14.00	4.25	0.20	0.13	3.50	0.16	0.10	2.50

Sub-Section	Authigenic Quartz	Authigenic Quartz**	Authigenic Quartz*	Total Cement	Pore Filling Clay	Pore Filling Clay*	Pore Filling Clay**	Pore Lining Clay	Pore Lining Clay*	Pore Lining Clay**	Undiss. Ferroan Dolomite [Rh]
	%	%	%	%	%	%	%	%	%	%	%
7K3z.6	3.25	0.08	0.14	15.50	5.00	0.22	0.13	2.00	0.09	0.05	1.50
Mean [K3z]	3.25	0.09	0.16	13.58	4.04	0.20	0.12	2.88	0.14	0.08	2.00
7M3z.1	3.00	0.09	0.16	11.50	4.75	0.25	0.14	2.75	0.14	0.08	1.50
7M3z.2	4.25	0.13	0.22	13.00	4.25	0.22	0.13	2.00	0.10	0.06	2.00
7M3z.3	1.00	0.03	0.05	14.75	4.00	0.20	0.12	1.25	0.06	0.04	1.75
7M3z.4	4.25	0.15	0.22	14.00	2.25	0.12	0.08	2.75	0.14	0.10	1.25
7M3z.5	2.75	0.09	0.16	13.00	1.75	0.10	0.06	2.00	0.12	0.07	1.75
7M3z.6	1.50	0.06	0.11	11.50	1.25	0.09	0.05	1.50	0.11	0.06	1.75
Mean [M3z]	2.79	0.09	0.15	12.96	3.04	0.16	0.10	2.04	0.11	0.07	1.67
7N3z.1	1.50	0.04	0.11	10.75	2.00	0.14	0.05	1.50	0.11	0.04	1.25
7N3z.2	2.75	0.09	0.22	10.50	1.75	0.14	0.05	0.50	0.04	0.02	1.25
7N3z.3	2.50	0.07	0.17	12.50	1.00	0.07	0.03	1.00	0.07	0.03	1.75
7N3z.4	2.25	0.07	0.16	10.00	2.75	0.19	0.08	1.50	0.11	0.04	1.25
7N3z.5	3.75	0.11	0.26	12.00	1.50	0.10	0.04	1.00	0.07	0.03	1.75
7N3z.6	3.50	0.09	0.22	12.00	2.25	0.14	0.06	1.50	0.10	0.04	1.25
Mean [N3z]	2.71	0.08	0.19	11.29	1.88	0.13	0.05	1.17	0.08	0.03	1.42
7O3z.1	3.25	0.12	0.21	13.00	2.25	0.14	0.08	0.50	0.03	0.02	1.75
7O3z.2	2.75	0.10	0.21	10.75	1.25	0.10	0.05	1.00	0.08	0.04	0.50
7O3z.3	2.50	0.08	0.15	13.75	1.25	0.08	0.04	1.25	0.08	0.04	1.25
7O3z.4	2.25	0.07	0.14	11.50	3.00	0.19	0.10	1.50	0.09	0.05	1.25
7O3z.5	4.25	0.13	0.29	13.75	0.75	0.05	0.02	0.25	0.02	0.01	0.75
7O3z.6	2.50	0.08	0.16	12.25	2.25	0.14	0.07	1.50	0.09	0.05	1.00
Mean [O3z]	2.92	0.10	0.19	12.50	1.79	0.12	0.06	1.00	0.07	0.03	1.08
7O3x.1	4.25	0.14	0.28	12.00	1.50	0.10	0.05	1.50	0.10	0.05	0.75
7O3x.2	4.50	0.16	0.35	11.25	0.75	0.06	0.03	0.75	0.06	0.03	1.75
Mean [O3x]	4.38	0.15	0.32	11.63	1.13	0.08	0.04	1.13	0.08	0.04	1.25
Mean [3OBS]	2.74	0.08	0.15	12.68	3.70	0.19	0.11	2.38	0.13	0.07	1.93

Sub-Section	Authigenic Quartz %	Authigenic Quartz** %	Authigenic Quartz* %	Total Cement %	Pore Filling Clay %	Pore Filling Clay* %	Pore Filling Clay** %	Pore Lining Clay %	Pore Lining Clay* %	Pore Lining Clay** %	Undiss. Ferroan Dolomite [Rh] %
7A2z.1	4.00	0.11	0.15	22.25	3.75	0.14	0.10	0.25	0.01	0.01	5.00
7A2z.2	1.75	0.06	0.07	22.00	1.75	0.07	0.06	0.50	0.02	0.02	3.50
7A2z.3	5.75	0.19	0.24	21.75	1.25	0.05	0.04	0.50	0.02	0.02	1.50
7A2z.4	3.75	0.10	0.14	25.50	1.50	0.05	0.04	0.50	0.02	0.01	6.25
7A2z.5	5.75	0.15	0.21	24.00	2.50	0.09	0.07	0.50	0.02	0.01	4.25
7A2z.6	3.00	0.08	0.10	26.75	2.25	0.08	0.06	1.00	0.03	0.03	2.50
Mean [A2z]	4.00	0.11	0.15	23.71	2.17	0.08	0.06	0.54	0.02	0.02	3.83
7C2z.1	0.75	0.02	0.04	11.25	7.00	0.33	0.21	2.75	0.13	0.08	1.75
7C2z.2	4.50	0.13	0.26	10.75	3.50	0.20	0.10	3.00	0.17	0.09	2.25
7C2z.3	2.50	0.08	0.12	10.00	6.25	0.31	0.19	4.00	0.20	0.12	1.50
7C2z.4	4.75	0.14	0.23	14.75	3.75	0.19	0.11	1.75	0.09	0.05	3.50
7C2z.5	2.75	0.08	0.12	13.75	6.00	0.26	0.16	3.00	0.13	0.08	2.00
7C2z.6	2.00	0.05	0.09	10.50	7.00	0.31	0.19	4.75	0.21	0.13	1.50
Mean [C2z]	2.88	0.08	0.14	11.83	5.58	0.27	0.16	3.21	0.16	0.09	2.08
7C2x.1	3.00	0.08	0.22	11.25	1.50	0.11	0.04	1.00	0.07	0.03	2.00
7C2x.2	2.75	0.08	0.16	12.75	2.25	0.13	0.06	2.50	0.14	0.07	1.50
Mean [C2x]	2.88	0.08	0.19	12.00	1.88	0.12	0.05	1.75	0.11	0.05	1.75
7L2z.1	2.25	0.07	0.11	13.50	5.25	0.25	0.16	2.50	0.12	0.08	4.00
7L2z.2	4.00	0.11	0.19	17.00	2.75	0.13	0.08	1.75	0.08	0.05	4.75
7L2z.3	2.25	0.07	0.11	13.00	4.00	0.19	0.13	3.75	0.18	0.12	2.00
7L2z.4	2.00	0.06	0.07	22.25	3.00	0.11	0.09	2.00	0.07	0.06	3.00
7L2z.5	1.00	0.03	0.04	20.00	1.75	0.08	0.06	1.25	0.05	0.04	4.25
7L2z.6	3.75	0.12	0.16	18.25	3.25	0.14	0.11	2.50	0.10	0.08	2.75
Mean [L2z]	2.54	0.08	0.11	17.33	3.33	0.15	0.10	2.29	0.10	0.07	3.46
7L2x.1	3.50	0.10	0.18	17.00	1.00	0.05	0.03	1.25	0.06	0.04	2.50
7L2x.2	3.75	0.11	0.18	15.75	2.00	0.10	0.06	3.00	0.14	0.09	3.25
Mean [L2x]	3.63	0.11	0.18	16.38	1.50	0.07	0.04	2.13	0.10	0.06	2.88
Mean [2OBS]	3.16	0.09	0.01	17.00	3.33	0.15	0.10	2.00	0.10	0.06	2.98

Sub-Section	Authigenic Quartz %	Authigenic Quartz** %	Authigenic Quartz* %	Total Cement %	Pore Filling Clay %	Pore Filling Clay* %	Pore Filling Clay** %	Pore Lining Clay %	Pore Lining Clay* %	Pore Lining Clay** %	Undiss. Ferroan Dolomite [Rh] %
7G1z.1	1.75	0.05	0.06	26.00	1.50	0.05	0.04	1.25	0.04	0.04	7.00
7G1z.2	0.25	0.01	0.01	28.50	1.50	0.05	0.04	0.50	0.02	0.01	6.75
7G1z.3	0.75	0.03	0.03	19.50	3.50	0.15	0.12	0.50	0.02	0.02	8.00
7G1z.4	1.00	0.04	0.07	10.75	2.75	0.19	0.12	0.75	0.05	0.03	1.00
7G1z.5	1.50	0.05	0.10	11.25	3.25	0.21	0.12	1.25	0.08	0.04	1.50
7G1z.6	0.50	0.02	0.04	11.00	2.25	0.16	0.08	0.75	0.05	0.03	2.50
Mean [G1z]	0.96	0.03	0.05	17.83	2.46	0.14	0.09	0.83	0.04	0.03	4.46
7G1x.1	1.75	0.05	0.08	21.25	0.75	0.03	0.02	1.25	0.05	0.04	1.75
7G1x.2	2.25	0.07	0.10	20.00	0.75	0.03	0.02	2.50	0.11	0.08	3.75
Mean [G1x]	2.00	0.06	0.09	20.63	0.75	0.03	0.02	1.88	0.08	0.06	2.75
Mean [1OBS]	1.22	0.05	0.08	18.53	2.03	0.11	0.07	1.09	0.05	0.04	4.03
WRM	2.71	0.08	0.14	14.10	3.48	0.18	0.11	2.19	0.11	0.07	2.33

Sub-Section	Diss. Ferroan Dolomite [Rd]	Ferroan Dolomite [Rh+Rd]	Ferroan Dolomite*	Ferroan Dolomite**	Original Porosity [Pi]	Mean [Pi]	100-(Mean [Pi])	100-[Pi]	IGV	100-[IGV]	COPL [mean]
	%	%	%	%	%	%	%	%	%	%	%
7B3z.1	0.50	3.25	0.14	0.09	41.50	39.30	60.70	58.50	34.50	65.50	7.33
7B3z.2	0.75	6.00	0.25	0.17	41.50	39.30	60.70	58.50	34.50	65.50	7.33
7B3z.3	0.00	3.00	0.16	0.07	41.50	39.30	60.70	58.50	40.50	59.50	-2.02
7B3z.4	0.75	4.25	0.18	0.12	38.40	39.30	60.70	61.60	36.00	64.00	5.16
7B3z.5	0.50	2.50	0.14	0.07	38.40	39.30	60.70	61.60	35.25	64.75	6.25
7B3z.6	0.25	4.25	0.22	0.13	41.50	39.30	60.70	58.50	33.00	67.00	9.40
Mean [B3z]	0.46	3.88	0.18	0.11	40.47	39.30	60.70	59.53	35.63	64.38	5.58
7D3z.1	0.00	1.00	0.07	0.03	41.50	39.30	60.70	58.50	32.00	68.00	10.74
7D3z.2	0.50	2.25	0.12	0.07	38.40	39.30	60.70	61.60	33.00	67.00	9.40
7D3z.3	0.25	3.25	0.14	0.09	41.50	39.30	60.70	58.50	35.00	65.00	6.62
7D3z.4	0.75	1.50	0.08	0.04	41.50	39.30	60.70	58.50	33.50	66.50	8.72
7D3z.5	0.25	1.50	0.08	0.04	41.50	39.30	60.70	58.50	40.50	59.50	-2.02
7D3z.6	0.00	2.75	0.17	0.09	38.40	39.30	60.70	61.60	31.25	68.75	11.71
Mean [D3z]	0.29	2.04	0.11	0.06	40.47	39.30	60.70	59.53	34.21	65.79	7.53
7E3z.1	0.75	1.50	0.07	0.05	38.40	39.30	60.70	61.60	30.50	69.50	12.66
7E3z.2	0.25	0.75	0.03	0.02	38.40	39.30	60.70	61.60	30.50	69.50	12.66
7E3z.3	0.50	2.25	0.12	0.07	41.50	39.30	60.70	58.50	31.00	69.00	12.03
7E3z.4	0.25	1.00	0.04	0.03	38.40	39.30	60.70	61.60	31.75	68.25	11.06
7E3z.5	0.25	1.50	0.08	0.04	41.50	39.30	60.70	58.50	33.75	66.25	8.38
7E3z.6	0.75	2.00	0.11	0.06	38.40	39.30	60.70	61.60	33.00	67.00	9.40
Mean [E3z]	0.46	1.50	0.07	0.05	39.43	39.30	60.70	60.57	31.75	68.25	11.03
7F3z.1	0.00	0.50	0.03	0.02	38.10	39.30	60.70	61.90	31.50	68.50	11.39
7F3z.2	0.50	1.25	0.06	0.04	38.10	39.30	60.70	61.90	31.25	68.75	11.71
7F3z.3	0.50	1.25	0.06	0.04	38.10	39.30	60.70	61.90	28.25	71.75	15.40
7F3z.4	0.50	0.50	0.03	0.01	38.40	39.30	60.70	61.60	34.00	66.00	8.03
7F3z.5	0.25	0.75	0.04	0.02	38.10	39.30	60.70	61.90	31.00	69.00	12.03
7F3z.6	0.25	1.00	0.05	0.03	38.10	39.30	60.70	61.90	33.75	66.25	8.38
Mean [F3z]	0.33	0.88	0.04	0.03	38.15	39.30	60.70	61.85	31.63	68.38	11.16

Sub-Section	Diss. Ferroan Dolomite [Rd]	Ferroan Dolomite [Rh+Rd]	Ferroan Dolomite*	Ferroan Dolomite**	Original Porosity [Pi]	Mean [Pi]	100-(Mean [Pi])	100-[Pi]	IGV	100-[IGV]	COPL [mean]
	%	%	%	%	%	%	%	%	%	%	%
7H3z.1	0.50	4.50	0.22	0.12	40.20	39.30	60.70	59.80	37.75	62.25	2.49
7H3z.2	0.50	2.00	0.12	0.05	38.10	39.30	60.70	61.90	40.00	60.00	-1.17
7H3z.s	1.00	2.25	0.13	0.06	38.10	39.30	60.70	61.90	37.50	62.50	2.88
7H3z.4	0.00	3.00	0.15	0.09	38.10	39.30	60.70	61.90	32.25	67.75	10.41
7H3z.5	0.50	2.00	0.11	0.05	38.10	39.30	60.70	61.90	39.00	61.00	0.49
7H3z.6	0.25	0.75	0.04	0.02	38.10	39.30	60.70	61.90	35.75	64.25	5.53
Mean [H3z]	0.46	2.42	0.13	0.07	38.45	39.30	60.70	61.55	37.04	62.96	3.44
7I3z.1	0.50	3.75	0.16	0.11	40.20	39.30	60.70	59.80	34.00	66.00	8.03
7I3z.2	0.50	3.25	0.14	0.09	38.10	39.30	60.70	61.90	35.50	64.50	5.89
7I3z.3	0.50	2.50	0.16	0.08	40.20	39.30	60.70	59.80	31.25	68.75	11.71
7I3z.4	0.25	2.50	0.12	0.08	40.20	39.30	60.70	59.80	29.75	70.25	13.59
7I3z.5	0.25	1.25	0.05	0.04	38.10	39.30	60.70	61.90	35.25	64.75	6.25
7I3z.6	0.50	2.25	0.10	0.07	38.10	39.30	60.70	61.90	34.50	65.50	7.33
Mean [I3z]	0.42	2.58	0.12	0.08	39.15	39.30	60.70	60.85	33.38	66.63	8.80
7I3x.1	0.50	5.75	0.30	0.18	38.10	39.30	60.70	61.90	32.00	68.00	10.74
7I3x.2	0.00	3.75	0.20	0.11	40.20	39.30	60.70	59.80	33.00	67.00	9.40
Mean [I3x]	0.25	4.75	0.25	0.15	39.15	39.30	60.70	60.85	32.50	67.50	10.07
7J3z.1	0.50	2.00	0.11	0.06	40.20	39.30	60.70	59.80	33.75	66.25	8.38
7J3z.2	0.25	4.50	0.24	0.13	40.20	39.30	60.70	59.80	33.75	66.25	8.38
7J3z.3	0.75	3.75	0.17	0.11	38.10	39.30	60.70	61.90	33.50	66.50	8.72
7J3z.4	0.25	3.00	0.15	0.09	38.10	39.30	60.70	61.90	32.25	67.75	10.41
7J3z.5	0.25	4.25	0.24	0.13	38.10	39.30	60.70	61.90	33.00	67.00	9.40
7J3z.6	0.50	6.25	0.35	0.20	38.10	39.30	60.70	61.90	32.00	68.00	10.74
Mean [J3z]	0.42	3.96	0.21	0.12	38.80	39.30	60.70	61.20	33.04	66.96	9.34
7K3z.1	0.25	3.00	0.15	0.09	38.10	39.30	60.70	61.90	34.25	65.75	7.68
7K3z.2	1.25	2.50	0.11	0.07	40.20	39.30	60.70	59.80	36.25	63.75	4.78
7K3z.3	0.50	3.25	0.19	0.11	38.10	39.30	60.70	61.90	28.50	71.50	15.10
7K3z.4	0.25	1.50	0.08	0.04	38.10	39.30	60.70	61.90	34.25	65.75	7.68
7K3z.5	0.75	3.25	0.15	0.10	40.20	39.30	60.70	59.80	33.50	66.50	8.72

169

Sub-Section	Diss. Ferroan Dolomite [Rd]	Ferroan Dolomite [Rh+Rd]	Ferroan Dolomite*	Ferroan Dolomite**	Original Porosity [Pi]	Mean [Pi]	100-(Mean [Pi])	100-[Pi]	IGV	100-[IGV]	COPL [mean]
	%	%	%	%	%	%	%	%	%	%	%
7K3z.6	1.50	3.00	0.13	0.08	38.10	39.30	60.70	61.90	39.50	60.50	-0.33
Mean [K3z]	0.75	2.75	0.14	0.08	38.80	39.30	60.70	61.20	34.38	65.63	7.27
7M3z.1	0.25	1.75	0.09	0.05	38.10	39.30	60.70	61.90	34.50	65.50	7.33
7M3z.2	0.25	2.25	0.12	0.07	38.10	39.30	60.70	61.90	32.25	67.75	10.41
7M3z.3	0.25	2.00	0.10	0.06	38.10	39.30	60.70	61.90	33.50	66.50	8.72
7M3z.4	0.50	1.75	0.09	0.06	38.10	39.30	60.70	61.90	28.75	71.25	14.81
7M3z.5	0.75	2.50	0.15	0.08	38.10	39.30	60.70	61.90	29.75	70.25	13.59
7M3z.6	0.00	1.75	0.12	0.07	38.10	39.30	60.70	61.90	26.75	73.25	17.13
Mean [M3z]	0.33	2.00	0.11	0.07	38.10	39.30	60.70	61.90	30.92	69.08	12.00
7N3z.1	0.00	1.25	0.09	0.03	38.40	39.30	60.70	61.60	37.50	62.50	2.88
7N3z.2	0.25	1.50	0.12	0.05	38.40	39.30	60.70	61.60	32.00	68.00	10.74
7N3z.3	0.00	1.75	0.12	0.05	38.40	39.30	60.70	61.60	36.75	63.25	4.03
7N3z.4	0.25	1.50	0.11	0.04	38.40	39.30	60.70	61.60	34.50	65.50	7.33
7N3z.5	0.00	1.75	0.12	0.05	38.40	39.30	60.70	61.60	35.50	64.50	5.89
7N3z.6	0.25	1.50	0.10	0.04	38.40	39.30	60.70	61.60	39.25	60.75	0.08
Mean [N3z]	0.13	1.54	0.11	0.04	38.40	39.30	60.70	61.60	35.92	64.08	5.16
7O3z.1	0.00	1.75	0.11	0.06	33.30	39.30	60.70	66.70	28.25	71.75	15.40
7O3z.2	0.00	0.50	0.04	0.02	33.30	39.30	60.70	66.70	26.50	73.50	17.41
7O3z.3	0.25	1.50	0.09	0.05	38.40	39.30	60.70	61.60	32.00	68.00	10.74
7O3z.4	0.00	1.25	0.08	0.04	38.40	39.30	60.70	61.60	31.25	68.75	11.71
7O3z.5	0.00	0.75	0.05	0.02	33.30	39.30	60.70	66.70	33.75	66.25	8.38
7O3z.6	0.00	1.00	0.06	0.03	38.40	39.30	60.70	61.60	32.50	67.50	10.07
Mean [O3z]	0.04	1.13	0.07	0.04	35.85	39.30	60.70	64.15	30.71	69.29	12.29
7O3x.1	0.75	1.50	0.10	0.05	38.40	39.30	60.70	61.60	29.50	70.50	13.90
7O3x.2	0.00	1.75	0.14	0.06	38.40	39.30	60.70	61.60	28.75	71.25	14.81
Mean [O3x]	0.38	1.63	0.12	0.06	38.40	39.30	60.70	61.60	29.13	70.88	14.35
Mean [3OBS]	0.37	2.30	0.12	0.07	38.74	39.30	60.70	61.26	33.35	66.65	8.72

Sub-Section	Diss. Ferroan Dolomite [Rd]	Ferroan Dolomite [Rh+Rd]	Ferroan Dolomite*	Ferroan Dolomite**	Original Porosity [Pi]	Mean [Pi]	100-(Mean [Pi])	100-[Pi]	IGV	100-[IGV]	COPL [mean]
	%	%	%	%	%	%	%	%	%	%	%
7A2z.1	0.00	5.00	0.19	0.13	34.20	38.30	61.70	65.80	38.00	62.00	0.48
7A2z.2	0.50	4.00	0.16	0.13	38.10	38.30	61.70	61.90	31.00	69.00	10.58
7A2z.3	0.75	2.25	0.10	0.07	38.40	38.30	61.70	61.60	30.50	69.50	11.22
7A2z.4	0.25	6.50	0.24	0.17	38.40	38.30	61.70	61.60	38.00	62.00	0.48
7A2z.5	1.00	5.25	0.19	0.14	38.40	38.30	61.70	61.60	37.25	62.75	1.67
7A2z.6	0.50	3.00	0.10	0.08	34.20	38.30	61.70	65.80	36.75	63.25	2.45
Mean [A2z]	0.50	4.33	0.16	0.12	36.95	38.30	61.70	63.05	35.25	64.75	4.48
7C2z.1	0.25	2.00	0.10	0.06	38.40	38.30	61.70	61.60	33.50	66.50	7.22
7C2z.2	0.50	2.75	0.16	0.08	41.50	38.30	61.70	58.50	34.00	66.00	6.52
7C2z.3	0.50	2.00	0.10	0.06	38.40	38.30	61.70	61.60	32.25	67.75	8.93
7C2z.4	0.50	4.00	0.20	0.12	41.50	38.30	61.70	58.50	34.00	66.00	6.52
7C2z.5	0.25	2.25	0.10	0.06	41.50	38.30	61.70	58.50	36.50	63.50	2.83
7C2z.6	0.25	1.75	0.08	0.05	38.40	38.30	61.70	61.60	37.25	62.75	1.67
Mean [C2z]	0.38	2.46	0.12	0.07	39.95	38.30	61.70	60.05	34.58	65.42	5.61
7C2x.1	0.25	2.25	0.16	0.06	41.50	38.30	61.70	58.50	35.75	64.25	3.97
7C2x.2	0.50	2.00	0.11	0.06	38.40	38.30	61.70	61.60	35.00	65.00	5.08
Mean [C2x]	0.38	2.13	0.14	0.06	39.95	38.30	61.70	60.05	35.38	64.63	4.52
7L2z.1	0.25	4.25	0.20	0.13	38.10	38.30	61.70	61.90	32.25	67.75	8.93
7L2z.2	0.00	4.75	0.22	0.13	38.10	38.30	61.70	61.90	35.25	64.75	4.71
7L2z.3	0.25	2.25	0.11	0.07	38.10	38.30	61.70	61.90	31.75	68.25	9.60
7L2z.4	0.50	3.50	0.13	0.10	38.10	38.30	61.70	61.90	34.00	66.00	6.52
7L2z.5	1.00	5.25	0.23	0.18	38.10	38.30	61.70	61.90	29.50	70.50	12.48
7L2z.6	0.50	3.25	0.14	0.11	34.20	38.30	61.70	65.80	30.25	69.75	11.54
Mean [L2z]	0.42	3.88	0.17	0.12	37.45	38.30	61.70	62.55	32.17	67.83	8.96
7L2x.1	0.50	3.00	0.16	0.08	38.40	38.30	61.70	61.60	35.50	64.50	4.34
7L2x.2	0.25	3.50	0.17	0.11	38.40	38.30	61.70	61.60	33.00	67.00	7.91
Mean [L2x]	0.38	3.25	0.16	0.10	38.40	38.30	61.70	61.60	34.25	65.75	6.13
Mean [2OBS]	0.42	3.40	0.15	0.10	38.31	38.30	61.70	61.69	34.15	65.85	6.17

171

Sub-Section	Diss. Ferroan Dolomite [Rd]	Ferroan Dolomite [Rh+Rd]	Ferroan Dolomite*	Ferroan Dolomite**	Original Porosity [Pi]	Mean [Pi]	100-(Mean [Pi])	100-[Pi]	IGV	100-[IGV]	COPL [mean]
	%	%	%	%	%	%	%	%	%	%	%
7G1z.1	0.25	7.27	0.25	0.22	38.10	38.90	61.10	61.90	33.75	66.25	7.77
7G1z.2	0.25	7.00	0.23	0.19	40.20	38.90	61.10	59.80	37.50	62.50	2.24
7G1z.3	0.50	8.50	0.36	0.28	40.20	38.90	61.10	59.80	30.00	70.00	12.71
7G1z.4	1.00	2.00	0.14	0.09	38.10	38.90	61.10	61.90	23.25	76.75	20.39
7G1z.5	0.75	2.25	0.14	0.08	38.10	38.90	61.10	61.90	28.00	72.00	15.14
7G1z.6	0.75	3.25	0.23	0.12	38.10	38.90	61.10	61.90	28.25	71.75	14.84
Mean [G1z]	0.58	5.05	0.23	0.16	38.80	38.90	61.10	61.20	30.13	69.88	12.18
7G1x.1	0.50	2.25	0.10	0.07	40.20	38.90	61.10	59.80	33.75	66.25	7.77
7G1x.2	0.25	4.00	0.17	0.13	38.10	38.90	61.10	61.90	31.75	68.25	10.48
Mean [G1x]	0.38	3.13	0.13	0.10	39.15	38.90	61.10	60.85	32.75	67.25	9.12
Mean [1OBS]	0.53	4.57	0.20	0.15	38.89	38.90	61.10	61.11	30.78	69.22	11.42
WRM	0.39	2.72	0.14	0.08	38.65	39.05	60.95	61.35	33.32	66.68	8.37

Sub-Section	COPL [original] %	CEPL [mean] %	Compaction Index	Total Cement* %	Total Cement** %	Total Clay %	Total Clay* %	Total Clay** %	Porosity %	Macroporosity %	Microporosity %
7B3z.1	10.69	14.83	0.33	0.67	0.46	7.75	0.33	0.22	14.50	14.25	0.25
7B3z.2	10.69	17.61	0.29	0.78	0.55	5.25	0.22	0.15	15.25	14.75	0.50
7B3z.3	1.68	14.79	-0.16	0.79	0.36	3.75	0.21	0.09	27.00	26.75	0.25
7B3z.4	3.75	15.65	0.25	0.71	0.46	6.75	0.29	0.19	17.75	17.75	0.00
7B3z.5	4.86	11.02	0.36	0.67	0.33	5.75	0.33	0.16	21.50	21.00	0.50
7B3z.6	12.69	14.27	0.40	0.83	0.48	3.25	0.17	0.10	19.50	19.25	0.25
Mean [B3z]	7.39	14.69	0.25	0.74	0.44	5.42	0.26	0.15	19.25	18.96	0.29
7D3z.1	13.97	8.48	0.56	0.67	0.30	4.75	0.33	0.15	20.75	20.75	0.00
7D3z.2	8.06	9.97	0.49	0.59	0.33	7.50	0.41	0.23	17.75	17.50	0.25
7D3z.3	10.00	11.91	0.36	0.57	0.36	9.75	0.43	0.28	14.50	13.75	0.75
7D3z.4	12.03	9.58	0.48	0.56	0.31	8.25	0.44	0.25	18.25	18.25	0.00
7D3z.5	1.68	11.48	-0.21	0.57	0.28	8.50	0.43	0.21	23.50	23.50	0.00
7D3z.6	10.40	9.49	0.55	0.65	0.34	5.75	0.35	0.18	17.00	16.75	0.25
Mean [D3z]	9.36	10.15	0.37	0.60	0.32	7.42	0.40	0.22	18.63	18.42	0.21
7E3z.1	11.37	11.57	0.52	0.60	0.43	9.00	0.40	0.30	12.00	12.00	0.00
7E3z.2	11.37	9.83	0.56	0.52	0.37	10.25	0.48	0.34	12.00	12.00	0.00
7E3z.3	15.22	8.58	0.58	0.51	0.31	9.25	0.49	0.30	18.00	18.00	0.00
7E3z.4	9.74	9.78	0.53	0.48	0.35	11.75	0.52	0.37	14.00	14.00	0.00
7E3z.5	11.70	11.22	0.43	0.62	0.36	7.50	0.38	0.22	17.75	17.75	0.00
7E3z.6	8.06	9.74	0.49	0.57	0.33	8.00	0.43	0.24	19.50	19.50	0.00
Mean [E3z]	11.24	10.12	0.52	0.55	0.36	9.29	0.45	0.29	15.54	15.54	0.00
7F3z.1	9.64	7.98	0.59	0.47	0.29	10.25	0.53	0.33	16.25	16.25	0.00
7F3z.2	9.96	10.37	0.53	0.55	0.38	9.75	0.45	0.31	13.75	13.75	0.00
7F3z.3	13.73	8.46	0.65	0.52	0.35	9.25	0.48	0.33	12.75	12.75	0.00
7F3z.4	6.67	7.82	0.51	0.44	0.25	11.00	0.56	0.32	18.75	18.50	0.25
7F3z.5	10.29	10.34	0.54	0.57	0.38	9.00	0.43	0.29	13.25	13.00	0.25
7F3z.6	6.57	12.83	0.40	0.68	0.41	6.50	0.32	0.19	16.25	16.25	0.00
Mean [F3z]	9.47	9.63	0.53	0.54	0.34	9.29	0.46	0.30	15.17	15.08	0.08

Sub-Section	COPL [original]	CEPL [mean]	Compaction Index	Total Cement*	Total Cement**	Total Clay	Total Clay*	Total Clay**	Porosity	Macroporosity	Microporosity
	%	%		%	%	%	%	%	%	%	%
7H3z.1	3.94	14.38	0.15	0.72	0.39	5.75	0.28	0.15	20.25	20.25	0.00
7H3z.2	-3.17	10.88	-0.12	0.64	0.27	6.00	0.36	0.15	26.00	26.00	0.00
7H3z.s	0.96	10.93	0.21	0.65	0.30	6.00	0.35	0.16	22.00	22.00	0.00
7H3z.4	8.63	12.77	0.45	0.70	0.44	6.00	0.30	0.19	15.00	14.75	0.25
7H3z.5	-1.48	12.94	0.04	0.70	0.33	5.50	0.30	0.14	22.75	22.75	0.00
7H3z.6	3.66	10.39	0.35	0.57	0.31	8.25	0.43	0.23	20.50	20.50	0.00
Mean [H3z]	2.09	12.05	0.18	0.67	0.34	6.25	0.33	0.17	21.08	21.04	0.04
7I3z.1	9.39	15.63	0.34	0.74	0.50	6.00	0.26	0.18	13.25	13.25	0.00
7I3z.2	4.03	14.59	0.29	0.65	0.44	8.25	0.35	0.23	14.25	14.25	0.00
7I3z.3	13.02	9.71	0.55	0.72	0.35	4.25	0.28	0.14	18.75	18.75	0.00
7I3z.4	14.88	11.23	0.55	0.63	0.44	7.50	0.37	0.25	12.25	12.25	0.00
7I3z.5	4.40	13.83	0.31	0.63	0.42	8.50	0.37	0.24	15.00	15.00	0.00
7I3z.6	5.50	15.75	0.32	0.76	0.49	5.50	0.24	0.16	14.00	14.00	0.00
Mean [I3z]	8.54	13.46	0.39	0.69	0.44	6.67	0.31	0.20	14.58	14.58	0.00
7I3x.1	8.97	15.84	0.40	0.92	0.55	1.50	0.08	0.05	14.50	14.50	0.00
7I3x.2	10.75	13.82	0.40	0.80	0.46	3.75	0.20	0.11	14.75	14.75	0.00
Mean [I3x]	9.86	14.83	0.40	0.86	0.51	2.63	0.14	0.08	14.63	14.63	0.00
7J3z.1	9.74	9.85	0.46	0.57	0.32	8.25	0.43	0.24	17.25	17.25	0.00
7J3z.2	9.74	9.85	0.46	0.57	0.32	8.00	0.43	0.24	17.50	17.25	0.25
7J3z.3	6.92	13.24	0.40	0.65	0.43	7.75	0.35	0.23	14.75	14.75	0.00
7J3z.4	8.63	10.08	0.51	0.56	0.35	8.75	0.44	0.27	14.75	14.50	0.25
7J3z.5	7.61	11.10	0.46	0.68	0.37	5.75	0.32	0.17	16.00	16.00	0.00
7J3z.6	8.97	12.50	0.46	0.78	0.44	4.00	0.22	0.13	15.75	15.50	0.25
Mean [J3z]	8.60	11.10	0.46	0.64	0.37	7.08	0.36	0.21	16.00	15.88	0.13
7K3z.1	5.86	11.54	0.40	0.63	0.36	7.25	0.37	0.21	17.75	17.75	0.00
7K3z.2	6.20	13.81	0.26	0.67	0.40	7.25	0.33	0.20	16.25	16.25	0.00
7K3z.3	13.43	10.19	0.60	0.70	0.42	5.25	0.30	0.18	13.00	13.00	0.00
7K3z.4	5.86	12.00	0.39	0.65	0.38	7.00	0.35	0.20	16.25	16.25	0.00
7K3z.5	10.08	12.78	0.41	0.64	0.42	7.75	0.36	0.23	14.25	14.25	0.00

Sub-Section	COPL [original] %	CEPL [mean] %	Compaction Index	Total Cement* %	Total Cement** %	Total Clay %	Total Clay* %	Total Clay** %	Porosity %	Macroporosity %	Microporosity %
7K3z.6	-2.31	15.55	-0.02	0.69	0.39	7.00	0.31	0.18	19.50	19.50	0.00
Mean [K3z]	6.52	12.64	0.34	0.66	0.40	6.92	0.34	0.20	16.17	16.17	0.00
7M3z.1	5.50	10.66	0.41	0.61	0.33	7.50	0.39	0.22	19.75	19.75	0.00
7M3z.2	8.63	11.65	0.47	0.68	0.40	6.25	0.32	0.19	14.25	14.25	0.00
7M3z.3	6.92	13.46	0.39	0.74	0.44	5.25	0.26	0.16	14.50	14.50	0.00
7M3z.4	13.12	11.93	0.55	0.74	0.49	5.00	0.26	0.17	11.00	11.00	0.00
7M3z.5	11.89	11.23	0.55	0.78	0.44	3.75	0.22	0.13	15.00	15.00	0.00
7M3z.6	15.49	9.53	0.64	0.81	0.43	2.75	0.19	0.10	14.50	14.50	0.00
Mean [M3z]	10.26	11.41	0.50	0.72	0.42	5.08	0.28	0.16	14.83	14.83	0.00
7N3z.1	1.44	10.44	0.22	0.75	0.29	3.50	0.25	0.09	26.25	26.25	0.00
7N3z.2	9.41	9.37	0.53	0.82	0.33	2.25	0.18	0.07	22.50	22.25	0.25
7N3z.3	2.61	12.00	0.25	0.86	0.34	2.00	0.14	0.05	24.25	24.25	0.00
7N3z.4	5.95	9.27	0.44	0.70	0.29	4.25	0.30	0.12	22.50	22.25	0.25
7N3z.5	4.50	11.29	0.34	0.83	0.34	2.50	0.17	0.07	22.00	22.00	0.00
7N3z.6	-1.40	11.99	0.01	0.76	0.31	3.75	0.24	0.10	24.75	24.75	0.00
Mean [N3z]	3.75	10.73	0.30	0.79	0.31	3.04	0.21	0.08	23.71	23.63	0.08
7O3z.1	7.04	11.00	0.58	0.83	0.46	2.75	0.17	0.10	14.00	14.00	0.00
7O3z.2	9.25	8.88	0.66	0.83	0.41	2.25	0.17	0.08	16.00	16.00	0.00
7O3z.3	9.41	12.27	0.47	0.85	0.43	2.50	0.15	0.08	19.00	18.75	0.25
7O3z.4	10.40	10.15	0.54	0.72	0.37	4.50	0.28	0.14	17.75	17.50	0.25
7O3z.5	-0.68	12.60	0.40	0.93	0.41	1.00	0.07	0.03	21.00	21.00	0.00
7O3z.6	8.74	11.02	0.48	0.77	0.38	3.75	0.23	0.12	21.75	21.75	0.00
Mean [O3z]	7.36	10.99	0.52	0.82	0.41	2.79	0.18	0.09	18.25	18.17	0.08
7O3x.1	12.62	10.33	0.57	0.80	0.41	3.00	0.20	0.10	16.75	16.75	0.00
7O3x.2	13.54	9.58	0.61	0.88	0.39	1.50	0.12	0.05	18.75	18.75	0.00
Mean [O3x]	13.08	9.96	0.59	0.84	0.40	2.25	0.16	0.08	17.75	17.75	0.00
Mean [3OBS]	7.91	11.59	0.40	0.68	0.38	6.08	0.32	0.18	17.49	17.41	0.08

Sub-Section	COPL [original]	CEPL [mean]	Compaction Index	Total Cement*	Total Cement**	Total Clay	Total Clay*	Total Clay**	Porosity	Macroporosity	Microporosity
	%	%		%	%	%	%	%	%	%	%
7A2z.1	-6.13	22.14	0.02	0.85	0.59	4.00	0.15	0.11	17.00	16.75	0.25
7A2z.2	10.29	19.67	0.35	0.91	0.71	2.25	0.09	0.07	11.25	11.25	0.00
7A2z.3	11.37	19.31	0.37	0.93	0.71	1.75	0.07	0.06	13.25	13.25	0.00
7A2z.4	0.65	25.38	0.02	0.93	0.67	2.00	0.07	0.05	12.75	12.25	0.50
7A2z.5	1.83	23.60	0.07	0.89	0.64	3.00	0.11	0.08	13.50	13.50	0.00
7A2z.6	-4.03	26.09	0.09	0.89	0.73	3.25	0.11	0.09	13.25	12.50	0.75
Mean [A2z]	2.33	22.70	0.15	0.90	0.68	2.71	0.10	0.08	13.50	13.25	0.25
7C2z.1	7.37	10.44	0.41	0.54	0.34	9.75	0.46	0.29	17.50	17.25	0.25
7C2z.2	11.36	10.05	0.39	0.62	0.32	6.50	0.38	0.19	19.00	19.00	0.00
7C2z.3	9.08	9.11	0.50	0.49	0.31	10.25	0.51	0.32	14.25	14.25	0.00
7C2z.4	11.36	13.79	0.32	0.73	0.43	5.50	0.27	0.16	19.00	18.50	0.50
7C2z.5	7.87	13.36	0.18	0.60	0.38	9.00	0.40	0.25	19.75	19.50	0.25
7C2z.6	1.83	10.32	0.14	0.47	0.28	11.75	0.53	0.32	19.50	19.50	0.00
Mean [C2z]	8.15	11.18	0.32	0.58	0.34	8.79	0.42	0.25	18.17	18.00	0.17
7C2x.1	8.95	10.80	0.27	0.82	0.31	2.50	0.18	0.07	23.75	23.75	0.00
7C2x.2	5.23	12.10	0.30	0.73	0.36	4.75	0.27	0.14	18.75	18.75	0.00
Mean [C2x]	7.09	11.45	0.28	0.77	0.34	3.63	0.23	0.10	21.25	21.25	0.00
7L2z.1	8.63	12.29	0.42	0.64	0.42	7.75	0.36	0.24	12.50	12.50	0.00
7L2z.2	4.40	16.20	0.23	0.79	0.48	4.50	0.21	0.13	14.75	14.75	0.00
7L2z.3	9.30	11.75	0.45	0.63	0.41	7.75	0.37	0.24	13.00	13.00	0.00
7L2z.4	6.21	20.80	0.24	0.82	0.65	5.00	0.18	0.15	8.50	8.50	0.00
7L2z.5	12.20	17.50	0.42	0.87	0.68	3.00	0.13	0.10	7.75	7.75	0.00
7L2z.6	5.66	16.14	0.42	0.76	0.60	5.75	0.24	0.19	7.75	7.75	0.00
Mean [L2z]	7.74	15.78	0.36	0.75	0.54	5.63	0.25	0.18	10.71	10.71	0.00
7L2x.1	4.50	16.26	0.21	0.88	0.48	2.25	0.12	0.06	19.00	19.00	0.00
7L2x.2	8.06	14.50	0.35	0.76	0.48	5.00	0.24	0.15	14.25	14.25	0.00
Mean [L2x]	6.28	15.38	0.28	0.82	0.48	3.63	0.18	0.11	16.63	16.63	0.00
Mean [2OBS]	6.18	15.98	0.28	0.75	0.50	5.33	0.25	0.16	15.00	14.89	0.11

Sub-Section	COPL [original]	CEPL [mean]	Compaction Index	Total Cement*	Total Cement**	Total Clay	Total Clay*	Total Clay**	Porosity	Macroporosity	Microporosity
	%	%		%	%	%	%	%	%	%	%
7G1z.1	6.57	23.98	0.24	0.90	0.77	2.75	0.10	0.08	6.00	6.00	0.00
7G1z.2	4.32	27.86	0.07	0.93	0.76	2.00	0.07	0.05	8.75	8.75	0.00
7G1z.3	14.57	17.02	0.43	0.83	0.65	4.00	0.17	0.13	8.00	7.75	0.25
7G1z.4	19.35	8.56	0.70	0.75	0.46	3.50	0.25	0.15	11.75	11.50	0.25
7G1z.5	14.03	9.55	0.61	0.71	0.40	4.50	0.29	0.16	15.50	15.50	0.00
7G1z.6	13.73	9.37	0.61	0.79	0.39	3.00	0.21	0.11	19.00	19.00	0.00
Mean [G1z]	12.09	16.06	0.45	0.82	0.57	3.29	0.18	0.11	11.50	11.42	0.08
7G1x.1	9.74	19.60	0.28	0.91	0.63	2.00	0.09	0.06	13.50	13.50	0.00
7G1x.2	9.30	17.90	0.37	0.86	0.63	3.25	0.14	0.10	10.75	10.75	0.00
Mean [G1x]	9.52	18.75	0.33	0.89	0.63	2.63	0.11	0.08	12.13	12.13	0.00
Mean [1OBS]	10.81	16.73	0.42	0.84	0.59	3.13	0.16	0.11	11.66	11.59	0.06
WRM	7.81	12.97	0.38	0.71	0.42	5.68	0.29	0.17	16.47	16.39	0.09

177

Sub-Section	Intergranular Porosity	Intergranular Porosity**	Intragranular Porosity	Mean Pore Width [MPW]	Mean Pore Width [MPW]	Inter Primary Porosity	Primary Mean Width	Inter Secondary Porosity	Secondary Mean Width	Fracture Porosity
	%	%	%	mm	phi	%	mm	%	mm	%
7B3z.1	10.75	0.31	3.75	0.13	2.94	0.25	0.15	10.50	0.13	0.00
7B3z.2	10.25	0.30	5.00	0.10	3.32	1.00	0.11	9.25	0.10	0.00
7B3z.3	22.25	0.55	4.75	0.19	2.40	1.50	0.13	20.75	0.19	0.00
7B3z.4	12.75	0.35	5.00	0.14	2.84	0.50	0.10	12.00	0.14	0.25
7B3z.5	17.75	0.50	3.75	0.15	2.74	0.50	0.20	17.25	0.15	0.00
7B3z.6	14.00	0.42	5.50	0.14	2.84	0.25	0.15	13.75	0.14	0.00
Mean [B3z]	14.63	0.41	4.63	0.14	2.85	0.67	0.14	13.92	0.14	0.04
7D3z.1	17.75	0.55	3.00	0.13	2.94	0.00	0.00	17.50	0.13	0.25
7D3z.2	14.50	0.44	3.25	0.11	3.18	0.50	0.10	14.00	0.11	0.00
7D3z.3	12.50	0.36	2.00	0.12	3.06	0.00	0.00	12.50	0.12	0.00
7D3z.4	14.75	0.44	3.50	0.13	2.94	0.50	0.14	14.00	0.13	0.25
7D3z.5	20.75	0.51	2.75	0.13	2.94	0.00	0.00	19.75	0.13	0.25
7D3z.6	14.75	0.47	2.25	0.11	3.18	0.00	0.00	13.50	0.11	0.00
Mean [D3z]	15.83	0.46	2.79	0.12	3.04	0.17	0.04	15.21	0.12	0.13
7E3z.1	8.25	0.27	3.75	0.09	3.47	0.00	0.00	7.50	0.09	0.25
7E3z.2	9.00	0.30	3.00	0.10	3.32	0.00	0.00	9.00	0.10	0.00
7E3z.3	12.00	0.39	6.00	0.09	3.47	0.00	0.00	12.00	0.09	0.00
7E3z.4	9.00	0.28	5.00	0.10	3.32	0.25	0.28	8.25	0.10	0.50
7E3z.5	14.00	0.41	3.75	0.12	3.06	0.25	0.12	13.25	0.12	0.50
7E3z.6	14.25	0.43	5.25	0.10	3.32	0.25	0.18	13.75	0.10	0.25
Mean [E3z]	11.08	0.35	4.46	0.10	3.33	0.13	0.10	10.63	0.10	0.25
7F3z.1	12.25	0.39	4.00	0.09	3.47	0.00	0.00	11.75	0.09	0.50
7F3z.2	9.75	0.31	4.00	0.10	3.32	0.50	0.10	9.25	0.10	0.00
7F3z.3	9.00	0.32	3.75	0.11	3.18	0.00	0.00	9.00	0.11	0.00
7F3z.4	14.50	0.43	4.25	0.11	3.18	0.25	0.09	14.00	0.11	0.25
7F3z.5	10.25	0.33	3.00	0.09	3.47	0.25	0.33	9.50	0.09	0.50
7F3z.6	13.25	0.39	3.00	0.10	3.32	0.25	0.07	12.75	0.10	0.25
Mean [F3z]	11.50	0.36	3.67	0.10	3.33	0.21	0.10	11.04	0.10	0.25

178

Sub-Section	Intergranular Porosity	Intergranular Porosity**	Intragranular Porosity	Mean Pore Width [MPW]	Mean Pore Width [MPW]	Inter Primary Porosity	Primary Mean Width	Inter Secondary Porosity	Secondary Mean Width	Fracture Porosity
	%	%	%	mm	phi	%	mm	%	mm	%
7H3z.1	17.25	0.46	3.00	0.12	3.06	0.00	0.00	17.00	0.12	0.25
7H3z.2	23.25	0.58	2.75	0.19	2.40	0.00	0.00	22.75	0.19	0.50
7H3z.s	20.25	0.54	1.75	0.15	2.74	0.00	0.00	20.00	0.15	0.25
7H3z.4	12.00	0.37	3.00	0.16	2.64	0.25	0.11	11.25	0.16	0.50
7H3z.5	20.50	0.53	2.25	0.18	2.47	0.25	0.20	19.50	0.18	0.75
7H3z.6	16.50	0.46	4.00	0.14	2.84	0.00	0.00	16.50	0.14	
Mean [H3z]	18.29	0.49	2.79	0.16	2.69	0.08	0.05	17.83	0.16	0.38
7I3z.1	11.00	0.32	2.25	0.09	3.47	0.00	0.00	10.75	0.09	0.25
7I3z.2	11.75	0.33	3.50	0.10	3.32	0.50	0.12	10.75	0.10	0.50
7I3z.3	16.00	0.51	2.75	0.11	3.18	0.00	0.00	15.50	0.11	0.50
7I3z.4	9.25	0.31	3.00	0.09	3.47	0.25	0.16	8.25	0.09	0.75
7I3z.5	12.00	0.34	3.00	0.08	3.64	0.00	0.00	11.75	0.08	0.25
7I3z.6	12.00	0.35	2.00	0.12	3.06	0.25	0.13	11.50	0.12	0.25
Mean [I3z]	12.00	0.36	2.75	0.10	3.36	0.17	0.07	11.42	0.10	0.42
7I3x.1	12.75	0.40	1.75	0.11	3.18	0.25	0.12	12.25	0.11	0.25
7I3x.2	14.00	0.42	0.75	0.11	3.18	0.25	0.16	13.25	0.11	0.50
Mean [I3x]	13.38	0.41	1.25	0.11	3.18	0.25	0.14	12.75	0.11	0.38
7J3z.1	14.75	0.44	2.50	0.10	3.32	0.25	0.11	14.25	0.10	0.25
7J3z.2	15.00	0.44	2.25	0.10	3.32	0.25	0.18	14.50	0.10	0.25
7J3z.3	11.25	0.34	3.50	0.12	3.06	0.50	0.17	10.75	0.12	0.00
7J3z.4	12.25	0.38	2.50	0.11	3.18	0.00	0.00	12.25	0.11	0.00
7J3z.5	15.00	0.45	1.00	0.13	2.94	0.00	0.00	14.50	0.13	0.50
7J3z.6	14.00	0.44	1.75	0.12	3.06	0.50	0.23	13.25	0.12	0.25
Mean [J3z]	13.71	0.41	2.25	0.11	3.15	0.25	0.12	13.25	0.11	0.21
7K3z.1	14.50	0.42	3.25	0.11	3.18	0.25	0.09	14.00	0.11	0.25
7K3z.2	14.50	0.40	1.75	0.15	2.74	0.00	0.00	13.25	0.15	0.50
7K3z.3	11.25	0.39	1.75	0.11	3.18	0.00	0.00	11.25	0.11	0.00
7K3z.4	14.25	0.42	2.00	0.12	3.06	0.00	0.00	14.00	0.12	0.25
7K3z.5	11.75	0.35	2.50	0.12	3.06	0.00	0.00	11.25	0.12	0.25

179

Sub-Section	Intergranular Porosity	Intergranular Porosity**	Intragranular Porosity	Mean Pore Width [MPW]	Mean Pore Width [MPW]	Inter Primary Porosity	Primary Mean Width	Inter Secondary Porosity	Secondary Mean Width	Fracture Porosity
	%	%	%	mm	phi	%	mm	%	mm	%
7K3z.6	17.00	0.43	2.50	0.15	2.74	0.00	0.00	17.00	0.50	0.00
Mean [K3z]	13.88	0.40	2.29	0.13	2.99	0.04	0.02	13.46	0.19	0.21
7M3z.1	15.50	0.45	4.25	0.12	3.06	0.00	0.00	15.50	0.12	0.00
7M3z.2	13.00	0.40	1.25	0.08	3.64	0.00	0.00	12.75	0.08	0.25
7M3z.3	13.50	0.40	1.00	0.08	3.64	0.00	0.00	13.25	0.08	0.25
7M3z.4	9.75	0.34	1.25	0.08	3.64	0.00	0.00	9.75	0.08	0.00
7M3z.5	13.00	0.44	2.00	0.07	3.84	0.25	0.11	12.50	0.07	0.25
7M3z.6	12.50	0.47	2.00	0.10	3.32	0.00	0.00	12.50	0.10	0.00
Mean [M3z]	12.88	0.42	1.96	0.09	3.53	0.04	0.02	12.71	0.09	0.13
7N3z.1	23.25	0.62	3.00	0.12	3.06	0.00	0.00	23.25	0.12	0.00
7N3z.2	19.25	0.60	3.25	0.12	3.06	0.00	0.00	19.25	0.12	0.00
7N3z.3	22.25	0.61	2.00	0.12	3.06	0.25	0.26	22.00	0.12	0.00
7N3z.4	20.25	0.59	2.25	0.12	3.06	0.75	0.17	19.25	0.12	0.25
7N3z.5	21.00	0.59	1.00	0.12	3.06	0.00	0.00	20.75	0.12	0.25
7N3z.6	23.50	0.60	1.25	0.12	3.06	0.25	0.18	23.00	0.12	0.25
Mean [N3z]	21.58	0.60	2.13	0.12	3.06	0.21	0.10	21.25	0.12	0.13
7O3z.1	12.50	0.44	1.50	0.14	2.84	0.00	0.00	12.50	0.14	0.00
7O3z.2	13.50	0.51	2.50	0.14	2.84	0.00	0.00	13.50	0.14	0.00
7O3z.3	15.75	0.49	3.25	0.13	2.94	0.00	0.00	15.75	0.13	0.00
7O3z.4	15.25	0.49	2.50	0.14	2.84	0.00	0.00	15.25	0.14	0.00
7O3z.5	19.00	0.56	2.00	0.11	3.18	0.00	0.00	18.75	0.11	0.25
7O3z.6	16.50	0.51	5.25	0.11	3.18	0.00	0.00	15.75	0.11	0.75
Mean [O3z]	15.42	0.50	2.83	0.13	2.97	0.00	0.00	15.25	0.13	0.17
7O3x.1	14.50	0.49	2.25	0.13	2.94	0.25	0.20	14.25	0.13	0.00
7O3x.2	16.00	0.56	2.75	0.13	2.94	0.25	0.09	15.75	0.13	0.00
Mean [O3x]	15.25	0.52	2.50	0.13	2.94	0.25	0.15	15.00	0.13	0.00
Mean [3OBS]	14.60	0.44	2.90	0.12	3.11	0.18	0.07	14.16	0.12	0.21

Sub-Section	Intergranular Porosity	Intergranular Porosity**	Intragranular Porosity	Mean Pore Width [MPW]	Mean Pore Width [MPW]	Inter Primary Porosity	Primary Mean Width	Inter Secondary Porosity	Secondary Mean Width	Fracture Porosity
	%	%	%	mm	phi	%	mm	%	mm	%
7A2z.1	11.75	0.31	5.25	0.08	3.64	1.25	0.08	10.25	0.08	0.25
7A2z.2	6.75	0.22	4.50	N/A	N/A	0.75	0.00	6.00	0.00	0.00
7A2z.3	7.00	0.23	6.25	0.06	4.06	0.50	0.12	6.50	0.06	0.00
7A2z.4	10.50	0.28	2.25	0.15	2.74	0.75	0.07	9.75	0.15	0.00
7A2z.5	10.25	0.28	3.25	0.14	2.84	0.75	0.19	9.50	0.14	0.00
7A2z.6	6.75	0.18	6.50	0.10	3.32	0.50	0.24	5.75	0.10	0.50
Mean [A2z]	8.83	0.25	4.67	0.09	2.77	0.75	0.12	7.96	0.09	0.13
7C2z.1	12.50	0.37	5.00	0.13	2.94	0.50	0.21	12.00	0.13	0.00
7C2z.2	16.75	0.49	2.25	0.14	2.84	0.50	0.22	16.25	0.14	0.00
7C2z.3	12.00	0.37	2.25	0.11	3.18	0.25	0.26	11.75	0.11	0.00
7C2z.4	13.75	0.40	5.25	0.14	2.84	0.75	0.15	13.00	0.14	0.00
7C2z.5	13.75	0.38	6.00	0.12	3.06	0.50	0.17	13.25	0.12	0.00
7C2z.6	15.00	0.40	4.50	0.13	2.94	0.25	0.16	14.75	0.13	0.00
Mean [C2z]	13.96	0.40	4.21	0.13	2.97	0.46	0.20	13.50	0.13	0.00
7C2x.1	22.00	0.62	1.75	0.20	2.32	0.25	0.34	21.50	0.20	0.25
7C2x.2	17.50	0.50	1.25	0.16	2.64	0.50	0.23	17.00	0.16	0.00
Mean [C2x]	19.75	0.56	1.50	0.18	2.48	0.38	0.29	19.25	0.18	0.13
7L2z.1	11.00	0.34	1.50	0.09	3.47	0.00	0.00	11.00	0.09	0.00
7L2z.2	13.75	0.39	1.00	0.09	3.47	0.00	0.00	13.50	0.09	0.25
7L2z.3	11.00	0.35	2.00	0.08	3.64	0.00	0.00	11.00	0.08	0.00
7L2z.4	6.75	0.20	1.75	0.06	4.06	0.00	0.00	6.75	0.06	0.00
7L2z.5	6.50	0.22	1.25	0.07	3.84	0.00	0.00	6.50	0.07	0.00
7L2z.6	6.25	0.21	1.50	0.07	3.84	0.00	0.00	6.25	0.07	0.00
Mean [L2z]	9.21	0.28	1.50	0.08	3.72	0.00	0.00	9.17	0.08	0.04
7L2x.1	16.25	0.46	2.75	0.15	2.74	0.50	0.15	15.50	0.15	0.25
7L2x.2	12.25	0.37	2.00	0.16	2.64	0.00	0.00	12.00	0.16	0.25
Mean [L2x]	14.25	0.41	2.38	0.16	2.69	0.25	0.08	13.75	0.16	0.25
Mean [2OBS]	11.82	0.34	3.18	0.11	3.05	0.39	0.12	11.35	0.11	0.08

181

Sub-Section	Intergranular Porosity	Intergranular Porosity**	Intragranular Porosity	Mean Pore Width [MPW]	Mean Pore Width [MPW]	Inter Primary Porosity	Primary Mean Width	Inter Secondary Porosity	Secondary Mean Width	Fracture Porosity
	%	%	%	mm	phi	%	mm	%	mm	%
7G1z.1	5.00	0.15	1.00	0.08	3.64	0.00	0.00	5.00	0.08	0.00
7G1z.2	7.00	0.19	1.75	0.07	3.84	0.00	0.00	7.00	0.07	0.00
7G1z.3	6.50	0.22	1.50	0.09	3.47	0.00	0.00	6.50	0.09	0.00
7G1z.4	9.00	0.39	2.75	0.10	3.32	0.25	0.10	8.75	0.10	0.00
7G1z.5	12.25	0.44	3.25	0.11	3.18	1.00	0.21	10.75	0.11	0.50
7G1z.6	14.25	0.50	4.75	0.15	2.74	0.75	0.24	13.25	0.15	0.25
Mean [G1z]	9.00	0.31	2.50	0.10	3.37	0.33	0.09	8.54	0.10	0.13
7G1x.1	10.50	0.31	3.00	0.09	3.47	0.00	0.00	10.50	0.09	0.00
7G1x.2	8.50	0.27	2.25	0.10	3.32	0.00	0.00	8.50	0.10	0.00
Mean [G1x]	9.50	0.29	2.63	0.10	3.40	0.00	0.00	9.50	0.10	0.00
Mean [1OBS]	9.13	0.31	2.53	0.10	3.37	0.25	0.07	8.78	0.10	0.09
WRM	13.55	0.41	2.93	0.12	3.12	0.23	0.08	13.11	0.12	0.17

APPENDIX D: A statistical summary of petrographic elements observed in the Massillon Sandstone's first, second and third-order structures. Individual and aggregate elements investigated include: permeability, porosity, mineralogy, texture and diagenetic alterations.

	First Order	Second Order	Third Order	Aggregate
Permeability (ln m^2)				
Number	8	22	69	99
Minimum	-28.979	-29.607	-28.758	-29.607
Maximum	-27.011	-25.721	-25.876	-25.721
Mean	-27.864	-27.586	-27.042	-27.229
Median	-27.814	-27.503	-26.962	-27.113
Standard Deviation	0.69881	1.1213	0.59607	0.79818
Variance	0.48974	1.2573	0.35529	0.63709
Standard Error	0.24742	0.23906	0.071758	0.08022
Porosity [point count] (%)				
Number	8	22	70	100
Minimum	6	7.75	11	6
Maximum	19	23.75	27	27
Mean	11.656	15	17.486	16.473
Median	11.25	14.25	16.875	16.125
Standard Deviation	4.2551	4.2426	3.7385	4.2612
Variance	18.106	18	14.315	18.158
Standard Error	1.5044	0.90453	0.45222	0.42612
Porosity [image analysis] (%)				
Number	8	22	70	100
Minimum	4.39	5.01	7.81	4.39
Maximum	13.43	22.93	23.16	23.16
Mean	7.6675	12.136	15.072	13.834
Median	7.285	10.22	14.785	13.775
Standard Deviation	3.1534	5.5873	3.6964	4.6524
Variance	9.944	31.218	13.663	21.645
Standard Error	1.1149	1.1912	0.4418	0.46524
Intergranular Macroporosity (%)				
Number	8	22	70	100
Minimum	5	6.25	8.25	5
Maximum	14.25	22	23.5	23.5
Mean	9.125	11.818	14.6	13.55
Median	8.75	11.875	14.125	13.375
Standard Deviation	3.088	4.1806	3.7968	4.1782
Variance	9.5357	17.477	14.416	17.457
Standard Error	1.0918	0.8913	0.4538	0.41782
Intergranular Pore Width (mm)				
Number	8	21	70	99
Minimum	0.07	0.06	0.07	0.06
Maximum	0.15	0.2	0.19	0.2
Mean	0.09875	0.11571	0.11786	0.11586
Median	0.095	0.12	0.12	0.11
Standard Deviation	0.024164	0.0388804	0.02437	0.028176
Variance	0.0005	0.001	0.0005	0.0007
Standard Error	0.009	0.008	0.003	0.003

	First Order	Second Order	Third Order	Aggregate
Framework Grain Sorting (phi)				
Number	8	22	70	100
Minimum	0.31	0.32	0.25	0.25
Maximum	0.41	0.51	0.56	0.56
Mean	0.36	0.41273	0.38214	0.3871
Median	0.365	0.405	0.38	0.38
Standard Deviation	0.03295	0.064674	0.057582	0.05914
Variance	0.001	0.004	0.003	0.003
Standard Error	0.012	0.014	0.007	0.006
Framework Grain Density (%)				
Number	8	22	70	100
Minimum	60.75	56.75	54.75	54.75
Maximum	74	69.25	71.25	74
Mean	66.688	62.67	63.761	63.755
Median	66.5	63.5	63.75	63.75
Standard Deviation	3.9771	3.5459	3.3942	3.5737
Variance	15.817	12.574	11.521	12.771
Standard Error	1.4061	0.756	0.40569	0.35737
Framework Grain Size (phi)				
Number	8	22	70	100
Minimum	1.1783	1.2776	1.3005	1.3005
Maximum	1.044	0.49882	0.61003	0.49882
Mean	1.1025	0.91591	0.98254	0.97748
Median	1.0838	0.9122	1.0173	1.0305
Standard Deviation	0.051665	0.23782	0.15354	0.17533
Variance	0.0026693	0.056559	0.023575	0.030741
Standard Error	0.018266	0.050704	0.018352	0.017533
Framework Grain Size (mm)				
Number	8	22	70	100
Minimum	0.4419	0.4125	0.406	0.406
Maximum	0.485	0.7077	0.6552	0.7077
Mean	0.46599	0.53699	0.50898	0.5117
Median	0.4718	0.5314	0.49405	0.48955
Standard Deviation	0.016528	0.089304	0.055204	0.06443
Variance	0.0002	0.008	0.003	0.004
Standard Error	0.006	0.019	0.007	0.006

	First Order	Second Order	Third Order	Aggregate
Quartz Component (%)				
Number	8	22	70	100
Minimum	90	86	87	86
Maximum	97	96	97	97
Mean	92.5	90.545	91.529	91.39
Median	92	90.5	92	91
Standard Deviation	2.3905	2.6317	2.2245	2.3609
Variance	5.7143	6.8312	4.9484	5.5736
Standard Error	0.84515	0.55723	0.26588	0.23609
Feldspar Component (%)				
Number	8	22	70	100
Minimum	1	1	0	0
Maximum	4	7	7	7
Mean	2.375	3.4091	2.9286	2.99
Median	2	3	3	3
Standard Deviation	1.1877	1.469	1.2548	1.3142
Variance	1.4107	2.158	1.5745	1.7272
Standard Error	0.41993	0.3132	0.14998	0.13142
Lithic Component (%)				
Number	8	22	70	100
Minimum	2	2	2	2
Maximum	8	10	9	10
Mean	5.125	6.0455	5.5429	5.62
Median	5	5.5	5.5	5
Standard Deviation	1.8851	2.2356	1.7149	1.8683
Variance	3.5536	4.9978	3.0344	3.4905
Standard Error	0.66648	0.47663	0.2082	0.18683
Intergranular Volume (%)				
Number	8	22	70	100
Minimum	23.25	29.5	26.5	23.25
Maximum	37.5	38	40.5	40.5
Mean	30.781	34.148	33.354	33.322
Median	30.875	34	33.5	33.5
Standard Deviation	4.3945	2.6034	3.1412	3.2177
Variance	19.3111	6.7777	9.8668	10.354
Standard Error	1.5537	0.55505	0.37544	0.32177

	First Order	Second Order	Third Order	Aggregate
Matrix Material and Cements (%)				
Number	8	22	70	100
Minimum	14	13.75	12.75	12.75
Maximum	30.5	30	24.25	30.5
Mean	21.656	22.33	18.754	19.773
Median	23.25	21.875	19	19.625
Standard Deviation	6.3849	3.8105	2.9597	14.542
Variance	40.767	14.52	8.76	0.38134
Standard Error	2.2574	0.81241	0.35375	0.37808
Total Cements (%)				
Number	8	22	70	100
Minimum	10.75	10	8.5	8.5
Maximum	28.5	26.75	19	28.5
Mean	18.531	17	12.679	14.098
Median	19.75	16.375	12.25	13
Standard Deviation	6.9275	5.2982	2.1749	4.1868
Variance	47.99	28.071	4.7303	17.529
Standard Error	2.4492	1.1296	0.25995	0.41868
Ferroan Cements (%)				
Number	8	22	70	100
Minimum	9.75	6.25	6.5	6.5
Maximum	28.25	23.75	15	28.25
Mean	17.346	13.841	9.9357	11.388
Median	18.25	12.5	9.75	10
Standard Deviation	6.9632	5.0724	1.9194	4.1414
Variance	48.486	25.729	3.6842	17.151
Standard Error	2.4619	1.0814	0.22942	0.41414
Hematite (%)				
Number	8	22	70	100
Minimum	7.25	3.5	5	3.5
Maximum	21.25	20.75	12	21.25
Mean	12.781	10.443	7.6393	8.6675
Median	12	8.625	7.625	8
Standard Deviation	5.3826	4.3772	1.4877	3.2359
Variance	28.972	19.16	2.2131	10.471
Standard Error	1.903	0.93323	0.17781	0.32359
Ferroan Dolomite (%)				
Number	8	22	70	100
Minimum	2	1.75	0.5	0.5
Maximum	8.5	6.5	6.25	8.5
Mean	4.565	3.3977	2.2964	2.7202
Median	3.625	3.125	2	2.25
Standard Deviation	2.6207	1.3226	1.2996	1.5938
Variance	6.8681	1.7599	1.6889	2.5401
Standard Error	0.92656	0.28283	0.15533	0.15938

	First Order	Second Order	Third Order	Aggregate
Authigenic Quartz (%)				
Number	8	22	70	100
Minimum	0.25	0.75	0.25	0.25
Maximum	2.25	5.75	5.5	5.75
Mean	1.2188	3.1519	2.7429	2.7125
Median	1.25	3	2.75	2.625
Standard Deviation	0.69997	1.3442	1.0153	1.1669
Variance	0.48996	1.8068	1.0307	1.3616
Standard Error	0.24748	0.28658	0.12135	0.11669
Allogenic and Authigenic Clay (%)				
Number	8	22	70	100
Minimum	2	1.75	1	1
Maximum	4.5	11.75	11.75	11.75
Mean	3.125	5.3295	6.075	5.675
Median	3.125	4.875	6	5.5
Standard Deviation	0.88641	2.9342	2.5659	2.6713
Variance	0.78571	8.6094	6.584	7.1357
Standard Error	0.31339	0.62557	0.30669	0.26713
Pore Filling Clay (%)				
Number	8	22	70	100
Minimum	0.75	1	0.75	0.75
Maximum	3.5	7	7	7
Mean	2.0312	3.3295	3.6964	3.4825
Median	1.875	2.875	3.875	3.375
Standard Deviation	1.0727	1.8746	1.6966	1.7438
Variance	1.1507	3.5142	2.8784	3.0407
Standard Error	0.37925	0.39967	0.20278	0.17438
Pore Lining Clay (%)				
Number	8	22	70	100
Minimum	0.5	0.25	0.25	0.25
Maximum	2.5	4.75	5.25	5.25
Mean	1.0938	2	2.375	2.19
Median	1	1.875	2.25	2
Standard Deviation	0.6538	1.2771	1.2487	1.2619
Variance	0.42746	1.631	1.5593	1.5923
Standard Error	0.23115	0.27228	0.14925	0.12619

188

APPENDIX E: Diagrams showing the correlation between MSP measured permeability and compositional and diagenetic phases observed from modal analysis. Analysis was performed on thin section sub-sections fabricated from billets cut from cored first, second and third-order structures inherent to the Massillon Sandstone block.

Permeability vs. Intergranular Porosity

Plot legend:
- Third Order Bounding Surface
- Second Order Bounding Surface
- First Order Bounding Surface

$y = -28.156 + 0.076107x$ $R = 0.48665$

$y = -29.859 + 0.19237x$ $R = 0.71724$

$y = -29.489 + 0.17812x$ $R = 0.78596$

Axis labels: Ln Permeability [m^2] (vertical); Intergranular Porosity [%] (horizontal)
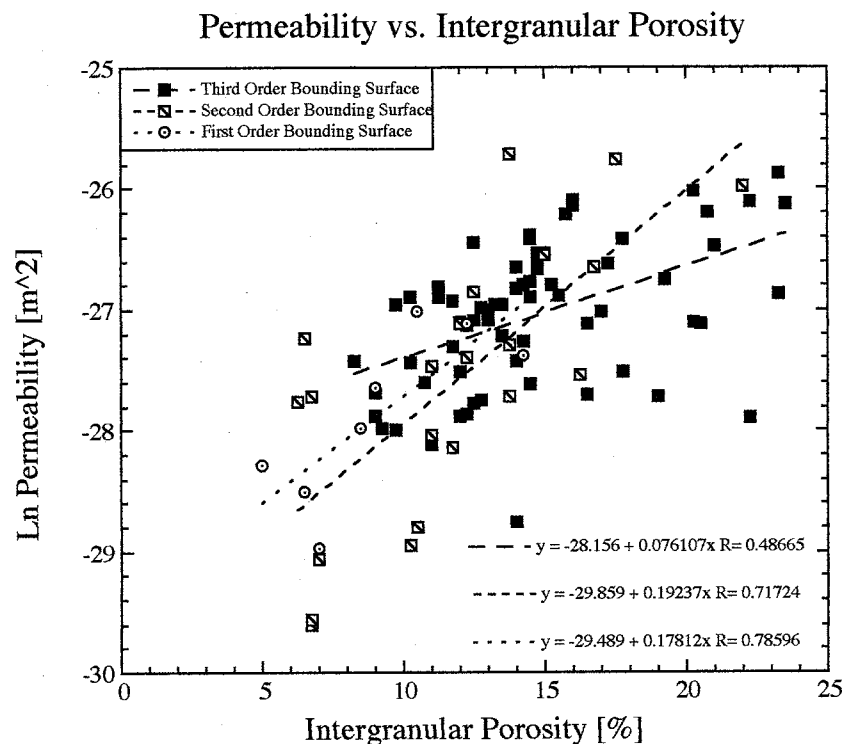
Figure E1

Diagram showing the correlation between permeability and intergranular porosity derived from MSP measurements and point counts of thin section subsections made from billets cut from cored first, second and third-order structures. The plot shows a weak, positive correlation between permeability and intergranular porosity ($R = 0.63$, $n = 99$) for cumulative measurements. Collectively, first and second-order structures exhibit good, positive correlations ($R = 0.79$, $n = 8$; $R = 0.72$, $n = 22$, respectively), whereas, third-order structures exhibit a weak, positive correlation with permeability ($R = 0.49$, $n = 69$). Assessed correlation coefficients: strong [$R \geq 0.90$], good [$0.90 > R > 0.71$], weak or insignificant [$R \leq 0.70$].
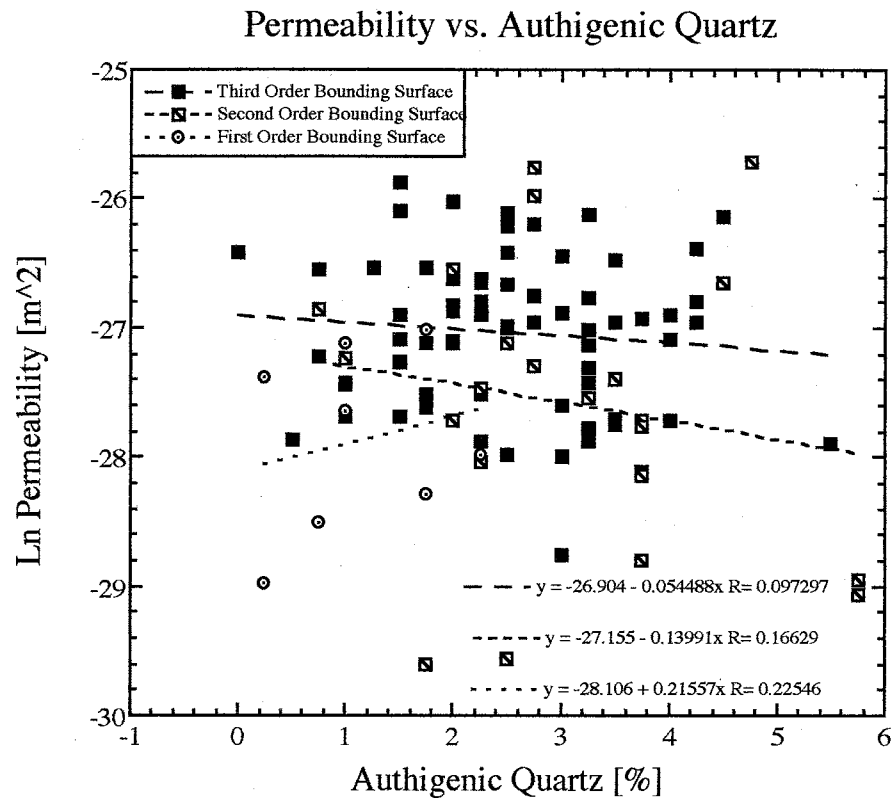
Permeability vs. Intragranular Porosity
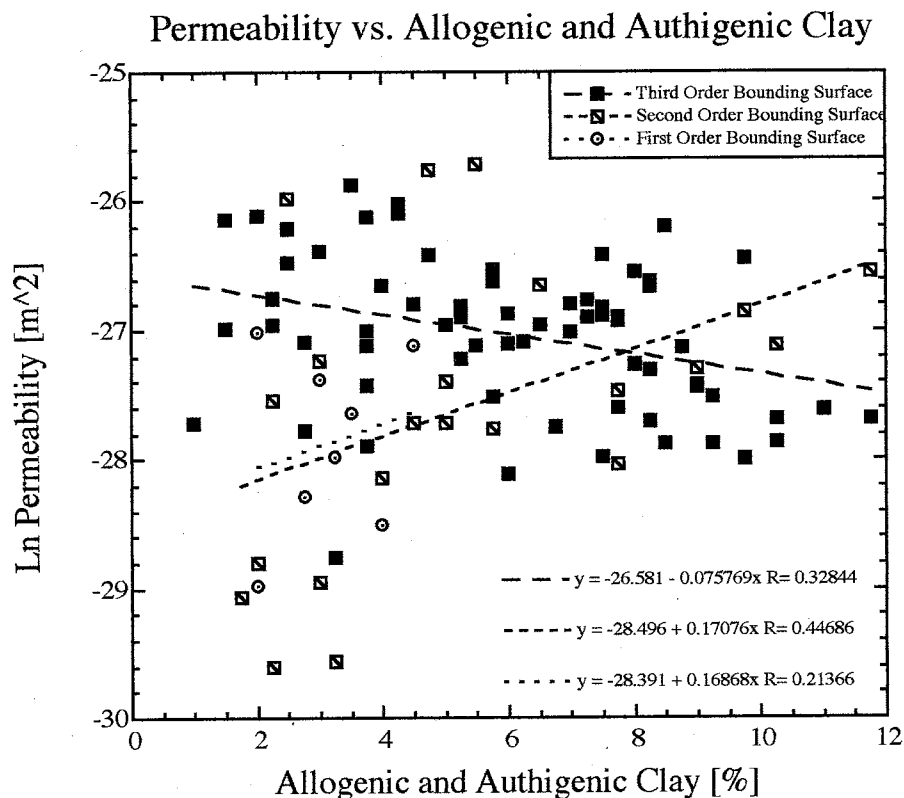
Legend:
- Third Order Bounding Surface
- Second Order Bounding Surface
- First Order Bounding Surface

$y = -26.441 - 0.20657x$ R= 0.41444
$y = -26.986 - 0.18866x$ R= 0.30997
$y = -28.972 + 0.43767x$ R= 0.74018

X-axis: Intragranular Porosity [%]
Y-axis: Ln Permeability [m^2]
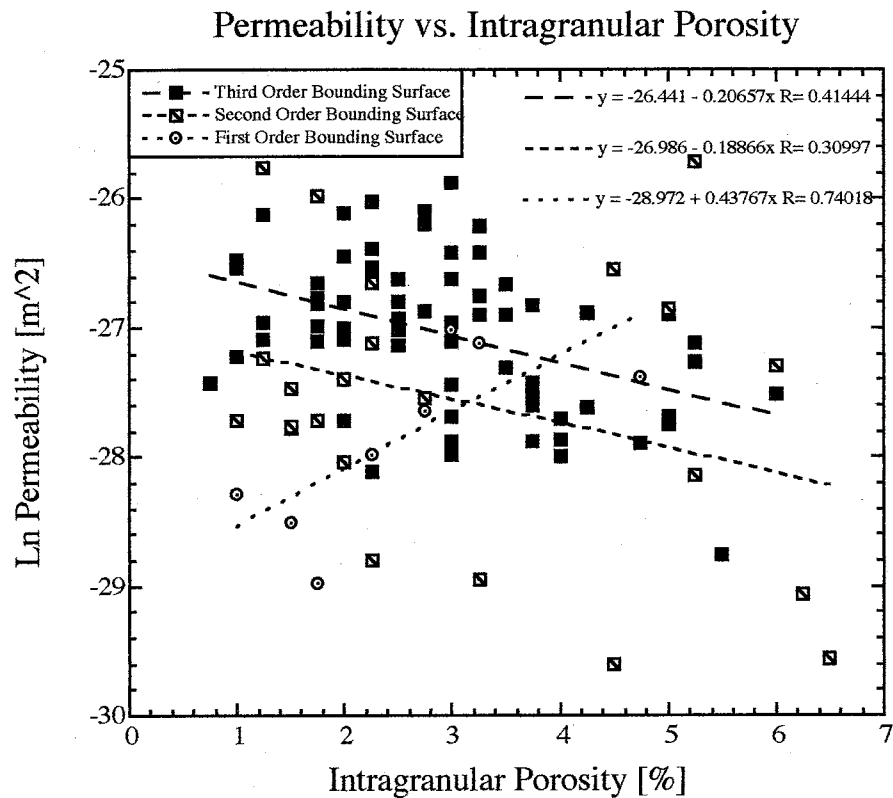
Figure E2

Diagram showing the correlation between permeability and intragranular porosity derived from MSP measurements and point counts of thin section subsections made from billets of cored first, second and third-order structures. The plot shows a weak, negative correlation between permeability and intragranular porosity (R= 0.28, n= 99) for cumulative measurements. Collectively, the first-order bounding structure exhibits a good, positive correlation with permeability (R= 0.74, n= 8). However, second and third-order structures exhibit weak, negative correlations (R= 0.31, n= 22; R= 0.41, n= 69, respectively). Assessed correlation coefficients: strong [R ≥ 0.90], good [0.90 > R > 0.71], weak or insignificant [R ≤ 0.70].

Permeability vs. Lithic Components

Figure legend: Third Order Bounding Surface; Second Order Bounding Surface; First Order Bounding Surface

y = -26.758 - 0.082074x R= 0.15656

y = -25.534 - 0.53732x R= 0.67687
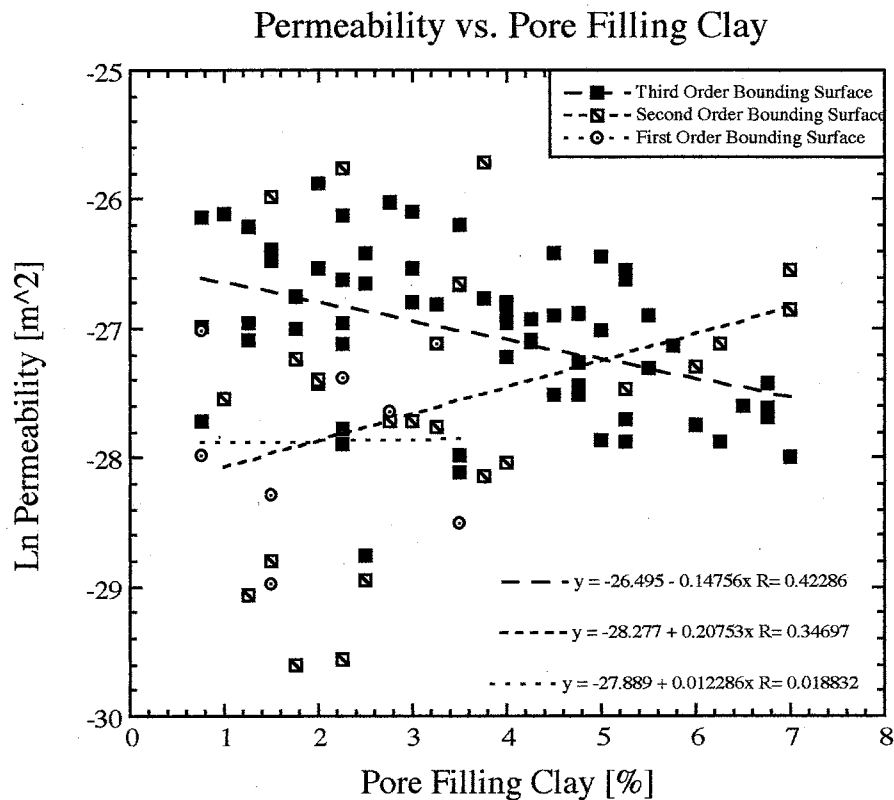
y = -27.888 + 0.0072298x R= 0.013801
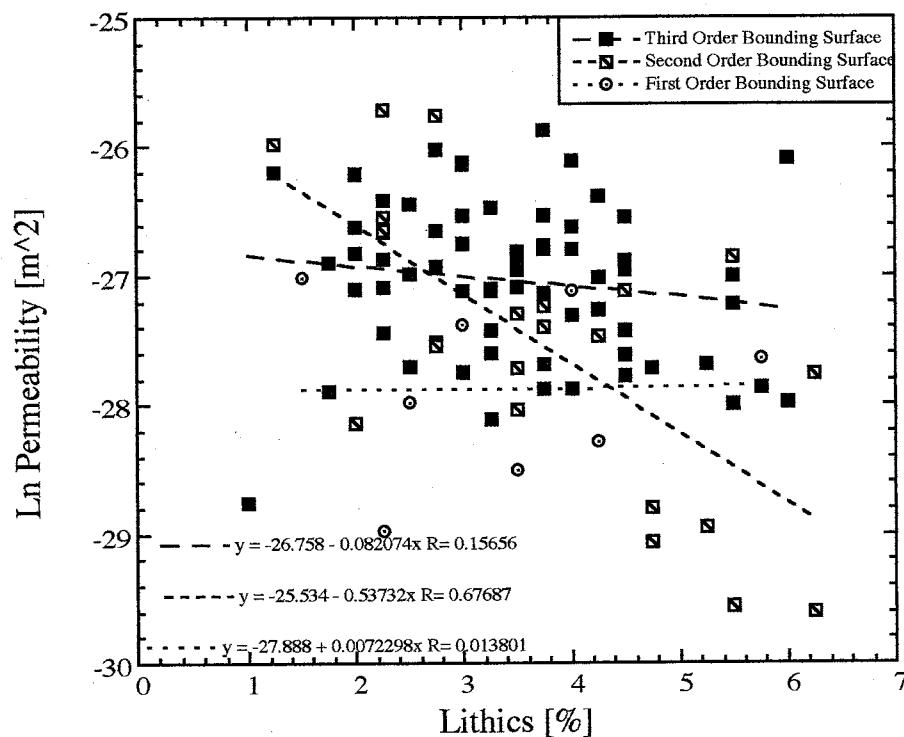
Figure E3

Diagram showing the correlation between permeability and lithic fragment content derived from MSP measurements and point counts of thin section subsections made from billets cut from cored first, second and third-order structures. The plot shows a weak, negative correlation between permeability and lithic content (R= 0.34, n= 99) for cumulative measurements. Collectively, the first-order bounding structure (R= 0.01, n= 8) does not exhibit a positive or negative correlation between permeability and lithic content. Second and third-order structures exhibit weak, positive correlations (R= 0.68, n= 22; R= 0.16, n= 69, respectively). Assessed correlation coefficients: strong [R ≥ 0.90], good [0.90 > R > 0.71], weak or insignificant [R ≤ 0.70].

Permeability vs. Authigenic Quartz and Ferroan Cement

Legend equations:
- y = -26.377 - 0.052396x R= 0.22388
- y = -24.74 - 0.16862x R= 0.79234
- y = -26.594 - 0.068888x R= 0.68959

Plot legend:
- Third Order Bounding Surface
- Second Order Bounding Surface
- First Order Bounding Surface

X-axis: Authigenic Quartz and Ferroan Cement [%]
Y-axis: Ln Permeability [m^2]
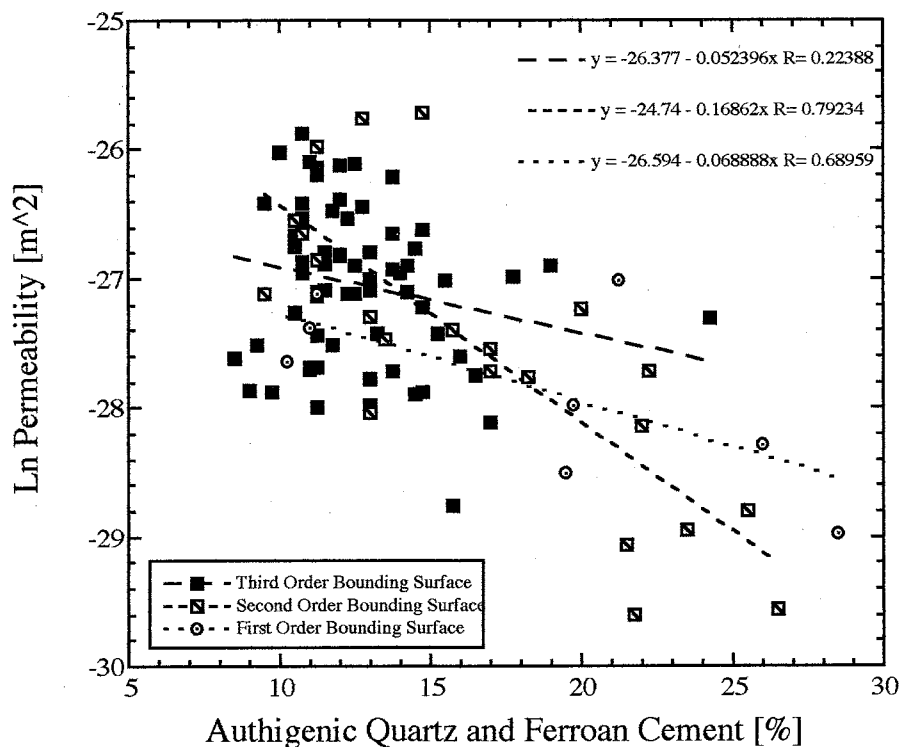
Figure E4

Diagram showing the correlation between permeability and total cement (authigenic quartz overgrowths and ferroan cements, including hematite and ferroan dolomite) derived from MSP measurements and point counts of thin section subsections made from billets cut from cored first, second and third-order bounding structures. The plot shows a weak, positive correlation between permeability and total cements (R= 0.64, n= 99) for cumulative measurements. Collectively, second-order bounding structures exhibit a good, positive relationship (R= 0.79, n= 22), whereas first and third-order structures exhibit weak, positive correlations (R= 0.69, n= 8; R= 0.22, n= 69, respectively). Increasing permeability with decreasing authigenic cements is considered a positive correlation. Assessed correlation coefficients: strong [R ≥ 0.90], good [0.90 > R > 0.71], weak or insignificant [R ≤ 0.70].

Permeability vs. Ferroan Dolomite

y = -27.055 + 0.0055439x R= 0.012176
y = -26.445 - 0.33581x R= 0.3973
y = -26.796 - 0.23392x R= 0.87599

Third Order Bounding Surface
Second Order Bounding Surface
First Order Bounding Surface

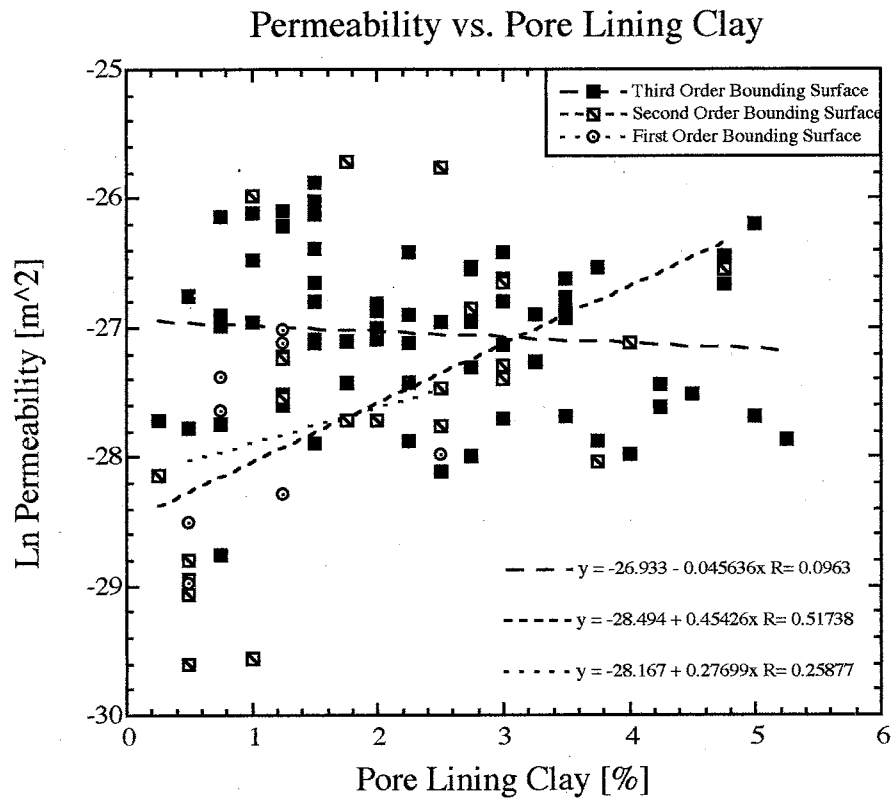Ln Permeability [m^2]
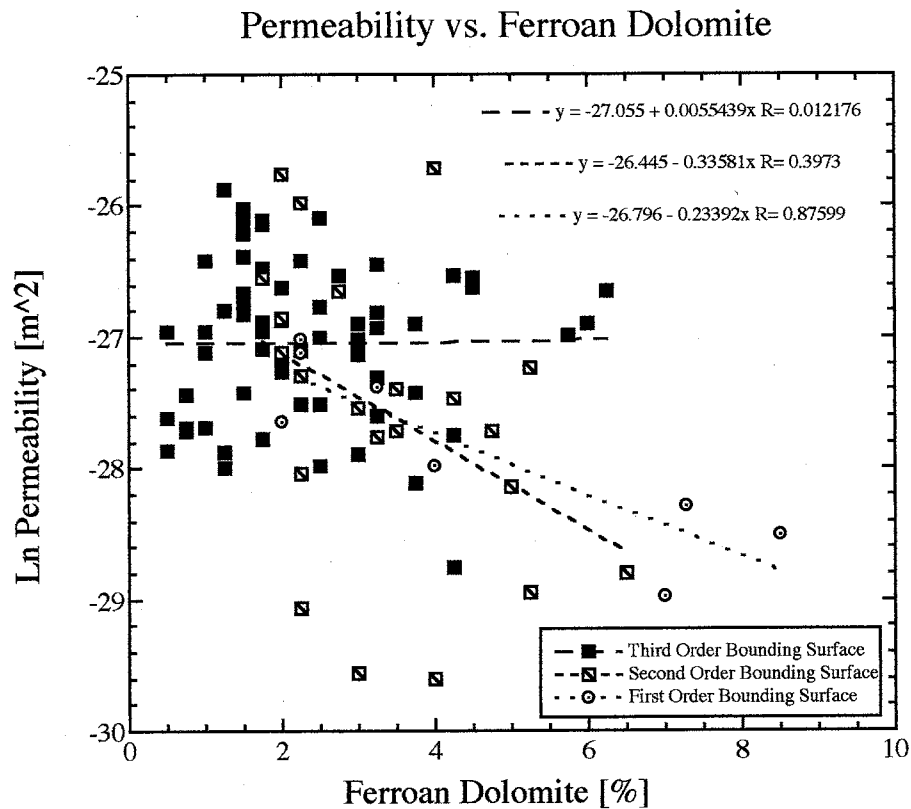
Ferroan Dolomite [%]

Figure E5

Diagram showing the correlation between permeability and ferroan dolomite derived from MSP measurements and point counts of thin section subsections made from billets cut from cored first, second and third-order structures. The plot shows a weak, positive correlation between permeability and ferroan dolomite (R= 0.34, n= 99) for cumulative measurements. Collectively, measurements of the first-order structure exhibits a good, positive correlation (R= 0.88, n=8), whereas second-order structures exhibit a weak, positive correlation (R= 0.40, n= 22). Third-order structures (R= 0.01, n= 69) exhibit neither a positive or negative correlation with permeability. A positive relationship exists as increasing permeability correlates with decreasing ferroan dolomite. Assessed correlation coefficients: strong [R ≥ 0.90], good [0.90 > R > 0.71], weak or insignificant [R ≤ 0.70].

Permeability vs. Authigenic Quartz

Legend:
- Third Order Bounding Surface
- Second Order Bounding Surface
- First Order Bounding Surface

$y = -26.904 - 0.054488x$ R= 0.097297

$y = -27.155 - 0.13991x$ R= 0.16629

$y = -28.106 + 0.21557x$ R= 0.22546

X-axis: Authigenic Quartz [%]

Y-axis: Ln Permeability [m^2]

Figure E6

Diagram showing the correlation between permeability and authigenic quartz overgrowth cement derived from MSP measurements and point counts of thin section subsections made from billets cut from cored first, second and third-order structures. The plot shows a weak, positive correlation between permeability and authigenic quartz cement (R = 0.06, n= 99) for cumulative measurements. Collectively, first-order bounding structures exhibit a weak, negative correlation (R = 0.23, n= 8). Conversely, second and third-order structures exhibit weak, positive correlations (R = 0.17, n= 22; R = 0.10, n= 69, respectively). Increasing permeability with decreasing authigenic quartz is considered a positive relationship. Assessed correlation coefficients: strong [R ≥ 0.90], good [0.90 > R > 0.71], weak or insignificant [R ≤ 0.70].

195

Permeability vs. Allogenic and Authigenic Clay

Legend:
- ■ - Third Order Bounding Surface
- ◫ - Second Order Bounding Surface
- ⊙ - First Order Bounding Surface

$y = -26.581 - 0.075769x$ $R = 0.32844$

$y = -28.496 + 0.17076x$ $R = 0.44686$

$y = -28.391 + 0.16868x$ $R = 0.21366$

Y-axis: Ln Permeability [m^2]

X-axis: Allogenic and Authigenic Clay [%]

Figure E7

Diagram showing the correlation between permeability and total allogenic and authigenic clay mineral content derived from MSP measurements and point counts of thin section subsections made from billets cut from cored first, second and third-order structures. The plot shows a weak, negative correlation between permeability total clay content (R= 0.09, n= 99) for cumulative measurements. Collectively, first and second-order structures exhibit a weak, negative correlation (R= 0.21, n= 8; R= 0.45, n= 22, respectively). Conversely, third-order structures exhibit a weak, positive correlation with permeability (R= 0.33, n= 69). Increasing permeability with decreasing clay content is a positive relationship. Assessed correlation coefficients: strong [R ≥ 0.90], good [0.90 > R > 0.71], weak or insignificant [R ≤ 0.70].

Permeability vs. Pore Filling Clay

Figure E8

Diagram showing the correlation between permeability and pore filling clay derived from MSP measurements and point counts of thin section subsections made from billets cut from cored first, second and third-order structures. The plot shows neither a positive or negative correlation between increasing permeability and decreasing pore filling clay ($R= 0.02$, $n= 99$) for cumulative measurements. The first-order structural measurements mirror that of the collective plot ($R= 0.02$, $n= 8$). Third-order structures exhibit a weak, positive correlation ($R= 0.43$, $n= 69$). Second-order structures exhibit a weak, negative correlation with permeability ($R= 0.35$, $n= 22$). Assessed correlation coefficients: strong $[R \geq 0.90]$, good $[0.90 > R > 0.71]$, weak or insignificant $[R \leq 0.70]$.

Permeability vs. Pore Lining Clay

Legend:
- Third Order Bounding Surface
- Second Order Bounding Surface
- First Order Bounding Surface

$y = -26.933 - 0.045636x \quad R = 0.0963$

$y = -28.494 + 0.45426x \quad R = 0.51738$

$y = -28.167 + 0.27699x \quad R = 0.25877$

X-axis: Pore Lining Clay [%]
Y-axis: Ln Permeability [m^2]

Figure E9

Diagram showing the correlation between permeability and pore lining clay derived from MSP measurements and point counts of thin section subsections made from billets cut from cored first, second and third-order structures. The plot shows a weak, negative correlation between permeability and pore lining clay (R= 0.21, n= 99) for cumulative measurements. Collectively, first and second-order structures exhibit a weak, negative correlation (R= 0.26, n= 8; R= 0.52, n= 22, respectively). Conversely, third-order structures exhibit a weak, positive correlation (R= 0.10, n= 69). Assessed correlation coefficients: strong [R ≥ 0.90], good [0.90 > R > 0.71], weak or insignificant [R ≤ 0.70].

APPENDIX F: Rendered two and three-phase images of first, second and third-order structural subsections produced for image analysis. Images are graphical representations of the various volume percentages of framework grains, porosities and matrix material in each subsection.
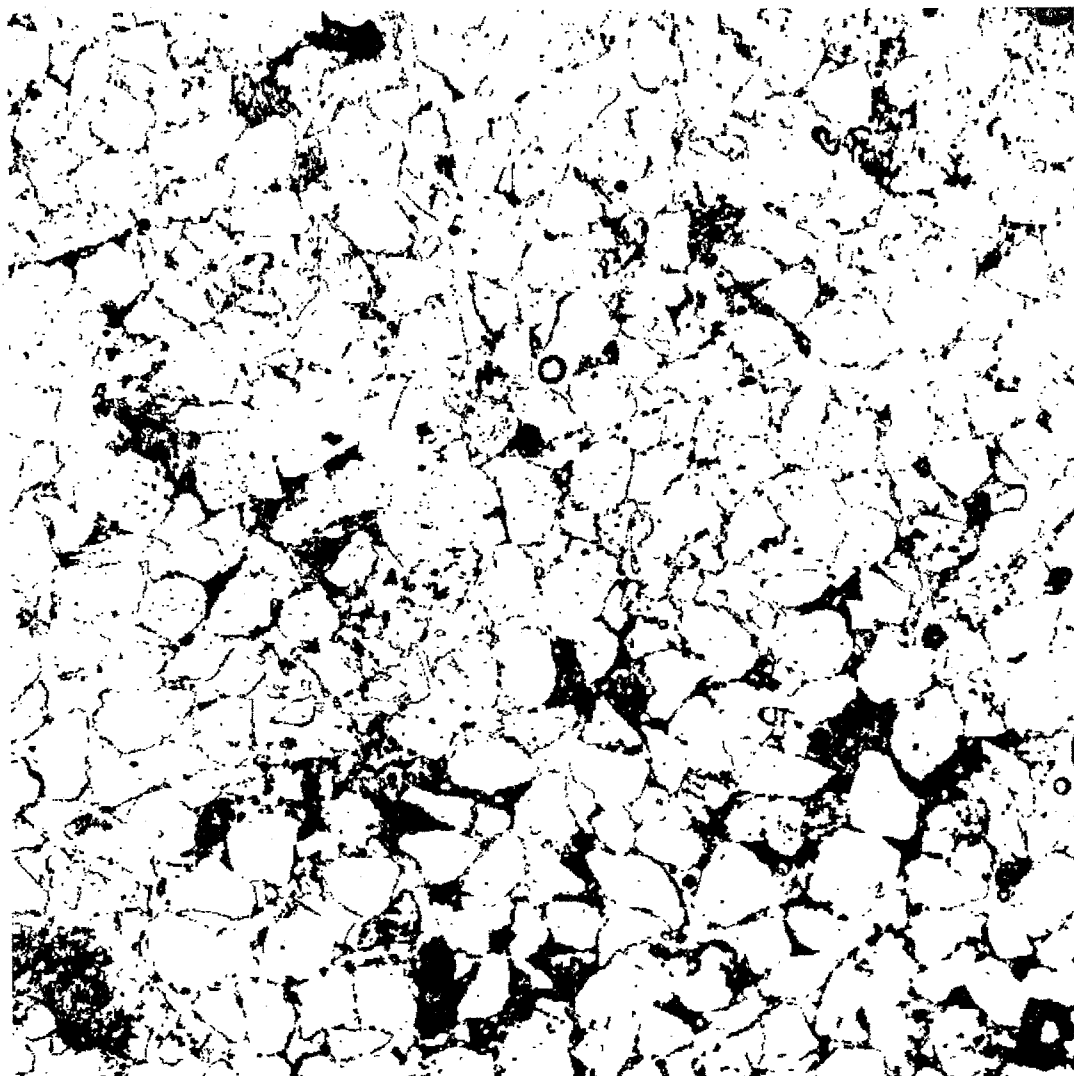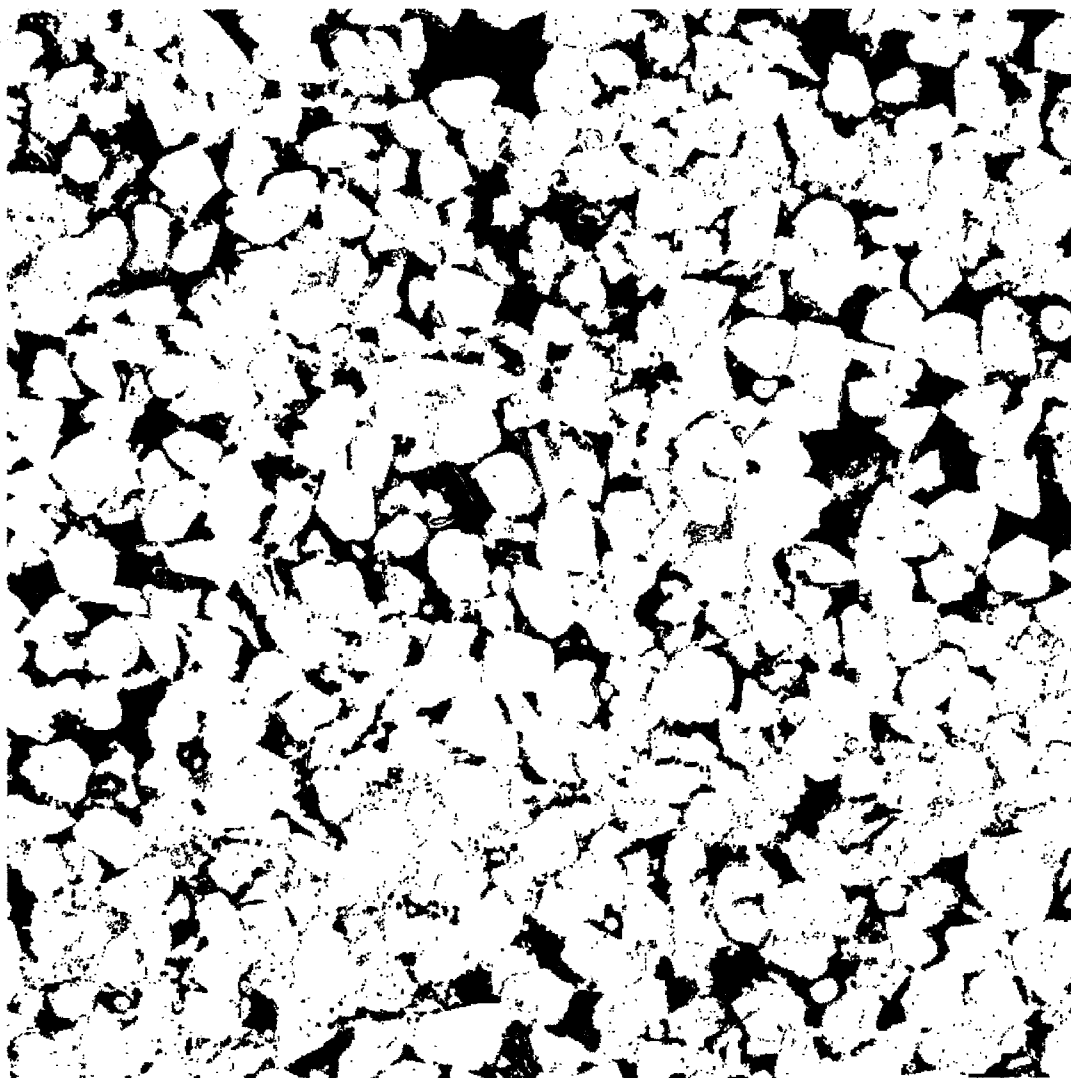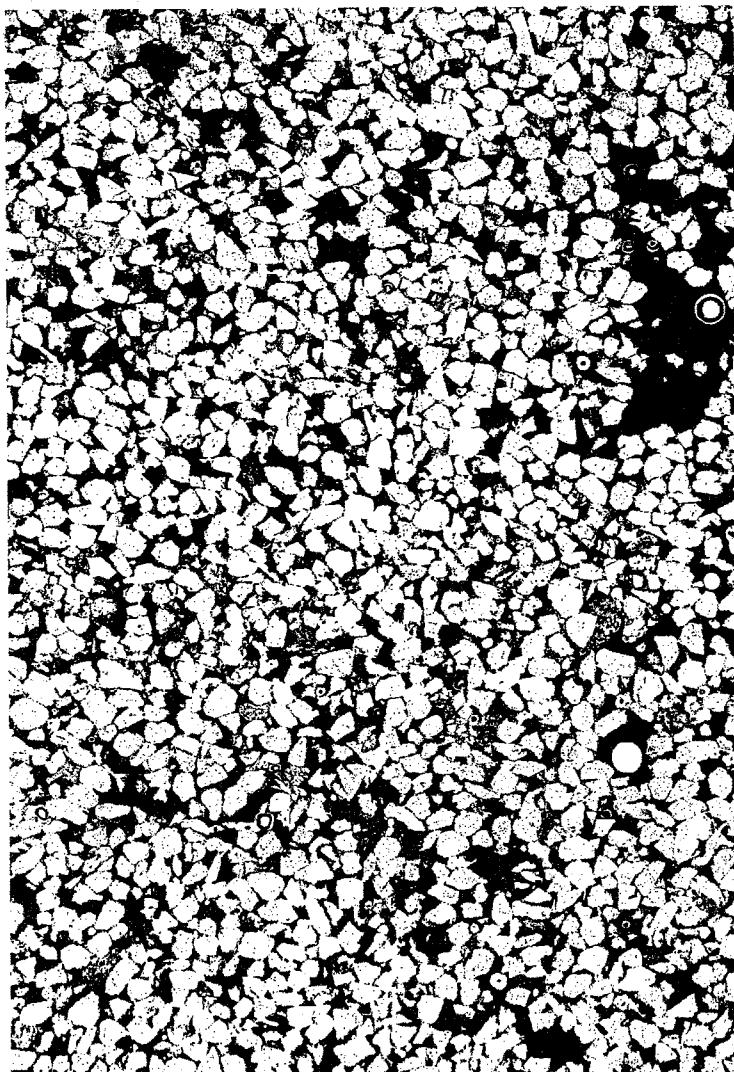
Figure F1

Rendered two-phase photomicrograph of subsection 7C2z.4. White pixels are detrital, frame-work grains including authigenic micro- and megaquartz and intergranular and intragranular macroporosity. Black pixels are matrix material, including authigenic iron oxide minerals, ferroan dolomite rhombohedra and allogenic and authigenic clay minerals. This thin section subsection was prepared from 2.5 cm core drilled from a second-order bounding structure, and has the highest permeability of all measured subsections. The permeability was measured using the MSP equipped with the 0.15 cm ri tip seal: k = 6.75E-12 m^2; ln k = -25.7213 m^2, k = 6839 millidarcies. Matrix material is 15.5% of the subsection (mean = 19.06%). Image dimensions are 7.929 mm x 7.929 mm: magnification is 850X.
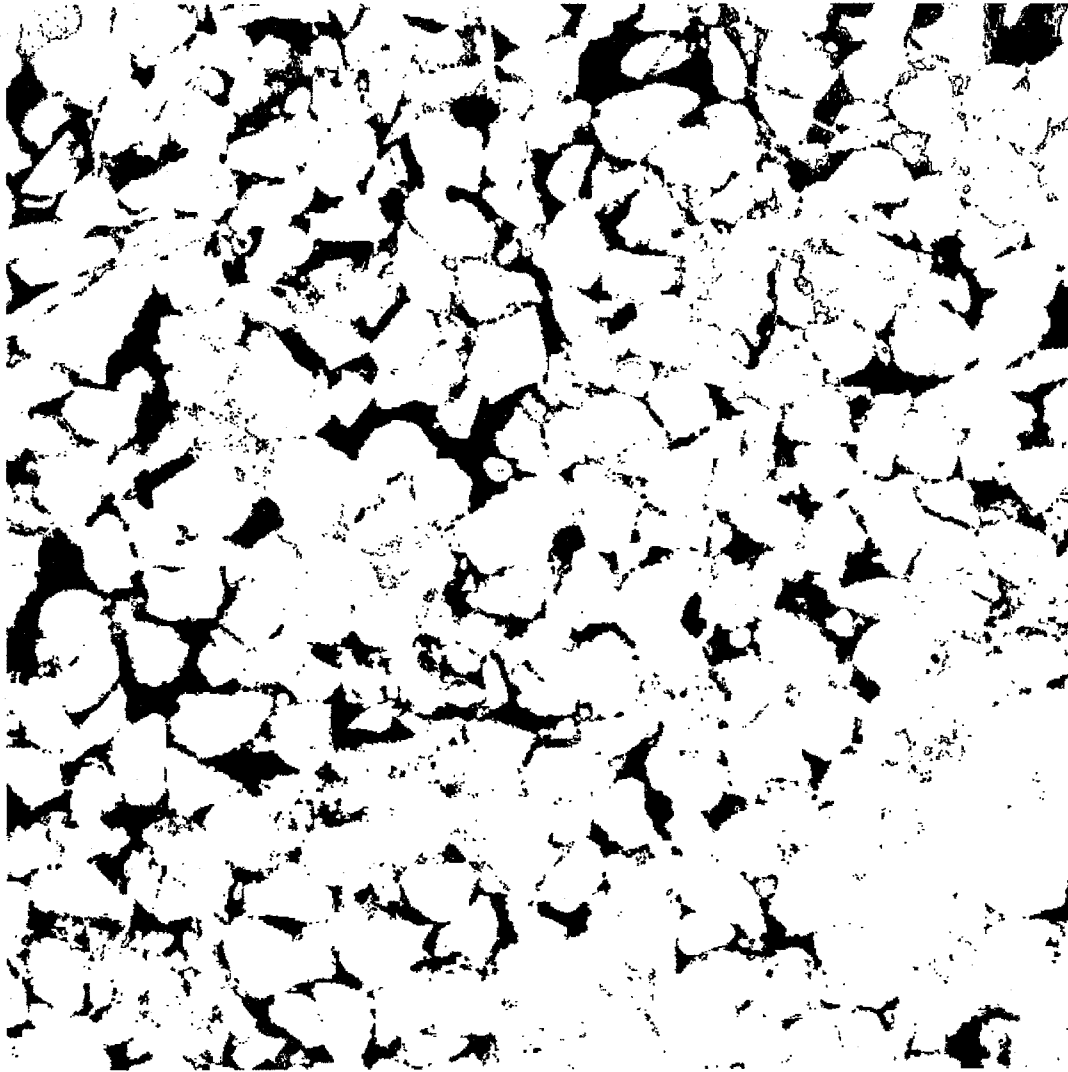
Figure F2

Rendered two-phase photomicrograph of subsection 7C2z.4. White pixels are detrital, framework grains including authigenic micro- and megaquartz and matrix material, including authigenic iron oxide minerals, ferroan dolomite rhombohedra and allogenic and authigenic clay minerals. Black pixels are intergranular and intragranular macroporosity. This thin section subsection was prepared from 2.5 cm core drilled from a second-order bounding structure and has the highest permeability of all measured subsections. The permeability was measured using the MSP equipped with the 0.15 cm ri tip seal: $k = 6.75E\text{-}12$ m^2; $\ln k = -25.7213$ m^2, $k = 6839$ millidarcies. Point count porosity was measured as 19.0%, image analysis porosity is 16.21% and matrix material consumes 15.5% of the subsection. Image dimensions are 7.929 mm x 7.929 mm: magnification is 850X.
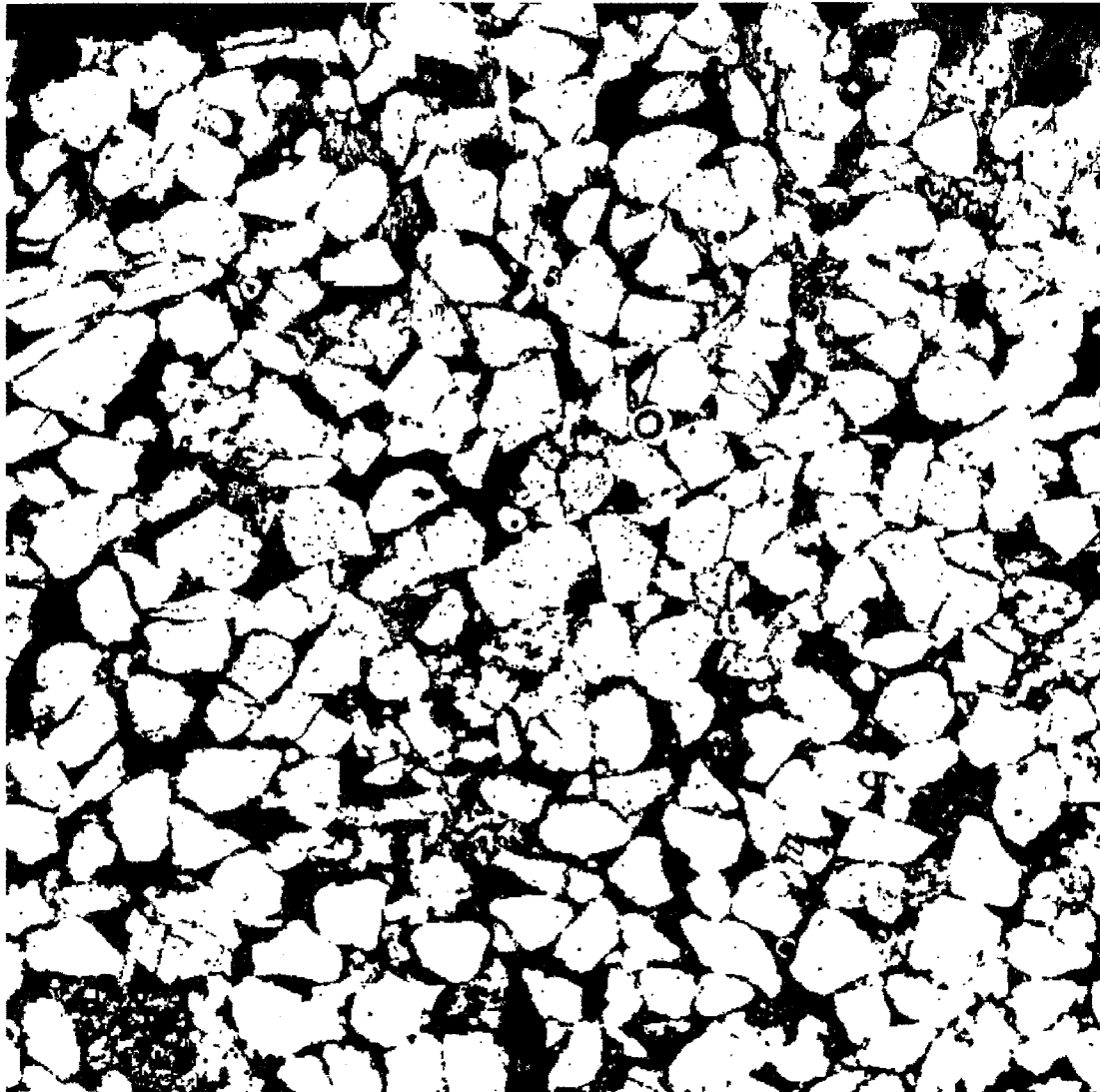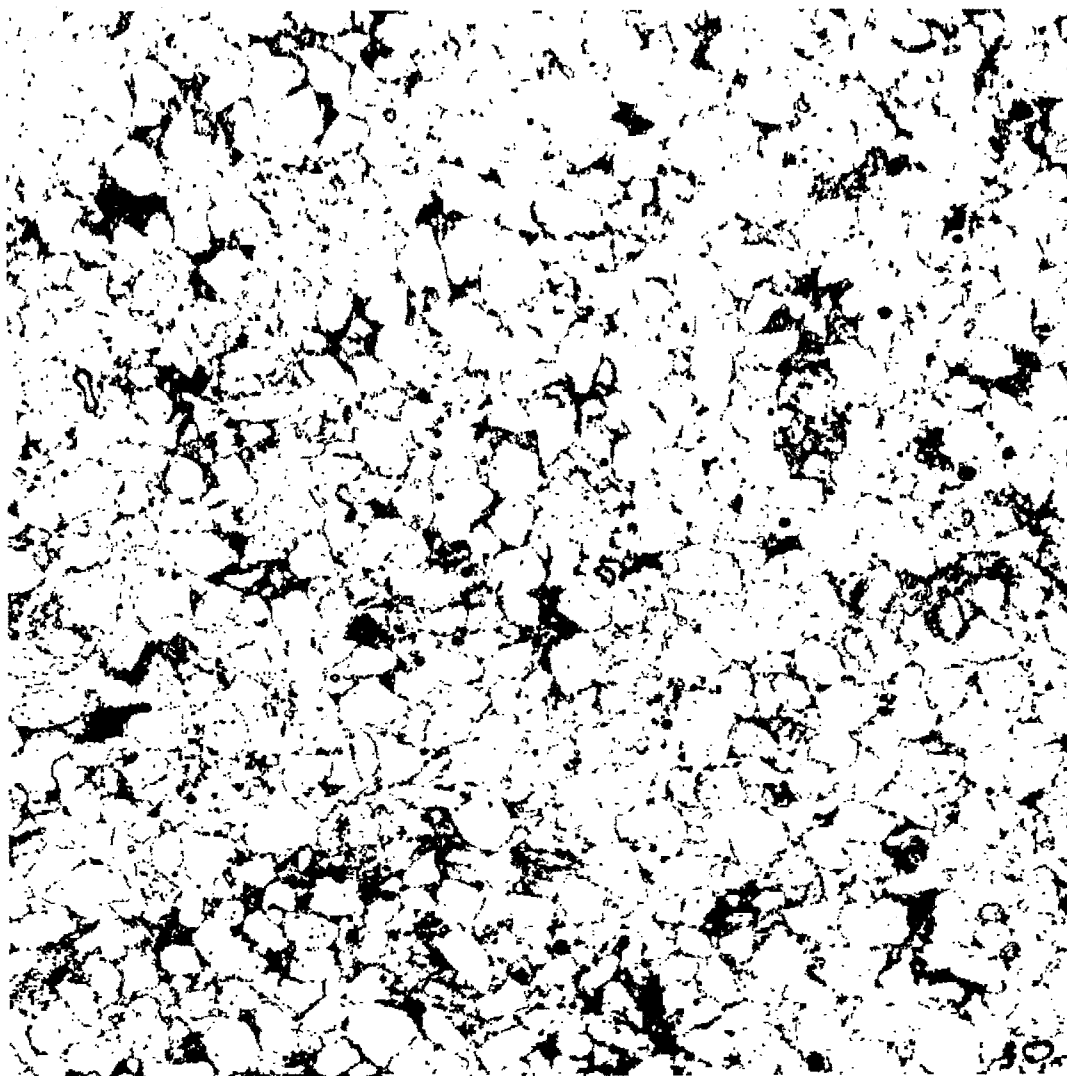
Figure F3

Rendered three-phase photomicrograph of subsection 7C2z.4. White pixels are detrital, framework grains including authigenic micro- and megaquartz. Black pixels are matrix material, including authigenic iron oxide minerals, ferroan dolomite rhombohedra and allogenic and authigenic clay minerals. Blue pixels are intergranular and intragranular macroporosity. This thin section subsection was prepared from 2.5 cm core drilled from a second-order structure and has the highest permeability of all measured subsections. The permeability was measured using the MSP equipped with the 0.15 cm ri tip seal: k = 6.75E-12 m^2; ln k = -25.7213 m^2, k = 6839 millidarcies. Point count porosity was measured as 19.0%, porosity derived from image analysis is 16.21% and matrix material consumes 15.5% of the subsection. The mean grain size is 0.499 phi (coarse-lower sand). The sorting is 0.33 phi (very well-sorted sand) and was determined using the inclusive graphic standard deviation between measured major axes of 242framework grains (Folk, 1974). Image dimensions are 7.929 mm x 7.929 mm: magnification is 850X. The red areas are uncounted portions of the subsection.
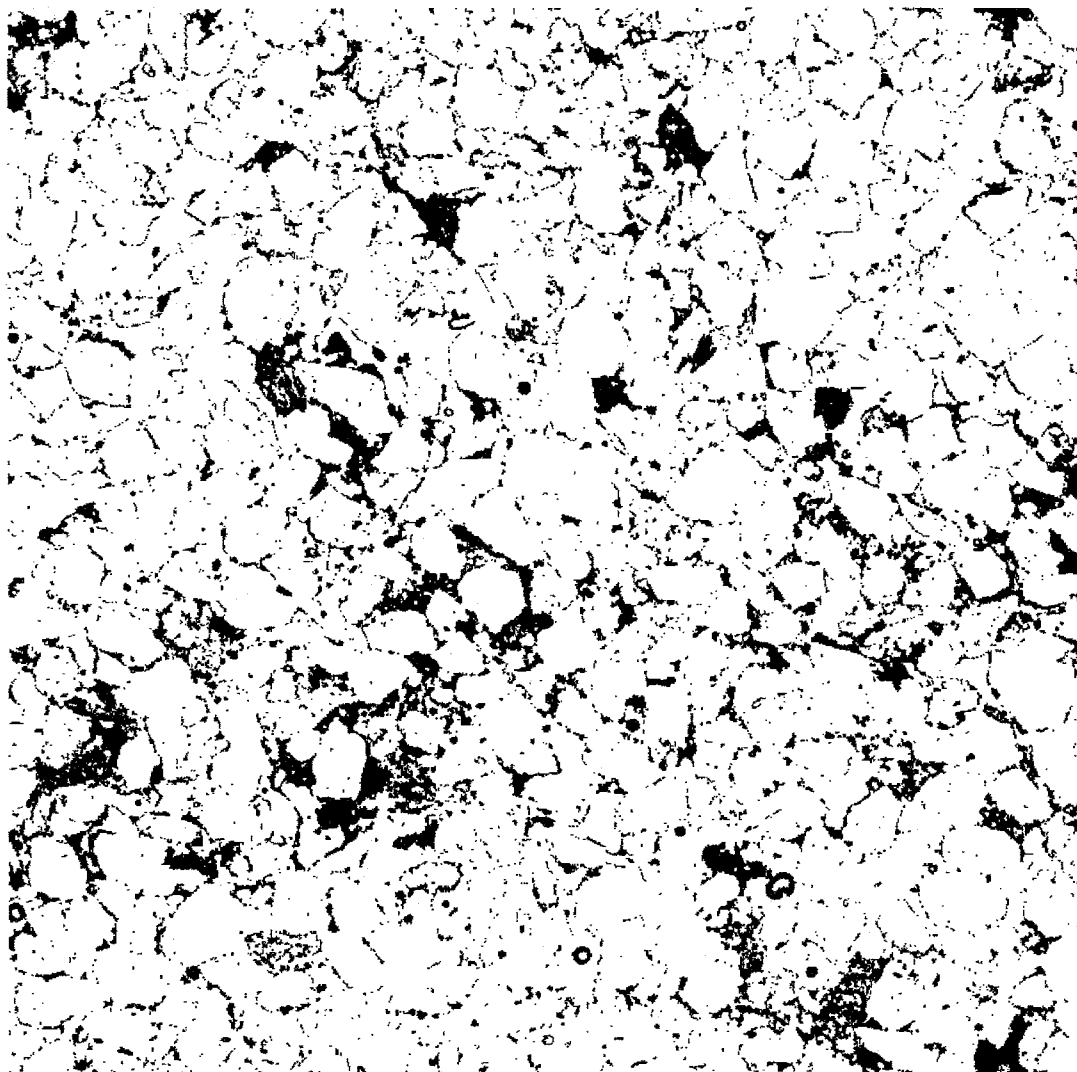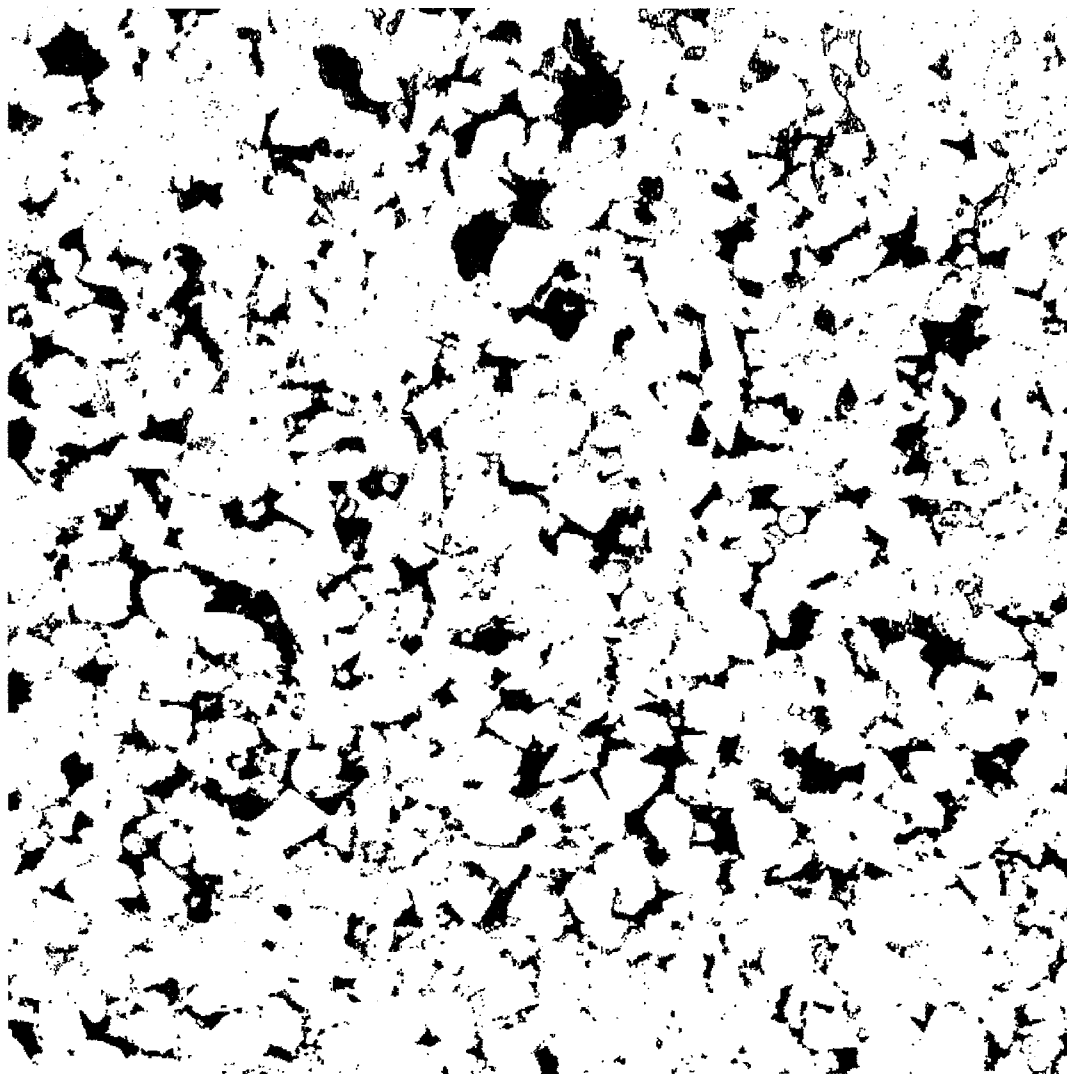
Figure F4

Rendered two-phase photomicrograph of subsection 7C2x.1. White pixels are detrital, framework grains including authigenic micro- and megaquartz and intergranular and intra-granular macroporosity. Black pixels are matrix material, including authigenic iron oxide minerals, ferroan dolomite rhombohedra and allogenic and authigenic clay minerals. This thin section subsection was prepared from 2.5 cm core drilled from a second-order bounding surface structure and has the 4th highest permeability of all measured subsections. The perm-eability was measured using the MSP equipped with the 0.15 cm ri tip seal: $k = 5.25E-12$ m^2; $\ln k = -25.9723$ m^2, $k = 5319$ millidarcies. Matrix material comprises 10.75% of the subsection. Image dimensions are 7.929 mm x 7.929 mm: magnification is 850X.
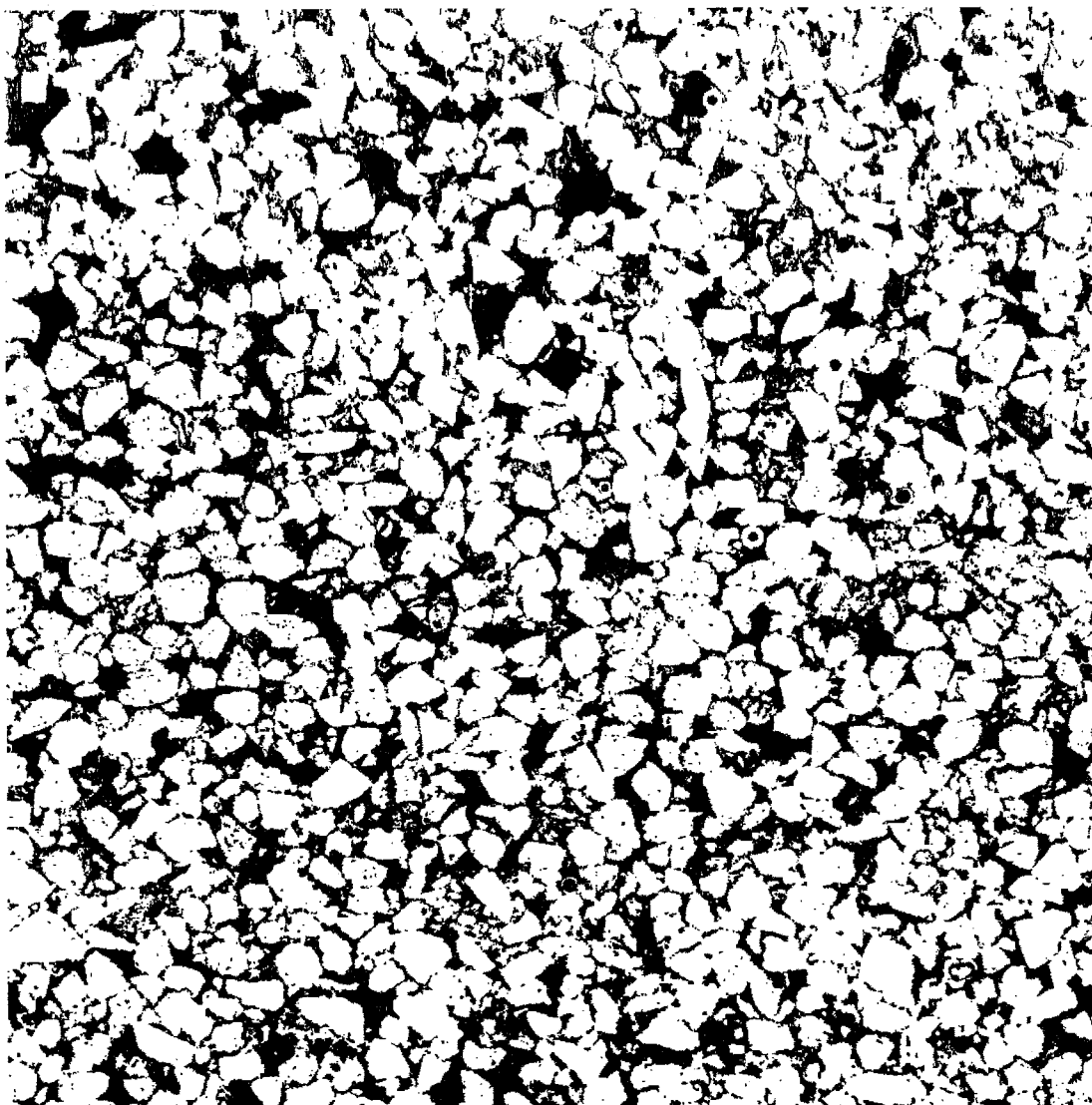
Figure F5

Rendered two-phase photomicrograph of subsection 7C2x.1. White pixels are detrital, framework grains including authigenic micro- and megaquartz and matrix material, including authigenic iron oxide minerals, ferroan dolomite rhombohedra and allogenic and authigenic clay minerals. Black pixels are intergranular and intragranular macroporosity. This thin section subsection was prepared from 2.5 cm core drilled from a third-order structure and has the 4th highest permeability of all measured subsections. The permeability was measured using the MSP equipped with the 0.15 cm ri tip seal: $k = 5.25E-12$ m^2; $\ln k = -25.9723$ m^2, $k = 5319$ millidarcies. Point count porosity was measured as 23.75%, porosity derived from image analysis is 22.54% and matrix material consumes 10.75% of the subsection. Image dimensions are 7.929 mm x 7.929 mm. Magnification is 850X.

204

Figure F6

Rendered three-phase photomicrograph of subsection 7C2x.1. White pixels are detrital, framework grains including authigenic micro- and megaquartz. Black pixels are matrix material, including authigenic iron oxide minerals, ferroan dolomite rhombohedra and allogenic and authigenic clay minerals. Blue pixels are intergranular and intragranular macroporosity. This thin section subsection was prepared from a 2.5 cm core drilled from the first-order bounding surface structure and has the 4th highest permeability of all measured subsections. The permeability was measured using the MSP equipped with the 0.15 cm ri tip seal: $k = 5.25E-12$ m^2; ln k = -25.9723 m^2, k = 5319 millidarcies. Point count porosity was measured as 23.75%, porosity derived from image analysis is 22.54% and matrix material consumes 10.75% of the subsection. The mean grain size is 0.783 phi (coarse-lower sand). The sorting is 0.34 phi (very well-sorted sand) and was determined using the inclusive graphic standard deviation between measured major axes of 250 framework grains (Folk, 1974). Image dimensions are 12.960 mm x 18.954 mm.
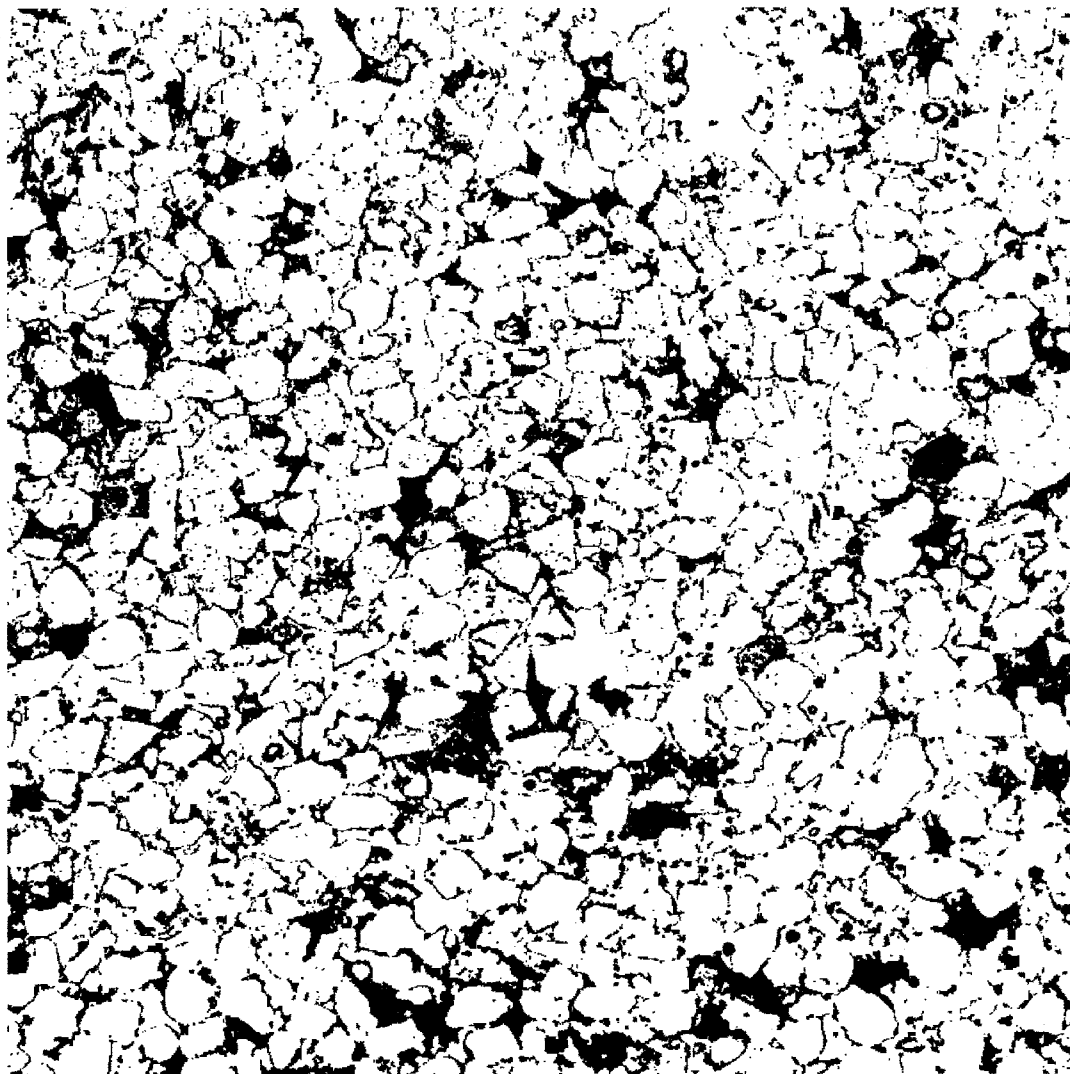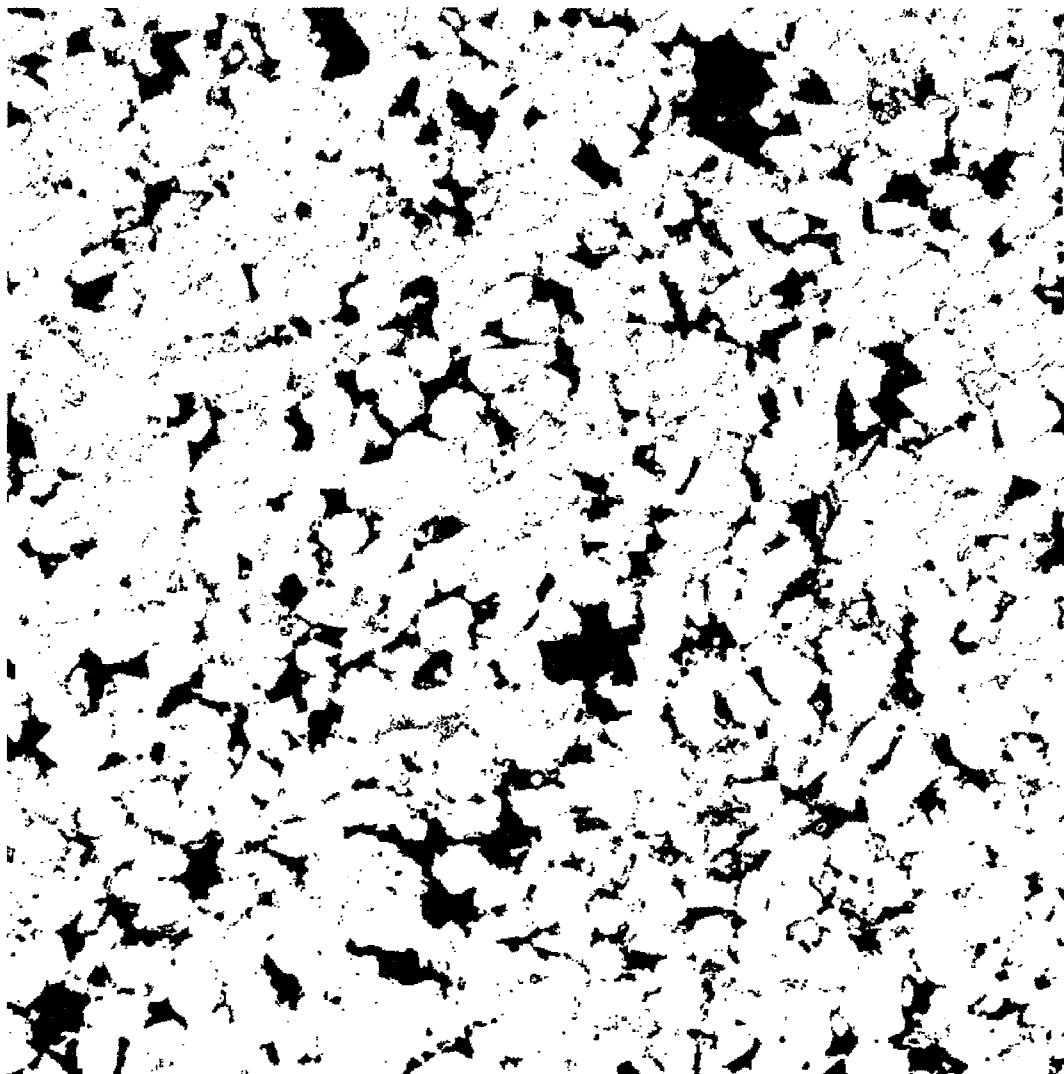
Figure F7

Rendered two-phase photomicrograph of subsection 7K3z.4. White pixels are detrital, framework grains including authigenic micro- and megaquartz and intergranular and intra-granular macroporosity. Black pixels are matrix material, including authigenic iron oxide minerals, ferroan dolomite rhombohedra and allogenic and authigenic clay minerals. This thin section subsection was prepared from 2.5 cm core drilled from a third-order structure and has the 28th highest permeability of all measured subsections. The permeability was measured using the MSP equipped with the 0.15 cm ri tip seal: $k = 2.32E-12$ m^2; ln k = -26.7913 m^2, k = 2351 millidarcies. Matrix material consumes 15.5% of the subsection. Image dimensions are 7.929 mm x 7.929 mm: magnification is 850X.

Figure F8

Rendered two-phase photomicrograph of subsection 7K3z.4. White pixels are detrital, framework grains including authigenic micro- and megaquartz and matrix material, including authigenic iron oxide minerals, ferroan dolomite rhombohedra and allogenic and authigenic clay minerals. Black pixels are intergranular and intragranular macroporosity. This thin section subsection was prepared from 2.5 cm core drilled from a third-order structure and has the 28th highest permeability of all measured subsections. The permeability was measured using the MSP equipped with the 0.15 cm ri tip seal: $k = 2.32E-12$ m^2; ln $k = -26.7913$ m^2, $k = 2351$ millidarcies. Point count porosity was measured as 16.25%, porosity derived from image analysis is 15.76% and matrix material consumes 15.5% of the subsection. Image dimensions are 7.929 mm x 7.929 mm. Magnification is 850X.
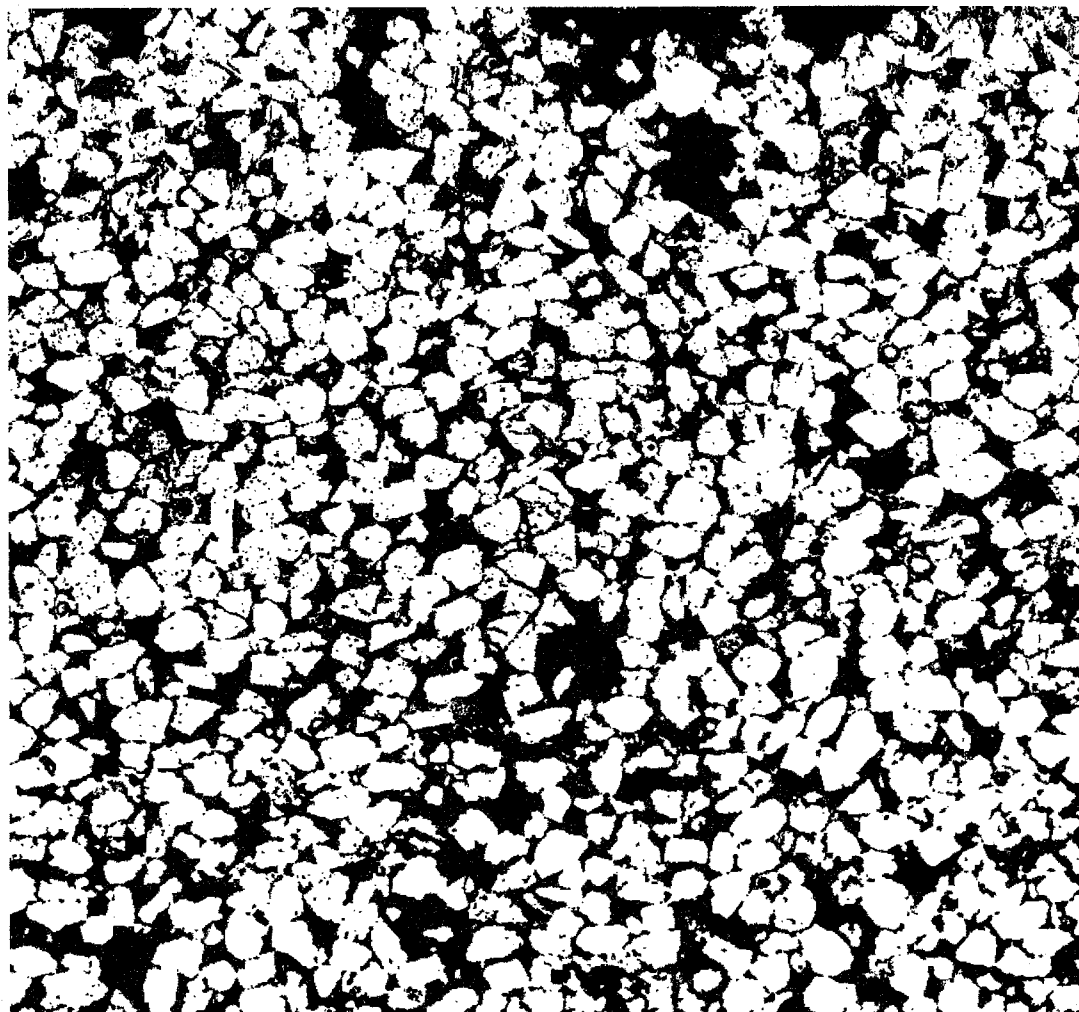
Figure F9

Rendered three-phase photomicrograph of subsection 7K3z.4. White pixels are detrital, framework grains including authigenic micro- and megaquartz. Black pixels are matrix material, including authigenic iron oxide minerals, ferroan dolomite rhombohedra and allogenic and authigenic clay minerals. Blue pixels are intergranular and intragranular macroporosity. This thin section subsection was prepared from 2.5 cm core drilled from a third-order structure and has the 28th highest permeability of all measured subsections. The permeability was measured using the MSP equipped with the 0.15 cm ri tip seal: $k = 2.32E-12$ m^2; ln $k = -26.7913$ m^2, $k = 2351$ millidarcies. Point count porosity was measured as 16.25%, porosity derived from image analysis is 15.76% and matrix material consumes 15.5% of the subsection. The mean grain size is 1.068 phi (medium-upper sand). The sorting is 0.43 phi (well-sorted sand) and was determined using the inclusive graphic standard deviation between measured major axes of 253 framework grains (Folk, 1974). Image dimensions are 9.90 mm x 9.963 mm.
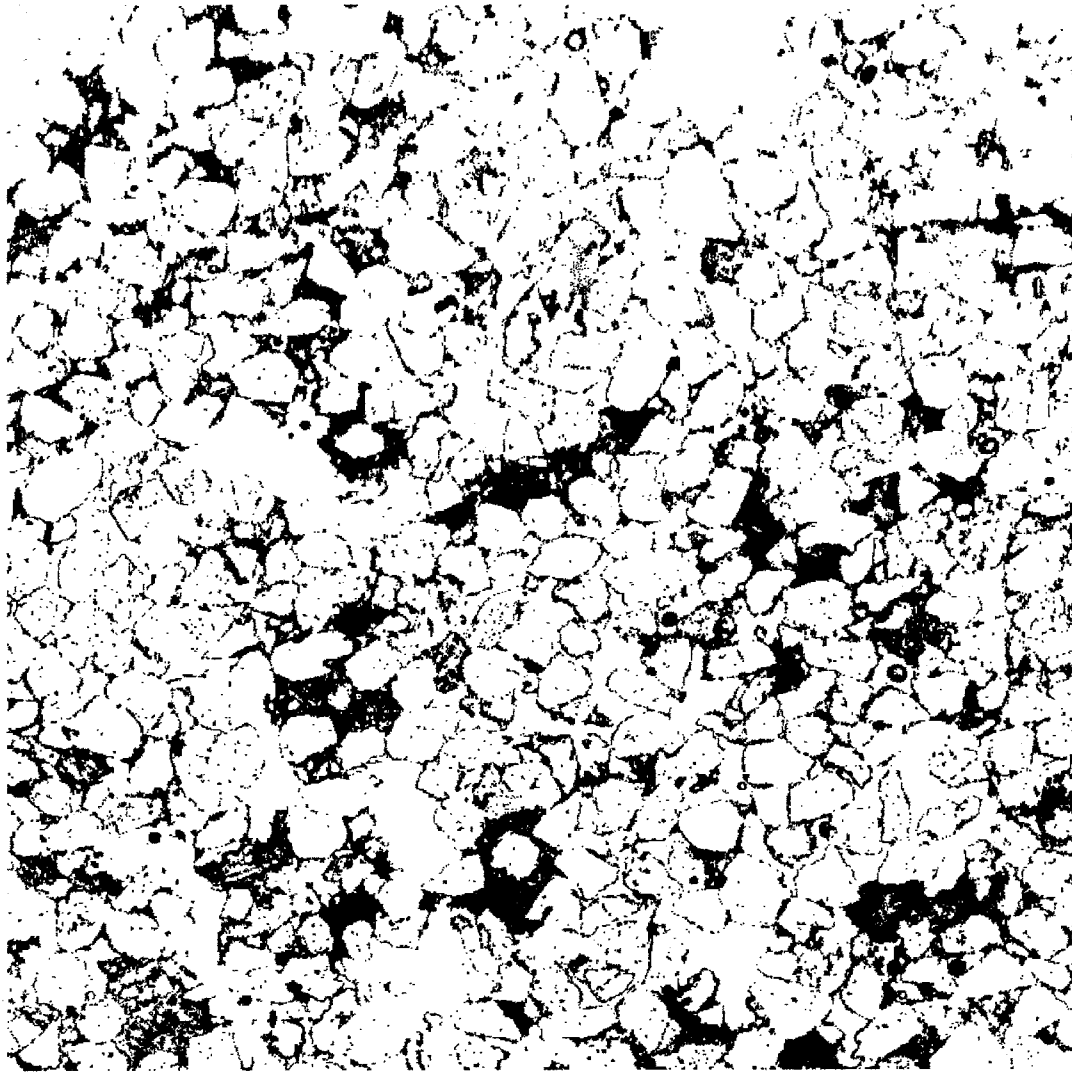
208

Figure F10

Rendered two-phase photomicrograph of subsection 7H3z.4. White pixels are detrital, framework grains including authigenic micro- and megaquartz and intergranular and intragranular macroporosity. Black pixels are matrix material, including authigenic iron oxide minerals, ferroan dolomite rhombohedra and allogenic and authigenic clay minerals. This thin section subsection was prepared from 2.5 cm core drilled from a third-order structure and has the 48th highest permeability of all measured subsections. The permeability was measured using the MSP equipped with the 0.15 cm ri tip seal: $k = 1.7E-12$ m^2; ln $k = -27.0991$ m^2, $k = 1722$ millidarcies. Matrix material is 17.75% of the subsection. Image dimensions are 7.929 mm x 7.929 mm: magnification is 850X.
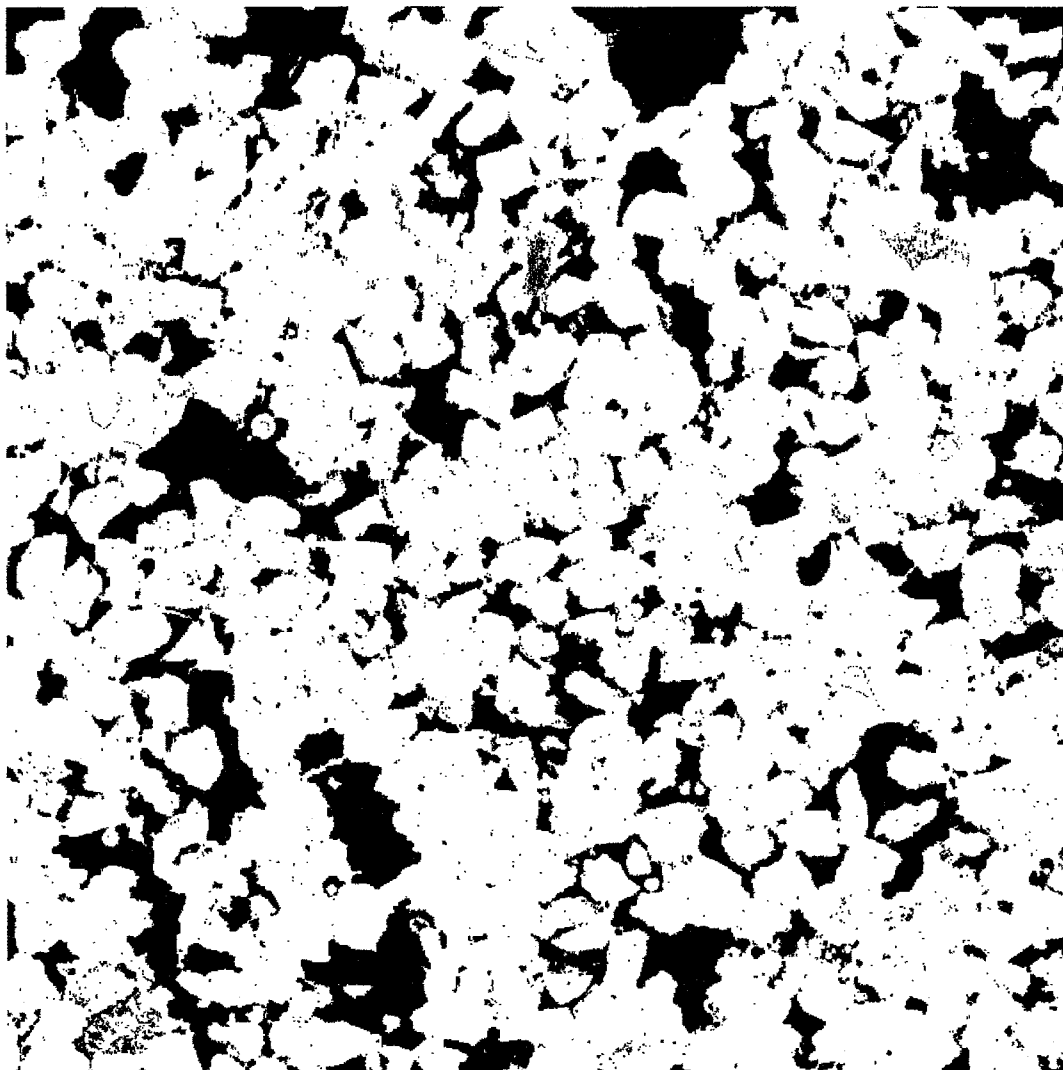
Figure F11

Rendered two-phase photomicrograph of subsection 7H3z.4. White pixels are detrital, framework grains including authigenic micro- and megaquartz and matrix material, including authigenic iron oxide minerals, ferroan dolomite rhombohedra and allogenic and authigenic clay minerals. Black pixels are intergranular and intragranular macroporosity. This thin section subsection was prepared from 2.5 cm core drilled from a third-order structure and has the 48th highest permeability of all measured subsections. The permeability was measured using the MSP equipped with the 0.15 cm ri tip seal: k = 1.7E-12 m^2; ln k = -27.0991 m^2; k = 1722 millidarcies. Point count porosity was measured as 15.0%, porosity derived from image analysis is 16.19% and matrix material consumes 17.75% of the subsection. Image dimensions are 7.929 mm x 7.929 mm. Magnification is 850X.
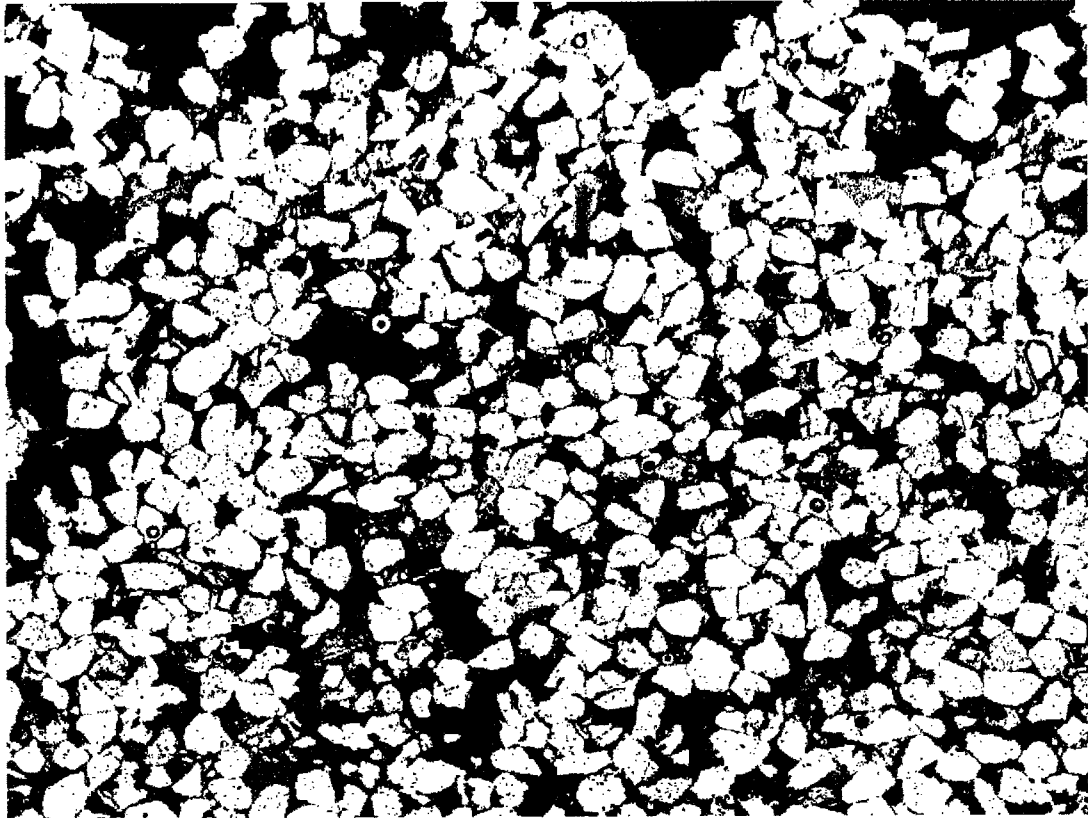
Figure F12

Rendered three-phase photomicrograph of subsection 7H3z.4. White pixels are detrital, framework grains including authigenic micro- and megaquartz. Black pixels are matrix material, including authigenic iron oxide minerals, ferroan dolomite rhombohedra and allogenic and authigenic clay minerals. Blue pixels are intergranular and intragranular macroporosity. This thin section subsection was prepared from 2.5 cm core drilled from a third-order structure and has the 48th highest permeability of all measured subsections. The permeability was measured using the MSP equipped with the 0.15 cm ri tip seal: $k = 1.7\text{E-}12$ m^2; $\ln k = -27.0991$ m^2, $k = 1722$ millidarcies. Point count porosity was measured as 15.0%, porosity derived from image analysis 16.19% and matrix material consumes 17.75% of the subsection. The mean grain size is 1.168 phi (medium-upper sand). The sorting is 0.45 phi (well-sorted sand) and was determined using the inclusive graphic standard deviation between measured major axes of 258 framework grains (Folk, 1974). Image dimensions are 9.333 mm x 8.748 mm. Red areas are uncounted portions of the subsection.
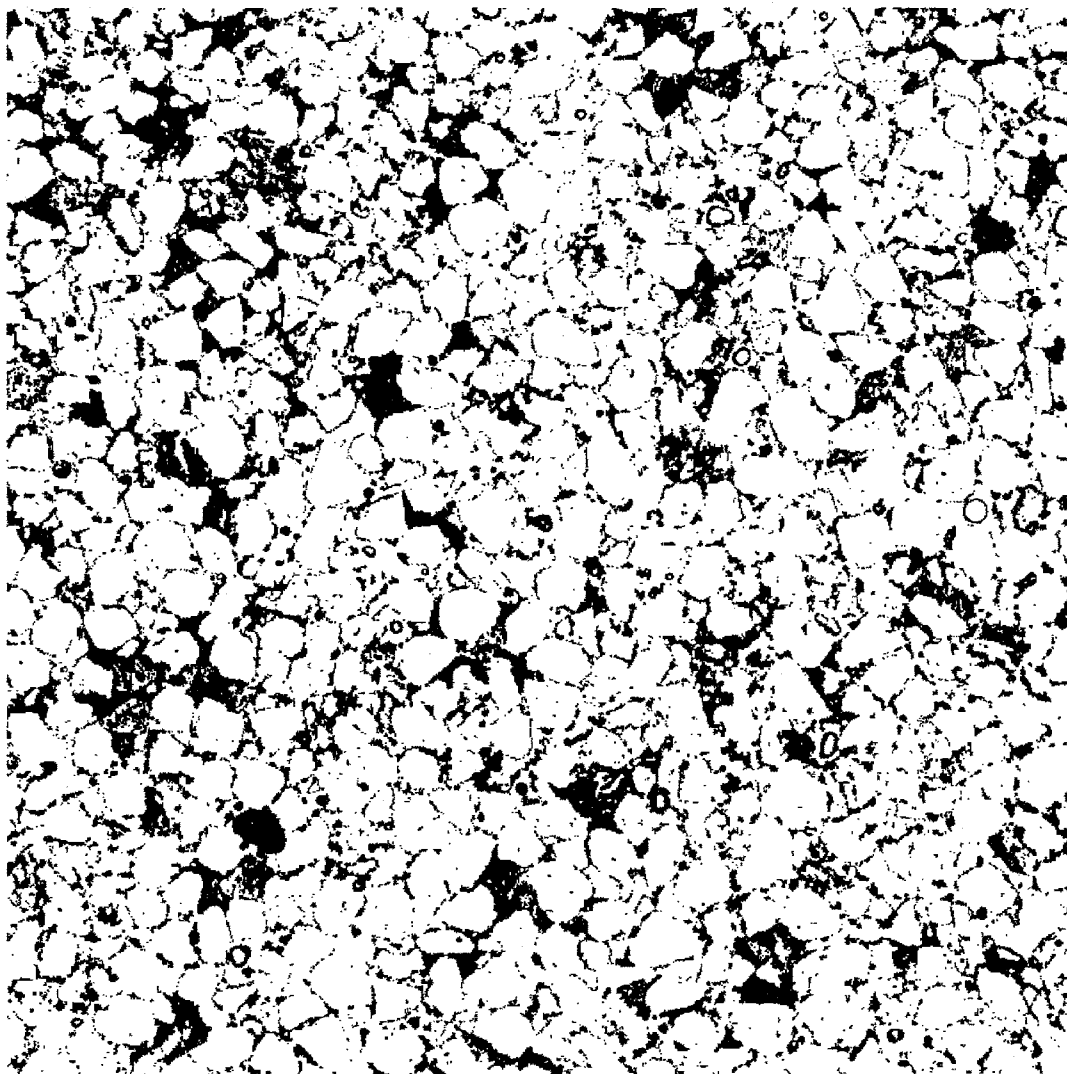
Figure F13

Rendered two-phase photomicrograph of subsection 7B3z.5. White pixels are detrital, framework grains including authigenic micro- and megaquartz and intergranular and intra-granular macroporosity. Black pixels are matrix material, including authigenic iron oxide minerals, ferroan dolomite rhombohedra and allogenic and authigenic clay minerals. This thin section subsection was prepared from 2.5 cm core drilled from a third-order structure and has the 66th highest permeability of all measured subsections. The permeability was measured using the MSP equipped with the 0.15 cm ri tip seal: $k = 1.13E-12$ m^2; $\ln k = -27.5095$ m^2; $k = 1145$ millidarcies. Matrix material consumes 15.25% of the subsection. Image dimensions are 7.929 mm x 7.929 mm: magnification is 850X.
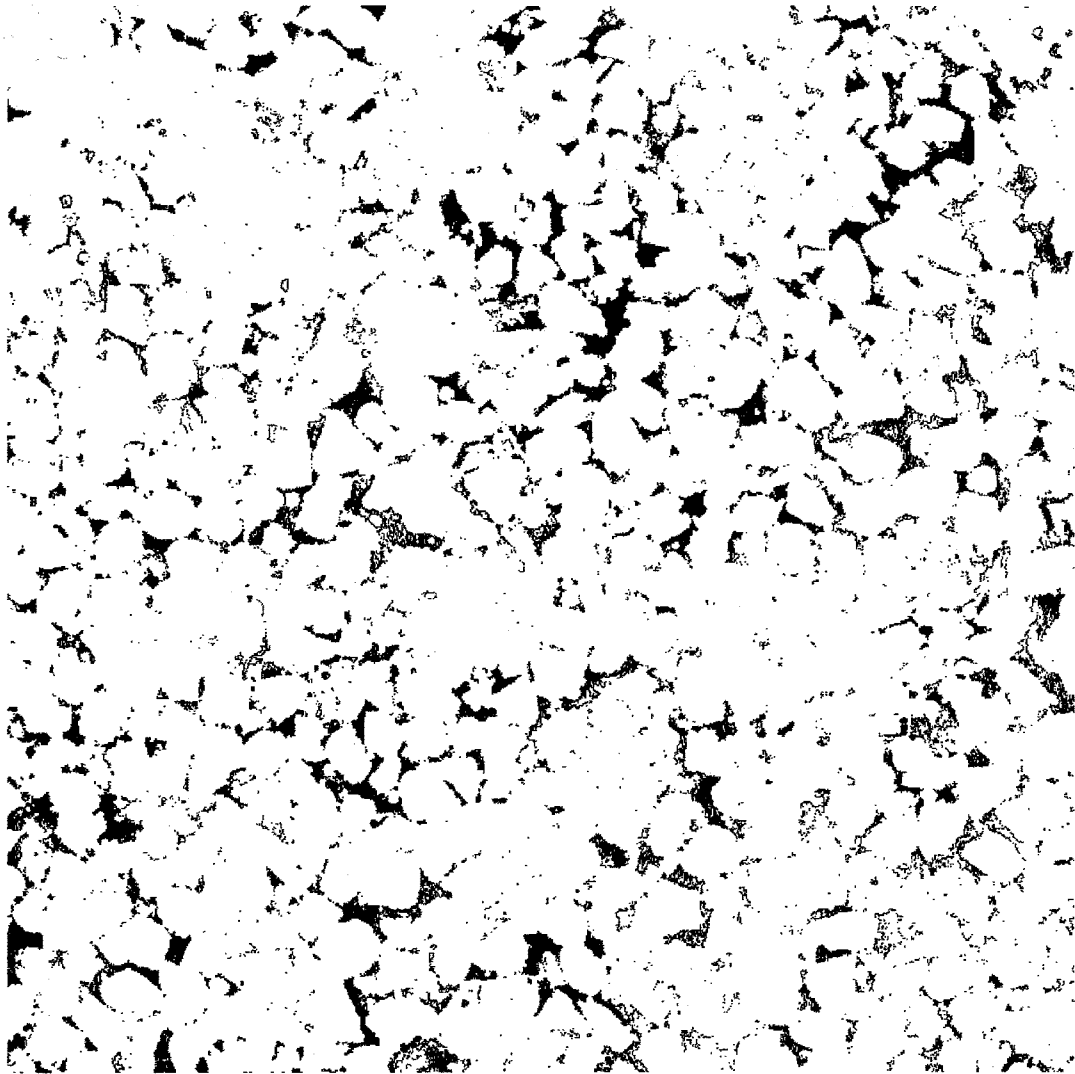
Figure F14

Rendered two-phase photomicrograph of subsection 7B3z.5. White pixels are detrital, framework grains including authigenic micro- and megaquartz and matrix material, including authigenic iron oxide minerals, ferroan dolomite rhombohedra and allogenic and authigenic clay minerals. Black pixels are intergranular and intragranular macroporosity. This thin section subsection was prepared from 2.5 cm core drilled from a third-order structure and has the 66th highest permeability of all measured subsections. The permeability was measured using the MSP equipped with the 0.15 cm ri tip seal: $k = 1.13E-12$ m^2; ln $k = -27.5095$ m^2; $k = 1145$ millidarcies. Point count porosity was measured as 21.5%, porosity derived from image analysis is 23.16% and matrix material consumes 15.25% of the subsection. Image dimensions are 7.929 mm x 7.929 mm; magnification is 850X.

213

Figure F15

Rendered three-phase photomicrograph of subsection 7B3z.5. White pixels are detrital, framework grains including authigenic micro- and megaquartz. Black pixels are matrix material, including authigenic iron oxide minerals, ferroan dolomite rhombohedra and allogenic and authigenic clay minerals. Blue pixels are intergranular and intragranular macroporosity. This thin section subsection was prepared from 2.5 cm core drilled from a third-order structure and has the 66th highest permeability of all measured subsections. The permeability was measured using the MSP equipped with the 0.15 cm ri tip seal: $k = 1.13E-12 \text{ m}^2$; $\ln k = -27.5095 \text{ m}^2$; $k = 1145$ millidarcies. Point count porosity was measured as 21.5%, porosity derived from image analysis is 23.16% and matrix material consumes 15.25% of the subsection. The mean grain size is 0.954 phi (coarse-lower sand). The sorting is 0.35 phi (well-sorted sand) and was determined by applying the inclusive graphic standard deviation to the measured major axes of 243 framework grains (Folk, 1974). Image dimensions are 10.962 mm x 8.253 mm.
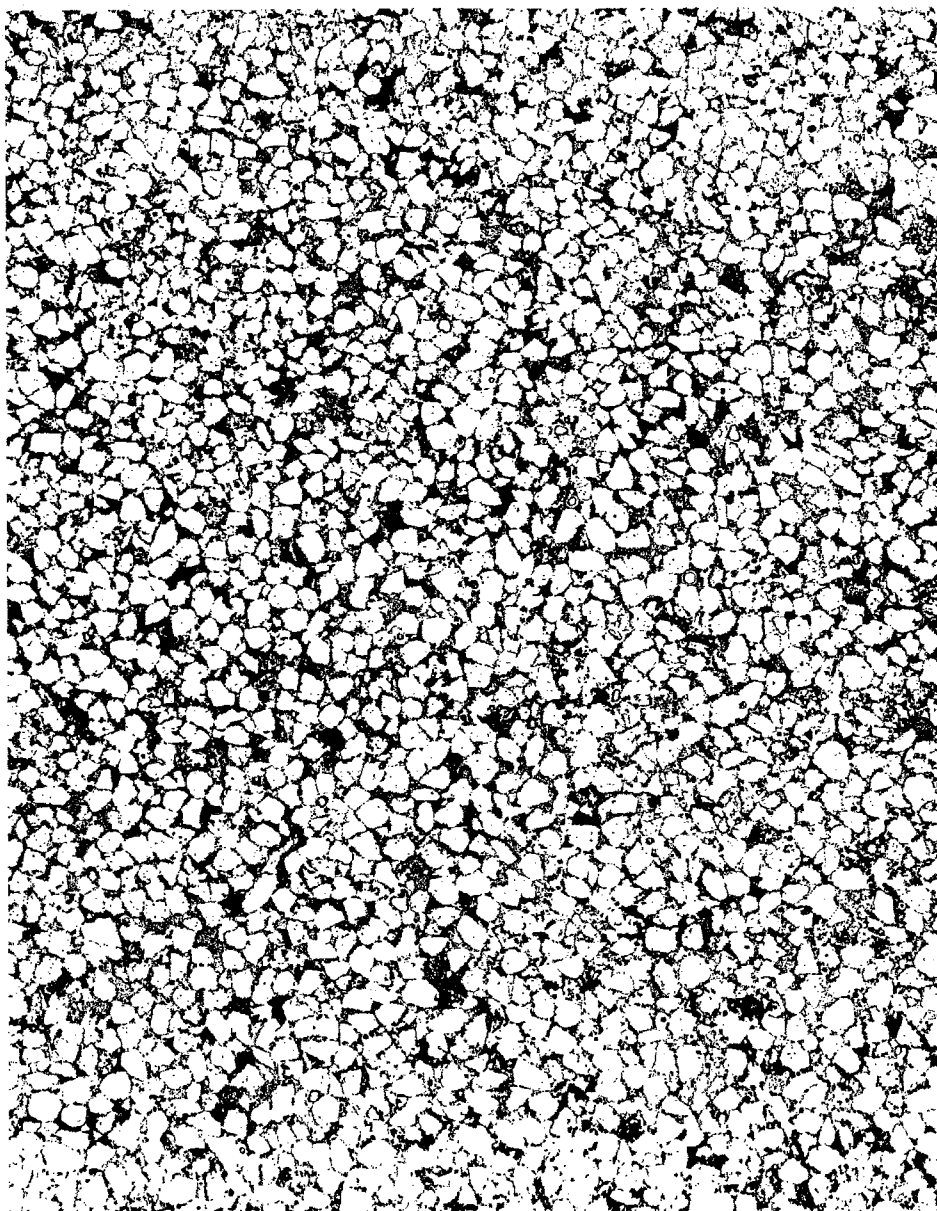
214

Figure F16

Rendered two-phase photomicrograph of subsection 7G1x.2. White pixels are detrital, framework grains including authigenic micro- and megaquartz and intergranular and intra-granular macroporosity. Black pixels are matrix material, including authigenic iron oxide minerals, ferroan dolomite rhombohedra and allogenic and authigenic clay minerals. This thin section subsection was prepared from 2.5 cm core drilled from the first-order bounding surface structure and has the 86th highest permeability of all measured subsections. The permeability was measured using the MSP equipped with the 0.15 cm ri tip seal: $k = 7.07E-13$ m^2; ln $k = -27.9771$ m^2; $k = 716$ millidarcies. Matrix material consumes 21.0% of the subsection. Image dimensions are 7.929 mm x 7.929 mm: magnification is 850X.
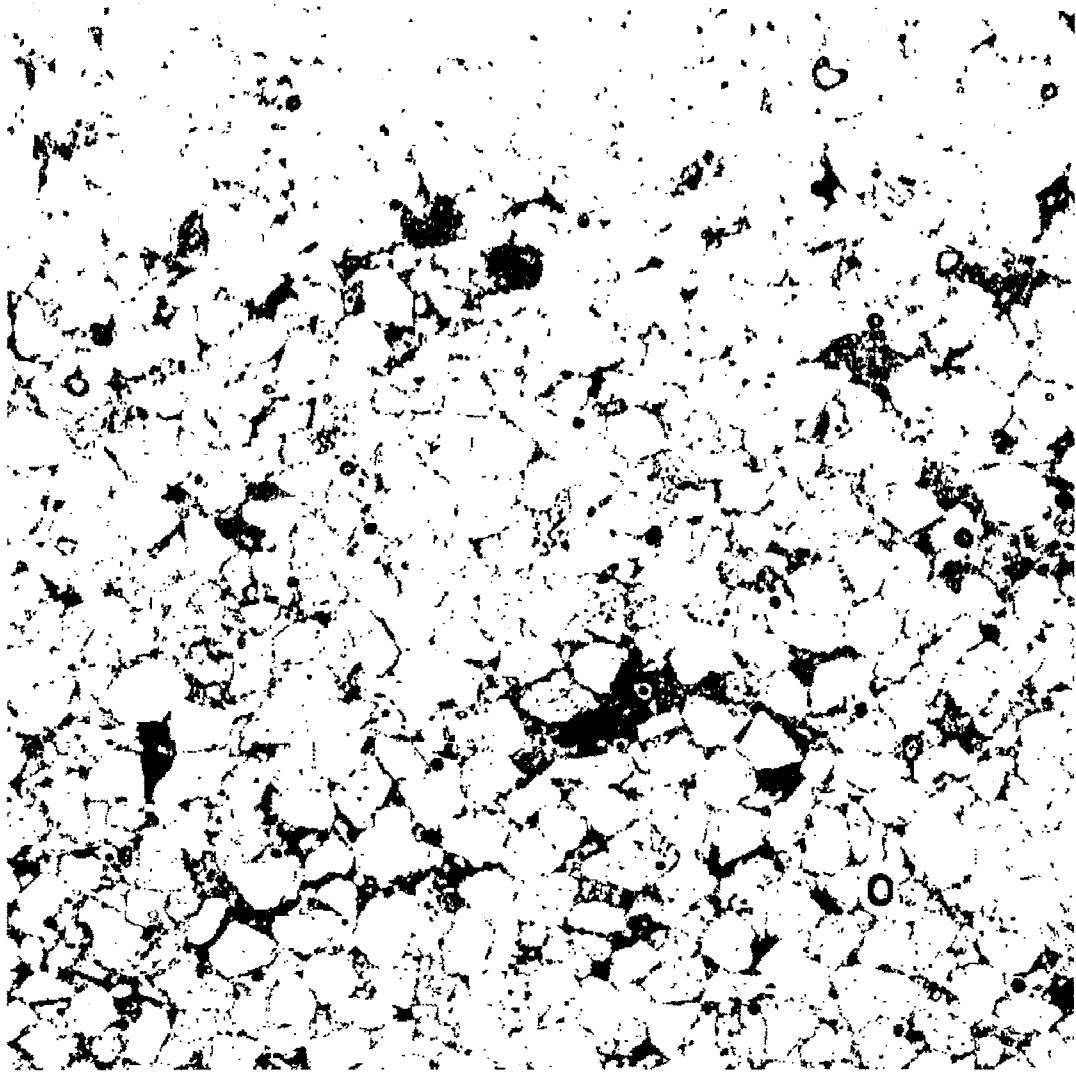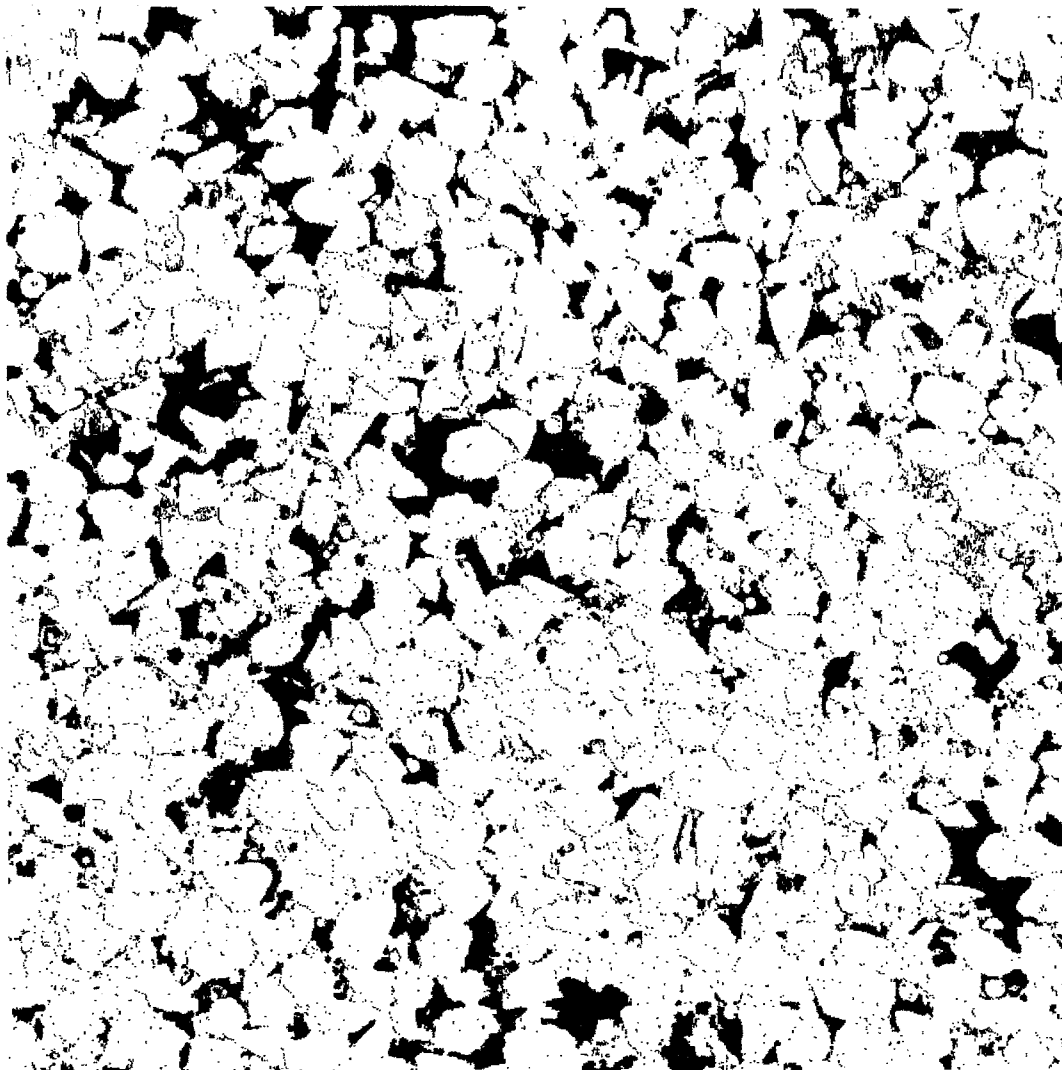
Figure F17

Rendered two-phase photomicrograph of subsection 7G1x.2. White pixels are detrital, framework grains including authigenic micro- and megaquartz and matrix material, including authigenic iron oxide minerals, ferroan dolomite rhombohedra and allogenic and authigenic clay minerals. Black pixels are intergranular and intragranular macroporosity. This thin section subsection was prepared from 2.5 cm core drilled from the first-order bounding surface structure and has the 86th highest permeability of all measured subsections. The permeability was measured using the MSP equipped with the 0.15 cm ri tip seal: $k = 7.07E-13$ m^2; ln k = -27.9771 m^2; $k = 716$ millidarcies. Point count porosity was measured as 10.75%, image analysis porosity is 8.71% and matrix material consumes 21.0% of the subsection. Image dimensions are 7.929 mm x 7.929 mm. Magnification is 850X.

216

Figure F18

Rendered three-phase photomicrograph of subsection 7G1x.2. White pixels are detrital, framework grains including authigenic micro- and megaquartz. Black pixels are matrix material, including authigenic iron oxide minerals, ferroan dolomite rhombohedra and allogenic and authigenic clay minerals. Blue pixels are intergranular and intragranular macroporosity. This thin section subsection was prepared from 2.5 cm core drilled from the first-order bounding surface structure and has the 86th highest permeability of all measured subsections. The permeability was measured using the MSP equipped with the 0.15 cm ri tip seal: k = 7.07E-13 m^2; ln k = -27.9771 m^2; k = 716 millidarcies. Point count porosity is 10.75%, porosity derived from image analysis is 8.71% and matrix material consumes 21.0% of the subsection. Image dimensions are 13.95 mm x 17.937 mm.
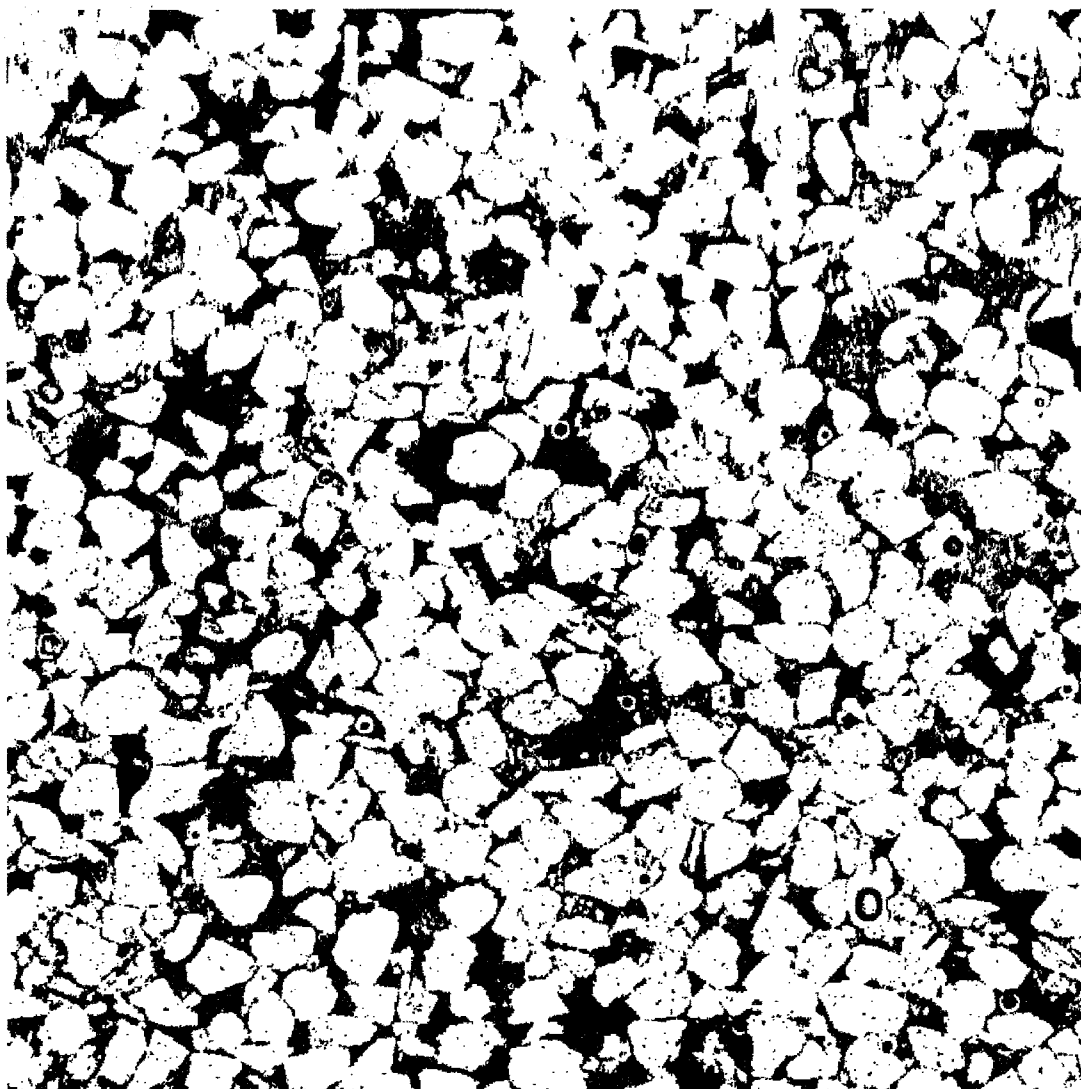
Figure F19

Rendered two-phase photomicrograph of subsection 7B3z.6. White pixels are detrital, framework grains including authigenic micro- and megaquartz and intergranular and intra-granular macroporosity. Black pixels are matrix material, including authigenic iron oxide minerals, ferroan dolomite rhombohedra and allogenic and authigenic clay minerals. This thin section subsection was prepared from 2.5 cm core drilled from a third-order structure and has the 93rd highest permeability of all measured subsections. The permeability was measured using the MSP equipped with the 0.15 cm ri tip seal: $k = 3.24E-13$ m^2; ln k = -28.7577 m^2; $k = 328$ millidarcies. Matrix material consumes 16.0% of the subsection. Image dimensions are 7.929 mm x 7.929 mm: magnification is 850X.

218

Figure F20

Rendered two-phase photomicrograph of subsection 7B3z.6. White pixels are detrital, framework grains including authigenic micro- and megaquartz and matrix material, including authigenic iron oxide minerals, ferroan dolomite rhombohedra and allogenic and authigenic clay minerals. Black pixels are intergranular and intragranular macroporosity. This thin section subsection was prepared from 2.5 cm core drilled from a third-order structure and has the 93rd highest permeability of all measured subsections. The permeability was measured using the MSP equipped with the 0.15 cm ri tip seal: $k = 3.24E\text{-}13$ m^2; ln $k = -28.7577$ m^2; $k = 328$ millidarcies. Point count porosity was measured as 19.5%, porosity derived from image analysis is 16.77% and matrix material consumes 16.0% of the subsection. Image dimensions are 7.929 mm x 7.929 mm: magnification is 850X.
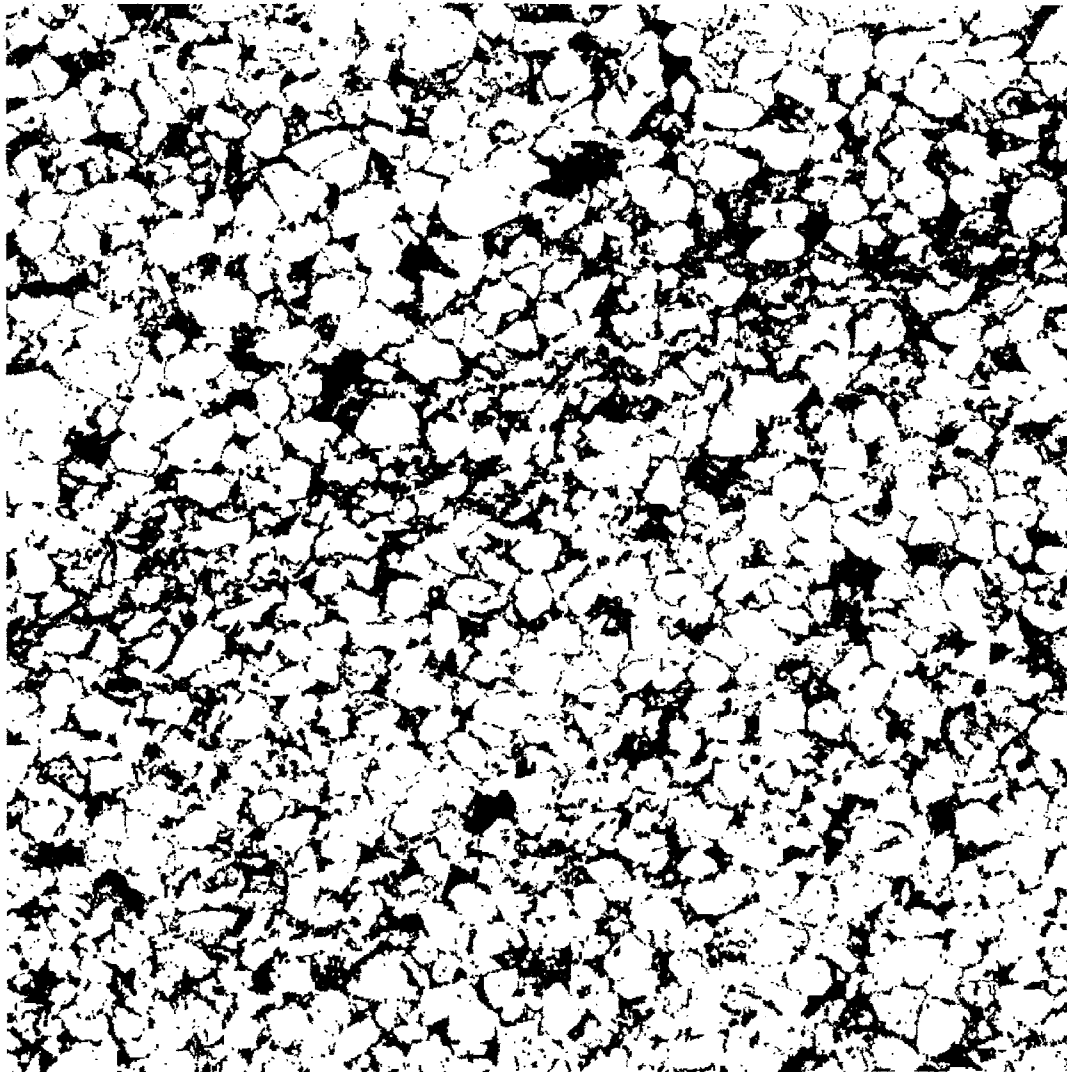
Figure F21

Rendered three-phase photomicrograph of subsection 7B3z.6. White pixels are detrital, framework grains including authigenic micro- and megaquartz. Black pixels are matrix material, including authigenic iron oxide minerals, ferroan dolomite rhombohedra and allogenic and authigenic clay minerals. Blue pixels are intergranular and intragranular macroporosity. This thin section subsection was prepared from 2.5 cm core drilled from a third-order structure and has the 93rd highest permeability of all measured subsections. The permeability was measured using the MSP equipped with the 0.15 cm ri tip seal: k = 3.24E-13 m^2; ln k = -28.7577 m^2; k = 328 millidarcies. Point count porosity was measured as 19.5%, porosity derived from image analysis is 16.77% and matrix material consumes 16.0% of the subsection. The mean grain size is 0.893 phi (coarse-lower sand). The sorting is 0.32 phi (very well-sorted sand) and was determined using the inclusive graphic standard deviation between measured major axes of 244 framework grains (Folk, 1974). Image dimensions are 7.929 mm x 7.929 mm: magnification is 850X.
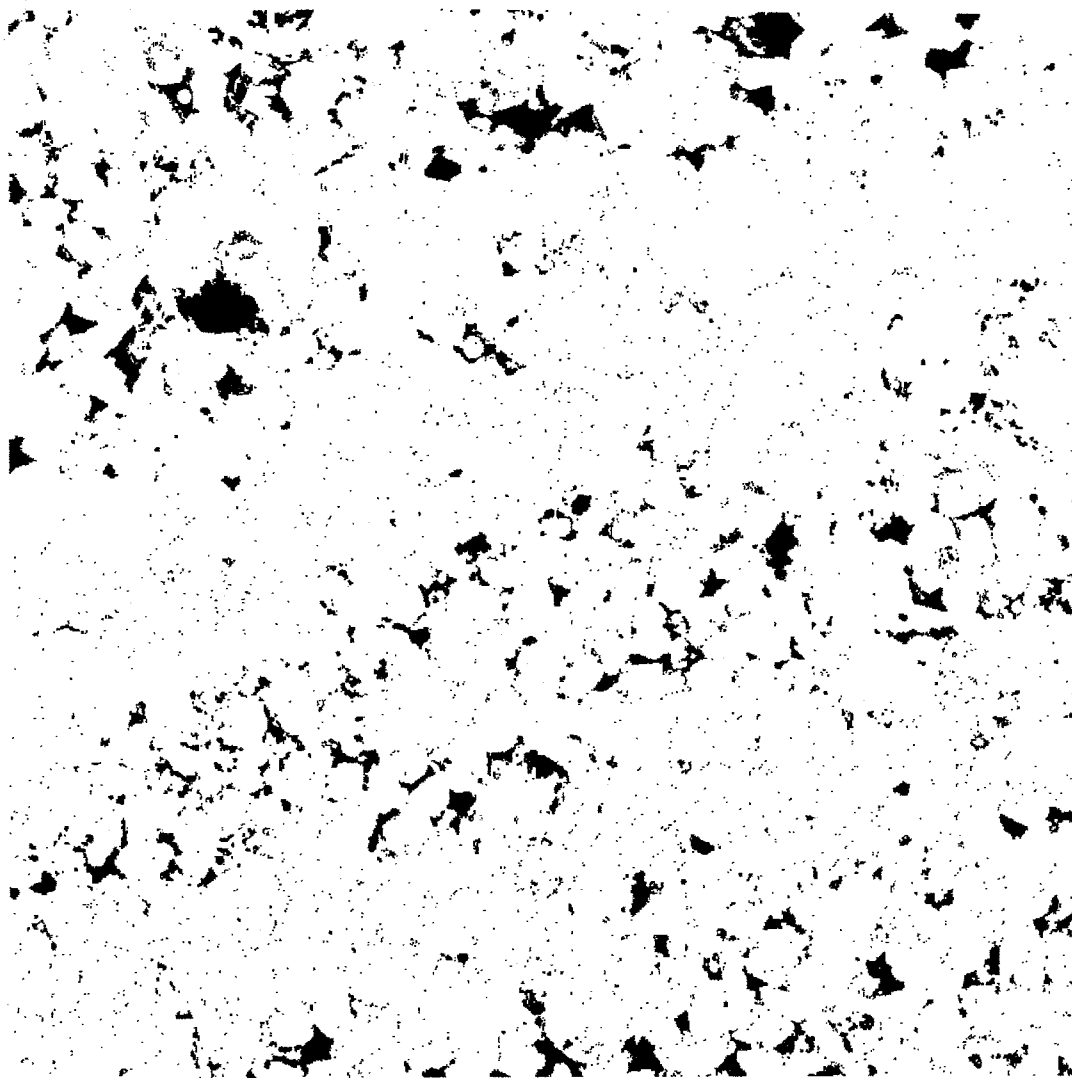
Figure F22

Rendered two-phase photomicrograph of subsection 7A2z.2. White pixels are detrital, framework grains including authigenic micro- and megaquartz and intergranular and intragranular macroporosity. Black pixels are matrix material, including authigenic iron oxide minerals, ferroan dolomite rhombohedra and allogenic and authigenic clay minerals. This thin section subsection was prepared from 2.5 cm core drilled from a second-order bounding surface structure and has the lowest permeability of all measured subsections. The permeability was measured using the MSP equipped with the 0.15 cm ri tip seal: $k = 1.39E-13$ m^2; $\ln k = -29.607$ m^2; $k = 141$ millidarcies. Matrix material consumes 22.25% of the subsection. Image dimensions are 7.929 mm x 7.929 mm: magnification is 850X.
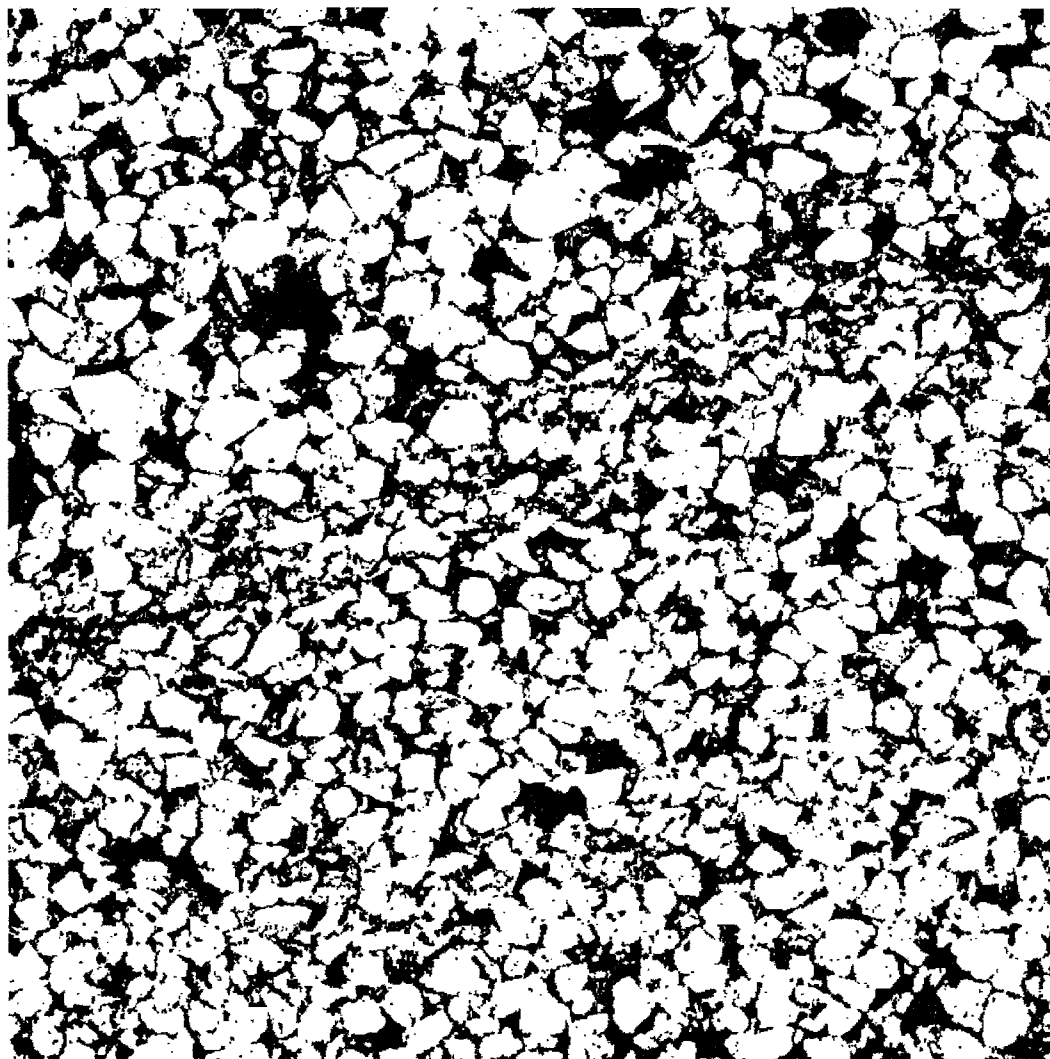
Figure F23

Rendered two-phase photomicrograph of subsection 7A2z.2. White pixels are detrital, framework grains including authigenic micro- and megaquartz and matrix material, including authigenic iron oxide minerals, ferroan dolomite rhombohedra and allogenic and authigenic clay minerals. Black pixels are intergranular and intragranular macroporosity. This thin section subsection was prepared from 2.5 cm core drilled from a second-order bounding surface structure and has the lowest permeability of all measured subsections. The permeability was measured using the MSP equipped with the 0.15 cm ri tip seal: $k = 1.39E-13$ m^2; ln $k = -29.607$ m^2; $k = 141$ millidarcies. Point count porosity was measured as 11.25%, porosity derived from image analysis is 6.18% and matrix material consumes 22.25% of the subsection. Image dimensions are 7.929 mm x 7.929 mm: magnification is 850X.

222

Figure F24

Rendered three-phase photomicrograph of subsection 7A2z.2. White pixels are detrital, framework grains including authigenic micro- and megaquartz. Black pixels are matrix material, including authigenic iron oxide minerals, ferroan dolomite rhombohedra and allogenic and authigenic clay minerals. Blue pixels are intergranular and intragranular macroporosity. This thin section subsection was prepared from 2.5 cm core drilled from a second-order bounding surface structure and has the lowest permeability of all measured subsections. The permeability was measured using the MSP equipped with the 0.15 cm ri tip seal: k = 1.39E-13 m^2; ln k = -29.607 m^2; k = 141 millidarcies. Point count porosity was measured as 11.25%, porosity derived from image analysis is 6.18% and matrix material consumes 22.25% of the subsection. The mean grain size is 1.278 phi (medium-upper sand). The sorting is 0.44 phi (well-sorted sand) and was determined using the inclusive graphic standard deviation between measured major axes of 256 framework grains (Folk, 1974). Image dimensions are 7.929 mm x 7.929 mm: magnification is 850X.

REFERENCES

Abell, A.B., Willis, K.L. and Lange, D.A., 1998, Mercury intrusion porosimetry and image analysis of cement-based minerals: Journal of Colloidal and Interface Science, 8 p.

Aharonov E., Rothman, D.H., Thompson, A.H., 1997, Transport properties and diagenesis in sedimentary rocks: The role of micro-scale geometry: Geology, v. 25, n. 6, p. 547-550.

Beard, D.C. and Weyl, P.K., 1973, Influence of texture on porosity and permeability of unconsolidated sand: AAPG Bulletin, v. 57, n. 2, p. 349-369.

Berryman, J.G. and Blair, S.C., 1986, Use of digital image analysis to estimate fluid permeability of porous materials: Application of two-point correlation functions: Journal of Applied Physics, v. 60, n. 6, 1930-1938.

Bjørlykke, K., 1984, Formation of secondary porosity: How important is it?, in D.A. McDonald and R.C. Surdam, eds., Clastic Diagenesis: AAPG Memoir 37, p. 277-286.

Bjørlykke, K., 1993, Fluid flow in sedimentary basins: Sedimentary Geology, v. 86, p. 137-158.

Bjørlykke, K. and Egeberg, P.K., 1993, Quartz cementation in sedimentary basins: AAPG Bulletin, v. 77, n. 9, p.1538-1548.

Blatt, H., 1979, Diagenetic processes in sandstones: SEPM Special Publication No. 26, p.141-157.

Bliefnick, D.M. and Kaldi, J.G., 1996, Pore geometry: Control on reservoir properties, Walker Creek Field, Columbia and Lafayette Counties, Arkansas: AAPG Bulletin, v. 80, n. 7, p. 1027-1044.

Bloch, S., 1994, Secondary porosity in sandstones: significance, origin, relationship to subaerial unconformities and effect on predrill reservoir quality assessment, in M.D. Wilson, ed., Reservoir Quality Assessment and Prediction in Clastic Rocks: SEPM Short Course 30, p. 137-159.

Bloch, S., 1994, Effect of detrital mineral composition on reservoir quality, in M.D. Wilson, ed., Reservoir Quality Assessment and Prediction in Clastic Rocks: SEPM Short Course 30, p. 161-182.

Bloch, S., 1994, Petrographic analysis of porosity and permeability, in M.D. Wilson, ed., Reservoir Quality Assessment and Prediction in Clastic Rocks: SEPM Short Course 30, p. 247-258.

Bloch S. and McGowen, J.H., 1994, Influence of depositional environment on reservoir quality prediction, in M.D. Wilson, ed., Reservoir Quality Assessment and Prediction in Clastic Rocks: SEPM Short Course 30, p. 41-57.

Boggs, Jr., S., 1995, Principles of Sedimentology and Stratigraphy: Upper Saddle River, NJ, Prentice Hall, 774 p.

Brookfield, M.E., 1977, The origin of bounding surfaces in ancient eolian sandstones: Sedimentology, v. 24, p. 303-332.

Bryant S., Cade, C. and Mellor, D., 1993, Permeability prediction from geologic models: AAPG Bulletin, v. 77, n. 8, p. 1338-1350.

Bryant, I.D., Greenstreet, C.W. and Voggenreiter, W., 1995, Integrated 3-D geological modeling of the C1 Sands Reservoir, Maui Field, offshore New Zealand: AAPG Bulletin, v. 79, n. 3, p. 351-374.

Burns, L. and Ethridge, F.G., 1979, Petrology and diagenetic effects of lithic sandstones; Paleocene and Eocene Umpqua Formation, Southwest Oregon: SEPM Special Publication 26, p. 307-317.

Byrnes, A.P., 1994, Measurement of dependent variables-petrophysical variables, in M.D. Wilson, ed., Reservoir Quality Assessment and Prediction in Clastic Rocks: SEPM Short Course 30, p. 231-246.

Cant, D.J., 1982, Fluvial facies models and their application, in P.A. Scholle and D. Spearing, eds., Sandstone Depositional Environments: AAPG Memoir No. 31, p. 115-137.

Clelland, W.D. and Fens, T.W., 1991, Automated rock characterization with SEM/image analysis techniques: SPE Formation Evaluation, p. 437-443.

Clelland, W.D., Kantorowicz, J.D. and Fens, T.W., 1993, Quantitative analysis of pore structure and its effect on reservoir behavior: Upper Jurrasic Ribble Member Sandstones, Fulmer Field, UK North Sea, in M. Ashton, ed., Advances in Reservoir Geology: London, UK, The Geological Society, p. 57-81.

Coskun, S.B., Wardlaw, N.C. and Haverslew, B., 1993, Effects of composition, texture and diagenesis on porosity, permeability and oil recovery in a sandstone reservoir: Journal of Petroleum Science and Engineering, v. 8, p. 279-292.

Davidson, G., Petford, N. and Miller, J.A., 1998, Application of confocal scanning laser microscopy to pore structure determination: Annales Geophysicae, pt. 1, European Geophysical Society, p. C253.

Davies, D.K. and Ethridge, F.G., 1975, Sandstone composition and depositional environment: AAPG Bulletin, p. 239-264.

Davis, J.C., 1986, Statistics and Data Analysis in Geology: John Wiley and Sons, NY, 646 p.

Daws, J.A. and Prosser, D.J., 1992, Scales of permeability heterogeneity within the Brent Group: Journal of Petroleum Geology, v. 15, n. 4, p. 397-418.

Doyle, J.D. and Sweet, M.L., 1995, Three-dimensional distribution of lithofacies, bounding surfaces, porosity and permeability in a fluvial sandstone-Gypsy sandstone of northern Oklahoma: AAPG Bulletin, v. 79, n. 1, p. 70-96.

Dullien, F.A.L., 1991, Characterization of porous media-pore level: Transport in Porous Media, v. 6, p. 581-600.

Dutton, S.P. and Diggs, T.N., 1992, Evolution of porosity and permeability in the lower Cretaceous Travis Peak Formation, East Texas: AAPG Bulletin, v. 76, n. 2, p. 252-269.

Dutton, S.P., 1997, Timing of compaction and quartz cementation from integrated petrographic and burial-history analysis, Lower Cretaceous Fall River Formation, Wyoming and South Dakota: Journal of Sedimentary Research, v. 67, n. 1, p. 186-196.
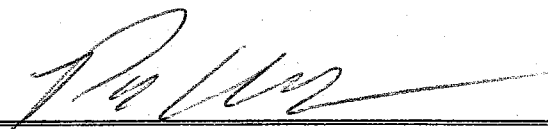
Ehrenberg, S.N., 1990, Relationship between diagenesis and reservoir quality in sandstones of the Garn Formation, Haltenbanken, Mid-Norwegian continental shelf: AAPG Bulletin, v. 74, n. 10, p. 1538-1558.

Ehrenberg, S.N. and Boassen, T., 1993, Factors controlling permeability variation in sandstones of the Garn Formation in Trestakk Field, Norwegian Continental Shelf: Journal of Sedimentary Petrology, v. 63, n. 5, p. 929-944.

Ehrenberg, S.N., 1995, Measuring sandstone compaction from modal analysis of thin sections: How to do it and what the results mean: Journal of Sedimentary Research, v. A65, n. 2, p. 369-379.

Ehrenberg, 1997, Influence of depositional sand quality and diagenesis on porosity and permeability: Examples from Brent Group Reservoirs, Northern North Sea: Journal of Sedimentary Research, v. 67, n. 1, p. 197-211.

Ehrlich, R., Crabtree, S.J., Horkowitz, K.O. and Horkowitz, J.P., 1991, Petrography and reservoir physics I: Objective classification of reservoir porosity: AAPG Bulletin, v. 75, n. 10, p. 1547-1562.

Ehrlich, R., Etris, E.L., Brumfield, D., Yuan, L.P. and Crabtree, S.J., 1991, Petrography and reservoir physics III: Physical models for permeability and formation factor: AAPG Bulletin, v. 75, n. 10, p. 1579-1592.

Ehrlich, R., Kennedy, S.K., Crabtree, S.J. and Cannon, R.L., 1984, Petrographic image analysis, I. Analysis of reservoir pore complexes: Journal of Sedimentary Petrology, v. 54, n. 4, p. 1365-1378.

Folk, R.L., 1974, Petrology of Sedimentary Rocks: Austin, TX, Hemphill Publishing Company, 182 p.

Galloway, W.E., 1979, Diagenetic control of reservoir quality in arc-derived sandstones: implications for petroleum exploration: SEPM Special Publication No. 26, p. 251-262.

Gelhar, L.W., 1993, Stochastic Subsurface Hydrology: New Jersey, Prentice Hall, 401 p.

Goggin, D.J., Thrasher, R.L. and Lake, L.W., 1988, A theoretical and experimental analysis of minipermeameter response including gas slippage and high velocity flow effects: In Situ, v. 12, n. 1-2, p. 79-116.

Hamlin, H.S., Dutton, S.P., Seggie, R.J. and Tyler, N., 1996, Depositional controls on reservoir properties in a braid-delta sandstone, Tirrawarra Oil Field, South Australia: AAPG Bulletin, v. 80, n. 2, p. 139-156.

Hartkamp, C.A., Arribas, J. and Tortosa, A., 1993, Grain size, composition, porosity and permeability contrasts within cross-bedded sandstones in Tertiary fluvial deposits of central Spain: Sedimentology, v. 40, n. 4, p. 787-799.

Harris, N., 1989, Diagenetic quartzarenite and destruction of secondary porosity: An example from the Middle Jurassic Brent Sandstone of northwest Europe: Geology, v. 17, p. 361-364.

Heald, M.T. and Renton, J.J., 1966, Experimental study of sandstone cementation: Journal of Sedimentary Petrology, v. 36, n. 4, p. 977-991.

Heydari, E., 1997, The role of burial diagenesis in hydrocarbon destruction and H2S accumulation, Upper Jurassic Smackover Formation, Black Creek Field, Mississippi: AAPG Bulletin, v. 81, n. 1, p. 26-45.

Houseknecht, D.W., 1984, Influence of grain size and temperature on intergranular pressure solution, quartz cementation and porosity in a quartzose sandstone: Journal of Sedimentary Petrology, v. 54, n. 2, p. 348-361.

Houseknecht, D.W., 1987, Assessing the relative importance of compaction processes and cementation to reduction of porosity in sandstones: AAPG Bulletin, v. 71, n. 6, p. 633-642.

Howard, J.J., Kenyon, W.E. and Straley, C., 1993, Proton magnetic resonance and pore size variations in reservoir sandstones: SPE Formation Evaluation, v. 8, n. 3, p. 194-200.

Jordan, D.W. and Pryor, W.A., 1992, Hierarchical levels of heterogeneity in a Mississippi River meander belt and application to reservoir systems: AAPG Bulletin, v. 76, n. 10, p.1601-1624.

Kumar, N. and Sanders, J.E., 1974, Inlet sequence, a vertical succession of sedimentary structures and textures created by lateral migration of tidal inlets: Sedimentology, v. 21, p. 491-532.

Land, L.S. and Dutton, S.P.,1978, Cementation of a Pennsylvanian deltaic sandstone: isotopic data: Journal of Sedimentary Petrology, v. 48, n. 4, p. 1167-1176.

Leder, F. and Park, W.C., 1986, Porosity reduction in sandstone by quartz overgrowth: AAPG Bulletin, v. 70, n. 11, p.1713-1728.

Lundegard, P.D., 1991, Sandstone porosity loss-a "Big Picture" view of the importance of compaction, Journal of Sedimentary Petrology, v. 62, n. 2, p. 250-260.

MacKenzie, W.S. and Adams, A.E., 1994, A Color Atlas of Rocks and Minerals in Thin Section: New York, Wiley and Sons, Inc., 192 p.

Marfil R., Scherer, M. and Turrero, M.J., 1996, Diagenetic processes influencing porosity in sandstones from the Triassic Buntsandstein of the Iberian Range, Spain: Sedimentary Geology, v. 105, p. 203-219.

McBride, E.F., 1989, Quartz cement in sandstones: A review: Earth Science Reviews, v. 26, p. 69-112.

McCubbin, D.G., 1982, Barrier island and strand-plain facies, in P.A. Scholle and D. Spearing, eds., Sandstone Depositional Environments: AAPG Memoir No. 31, p. 247-279.

McDonald, D.A. and Surdam, R.C. eds., 1984, Clastic Diagenesis: AAPG Memoir 37, 434 p.

Miall, A.D., 1977, A review of the braided-river depositional environment: Earth Science Reviews, v. 13, p. 1-62.

Miall, A.D., 1992, Alluvial Deposits, in R.G. Walker and N.P. James, eds., Facies Models; Response to Sea Level Change: Geological Association of Canada, p. 119-142.

Miall, A.D., 1996, The Geology of Fluvial Deposits: New York, Springer-Verlag, 582 p.

Mitra, S. and Beard, W. C., 1980, Theoretical models of porosity reduction by pressure solution for well-sorted sandstones: Journal of Sedimentary Petrology, v. 50, n. 4, p. 1347-1360.

Morse, D.G., 1994, Siliciclastic reservoir rocks, in L.B. Magoon and W.G. Dow, eds., The Petroleum System-from Source to Trap: AAPG Memoir 60, 655 p.
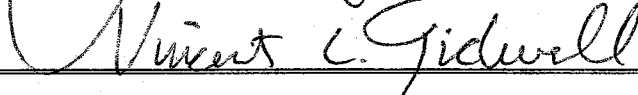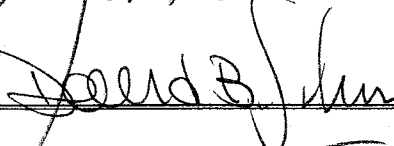
Mou, D.C. and Brenner, R.L., 1982, Control of reservoir properties of Tensleep Sandstone by depositional and diagenetic facies: Lost Soldier Field, Wyoming: Journal of Sedimentary Petrology, v. 52, n. 2, p. 367-381.

Muchez, P., Viaene, W. and Dusar, M., 1992, Diagenetic controls on secondary porosity in flood plain deposits: an example of the lower Triassic of northeastern Belgium: Sedimentary Geology, v. 78, n. 3-4, p. 285-298.

Nelson, P.H., 1994, Permeability-porosity relationships in sedimentary rocks: The Log Analyst, May-June 1994, p. 38-62.

Pate, C.R., 1989, Assessing the relative importance of compaction processes and cementation to reduction of porosity in sandstones: Discussion: AAPG Bulletin, v. 73, n. 10, p. 1270-1273.

Pettijohn, F.J., Potter, P.E. and Siever, R., 1973, Sand and Sandstone: New York, Springer Verlag, 618 p.

Pittman, E.D., 1979, Porosity, diagenesis and productive capability of sandstone reservoirs: SEPM Special Publication, No. 26, p. 159-173.

Pittman, E.D. and Larese, R.E., 1991, Compaction of lithic sands: Experimental results and applications: AAPG Bulletin, v. 75, n. 8, p. 1279-1299.

Pollastro, R.M., 1991, Composition, clay mineralogy and diagenesis of the Simpson Group (Middle Ordivician), Grady County, Oklahoma: U. S. Geological Survey Bulletin, v. 1866, p. H1-H19.

Prince, C.M., 1999, Textural and diagenetic controls on sandstone permeability: GCAGS Proceedings, Lafayette, LA, 21 p.

Pryor, W.A., 1973, Permeability-porosity patterns and variations in some Holocene sand bodies: AAPG Bulletin, v. 57, n. 1, p. 162-189.

Reed, S.J.B., 1997, Electron Microprobe Analysis and Scanning Electron Microscopy in Geology: New York, Cambridge University Press, 326 p.

Reineck, H.E. and Singh, I.B., 1975, Depositional Sedimentary Environments: New York, Springer-Verlag, 439 p.

Rizzo, J.S., 1993, Hydrogeology of the River Styx Basin, Medina and Wayne Counties, Ohio: Master's Thesis, University of Akron, OH, 112 p.

Rubin, D.M., 1987, Cross-bedding, bedforms and palaeocurrents: SEPM's Concepts in Sedimentology and Paleontology, v. 1, 187 p.

Russ, J.C., 1992, The Image Processing Handbook: CRC Press Inc., Boca Raton, FL, 445 p.

Ruzyla, K., 1986, Characterization of pore space by quantitative image analysis: SPE Formation Evaluation, p. 389-398.

Sanderson, I.D., 1984, Recognition and significance of inherited quartz overgrowths in quartz arenites: Journal of Sedimentary Petrology, v. 54, n. 2, p. 473-486.

Scherer, M., 1987, Parameters influencing porosity in sandstones: A model for sandstone porosity prediction: AAPG Bulletin, v. 71, n. 5, p. 485-491.

Schmidley, E.B., 1987, The sedimentology, paleogeography and tectonic setting of the Pennsylvanian Massillon Sandstone in East-central Ohio: Master's Thesis, University of Akron, OH, 155 p.

Schmidt, V., McDonald, D.A. and Platt, R.L., 1977, Pore geometry and reservoir aspects of secondary porosity in sandstones: Bulletin of Canadian Petroleum Geology, v. 25, p. 271-290.

Schmidt, V. and McDonald, D.A., 1979, The role of secondary porosity in the course of sandstone diagenesis, *in* Aspects of Diagenesis: SEPM Special Publication No. 26, p. 175-207.

Schmidt, V. and McDonald, D.A., 1979, Texture and recognition of secondary porosity in sandstones, *in* Aspects of Diagenesis: SEPM Special Publication 26, p. 209-225.

Scholle, P.A., 1979, A Color Illustrated Guide to Constituents, Textures, Cements and Porosities of Sandstones and Associated Rocks: AAPG Memoir 28, 201 p.

Shumway, R.H., 1988, Applied Statistical Time Series Analysis: New Jersey, Prentice Hall, 173 p.

Siebert, R.M., Moncure, G.K. and Lahann, R.W., 1984, A theory of framework grain dissolution in sandstones, *in* D.A. McDonald and R.C. Surdam, eds., Clastic Diagenesis: AAPG Memoir 37, p. 163-175.

Tang, Z., Parnell, J. and Longstaffe, F.J., 1997, Diagenesis and reservoir potential of Permian-Triassic fluvial/lacustrine sandstones in the southern Junggar Basin, northwestern China: AAPG Bulletin, v. 81, n. 11, p. 1843-1865.

Tidwell, V.C. and Wilson, J.L., 1997, Laboratory method for investigating permeability upscaling: Water Resources Research, v. 33, n. 7, p. 1607-1616.

Tidwell, V.C. and Wilson, J.L., 2000, Heterogeneity, permeability patterns, and permeability upscaling; physical characterization of a block of Massillon Sandstone exhibiting nested scales of heterogeneity: SPE Reservoir Evaluation and Engineering, v. 3, n. 4, p. 283-291.

Van der Plas, L. and Tobi, A.C., 1965, A chart for judging the reliability of point counting results: American Journal of Science, v. 263, p. 87-90.

Weedman, S.D., Brantley, S.L., Shiraki, R. and Poulson, S.R., 1996, Diagenesis, compaction and fluid chemistry modeling of a sandstone near a pressure seal: Lower Tuscaloosa Formation, Gulf Coast: AAPG Bulletin, v. 80, n. 7, p.1045-1064.

Welton, J.E., 1984, SEM Petrology Atlas: AAPG Methods in Exploration Series, 237 p.

Williams, L.A. and Crerar, D.A., 1985, Silica diagenesis, II. General mechanisms: Journal of Sedimentary Petrology, v. 55, n. 3, p. 312-321.

Williams, L.A., Parks, G.A. and Crerar, D.A., 1985, Silica diagenesis, I. Solubility controls: Journal of Sedimentary Petrology, v. 55, n. 3, p. 301-311.

Wilson, M.D. ed., 1994, Reservoir quality assessment and prediction in clastic rocks: SEPM Short Course 30, 432 p.

Wilson, M.D. and Stanton, P.T., 1994, Diagenetic mechanisms of porosity and permeability reduction and enhancement, *in* M.D. Wilson, ed., Reservoir Quality Assessment and Prediction in Clastic Rocks: SEPM Short Course 30, p. 59-118.

Wood, J.R., 1994, Chemical diagenesis, *in* M.D. Wilson, ed., Reservoir Quality Assessment and Prediction in Clastic Rocks: SEPM Short Course 30, p. 119-136.

This thesis is accepted on behalf of the
Faculty of the Institute by the following committee:

_____
Advisor

_____

_____

_____

12-18-01
_____
Date

I release this document to the New Mexico Institute of Mining and Technology.

_____   12/14/01
Student's Signature   Date